Performance enhancement of Building-Integrated Concentrator Photovoltaic system using Phase Change Materials

Submitted by Shivangi Sharma to the University of Exeter

as a thesis for the degree of

Doctor of Philosophy in Renewable Energy

In October 2017.

I certify that all material in this thesis which is not my own work has been identified and that no material has previously been submitted and approved for the award of a degree by this or any other University.

Signature: ……..

Dedication

The Omnipresent, Omnipotent and Omniscient, ever beginning and the everlasting;

the Alpha and the Omega.

Abstract

Building-integrated Concentrator Photovoltaic (BICPV) technology produces noiseless and pollution free electricity at the point of use. With a potential to contribute immensely to the increasing global need for a sustainable and low carbon energy, the primary challenges such as thermal management of the panels are overwhelming. Although significant progress has been made in the solar cell efficiency increase, the concentrator photovoltaic industry has still to go a long way before it becomes competitive and economically viable. Experiencing great losses in their electrical efficiencies at high temperatures that may eventually lead to permanent degradation over time, affects the market potential severely. With a global PV installed capacity of 303 GW, a nominal 10 °C decrease in their average temperatures could theoretically lead to a 5 % electricity efficiency improvement resulting in 15 GW increase in electricity production worldwide. However, due to a gap in the research knowledge concerning the effectiveness of the available passive thermal regulation techniques both individually and working in tandem, this lucrative potential is yet to be realised.

The work presented in this thesis has been focussed on incremental performance improvement of BICPV by developing innovative solutions for passive cooling of the low concentrator based BICPV. Passive cooling approaches are selected as they are generally simpler, more cost-effective and considered more reliable than active cooling. Phase Change Materials (PCM) have been considered as the primary means to achieve this. The design, fabrication and the characterisation of four different types of BIPCV-PCM assemblies are described. The experimental investigations were conducted indoors under the standard test conditions. In general, for all the fabricated and assembled BICPV-PCM systems, the electrical power output showed an increase of 2 %-17 % with the use of PCM depending on the PCM type and irradiance. The occurrence of hot spots due to thermal disequilibrium in the PV has been a cause of high degradation rates for the modules. With the use of PCM, a more uniform temperature within the module could be realised, which has the potential to extend the lifetime of the BICPV in the long-term. Consequentially, this may minimise the intensive energy required for the production of the PV cells and mitigate the associated environmental impacts.

Following a parallel secondary approach to the challenge, the design of a micro-finned back plate integrated with a PCM containment has been proposed. This containment was 3D printed to save manufacturing costs and time and for reducing the PCM leakage. An organic PCM dispersed with high thermal conductivity nanomaterial was successfully tested. The cost-benefit analysis indicated that the cost per degree temperature reduction (£/°C) with the sole use of micro-fins was the highest at 1.54, followed by micro-fins + PCM at 0.23 and micro-fins + n-PCM at 0.19.

The proposed use of PCM and application of micro-finned surfaces for BICPV heat dissipation in combination with PCM and n-PCM is one the novelties reported in this thesis. In addition, an analytical model for the design of BICPV-PCM system has been presented which is the only existing model to date. The results from the assessment of thermal regulation benefits achieved by introducing micro-finning, PCM and n-PCM into BICPV will provide vital information about their applicability in the future. It may also influence the prospects for how low concentration BICPV systems will be manufactured in the future.

Acknowledgements

While writing the concluding sections of my thesis, I revisited the brief history of my last three and a half years; the last 182 weekends and 1278 days of my life that have been filled with overwhelming emotions; magnitude of struggles, anxieties, fears and tears gradually giving way to faith, hope, strength and smiles. The seed for the PhD plant germinated in my mind long ago. I was always motivated me to complete my father's dream, since I was seven. The great sacrifices him and my mother made in their lives for me to achieve this is beyond human explanation. Thank you Maa and Papa!

My dream was shaped by my supervisor Prof. Tapas Mallick, without whose confidence in me, this thesis wouldn't have been here. Thank you Tapas, for the willingness to have me in your group, for giving the opportunity to explore and for overlooking my trivial mistakes. My co-supervisor, Dr. Asif Tahir has been my teacher, proof-reader, friend, and guide through all thick and thin. Thank you Asif, for listening to me patiently and for the objective advices that you shared. The interesting discussions with Senthil helped in unwinding and Mohammad's kind words always encouraged me.

Thanks to James, Mark, Chris and Daniela for timely remedy to ESI issues and to Malcolm and Bahareh for their help with running the intricate instruments. I cannot forget the teaching experience given by Adam, Ken, Justin and the students; I possibly learnt more from you guys than you from me. During my visit to Prof. Reddy's & Subarna di's labs, I was glad to meet: Jawahar, Ajas, Nehal, Ruchita, Harsh & Sumit. My fellow researchers contributed in more than one ways to shape my research; Garry, Nazmi and Rashid, your backing can't be forgotten. Nabin, Thank you for your selfless help. My lab-buddies burning the midnight oil- Joe, Hameed, Prabhu, Wayne and Bandar, kudos to you guys. Cheers to you Leo, my hard working secret third supervisor! Katie, you are an inspiration! Thank you Idris, Adrian, Walid, Hasan, Alice and Sourav. My friends at work: Sam & Adeline, Tomasa & Atta, Burcin & Rob, Sidan, Nadia, Homan, Esra, Imran, Jess & Gio, Ben, Pavel, Viviana, Maru Lucy, Rachel and many more, I look forward to more fun-filled moments with you all, we are a family!

My pillar of support, without whose unconditional love and affection, I wouldn't stand up after those multiple breakdowns. A big Thank you, Ben & Jasmine, and my beloved Isaac; my home away from home. Thank you Harsh & Sweta, my soulmate Mitina and

Khadija, and Nick. I thank Amy, Leena di, and Roy & Naghme for their support. Thank you to Julie, Phil, and Janet.

My friends from school and undergrad: Gaurav, Malli, Neeru di, Rohit, Jyani saab, Lambaji & Renu, Raharji, deserve my grateful Thanks for taking time out to listen to my ranting. My ex-colleagues and my lifelong friends who embraced my decision to quit the high profile job for undertaking PhD, and also continued to support me emotionally and financially: Raj & Neelam Bhabhi, Srinu & Nalini, Martin and Anand, Sameera, Lynne, Suzy, Dhruw, Jags, Rupesh, Umesh, Chuchu, Richa, Sunny & family, Chumki, Tutu, Ornob, Bagho & Sharada, Rahul & Pilar, I thank you all for making my life colourful with what we share. Dave and Derek, I'd love to watch another play at Royal Shakespeare.

Thank you Gill, my yoga teacher, your sense of compassion is amazing! Thanks to Stacey, my ex-Zumba instructor, and to Dr. Yadav for the amazing medical advises. Chrissie & Tony, my amazing landlords, thank you for your kindness and timely repairs, you made the house a comfortable place to write in. My flatmates Debbie and Gosia are priceless.

My special thanks to the people at Emmanuel, whose words of encouragement showed me the silver lining whenever I felt disappointed; Charles, Nigel & Kate, Yinka & Ley, Loyda, Yan & Teo, Lynda & John, Chris & Nicky, David & Wendy, Annie, Carrie, Nathan & Sophie, Roman, Jane and others. From giving hugs and lifts, to sharing your food and families, you have set yourselves class apart as true followers of Christ. You all will always have a special place in my heart. No words can compare to your affection towards me: Sue and Colin, Thank you. I am grateful to you, Mr. Aitken for the encouragement and the gift of your recently published book *Psalms for people under pressure*, it's truly motivating.

My strongest support of all times David (how badly I miss you), and Burcin, you're adorable and the foundation of my life in Penryn, thank you. Thank you Joe for helping me improve my writing skills and much more, as a person. To conclude, a bouquet of Thanks to my family of mum and dad, my little wonder, brother Antariksha, my beloved sister, Shubhangi Jiji and the newest addition on our family, Raj Jeeju, for putting up with me for the last three decades.

List of Contents

List of Tables

List of Figures

Nomenclature

a	Minor axis of ellipse (cm)
A	Front surface area of the system (m^2)
A_a	Collector or entry area of the concentrator (m^2)
A_{fins}	Area of micro-fins (m^2)
A_r	Receiver or exit area where the light leaves the concentrator (m^2)
b	Major axis of ellipse (cm)
c	Speed of light in vacuum ($c = 2.998 \times 10^8$ ms^{-1})
C_g	Geometrical concentration ratio (aperture area ÷ receiver area)
C_o	Optical concentration ratio
C_P	Specific heat of PCM ($Jkg^{-1}K^{-1}$)
d	Interatomic layers distance in a crystal
E	E is the energy of a photon (J)
E_g	Band gap (V)
EAR	Elliptical Aperture Ratio
h	Planck's constant ($h = 6.626 \times 10^{-34}$ J·s)
H	Height of micro-fins (m)
He	Heliocon value
H_L	Latent heat of PCM (Jkg^{-1})
h_{fins}	Heat transfer coefficient of the micro-finned surface ($Wm^{-2}K^{-1}$)
h_{flat}	Heat transfer coefficient of the un-finned surface ($Wm^{-2}K^{-1}$)
h_1	Heat transfer coefficient at front surface ($Wm^{-2}K^{-1}$)
h_2	Heat transfer coefficient at rear surface ($Wm^{-2}K^{-1}$)
I	Applied direct current (A)
I_c	Characteristic current of solar cell (A)
I_{ph}	Photocurrent (A)
I_{Max}	Maximum current generated by the PV (A)
I_{Max_Conc}	Maximum current generated by the CPV (A)
I_r	Irradiance on photovoltaic (Wm^{-2})
I_{SC}	Short circuit current (A)
k	Boltzmann's constant
k_p	Thermal conductivity of PCM ($Wm^{-1}K^{-1}$)
$k_{n,PCM}$	Thermal conductivity of n-PCM ($Wm^{-1}K^{-1}$)
k_n	Thermal conductivity, nano CuO ($Wm^{-1}K^{-1}$)

L	Length of micro-fin base (m)
m	Mass of the PCM (kg)
n	Number of micro-fins
P_m	Maximum power output (W)
q	Electron charge (C)
Q_{in}	Heat supplied by the DC supply (W)
Q_l	Latent thermal energy (J)
$Q_{l,\ overall}$	Overall thermal energy for phase change (J)
Q_s	Heat energy stored in the PCM (J kg^{-1})
R_s	Series resistance (Ω)
R_{sh}	Shunt resistance (Ω)
S	Spacing between micro-fins (m)
ΔT	Change in PCM temperature (°C)
T_{amb}	Ambient temperature (°C)
T_{air}	Steady state air temperature (°C)
T_c	Module central temperature (°C)
T_{fins}	Steady state micro-fin temperature (°C)
T_m	PCM melting peak temperature (°C)
$T_{PV,t}$	Temperature on PV at time t (°C)
$T_{PV,\ t+\Delta t}$	Temperature on PV at time t + Δt (°C)
t_b	Thickness of the micro-fin array's base (m)
t	Thickness of micro-fins (m)
Δt	Time step (s)
t	Time (s)
Uh	Prefix for uncertainty
V	Applied direct voltage (V)
V_c	Characteristic voltage of the solar cell (V)
V_{OC}	Open circuit voltage (V)
W	Width of the micro-fin array base (m)
W_e/kg	Unit for mass-specific power
Δx	Depth of the PV/PCM system (m)

Greek Symbols

α	Volumetric expansion coefficient (%)

Φ	Particle volumetric concentration
λ	Wavelength of the photon (nm or m)
ρ	Density (kgm^{-3})
η_{elec}	Electrical efficiency of the solar cell
θ	Angle of incidence at which the cleavage faces of crystals reflect
ν	Frequency (s^{-1} or Hz)

List of Publications

Published with peer review process

1. **Sharma, S.**, Micheli, L., Chang, W., Tahir, A., Reddy, K. S., Mallick, and T.K.: *Nano-enhanced Phase Change Materials for Thermal Management of BICPV Applications.* Applied Energy, **2017** (Available online 21 September 2017).

2. **Sharma, S**., Tahir, A., Reddy, K. S., Mallick, and T.K.: *Performance enhancement of a Building-Integrated Concentrating Photovoltaic system using phase change material*. *Solar Energy Materials and Solar Cells* **2016**, 149, 29-39.

3. Siyabi, I., **Sharma, S**., Mallick, T.K., Sundaram, and S.: *Thermal regulation of building-integrated concentrating photovoltaic system using phase change material*. AIP Proceedings, **2016**, 1766, 090001.

4. **Sharma, S**., Sellami, N., Tahir, A., Reddy, K. S., Mallick, and T.K.: *An experimental investigation into passive temperature regulation of a novel WICPV system with phase change material. EUPVSEC-32* Proceedings, **2016**.

5. **Sharma, S**., Tahir, A., Reddy, K. S., Mallick, and T.K: *Enhancing the performance of BICPV systems using phase change materials*. AIP Proceedings, **2015**, 1679, 110003.

Conferences

1. **Sharma, S**., Micheli, L., Tahir, A., Reddy, K. S., Mallick, and T.K.: *Nanomaterial Enhanced PCM for Micro-Finned Thermal Management Applications: An Experimental Investigation*. International Conference on Nanotechnology, Nanomaterials &Thin Films for Energy Applications, Liverpool, UK, **2016.**

2. **Sharma, S**., Tahir, A., Mallick, and T.K.: *Thermal regulation of a BICPV system using Phase Change Material: Experimental simulation*. The UK Thermal Energy Storage Workshop, London, UK, **2016**.

3. **Sharma, S**., Sellami, N., Tahir, A., Reddy, K. S., Mallick, and T.K.: *An Experimental Investigation of Passive Cooling of a BICPV System Using PCM*. UK Energy Storage Conference, University of Birmingham, **2015**.

4. **Sharma, S**., Tahir, K. S., Mallick, T.K.: *Phase-Change Materials for Cooling Of Concentrating Photovoltaic Systems*. Exploring Research in Cornwall Conference, Penryn, Cornwall, UK, **2015**.

5. **Sharma, S**., Tahir, A., Reddy, K. S., Mallick, and T.K.: *Utilisation of Phase-Change Materials for Concentrating Photovoltaic Applications*. International Workshop on Integrated Renewables for Autonomous Power Supply, Cornwall, UK, **2014.**

Chapter 1. Introduction

Solar energy is the largest renewable energy resource available on Earth. In one hour the solar energy received by the Earth is sufficient to satisfy the global human energy needs for an entire year. The elegance of solar energy being harnessed and made useable in general lies in a very simple scientific phenomenon where light falls on a semiconductor and produces noiseless, pollution-free electricity. The semiconductor revolution, advancement in production technology and policies supporting solar energy have all contributed immensely to realise its potential during the last four decades. Concentrating photovoltaic (CPV) technology has added a new dimension to the traditional solar Photovoltaic (PV). Integration of CPV into buildings for producing electricity at the source of use and the potential for saving costs by replacing building elements drives building-integrated concentrating photovoltaic (BICPV) into emerging new markets.

This chapter starts with an overview on PV, CPV and BICPV and reviews the state of the art of these technologies along with the associated technical parameters in the first part. PV is further categorised into BAPV (building-attached photovoltaic) and BIPV (building-integrated photovoltaic). From here, it follows on with an introduction to the different types of solar concentrators; a feature that differentiates a traditional PV from a CPV. The advantage and limitations of these technologies, areas of existing as well as proposed applications, current challenges and some available solutions pertaining to each of these areas are discussed. In latter sections following the background information, the important research questions related to challenges with BICPV thermal regulation, the rationale for pursuing this research, the key aims and the employed research methodology are summarised. Finally, in the last part, the salient features of this research work based on low concentration BICPV, the distinguishable in-scope elements and the thesis organisation are elucidated.

1.1 Background

Solar energy, with its tremendous availability of 120 petajoules per second on the Earth shows immense potential, having annual net energy production increase by an average 8.3 % and a projected generation of 859 billion kWh, which was accountable for a 15 % of the 5.9 trillion kWh of new renewable generation by 2014 [1]. Over the last one and a

half decades, PV markets have grown at a rate of 42 % compounded annually (2000-15) out of which Si-based PV accounted for about 93 % (with 68 % contribution was from multi-crystalline) and about 7 % from thin film technologies to the total annual production in 2015 [2]. Owing to increasing efficiencies, the Si usage in cells in the last decade have reduced from around 16 g/W_p to 6 g/W_p. [2]. Fig. 1 shows the global PV power production capacity (in GW) and annual additions since 2005, when solar PV contributed to 40 GW_p growing to a 227 GW_p in 2015, an almost six-fold increase within a decade.

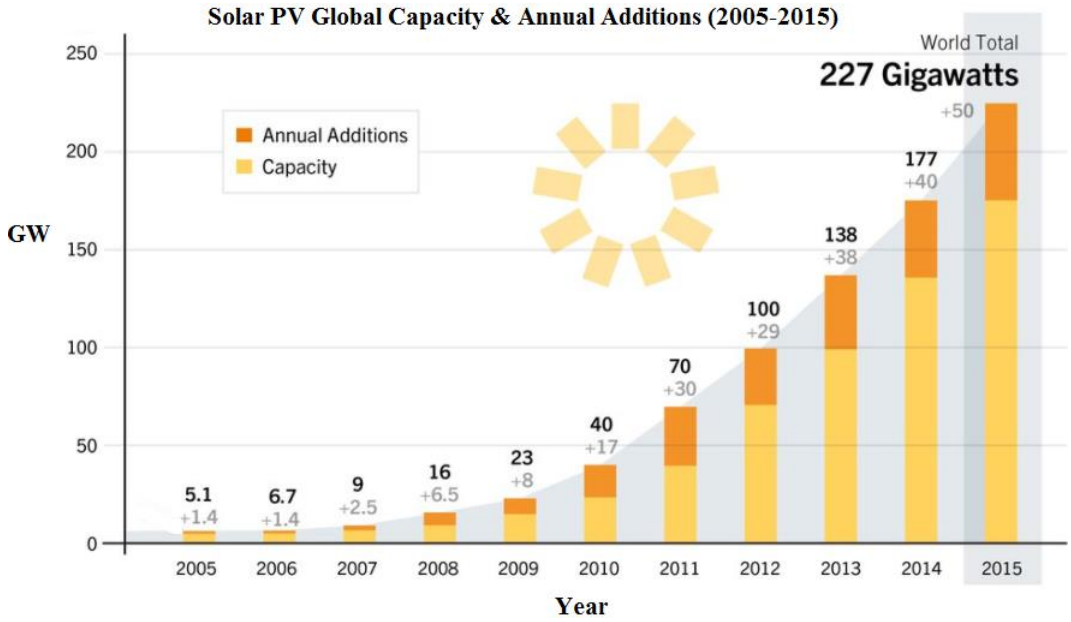

Figure 1: Global PV power production capacity and annual additions (2010-2015)[3].

Considering U.K. scenario (Fig. 2), by April 2017, the overall PV capacity stood at 12,098 MW across 913,669 installations, with an increase of 7 % (792 MW) compared to compared to last year [4]. Of this total installed solar PV capacity, 47 % (5718 MW) is contributed by large-scale installations (>5 MW) and 21 % (2486 MW) by small-scale (0-4 kW) installations. The commercial roofs account for only 5 % of all solar deployment to date [4]. The integration of PV into architectural design is both significant and innovative because buildings are responsible for a major proportion of total energy usage. The data for the primary energy consumption in the domestic sector buildings in the U.K. Fig. 3 shows that a major 66 % of the share goes towards space heating, followed by 17 % towards water heating. The use of PV with the buildings can act as a stand-alone or a grid-connected micro-renewable electricity energy source.

BIPV/BAPV have the potential to contribute to clean energy production at the site of use and unburden the load on the grid by decentralising electricity production.

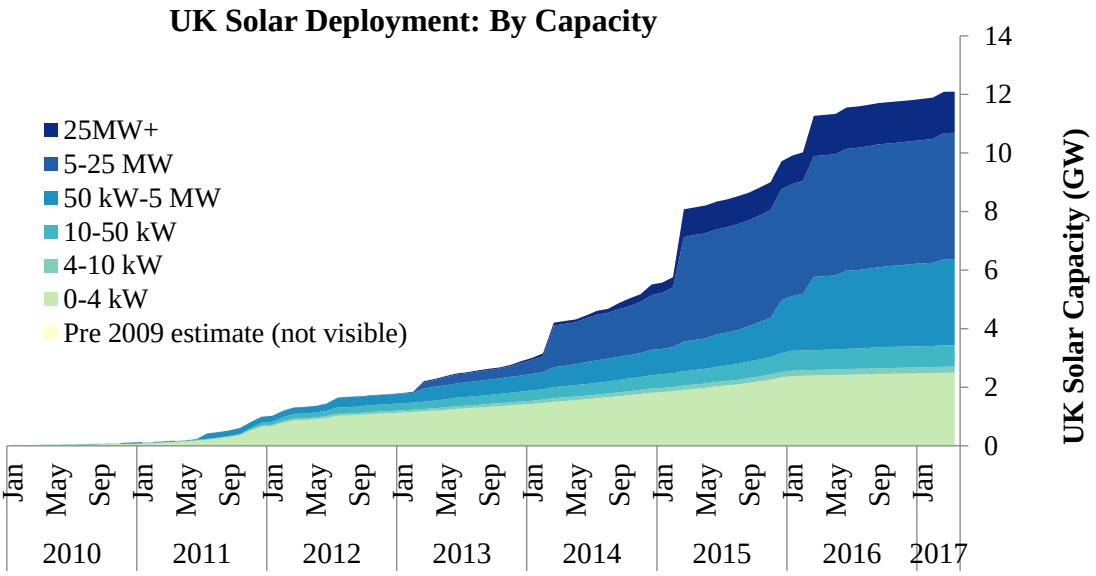

Figure 2: Solar photovoltaic deployment in the UK since 2010 [4].

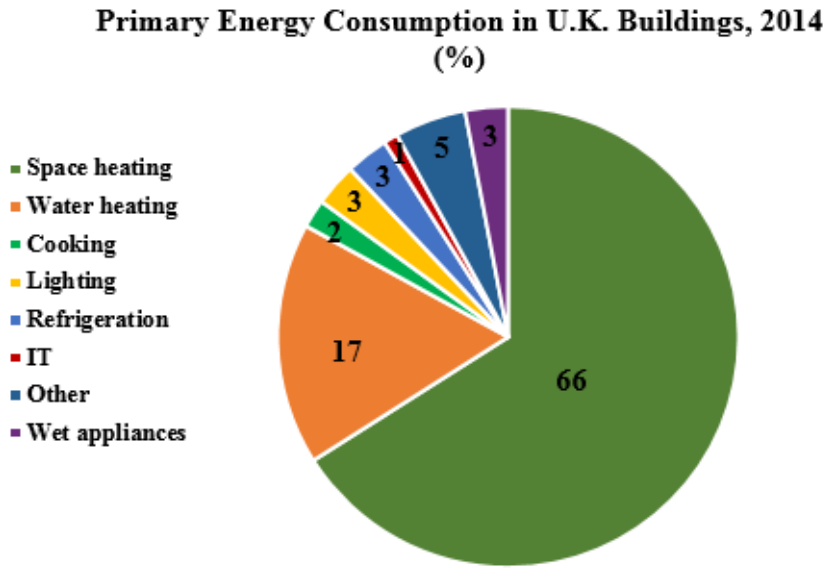

Figure 3: U.K. primary energy consumption within domestic sector [5].

A summary of the international BIPV research activities that have taken place over the last four decades clearly shows the exponential growth in the sector. In particular, the last decade has seen the evolution of new societies, task committees, international conferences and events, which signifies the presence of BIPV knowledge spreading globally (Fig. 4).

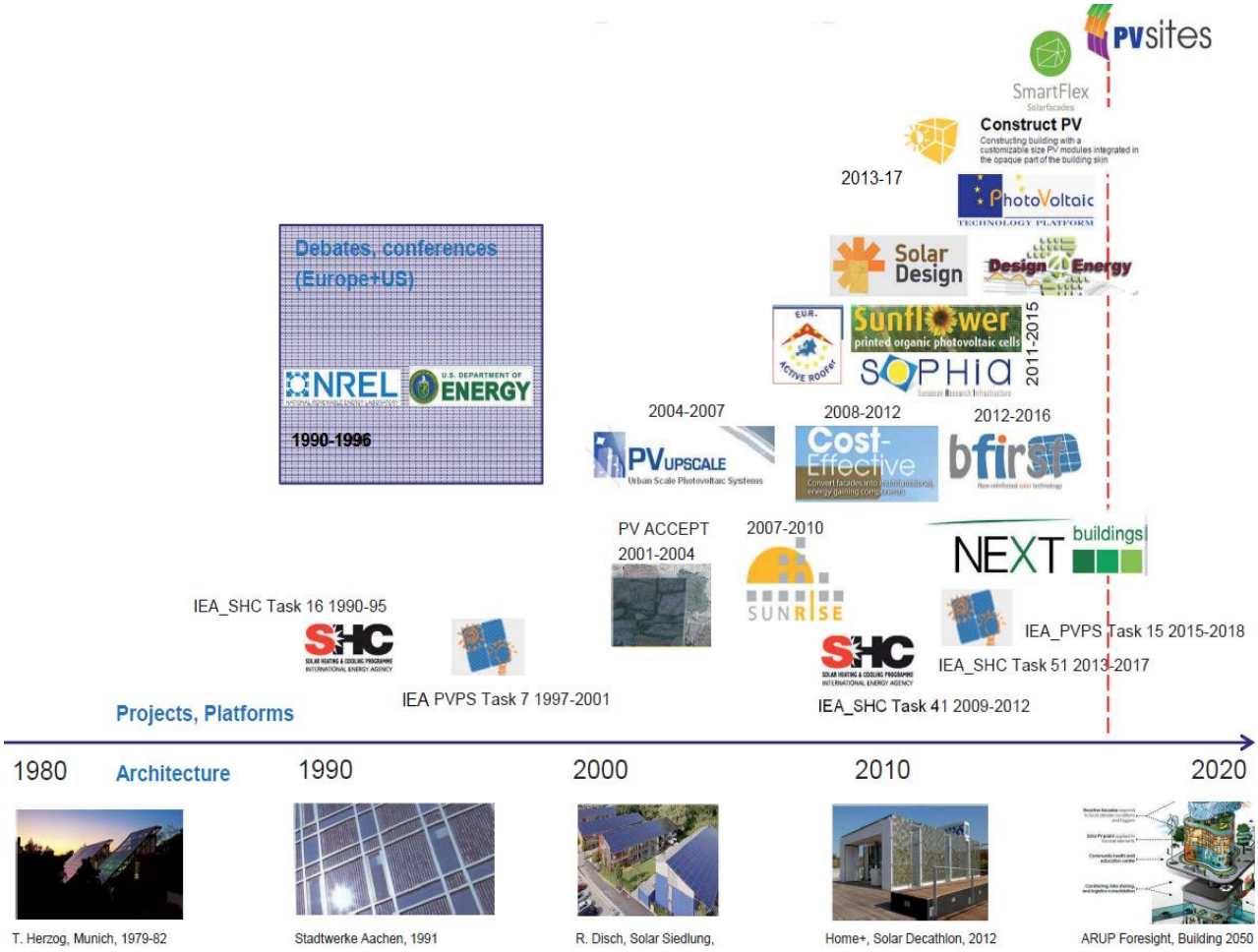

Figure 4: International BIPV research activities [6].

PV attached to buildings contribute to: (a) electricity production at the point of use thereby reducing electricity transmission and distribution losses, (b) economic savings in terms of building materials replacement, and (c) provision of several types of flexible and innovative solutions based on less material requiring PV technologies [7]. They also offer a promising solution for electrification of rural areas cut off from main electricity grids, especially in developing countries. Besides, the recent government policies in many countries such as the European Union pushes towards energy-neutral buildings, which not only drive building integration of PV but also benefits by heat generation and daylight regulation by transmission of diffuse sunlight through transparent parts of the emerging PV systems [8]. However, there are policy-related and technical challenges to adopting BIPV, and more importantly, BICPV, on a larger scale, some of which are explored within this thesis and the potential solutions are suggested.

1.2 Overview of Photovoltaics

The term *Photovoltaic*, abbreviated as PV is defined in Collins English Dictionary, 2012 as (adj.) *of, concerned with, or producing electric current or voltage caused by electromagnetic radiation, especially visible light from the sun*. The origin of the term lies in the Greek words *phôs* or *phōt* meaning light and *voltaic* meaning *pertaining to electricity or electric current.* PV technology is based on the science of photovoltaic effect, which is used to convert sunlight directly into electricity when exposed to radiant light carrying higher energy than their band gap energy. The electrons in the valence band gain energy from the incident photons get excited and jump up to the conduction band, thereby conducting electricity. The energy and wavelength or frequency correlation for an electromagnetic wave is given by Planck's equation (Eqn. 1)

$$E = h\nu = \frac{hc}{\lambda} \quad \textbf{(1)}$$

Where E is the energy of a photon (J), h is the Planck's constant (h = 6.626 × 10^{-34} J·s), c denotes the speed of light in vacuum (c = 2.998 × 10^{8} ms^{-1}), ν is the frequency (s^{-1} or Hz) and λ is the wavelength of the photon (nm or m).

PV conversion of solar energy directly into electricity without the need for a heat engine make them rugged and simple in design with few maintenance needs [9]. Amongst all other renewable sources, the energy produced by PV systems are deemed advantageous due to the reasons [10] cited below:

- No moving parts; reduced wear and tear, Noiseless operation
- No threat of fluids or gas leakage compared to some solar-thermal systems
- No fuel consumption to operate or for start-up
- Provide a quick response producing full output almost instantaneously
- No pollutants during electricity production (except manufacturing, disposal)
- Involve less maintenance time and cost after appropriate installation
- Majorly dependent on abundantly available silicon for manufacturing
- Modularity allows wide-range of applications. Small-scale (remote and residential use), Intermediate-scale (community, small business), Large-scale (centralised)
- Extensive power-handling ability, range from microwatts to megawatts

- High power-to-weight ratio: suitable for building application such as roof-top
- Can be installed on-site for decentralised power production or grid-connected for centralised power production and distribution

1.3 PV: Building applications

Depending on the point of application, PV could be either retrofit to an existing and already constructed building (externally) or integrated with the building, replacing the building material (internally) wherein the PV panel forms an integral part of the building itself, hence the names building-applied or building-attached (BAPV) and building-integrated (BIPV) respectively. As a part of the building skin, PV can be used as a basic or functional construction element such as tile or cladding panel and as modular-unitized system combining BIPV modules with the building or electrical sub-constructions (prefabrication, plug & play etc.) [6]. BAPV systems are simpler and quicker in installation with lower installation costs but they increase the building load and due to repeated constructions, there is a waste of the building materials that isn't the case for BIPV systems as PV arrays are integrated directly into the building skeleton [11]. PV installers and commercial companies [12] believe that retrofitting or BAPV is "neither a good use of material resources nor does it achieve the best aesthetic, functional or cost effective outcomes". Further, a study in Shanghai compared the environmental and economic benefit in terms of payback period for a 3 kW BAPV and a 10 kW BIPV panel under the yearly total solar radiation quantity of 1181.3 kWh/m^2 and concluded that the two installations produced 3114.3 kWh and 9890.7 kWh respectively at the monthly performance ratios (relates the actual and theoretical energy outputs of the PV system) of 80.8 % and 80.3 % and system efficiencies of 10.8 % and 11.2 % [11]. The energy payback time and greenhouse-gas payback time were 4.2 years and 3.1 years respectively, thus suggesting that BIPV perform better than BAPV, and hence the obvious choice for building application of PV.

BIPV, within the building envelopes, solve the primary purpose of generating electrical energy for use at the point of generation, however, the device itself can work as a replacement for construction elements such as roofs, facade claddings, windows, and static or dynamic shading elements [13] and are capable of delivering electricity at less than the cost of grid electricity to end users in certain peak demand niche markets [14].

BIPV are modular in nature, leading to reduced installation time with less regular maintenance needs and offer an alternative to the use of land for PV modules especially in urban areas where land availability is a challenge. In addition, the cost for free land needed for installation can be saved. The technical standards of BIPV are defined in BS EN 50583. BIPV system performance depends on (a) the solar radiation availability which in turn depends on the geographical location, climate and building orientation and (b) the collection ability of the device, which is determined by the PV efficiency, inclination etc. [15]. The integration of PV into buildings are based on many factors such as their design, purpose, building and safety regulations and aesthetics, which are schematically illustrated in Fig. 5. As building elements, BIPV can contribute in one or more of the following ways: by providing mechanical rigidity, structural integrity, weather protection, energy economy and thermal insulation, fire and noise protection, and function as a partition between the indoor and the outdoor surroundings [13].

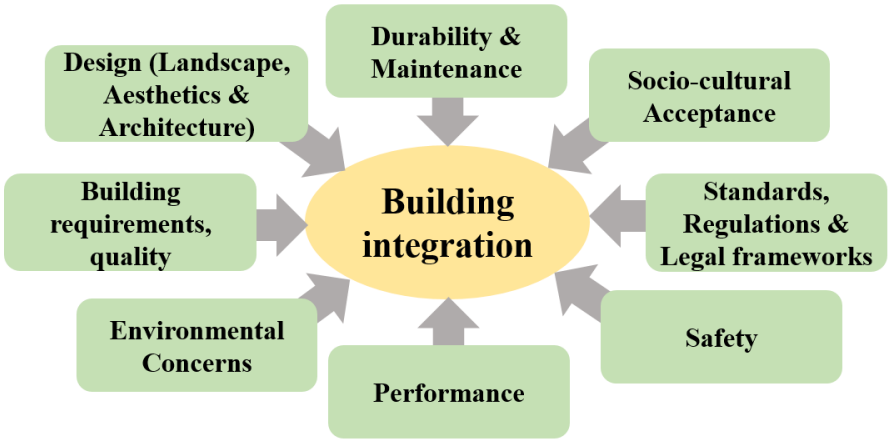

Figure 5: Important parameters for building integration or application of PV technology.

Depending on the back sheet material, BIPV modules can be classified into rigid (glass, metal etc.) or flexible (organic, dye-sensitized, perovskite solar cells or thin-film technologies). While rigid BIPV can be used to replace traditional cladding materials, flexible BIPV are used mostly in portable applications such as building fabrics. The majority of BIPV relies on crystalline silicon solar cell based panels in which the level of light transmission through the modules can be altered only by adjusting the inter-cell spacing, whereas BIPV based on thin-film solar cells (a few μm thick semiconductor, vapour deposited on the conductive glass with a metal backed structure), offer semi-transparency through the use of laser ablation technology to selectively eliminate the

layers of material for light penetration [12]. For instance, a modern commercial design of using BIPV as a building element as shown in Fig. 6, where the completely recyclable, natural and fire resistant air incorporated rock-wool brings thermal insulation while the monocrystalline silicon solar cells protected by two layers of glass provide high structural rigidity forming a walkable roof for easy installation and maintenance [16]. In case of lightning, the protection is provided as all the elements are already connected and form the lightning grid, once connected to the ground, thus assuring the safety of occupants.

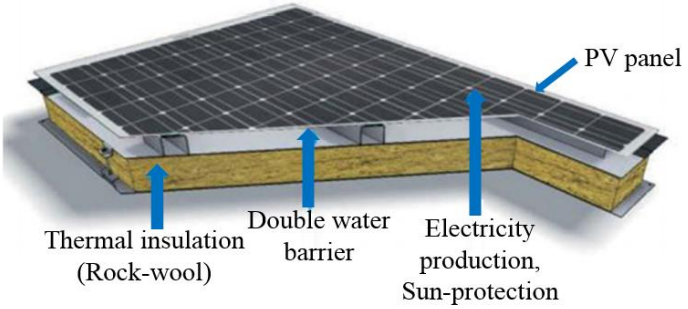

Figure 6: Design of a commercial BIPV by Designergy® (adapted from [16]).

BIPV systems can be categorised based on the PV technology they are built on, their applications and commercial availability, explained more clearly in Fig. 7.

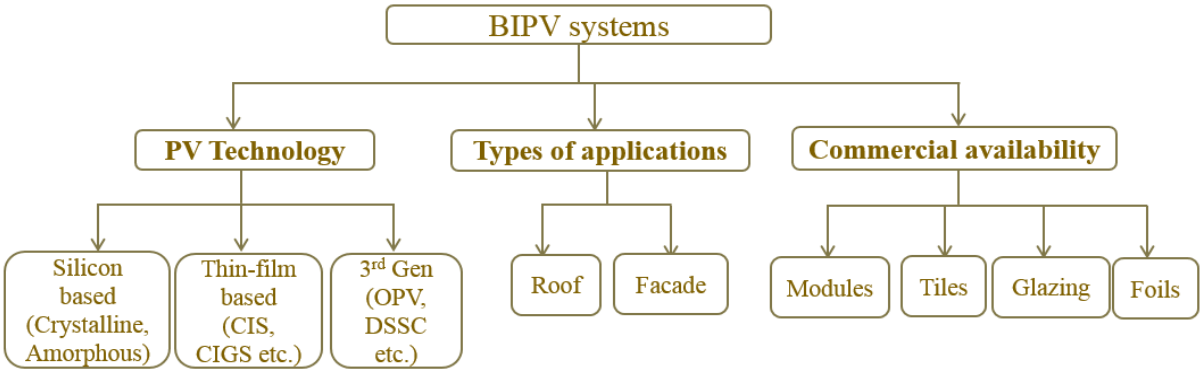

Figure 7: Classification of BIPV systems.

Although BIPV isn't a new concept, there are still many challenges related to the large scale adoption of this technology mostly due to the requirement of extensive planning and architectural challenges while further challenges include a lack of consistent markets, complexities in planning and construction process, a gap in available certified construction products, complicated installation methods requiring specialist know-how, lack of technical awareness in architects and planners and higher costs in addition to

constraints related to locations such as solar radiation availability throughout the day and maintenance etc. [6].

1.4 CPV: an overview

Concentrator Photovoltaic (CPV) technology is based on the general principle of using optical elements (working as radiation collectors) such as mirrors or lenses, to focus solar irradiance on a solar cell area, which is much smaller, compared to a conventional PV panel. The benefits of using concentration are:

- Increased solar radiation for photovoltaic conversion; higher electrical output
- Reduced semiconductor material usage for the same power output; saving costs and environmental impacts caused during solar cell manufacturing

1.4.1 Components

A schematic of the components forming a CPV assembly is given in Fig. 8. The key elements forming a CPV system are reflective or refractive optics, solar cells soldered to form a structure for desired electrical output and an external casing to support the assembly. Additionally, thermal management could be achieved by using heat dissipation methods such as active or passive cooling.

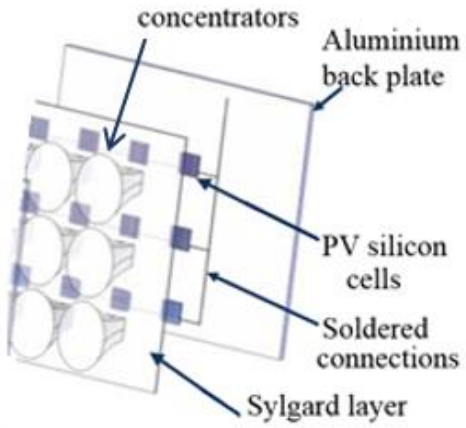

Figure 8: General components of a CPV system assembled together.

Tracking mechanism is required for accuracy in tracking the sun especially for high concentration systems based on more expensive multi-junction solar cells and it enables electricity production for prolonged hours. Each of these elements or components contributes individually and collectively to overall performance of CPV [17].

1.4.2 Concentration Parameters

The key parameters associated with concentrators are defined as:

- Geometric concentration ratio (C_g) or the number of suns, is the ratio of collector (entry) aperture area and receiver (exit) aperture area of the concentrator and is given by Eqn. 2

$$C_g = \frac{A_a}{A_r} \quad \textbf{(2)}$$

Where: A_a is the collector or entry area of the concentrator, the surface on which light is first incident; and A_r is the receiver or exit area where the light leaves the concentrator; (m^2)

- Optical concentration ratio (C_o), defined as the ratio of averaged irradiance or radiant flux integrated over the exit area and the insolation incident on the entry aperture (Eqn. 3).

$$C_o = \frac{\frac{1}{A_r}\int I_r dA_r}{I_a} \quad \textbf{(3)}$$

Where: I_r is the averaged irradiance or radiant flux; and I_a is incident irradiance; (Wm^{-2})

- The optical efficiency of CPV is given by (Eqn. 4).

$$\eta_{opt} = \frac{I_{Max\_Conc}}{C_g\, I_{Max}} \quad \textbf{(4)}$$

Where: I_{Max_Conc} is the maximum current generated by the CPV; (A) and I_{Max} is the maximum current generated by the PV (without the concentrator); (A).

Optical efficiency is an important parameter in determining the maximum limit of the concentration collection efficiency. Literature suggests that as it's possible to obtain over 90 % of optical efficiency which could contribute to the module efficiency reaching 45 % and full annual plant efficiency to increase from the current value of 12 % to 40 % [18]. The cost of concentration optics is generally lower than that of solar cells [19]. IEC 62108, a combination of two previous standards, IEEE 1513 and IEC 61215, are the primary standards for determining the electrical, mechanical, and thermal characterisation of CPV modules [20]. It is imperative to classify the concentrator type for deciding the

feasibility of use and assessing the suitability for an application and the cooling mechanism to be employed alongside.

1.4.3 Classification

The classification of solar concentrators can be based on optical characteristics; concentration factor or concentration ratio, distribution of illumination, focal shape and optical standards [21]. CPV classification based on concentration mode, geometry, primary and secondary optics and applications are discussed below (Fig. 9).

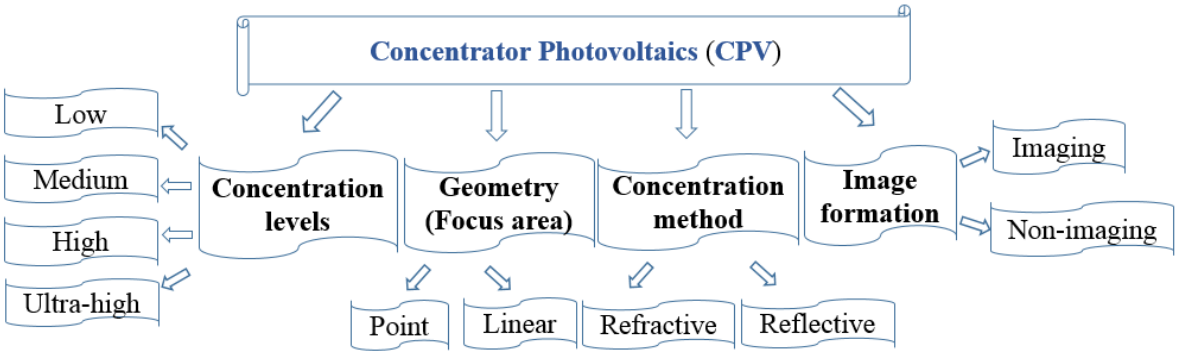

Figure 9: Classification of CPV systems.

i. Concentration Levels (Low, Medium, High)

Depending upon the geometrical concentration (C_g), CPV can be classified as low concentration (LCPV, with $2x < C_g < 10x$), medium concentration (MCPV, $10x < C_g < 100x$), high concentration (HCPV, $C_g > 100x$) [22] and ultrahigh concentration ($C_g > 2000x$) [23] where x signifies the number of times the solar light is concentrated, often expressed as the *number of suns*. Some authors have classified them as low (with C_g: 1-4x), medium (C_g: 40-300x) and high (C_g: 300-2000x) concentration [21, 24].

LCPV can be easily building-integrated as they mostly do not require electromechanical tracking of the sun and optical gain is achieved under both direct and diffuse radiation [25]. LCPV with higher concentrations can work efficiently with single-axis tracking [22]. The higher end of MCPV ($60 < C_g < 85$) is not deemed suitable for building applications due to their size. They can be used for power plants and many MCPV designs differ from typical planar modules. The optical precision and tracker accuracy requirements are not extreme but there are challenges during cell mounting for good voltage standoff and thermal management [26]. For HCPV, however, very high precision

two-axis tracking is mandatory, which is why HCPV can't be used for building integration. They also cause architectural and aesthetics issues. In some cases of HCPV, highly efficient but expensive solar cells are used, but concentration can still provide economic viability since the area of the cells can be up to about 100 times smaller than the light collection area [27].

Fresnel lenses, *Cassegrain* optics and point concentration reflector are generally used for HCPV applications while MCPV relies on either parabolic troughs or Fresnel optics (lens or mirror). LCPV uses either V-trough reflectors or compound parabolic concentrator (CPC) [28]. V-troughs direct light onto the receiver using flat mirrors and can achieve up to $C_g \sim 3x$. They are very easy to fabricate and capable of giving more output from PV as well as solar-thermal systems. The authors of [29] published that static V-trough collectors provide over an annual average $C_g > 1.2$ in highly diffuse solar fraction conditions, and were found suitable for PV. For convenience, $2 < C_g < 10$ is referred to as the low concentration within this thesis.

ii. Concentration Method (Refractive, Reflective, Luminescent)

The key approaches to achieve concentration are reflective, refractive and luminescent, plus total internal reflection which is included within refractive and luminescent types [23]. The fundamental difference between reflective and refractive modes is that the former is based on parabolic reflectors/mirrors (e.g. Cassegrain) while latter work with lenses (e.g. Fresnel lens). Fig. 10 schematically differentiates between (a) reflective versus refractive optics while (b) Fresnel lens versus conventional curved lens. Cassegrain mirror assemblies are made of a parabolic primary optic and a hyperbolical secondary optic [30]. The mirrors can achieve ultra-high concentrations ranging from 500-1000x and they are beneficial, as they don't have chromatic aberration. Fresnel lenses comprise of discrete concentric prisms patterned on a superstrate, either monolithically or with a separate material layer with the advantage of a high optical efficiency that can reach values up to 86 % [31]. Compared to ellipsoidal concentrators, the large size commercial Fresnel lenses (made of poly methyl methacrylate or silicone-on-glass) cost about 100 US$ each [32]. As compared to conventional lenses, Fresnel lenses use lesser material and have thinner dimensions for providing similar concentration levels as can be seen from Fig. 10 (b). Parabolic troughs are mostly utilised for concentrated solar power

using thermal generators and require single axis solar tracking, which is based on the rotation of the concentrator or receiver.

In mirror based systems, the solar cells are normally illuminated from below while in refractive set-ups, the cells are under the light source, which means that the cooling system may not cause any shading issues in case of lenses whereas for mirrors based set-ups, it's an important design consideration [33]. The benefits of using a Fresnel lens refractor or a parabolic mirror are comparable as a function of the luminosity of the concentrator, however, the achievable gain is greater for a parabolic mirror than a flat lens but is lower than a curved lens [34]. As Fresnel lenses offer more flexibility in optical design, allow for uniform flux on absorber, and are less prone to manufacturing errors, they are more suitable for PV systems [35]. In fact, due to the reasons mentioned above, refractive mode is generally deemed more appropriate for PV while reflective optics find their applications in solar thermal systems.

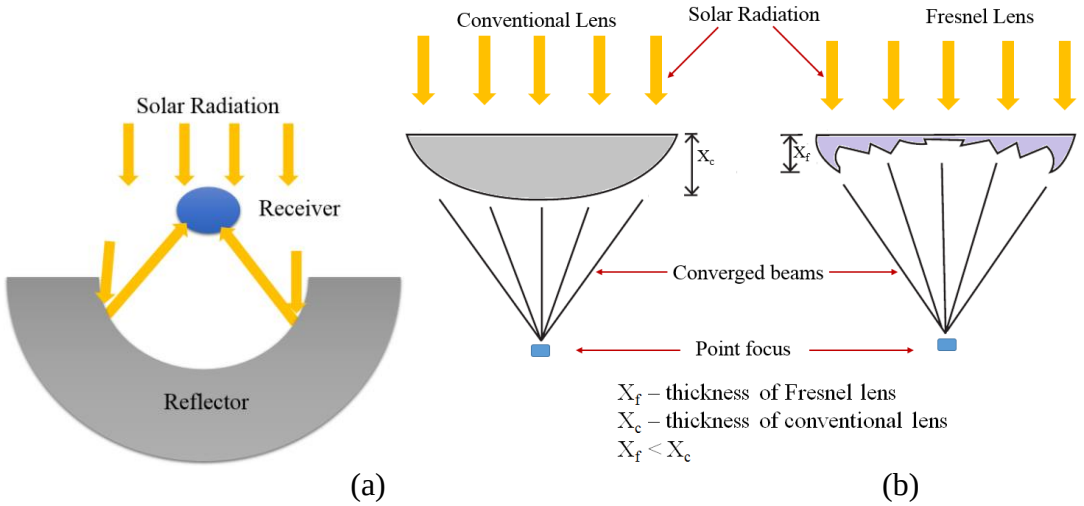

Figure 10: Schematics of a: (a) parabolic trough (reflective) solar collector versus (b) conventional lens and Fresnel lens (refractive). The Fresnel lens thickness (X_f) is much lesser than that for a curved conventional lens (X_c) for the same concentration.

The third category of concentrators falling under this sub-category are the Fluorescent / Luminescent Concentrators (LSC), which are capable of concentrating both the direct and the diffuse radiations without any tracking systems. *Weber* and *Lambe* [36] proposed LSC for PV applications in 1976. LSC consists of a transparent sheet doped with luminescent organic dyes to absorb sunlight and focus it on to the solar cell using the principle of total internal reflection. Their efficiencies are limited because of photon emission within the escape cone, re-absorption of emitted photons by the dye and the matrix absorption [37].

Quantum dot concentrators comprise of quantum dots seeded in a plastic material suitable for building-integration and capable of using both direct and diffuse solar radiation [38]. A typical example is an organic solar concentrator.

iii. Image Formation (Imaging and non-imaging)

Imaging concentrators are classified as the more conventional optics such as parabolic reflectors/mirrors or Fresnel lenses in which the formation of an image is a necessary or fundamental requirement. Non-imaging concentrators (*anidolic* optics) on the other hand, refer to those concentrators that collect the radiation on a larger aperture area and focus on to a smaller area, which is wider compared to a focal point, without forming an image of the light source. Proposed by *Hinterberg* and *Winston* in 1965 and grown to popularity with design modifications in the early 1970s, CPC are a classic example of non-imaging concentrators [39]. CPC can collect a wide proportion of the available direct and diffuse radiations. A schematic of a CPC is given in Fig. 11(a) and the working in Fig. 11(b).

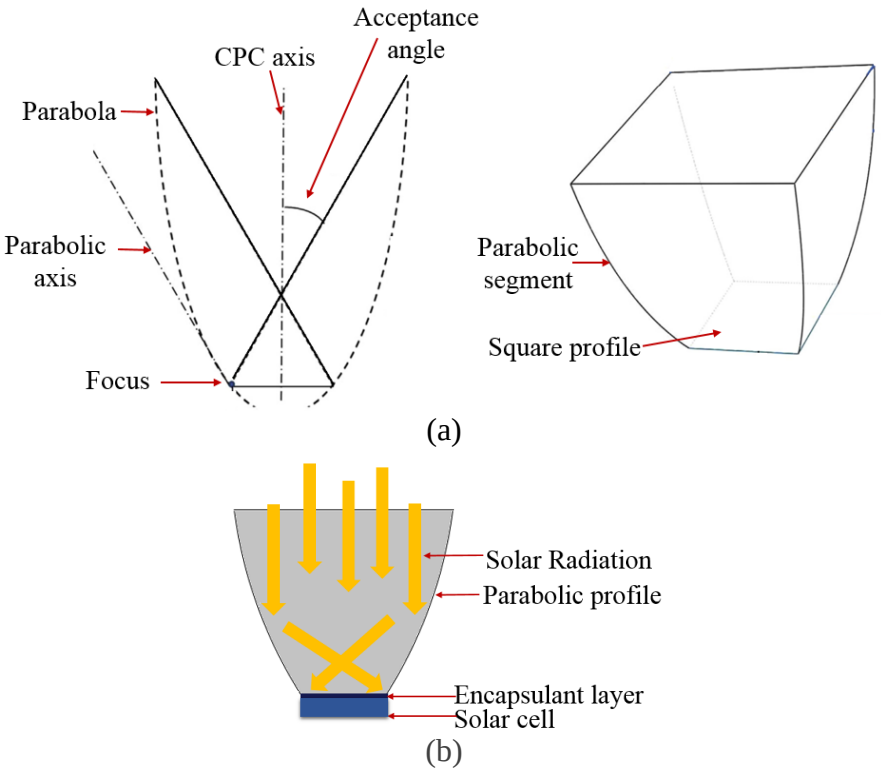

Figure 11: (a) Schematic design and (b) working of a CPC.

The term non-imaging has often been referred to as a misnomer as the non-imaging concentrators are also imaging devices. Nevertheless, the image formation is not required or the quality of image at the exit aperture is not of much importance, although image

formation is not necessarily excluded [40]. Non-imaging concentrators obey the *edge-ray* principle, which states that non-imaging devices can be designed by mapping the edge rays from the source to the target edge, or if the source boundary rays can be directed to the edges of the target, then all the rays in between will also be directed to the target area [41]. As these designs offer more simplicity and superior collection efficiency in terms of concentrating the incident radiation much greater than the imaging systems, ideally non-imaging concentrators are preferred especially for stationary applications. Other advantages include uniformity in radiation on flat absorbers, widest acceptance angles and economic benefits in terms of no investment in tracking costs such as installation, operation and maintenance [39].

iv. Focus area (Point or Linear focus)

Both Fresnel lens refractors and parabolic reflectors can be further designed as either point-focus (3D) or linear-focus (2D) concentrators. The point-focus concentrators focus the light on each individual solar cell while in line-focus systems such as parabolic troughs or linear Fresnel lenses the light is focused on a row of solar cells [33] as illustrated in Fig. 12.

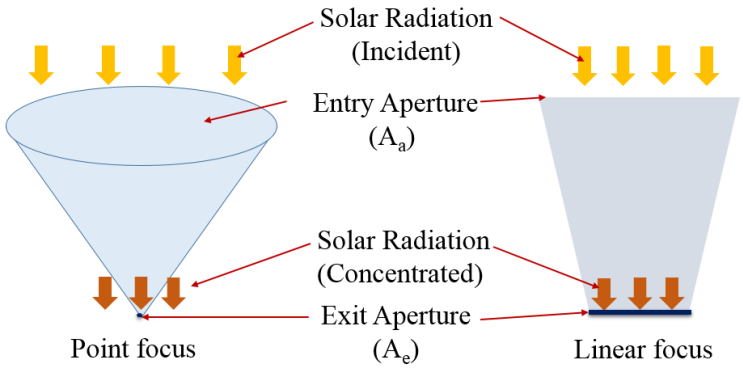

Figure 12: Schematics of a point focus versus linear focus refracting concentrator.

v. Geometry of Optics

On the basis of geometry (shape, size), the concentrating elements can be classified as parabolic, hyperbolic, elliptical, dish, trough etc. The optical designs specific to this research are parabolic and elliptical, the details of which are discussed in later chapters.

vi. Miscellaneous bases of classification

In addition, concentrating systems can be classified based on tracking mechanism such as stationary (without applied tracking), 2D (linear or single axis tracking), 3D (point or

dual axes tracking) and quasi-static. It can be further categorised on the basis of secondary optics designs, homogeniser and conic reflector etc. [23]. The two primary concentrating elements used within this thesis are based on non-imaging 2D LACPC (Linear Asymmetric Compound Parabolic Concentrator) and 3D SEH (Square Elliptical Hyperboloid) concentrator. Both the concentrators provide low concentration (C_g < 10x) and hence they aren't dependent on solar tracking and require no active cooling. They offer a wide range of acceptance angles and can be used as stationary concentrators. Also, CPC have other advantages over parabolic reflectors in that they require less precise tracking due to flat optical efficiency response, in comparison to Fresnel lenses they offer higher optical efficiency (>90 % with advanced reflective films or coatings), the smoothness in the CPC surface minimises manufacturing defects and the option to filter portions of the solar spectrum helps reduce cooling requirements for solar cells [42]. SEH concentrators, on the other hand, offer high transparency allowing daylight penetration into buildings. The details on the concentrators used within this thesis including their designs and fabrication are covered further in section 3.2.

1.4.4 Pros and Cons of CPV technology

As with any technology, CPV has its own advantages that come with a few limitations, which are described in Table 1. In addition to limited niche market and high risk investment, the requirement for solar tracking comes at the cost of increasing system bulk, capital, operational, electricity and maintenance costs, which seems like a necessary evil for high and medium concentration systems. Their costs may exceed the PV costs, they may be difficult to install especially in residential applications and may reduce the CPV lifetime due to mechanical wear and tear [43].

Table 1. Advantages and Limitations of the CPV Technology [44].

Advantages	Limitations
High efficiencies for direct-normal irradiance	HCPV cannot utilise diffuse radiation LCPV can only utilise a fraction of diffuse radiation
Low-temperature coefficients	Tracking with sufficient accuracy and high reliability is required

Additional use of waste heat possible for systems with active cooling possible (e.g. large mirror systems)	May require frequent cleaning to mitigate soiling losses, depending on the site
Less sensitive to variations in semiconductor prices	New generation technologies without history of production (thus increased risk)
Greater potential for efficiency increase in future (vs. flat plate system) could lead to greater improvements in land area use, system and balance of system costs	Strong cost decrease required in short duration for competing technologies for electricity production
Increased and stable energy production throughout the day due to tracking	Bankability and perception issues due to shorter track record compared to PV
Lower energy payback time when compared to PV	Additional optical losses
Modular – from kW to GW scale	Limited market, can only be used in regions with high DNI
Opportunities for cost-effective local manufacturing	Lack of technology standardisation

1.5 BICPV systems: an overview

CPV, when integrated with the buildings are termed as building-integrated CPV or BICPV. The many benefits of using BICPV, over conventional BIPV are higher electrical power output, simplicity in recycling the constituent materials due to less cell usage, lesser space requirement, improved use of the building space as well as environmental implications such as lesser toxic by-products from solar cell manufacturing [22] which are summarised in Table 2 as a qualitative comparison and a few examples of BICPV are shown in Fig. 13 (a, b, c).

Table 2. Qualitative comparison between BIPV and BICPV systems.

Features	BIPV	BICPV
Power output for same size of PV	Lesser	More
Cost (fixed and installation)	Higher	Lower
Cost (operation and maintenance)	Lesser	Maybe higher
Solar cell area for same power	Up to 100x more	Lesser
Space requirement for installation	More	Lesser
Tracking	Not required	Required for
Capability to replace building	Yes, more	Yes but lesser

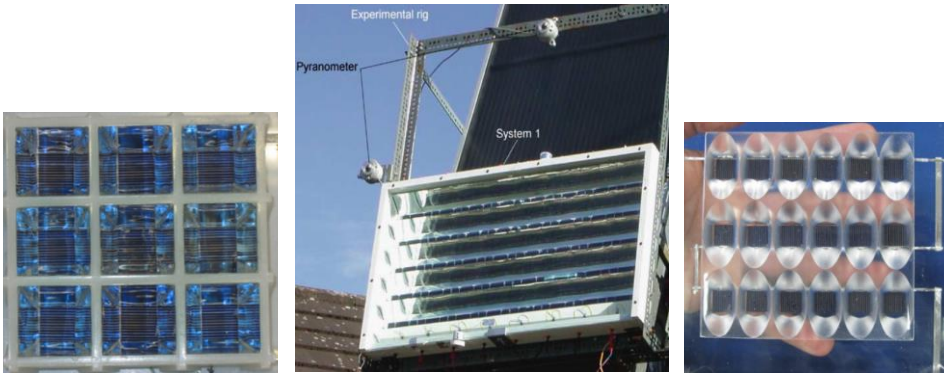

(a) (b) (c)

Figure 13: Low concentration BICPV based on (a) CPC with silicon cells [45] (b) LACPC under outdoor experimental characterisation [46] and (c) Semi transparency effect of the SEH based BICPV suitable for Window applications [47].

Relevant work on the BICPV systems used within this PhD work has been referred from the following literature: Mallick et al, [46] designed and characterised a novel non-imaging linear asymmetric compound parabolic photovoltaic concentrator (LACPC), with 0° & 50° acceptance-half angles and concentration ratio of 2.0. They characterised the BIPV system with and without LACPC under outdoor conditions in Northern Ireland (54°36`N, 5°37`W). The thermal and electrical analysis was carried out for 20 days with an average of 10 hours each day. The results revealed a 62 % increase in the maximum power point in BIPCV with respect to BIPV. Sarmah et al, 2014 [15] further designed, developed and analysed the indoor performance of a BICPV module made using clear polyurethane based LACPC and eight silicon solar cells in series (1.89 W_p) under different incidence angles. Their concentrator design differed from the one designed previously with acceptance-half angles as 0° & 33° and C_g of 2.8. Average AM 1.5G spectrum-weighted transmittance (in the spectral range 300–1100 nm) for the concentrator was 81.9 %. Indoor characterisation using a solar simulator (1000 Wm^{-2} at 20° inclination) ensured maximum power ratio of 2.27 compared to the non-concentrating system. Within the designed concentrator's acceptance angle range, 80.5 % optical efficiency, 12.1 % maximum and 9.43 % average electrical power conversion efficiency was achieved. Additionally, these BICPV achieved 20 % cost reduction (£0.80 for PV and £0.64 for CPV for a 1 kW system) calculated on per unit power output basis. Additionally, [48] developed the numerical model for the system and performed an experimental validation considering concentration ratios, solar cell material properties,

operating temperatures, solar cell dimensions, bus bar configurations and the number of fingers (including their size and spacing). Issues with concentrated irradiance such as non-uniformity of the incident flux, hot spots, current mismatch and efficiency reduction were considered for simulation. It was found that non-uniformity in illumination accounts for around 0.5 % loss in absolute electrical efficiency and a relative fill factor loss of 1.85 % at 5° incident angle. Ray tracing and finite element methods were employed to carry out the optical analysis and electrical and thermal analysis respectively. The difference in maximum output power, P_m, between numerical model (262.6 mW) and experiment results (231.6 mW) was 11.4 % which was attributed to the inherent defects in the concentrator (optical) and solar cell, misalignments between cell and concentrator, junction temperature difference causing open circuit voltage variation, current mismatch between series connected cells and modelling constants used in the electrical model.

1.5.1 Challenges

Many drawbacks associated with BIPV and CPV become a natural challenge for BICPV systems to overcome. In addition, in comparison to BIPV, BICPV is often difficult to mount or used as a construction element such as the installation on façades, as the mirrors can prevent light entrance inside the building and the outwardly protruding receivers creating strain on the structure as well as are have unpleasant aesthetics [22]. In addition, higher temperature in linear CPV systems produced due to higher light flux density incident upon the cells is also a major issue [22]. The factors affecting a BICPV electrical power output are the material, type and quality of the solar cells used, the concentration level achieved by the concentrator, the incident solar radiation and the operating temperature [49]. For a given BICPV working under constant irradiance, the temperature increase limits the efficiency of the system. The panel manufacturers measure the efficiency under the Standard Test Conditions (STC) of 1 kWm^{-2} irradiance at 25°C temperature, whereas the electrical efficiency is significantly affected by the outdoor weather conditions [50].

At present most commercial Si-based solar cells used in BICPV can convert only up to 18-20 % of the available solar irradiance to electrical energy and the rest is converted into heat, increasing the junction temperature [51] unless the heat is efficiently dissipated. Various studies have been undertaken to experimentally investigate the effect of

operating cell temperature over output parameters. In mono and polycrystalline solar cells, the increase in temperature led to slight increase in short circuit current (0.06–0.1 % /°C), but higher voltage drops (2–2.3 mV/°C), and fill factor reduction (0.1–0.2 %/°C) causing the electrical power output to drop by 0.4–0.5 %/°C in one of the studies [52]. This undesirable performance degradation owes its existence to the negative temperature coefficient of the silicon cells [27]. At one sun, the temperature coefficient was found to be 1.7 mV/°C for highly efficient solar cells and at 200 suns, this reduced to 1.4 mV/°C in another study [53]. Furthermore, [54] investigated the influence of temperature and wavelength on the electrical parameters of crystalline silicon solar cell. Under a halogen lamp (irradiation intensity 618–756 Wm^{-2}) the single crystalline solar cell showed a decrease in maximum output voltage and power with increasing cell temperature between 25 °C and 60 °C. The temperature coefficient for the decrease in power output from the module was found to be -0.66 %/°C, with 0.2 %/°C decrease in fill factor and 0.08 %/°C decrease in conversion efficiency. The authors of [55] investigated the effect of cell temperature on the photovoltaic parameters of mono-crystalline silicon cell and reported that the open circuit voltage, maximum power output, fill factor and conversion efficiency were decreased following cell temperature. Further details on the effects of temperature, concentration and radiation over solar cells or PV panels can be referred to from [56-67]. In order to analyse the effect of the cell temperature on the electrical output relationship, it's important to understand the underlying mathematical and physical principles. The output electrical current for a solar cell is related to its temperature as given in Eqn. 5 [68, 69].

$$I = I_{Ph} - I_O \left\{ e^{\frac{q(V+R_S I)}{nkT}} - 1 \right\} - \frac{V+R_S I}{R_{sh}} \quad \textbf{(5)}$$

Where I-characteristic current of solar cell, I_{ph}-photocurrent, I_o-reverse saturation current, R_s-series resistance, R_{sh}-shunt resistance and k-Boltzmann's constant, n-ideality factor, q-electron charge, R_s-series resistance, R_{sh}-shunt resistance, T-cell temperature and V-characteristic voltage of the solar cell. It is based on the single-diode model, the most widely accepted approach for circuit-based PV which accurately predicts the I-V characteristics of the solar cells, especially at T >300 K [68, 69]. V_{oc} is related inversely to the cell temperature as given by Eqn. 6.

$$\frac{dV_{oc}}{dT} = -\{\left(\frac{E_g}{q} - V_{oc}\right) + \frac{nkT}{q}\}\frac{1}{T} \quad \textbf{(6)}$$

Where E_g-band gap and V_{oc}-open circuit voltage.

The effect of temperature on a typical solar cell performance is demonstrated as I-V curve in Fig. 14(a) and other cell parameters as Fig. 14(b). With every 100 K rise in temperature, the initial output current remains about the same but the output voltage decreases sharply. Also, the short circuit current increases slightly with temperature due to the diminishing of the Hall–Shockley–Read single-level trap-assisted recombination rate because of the decrease of effective traps cross-section with temperature [70]. At the same time, the open circuit voltage decreases drastically thereby reducing both the fill factor and the cell efficiency.

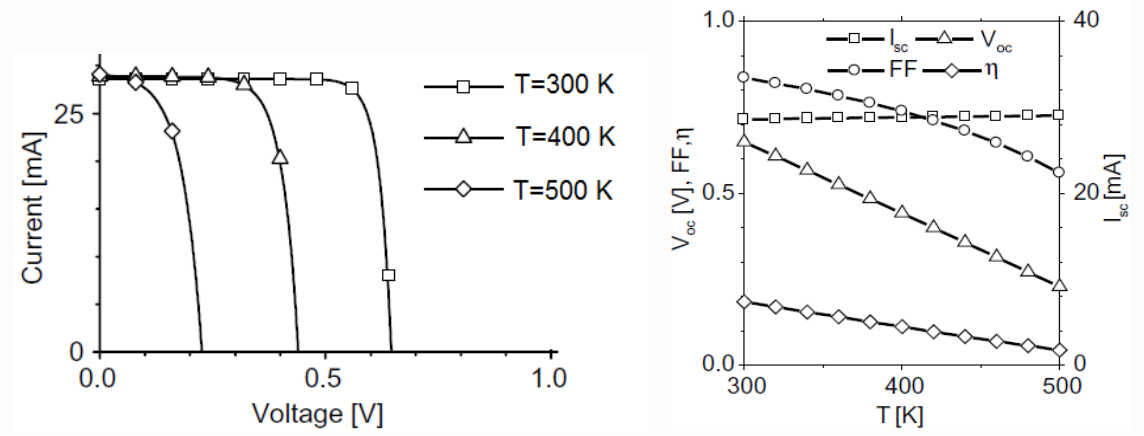

(a) (b)

Figure 14: (a) Temperature effect on I-V characteristic of a solar cell and (b) cell parameters such as Voc, Isc, fill factor and efficiency [70].

The authors of [68] proposed the electrical characterisation of PV modules using the Approximate Single-Diode Model (ASDM) simulation and reported that the I-V curves for two different modules (Fig. 15 (a, b)) at different temperatures follow the same trend as the experimentally obtained results with high accuracy. This also shows that for any module with varying efficiency, the I-V curve always shifts leftwards at higher temperatures. From the above experimental results and numerical simulations, it's evident that the efficiency and output of a solar cell are degraded at elevated temperature. Not only this, the temperature rise has other disadvantages such as being detrimental to the longevity of the silicon solar cells and is a challenge for the effective functioning of the solar cells within safe operating temperatures [69, 71]. Amongst the other challenges

faced by BICPV are a lack of available models for predicting the output energy yield and calculating the maximum power [72].

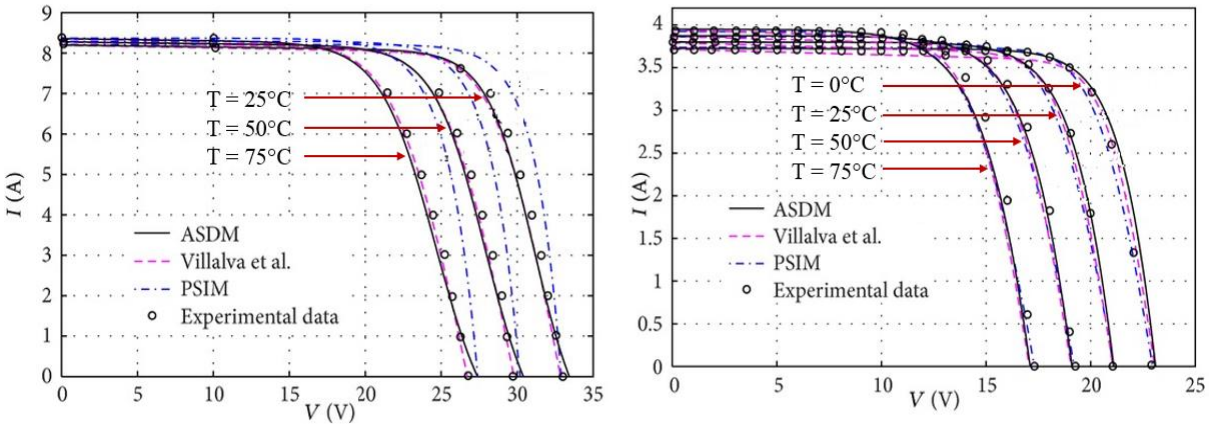

(a) (b)

Figure 15: I-V curves at various cell temperatures: (a) KC200GT PV module and (b) MSX60 PV module. The curves are obtained using: ASDM, simulation by [73], PSIM electronic circuit simulation software package and the experimental results [68].

1.5.2 WICPV: a type of BICPV

A Windows-Integrated Concentrated Photovoltaic (WICPV) is a special case of BICPV and is based on the SEH concentrators (Fig. 13(c)) which focusses sunlight onto a smaller area of 1 cm^2 square silicon solar cells, thereby saving more than 60 % of the solar cells against that used for a conventional PV [47]. Being fixed or stationary in nature, these concentrators can be used without the need for an all-day tracking system, thereby saving operation costs. This distinctive SEH optical concentrator design aids the high efficiency of the system and delivers hassle-free power from the window [74]. This WICPV can be integrated into glazing building façades and contribute to (i) daylight penetration through windows due to their transparent nature (ii) low-cost electricity production at the site of use reducing the energy dependency of buildings and (iii) extremely low solar heat gain [75].

1.6 Current scenario and future: BIPV, CPV and BICPV

The energy payback time for a PV panel, which is the time required to balance the input energy required for manufacturing the panel or to recover the initial investment, is a function of the geographical location and is normally calculated in terms of time (years). For example, for Northern European countries, it's calculated as around 2.5 years, for

Southern European countries it's less than 1.5 years (1 year for CPV) and for Italy, it's 1 year for multi-crystalline Si modules, thereby implying that PV systems are capable of producing twenty times the energy required to manufacture them, assuming a 20 years lifespan [2]. The culmination of BIPV and CPV gives rise to BICPV, which is the foundation of this thesis, hence their current and future scenarios are discussed here. BIPV market worth increased from US $\$1.8\times10^9$ in 2009 to US $\$ 8.7\times10^9$ in 2016 globally while CIGS contributed to 17 % of this volume and polysilicon based BIPV volume saw a decline from 75 % of the market to 33 % [76]. The future of BIPV development is forecasted for the period 2017-2020 (in MW of electricity production) for the global market as shown in Fig. 16. The compounded annual growth rate (CAGR) is the business term for the geometric progression ratio that provides a constant rate of return over the time period and it measures the return on an investment over that certain period of time.

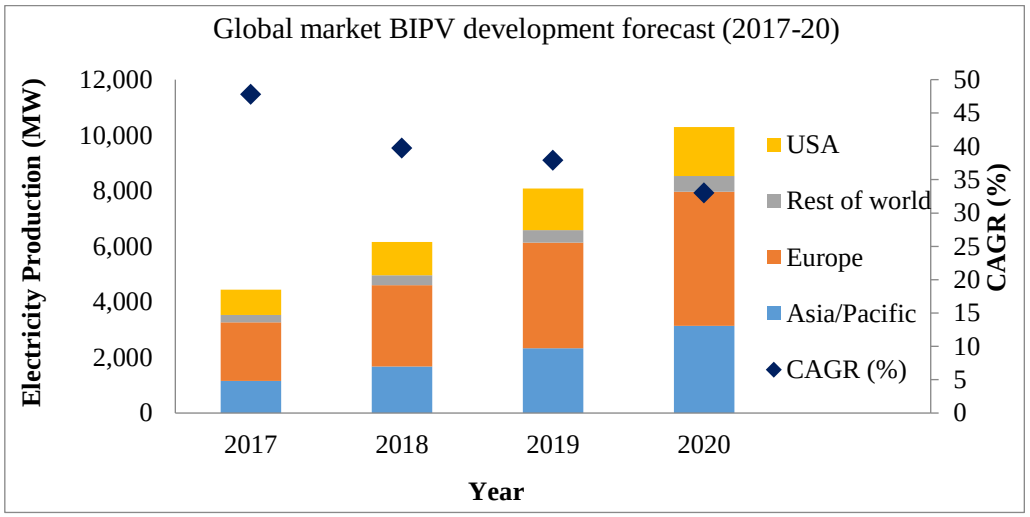

Figure 16: BIPV development and forecast from 2017-2020 (in MW) for global market and percentage compounded annual growth rate (CAGR) (Data source: [77]).

While the predicted annual growth is highest for Europe, followed by Asia-Pacific region, the USA and rest of the world, the % CAGR is estimated to be the highest for Asia-Pacific (47.8 %) followed by European region (39.7 %), rest of the world (37.9 %) and the USA (33 %). Concentration effect has been used since ancient times; mostly as parabolic reflectors, to focus parallel beams to a point, as mentioned in the translated from Greek version of the book *On burning mirrors* from the 2nd century AD [78]. In the last few centuries, further improvements in concentration technologies and innovative approaches

to achieve solar concentration and more recently, for PV concentration have taken place (Fig. 17).

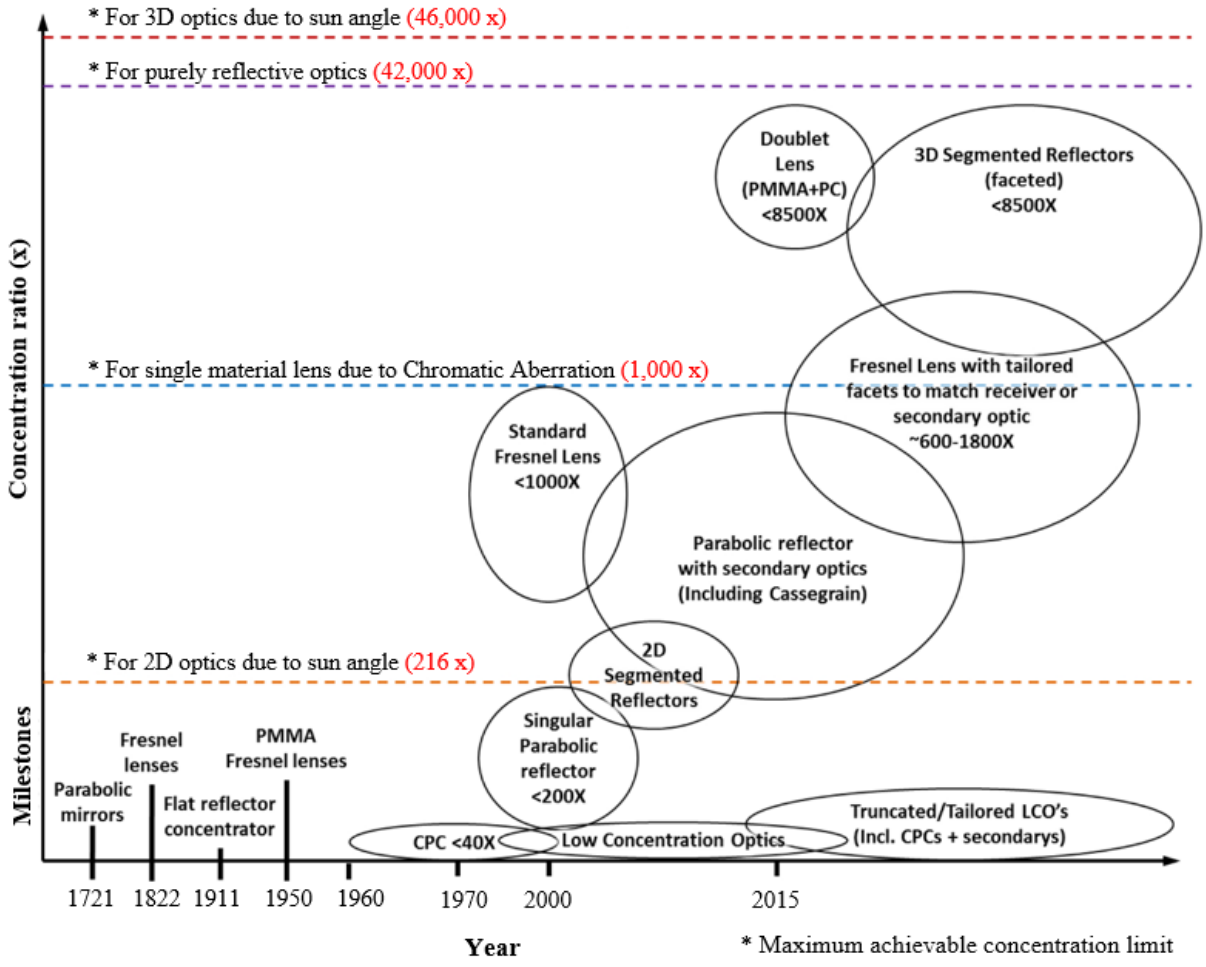

Figure 17: The CPV designs: past and predicted future trends on a timeline. The circles in upper half denote the requirements of high accuracy manufacturing and quality materials while in the bottom half, the most reliable versions are shown [23].

Over a period of time, more attention has been paid to improve optical surface structure, employing a secondary or homogenising optical element and towards reducing the path length of light rays with an aim to improve optical efficiency, tolerance and irradiance uniformity [23]. CPV technology seem a commercially viable solution to increase PV efficiency and reduce the module costs as the typical cost of silicon solar cells are about 160 US $/m^2 in comparison to the lenses available at 30 US $/m^2 and the mirrors at 17 US $/m^2 [43]. It is envisaged that the robust, easily manufactured, and based on an Earth-abundant material, silicon, the crystalline silicon based PV will become more cost-competitive without subsidies in the US at the module costs of US $ 0.50–0.75 per peak watt,

enabling electrical production at a levelised cost of electricity of US $ 0.06/ kW·h, which is comparable with the present baseload fossil-fuel electrical utility plants [79]. CPV has already entered market as a utility-scale option for solar electricity generation since several of the global cumulative 360 MW instalments are beyond 30 MW per site [44]. As per the data available for until 2016, the few remarkable developments in the CPV market and industry include [80]:

- Cumulative installations (already grid-connected): 360 MW_p, certified record value of cell efficiency of 46.0 % (Fraunhofer ISE, Soitec, CEA-LETI)
- Certified record efficiency of 43.4% for a mini-module consisting of a single full glass lens, wafer-bonded four-junction solar cell (Fraunhofer ISE)
- Certified record value for module efficiency of 38.9 % (Soitec)
- Averaged yearly field performance data for power plants with > 100 kW_p reported with performance ratios of 74-80 % achieved

The comparable economic advantage of CPV systems at present in comparison to conventional PV is still challenging [81]. It demands the optical systems to be more reliable, an increasing number of higher concentration based systems, lesser reliance on costly electromechanical tracking mechanisms and a reduced requirement of cooling systems. This, in turn, needs greater innovation to be incorporated into new designs, search for novel materials and discovery of newer applications.

In the long run, BICPV viability will depend on the relative ease of replacement of structural elements and provide versatile usage with aesthetics plus cost competitiveness over conventional flat panel PV which already has started declining in prices [22]. The decrease in PV prices in the last four decades has positively influenced their market expansion. In addition, the government policies and incentives such as feed-in tariffs in Europe and investment tax credits in the US have contributed to their penetration [82]. As a result, BIPV can overcome the shortcomings generated by the BAPV systems. While selecting the appropriate BICPV system for a building, it’s worth considering the given advantages and disadvantages of the available panel types, ease of integration, type of building architecture, aesthetics, costs, building and government regulations, grid connectivity if feeding into the grid is feasible and the available incentives.

1.7 Research Questions and Aims

The objective of the current work is to contribute to the growing research in the field of BICPV and aiming to address the thermal management issues. This PhD thesis primarily investigates ***the effectiveness of passive thermal management of BICPV, specifically using latent heat in PCM and/or nanomaterial enhanced PCM (n-PCM)*** based on experimental methods. A small section of this thesis is dedicated to study of micro-fins as secondary temperature regulation in tandem with PCM and/or n-PCM and the relative effect of PCM are compared with a sensible cooling media, water.

The following key **research questions** are attempted to be addressed:

- What will be the quantified electrical and thermal performance enhancement achieved by BICPV-PCM systems compared to naturally ventilated BICPV?
- Can laboratory synthesised nanomaterial enhanced PCM (n-PCM) enhance thermal conductivity of PCM
- Which new n-PCM composition would be useful, their morphology, thermo-physical properties and expected performance enhancement of BICPV?
- How does any variation in the following parameters affect the output power from, and the efficiency of, the BICPV in question?
    - Levels of concentration
    - Solar irradiance levels
    - Material used for PCM containment
    - Heat exchanging media
- Can BICPV-PCM/n-PCM systems work in tandem with micro-finned back-plate, and if so, what will be the individual as well as the combined effectiveness?
- What will be the quantifiable effect of applying a sensible versus a latent heat media, to the thermal regulation of BICPV systems?

This PhD work was undertaken with the following elements of work plan, a **set of deliverables** or features to be produced at the end, which are as follows:

- To design and develop different BICPV-PCM systems to experimentally examine the effects of implementing PCM/ other passive cooling solutions for thermal management of BICPV. This further includes:

  - Selecting a few low concentration designs from the available literature and fabricate BICPV system by replacing glass back plate with a metallic plate.
  - Designing and fabricating passive cooling containments attached to the BICPV back plate for introducing (i) PCM and (ii) n-PCM.
- To develop new composite materials through enriching PCM with nanomaterials (n-PCM) for the thermal management of the BICPV.
- To characterise PCM and n-PCM using X-ray diffraction (XRD), scanning electron microscopy (SEM) and differential scanning calorimetry (DSC).
- To study the suitability of these novel materials with respect to their heat transfer characteristics, thermal conductivity, melting point, specific and latent heat.
- To investigate the thermal enhancement effect of using multiple passive cooling techniques in tandem such as micro-fins with PCM and micro-fins with n-PCM based on BICPV temperature emulation, for assessing BICPV suitability.
- A brief experimental work to compare the latent heat medium (PCM) with the sensible medium (water) used in passive cooling, for BICPV thermal control.

1.8 Scope of research: Features and Limitations

Given the numerous technologies accessible and options obtainable within this research area, it becomes imperative to set the boundaries of the project, define the in-scope elements and clearly distinguish them at the very outset. Within this thesis, the challenges related to thermal regulation of BICPV systems are attempted to address using a narrow spectrum of the potential solutions. A simple grouping of these technologies using a flow diagram will aid an easy comparison of the relevant research areas and distinguish the selected pathways to addressing them (Fig. 18). The salient features are listed below:

- Solar cells: Laser Grooved Buried Contact (LGBC) types of crystalline silicon solar cells were used for all the experimental set-ups.
- Concentrators: the designs (LACPC, SEH) were taken from the published literature mostly designed by the researchers from within the same research group.
- BICPV: Only low concentration BICPV were considered for the study.
- Media: passive cooling; most of the experimental focus was on latent storage media with one reference to using a sensible medium, water for the experiment.

- PCM type: the majority of experiments were conducted using organic PCM, due to the reasons discussed in subsequent chapters. However, other PCM types such as granulated forms were analysed for the thermophysical properties using DSC.

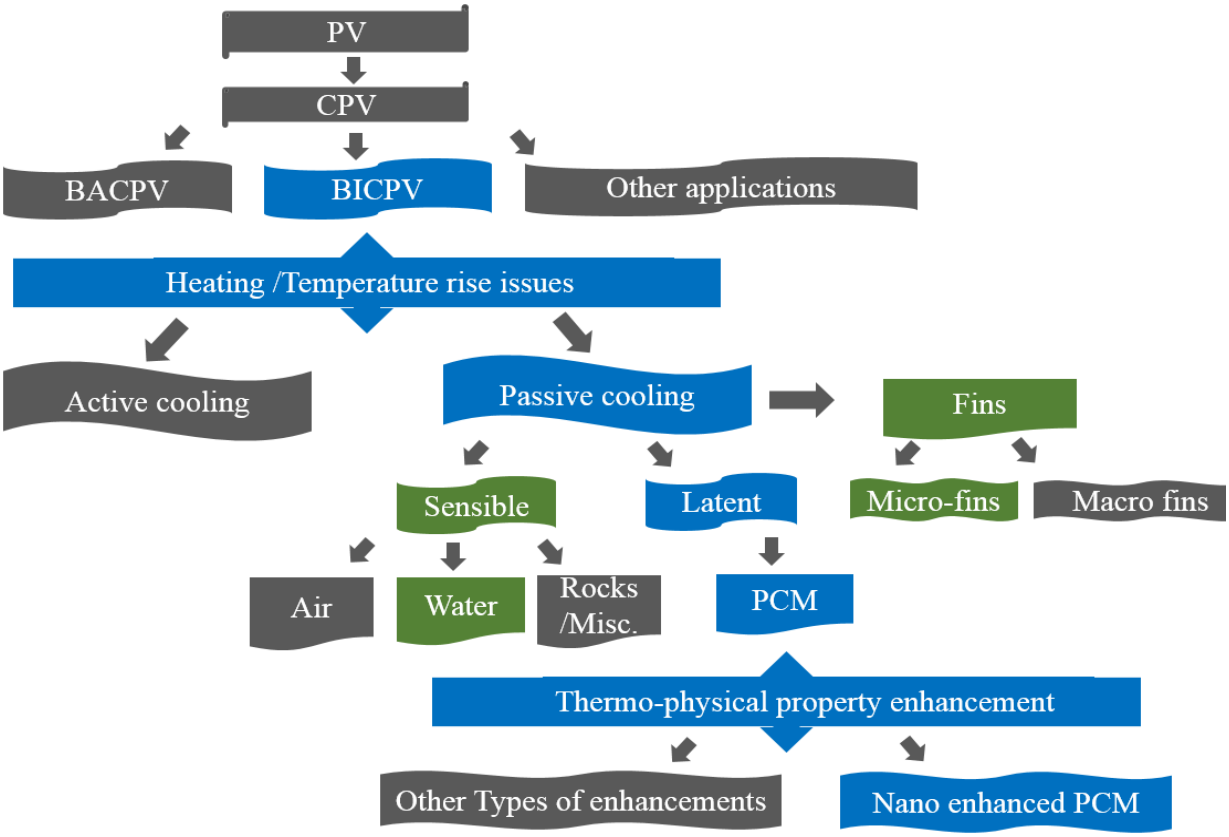

Figure 18: Overview of BICPV system challenges and available solutions. In blue: key areas of focus while in green are the secondary areas of investigation.

- Mode: passive cooling using PCM formed the foundation of this thesis but some work on combined usage of micro-fins with PCM has also been reported.
- Sourcing: all PCM and nanomaterials used were sourced from the manufacturers. However, n-PCM was manually synthesised in the laboratory.
- Thermal conductivity enhancement (TCE): of all the available TCE, CuO nanoparticles were selected in the first instance to develop the n-PCM. The reasons are discussed in subsequent chapters on materials (Chapter 4).

The **Limitations** of the work are as follows:

- BICPV issues: amongst the various challenges faced by the BICPV, only temperature rise or overheating issues were considered.
- Characterisation: all characterisations have taken place indoors, within the lab, so outdoor behaviours of the BICPV and BICPV-PCM systems are not included.

- PCM issues: the major drawback of organic PCM, i.e. low thermal conductivity, was focussed for remediation. Other limitations such as subcooling, low volumetric latent heat storage capacity and flammability etc. are not studied.
- Role of PCM: PCM serve a dual purpose; for heat removal and a buffer for heat storage, depending on the application. This thesis only involves PCM as a heat removal medium. Thereby, it contrasts with photovoltaic/thermal (PV/T) system because the thermal usage of the stored heat within PCM is not considered. Nevertheless, this area can be an opportunity for the future work in this field.
- Micro-fins: only one particular kind of micro-finned plate has been used to study its effectiveness as a BICPV back plate feature; the effect of varying the dimensions and specifications of the micro-fins are not covered here.
- BICPV-PCM system: only the charging cycle of the PCM has been studied in detail as most of the experiments have been conducted indoors using a solar simulator with constant irradiance for the duration of the simulator running.
- The thesis is mostly based on experimental results and the obtained data and mathematical analysis with some application of numerical simulation.

1.9 Organisation of thesis

Chapter 1 gives an overview on PV (BIPV, BAPV), CPV and BICPV technologies; components, classification and trends in deployment. Further, it highlights the aims, research questions, deliverables and scope of the thesis and the thesis organisation.

Chapter 2 reviews the existing literature on the state of the art of the BICPV thermal management with particular focus on passive cooling with PCM. PCM classification, properties, applications, challenges and means to address low thermal conductivity using nanomaterials are discussed. In addition, passive temperature regulation using micro-fins is considered as a potential candidate. This chapter forms the basis of identifying the knowledge gaps within BICPV cooling and the ways to address them.

Chapter 3 provides the details on materials, methods and design and fabrication for the modules used for experiments. The key instruments, devices and auxiliary equipment used during the preparation and running of the experiments along with their technical

specifications are described here. Steps by step engineering design, construction and fabrication processes for the BICPV and the PCM part of BICPV-PCM system set-up.

Following on from here, Chapter 4 describes the methodology followed for electrical and thermal characterisation of these various BICPV modules with natural convection and with PCM applied. The procedure for instrument calibration and varying the test parameters is also detailed here. The four key systems studied are (i) an LACPC based BICPV system for studying the effect of PCM and irradiance, (ii) an SEH based WICPV system with Copper tubes for studying the effect of thermal conductivity enhanced PCM containments and sensible cooling media such as water, (iii) a micro-finned thermal system emulating BICPV temperature for investigating the effectiveness of micro-fins and a synthesised n-PCM and (iv) an SEH based BICPV system for examining the effect of n-PCM on BICPV performance enhancement.

The following chapter, Chapter 5, presents the results from the experimentally obtained thermal and electrical response as measured using the various set-ups as detailed in the previous chapter. It also contains results in terms of analysis of PCM thermo-physical properties (using DSC), morphology (using SEM) and some preliminary results for the material composition and purity analysis (using XRD). The numerical schemes, simulation validations and the qualitative and quantitative comparisons between the different experimental set-ups have also been explained in detail. The results in appendices give details on thermo-physical properties from DSC, and morphology from SEM instruments which will be useful for further work in this field.

The final chapter, Chapter 6, gives a general conclusion to the thesis, the lessons learnt during the entire lifecycle of the experimental work carried out throughout the period of the research. The second part of the chapter outlines the recommendations for the future work that can be carried out to enhance the research. This covers many aspects of research ranging from additional means for thermal energy harvesting from stored PCM energy, advanced level synthesis of n-PCM and characterisation, outdoor characterisation of the BICPV-PCM module to account for the ambient air cooling and the practical effects of non-uniformity of the irradiance on the module.

Chapter 2. BICPV Thermal Management: State of the art

This chapter presents the state of the art of BICPV thermal management technologies, drawing a comparison between the various modes, mechanisms and mediums for heat removal. With a focus on passive cooling, secondary options based on micro-technologies such as micro-fins are explored as opposed to active cooling, which are more energy intensive. Passive cooling techniques can improve the thermal behaviour of BICPV systems reducing operational costs and material usage at the same time. A broad classification of the Phase Change Material (PCM) types, their comparative advantages, limitations and applications in various fields are discussed. The scientifically accepted definitions relevant to these technologies, their modes of working, salient features and material availability are also reported. Further, the available passive-passive cooling systems working in-tandem are reviewed. In this chapter, the opportunities for thermal management of low concentration BICPV based on micro-finned back plate and PCM are proposed and the fundamental issues concerning their successful applications are discussed. In addition, the use of thermal conductivity enhancers, especially the nanomaterials and their available forms are presented. Metal oxide based nano-materials are selected to incorporate into PCM to address low thermal conductivity, a major drawback of organic PCM.

2.1 Introduction

Improving electrical efficiency for the low concentration BICPV systems require efficient heat removal, without a lot on investment and without increasing system bulk. The heat transfer rate from a surface can be enhanced either by increasing the heat transfer coefficient (i.e. by using a pump or fan) or by increasing the surface area (by attaching fins). Another way of looking at this is the option of either employing active cooling (such as water pumped cooled systems, which require mechanical or electrical power for operation), or enhancing passive heat transfer, for example, by changing the geometry (i.e. by introducing fins), or by utilising phase change materials (PCM). PCM are thermal energy storage material used for heat absorption, storage and recovery and are often employed in renewable energy systems due to their intermittent and unpredictable nature. PCM contribute to the applied system for rationalising and uniformly spreading the use

of energy over a period of time. Heat removal can be classified as sensible or latent depending upon whether the storage media removes heat in a sensible or a latent form. Sensible heat and latent heat describe the heat exchanges taking place under the specific conditions described by their effect on a thermodynamic system. Often, the best option to store energy in these systems is to take advantage of the enthalpy of phase change. The resulting system is typically a latent heat based. Various kinds of sensible and latent heat storage material and system options have been employed for BICPV cooling systems in literature. The classification of PV thermal management modes, mechanisms and mediums is presented in the next section.

2.2 Thermal management: modes, mechanisms and mediums

The six main PV thermal management techniques mentioned in literatures are (a) natural and forced air circulation, (b) extensions or fins, (c) hydraulic, (d) thermoelectric, (e) heat pipes and (f) the use of phase change material (PCM) [75]. In order to keep in line with the research questions to be addressed within this thesis, (a), (b) and (f) are primarily focussed. As briefed in 2.1 the two modes of cooling (active and passive) and the two key mechanisms (sensible and latent) by which the media are utilised, have a certain degree of overlap, which is shown in Fig. 19. It is based on the application of most commonly used latent and sensible heat removal media. Both, passive and active cooling modes can utilise sensible mechanism using mediums such as air, water, oil. Latent mechanism based on PCM mediums have not been traditionally used as the idea of pumping PCM is a rather challenging one itself.

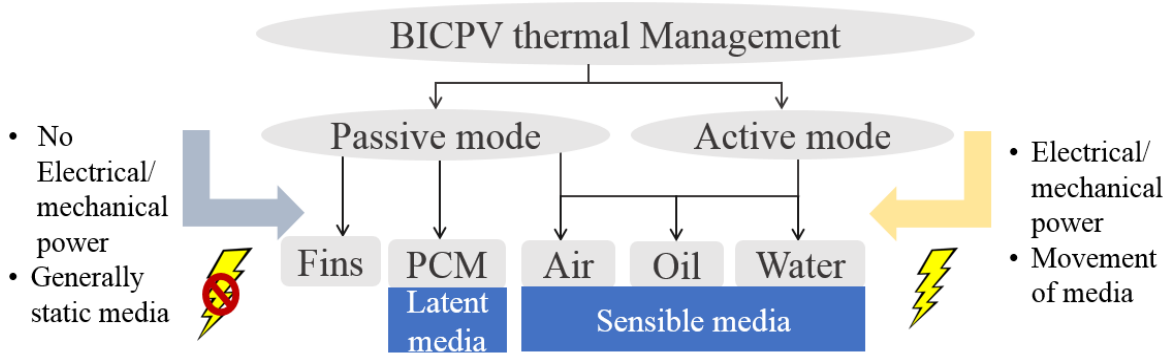

Figure 19: BICPV thermal regulation options: passive vs. active cooling mode, latent and sensible media and the overlap.

2.2.1 Modes: Active and Passive

To address the challenges related to BICPV temperature rise, thermal regulation can be achieved via either active or passive modes of cooling, which are also the established methods for cooling electronic devices [83] and PV panels [84]. Passive cooling doesn't require any mechanical or electrical power input for heat extraction from the system, exploiting natural laws such as free air convection and buoyancy, whereas active cooling depends on externally supplied energy to cool the solar cells [85]. The two modes are distinguished in Table 3. Active cooling has been established as an effective means for PV applications by numerous authors through their experimental and simulation works. To list a few, [86] achieved a temperature reduction by up to 22 °C , by spraying water over the PV frontal surface using water pumping systems, mean PV array power increase in the range of 21 % [87] and by 9–22 % from the reference values [88]. The authors of [84] experimentally proved that actively cooled PV cells, using an air blower, showed an increase in electrical efficiency from 8–9 % to 12–14 %. Using a parallel array of ducts with inlet/outlet manifold for uniform airflow distribution at the rear side of the panel, the temperature dropped from 68 °C to 38 °C with active cooling.

Table 3. Difference between active and passive cooling modes (1:[33, 85, 89]; 2:[90]).

Cooling Methods	Definition[1]	Definition[2]	Features	E.g.:	Uses
Active Cooling	• Requires external energy (may be a portion of obtained cell power output) to cool solar cells • Micro-channels heat sink, impinging jets -most promising technologies for active cooling of a CPV plant	• Also known as heat collector technology • Collects PV produced heat; uses for heating ventilation, hot water etc.	• Independent of work conditions • Usually easily controllable • Bulky and complex machinery • Costly because of parasitic power loss • Additional equipment costs	Forced air/liquid cooling	• Densely packed cells • Ultra high and high temperature applications
Passive Cooling	• Does not require mechanical or electrical power input • Strategically use natural laws to reduce cooling energy requirement, dissipation of excess heat to sink etc.	• Meant to remove heat by flow of water or other medium which may not be utilised further	• High reliability, preferred way for cells cooling when safety is important • Low heat transfer rate • Simpler and cheaper	Natural air circulation, fins, PCM etc.	• Single cell, Linear cells • Medium, low temp. applications

However, the additional costs of operating the blower or pump for active cooling are not reported and could be higher than the electrical efficiency improvement produced. Examples of passive cooling using micro-channels [91], micro fins [92] and with PCM

[83] are commonplace. PCM cooling for electronic devices is elaborated in [93-99] whereas PCM applications in PV and BIPV are further discussed in subsequent sections. Previously, passive cooling was not considered feasible for densely packed cells or for linear concentrators with $C_g > 20$. However, in recent years, passive cooling technologies have become more acceptable for CPV applications as they possess greater reliability and are safer than forced flow, which has a higher damage probability caused by the active cooling failures [100]. A comparison between active (forced air) and passive cooling (PCM) modes by the authors of [101] revealed that passively cooled systems showed better performance at high discharge rates, high operating temperatures and ambient temperatures of over 40 °C without expending significant fan power, in cooling a Li-ion battery pack used for plug-in hybrid electric vehicle propulsion. With PCM, the cell temperature remained below the upper safety limit of 55 °C in high constant-rate discharge with an ambient temperatures up to 52 °C. This was not feasible using active cooling due to the high airflow rate demand close to the turbulent range that is beyond practical range for vehicular applications. However, the authors suggest that in this case, the expense of electric power for running the fan was relatively small.

Other reported passive thermal management methods include silicon cell cooling using immersion in an appropriate isotropic liquid dielectric with high refraction factor, dielectric constant and specific resistance such as glycerine, which has shown to increase the solar cell efficiency by 40–60% [102]. Using thermoelectric technology, PV heat sinking by thermoelectric module tile has shown an increase in electrical efficiency by 1–18 % and panel temperature reduction by 6–26 % for a range of irradiance from 800 to 1000 Wm^{-2} within 25–45 °C based on Matlab and PV modelling [103]. The applicability of these methods for BICPV is yet to be confirmed.

Within the thesis, keeping in view that BICPV is based on low concentration concentrators, $C_g < 10$, passive cooling is selected as the primary mechanism as it seems to offer a convenient, cost-effective and simple way of temperature reduction. Therefore, passive cooling with PCM will be discussed more elaborately hereafter.

2.2.2 Mechanisms and Media: Sensible, Latent and Thermochemical

Heat removal mechanism can be classified as sensible or latent depending upon whether the storage media removes heat in sensible or latent form and they are described below.

2.2.2.1 Sensible medium

Sensible medium remove and store the heat energy by means of raising the media temperature such as in dwellings and building structures, where the thermal mass of the materials act as a heat store. The commonly used sensible heat storage media are water (in hot water tanks), ground/soil/earth, bricks, concrete and rock (in rock beds) systems. Traditionally, energy was stored in the form of sensible heat which required large volume of storage material, while now more emphasis is being laid on latent form in PCM [104]. The sensible heat in a system can be expressed in terms of Eqn. 7 [105].

$$Q_s = mC_p\Delta T \quad \textbf{(7)}$$

Where Q_s is the sensible heat storage (J), m is the mass of the material, C_p is the specific heat capacity of the material at constant pressure (J/kg/K) and ΔT is the change in temperature (K).

The drawbacks of sensible media are: incapability to remove heat at constant temperatures and it is a less efficient method because it takes more energy to change the state of a material compared to raising its temperature by a reasonable degree. They also require significantly larger quantities of media for removing the same amount of energy as in a latent [106].

2.2.2.2 Latent medium

Latent heat removal mechanism, with media such as PCM is preferred where higher storage densities with a smaller volume of the material (with high latent heat) are required [107]. Operational advantages using PCM over a sensible heat removal system include smaller temperature fluctuations, smaller size, lesser weight per unit of storage capacity and high energy density (typically 5 to 14 times of that based on sensible media for a given working temperature range) meaning lesser area requirement, more reliability and flexibility [104]. In real-life scenarios, the latent heat changes are accompanied by sensible heating, before and after the phase change, hence Eqn. 8 gives the mathematical expression for the phase change. However, the sensible heat effect is often negligible compared to the latent heat during phase transformations, therefore, to calculate purely the latent heat Eqn. 9 [105] can be used.

$$Q_{l,overall} = mC_p\Delta T_{s-l} + mH + mC_p\Delta T_{l-s} \quad \textbf{(8)}$$

$$Q_l = mH \quad \textbf{(9)}$$

Where Q_l is latent heat (J), $Q_{l,\ overall}$ is overall heat storage during phase change, $\Delta T_{s\text{-}l}$ is the solid-liquid phase change temperature, (K), $\Delta T_{l\text{-}s}$ is the liquid-solid phase change temperature, (K) and H is the latent heat capacity of PCM (J/kg). The key differentiating points between the two mechanisms of heat removal are highlighted in Table 4.

Table 4. Distinction between sensible and latent heat transfer (data source [108-111]).

Mechanism	Features	Materials
Sensible Heat transfer	• The media undergoes temperature change • Heat transfer by means of conduction, convection, or radiation • Most common and mature technology, implemented in many large-scale demonstration plants. • Bulkier system due to less energy density of the material	Stones, Bricks, Rocks, Ground, Concrete, Pebble, Gravel etc.
Latent Heat transfer	• The media remains at nearly constant temperature • Evolving field as compared to sensible systems • Higher energy density, requires less storage space	PCM of organic, inorganic and eutectic nature

Though the high energy density of latent media reduces the heat losses to the surroundings due to the reduced storage sizes, the authors of [112] concluded that it was uncertain whether the energy density benefits offered by the latent materials were useful for a typical solar cooling application. However, higher annual collector performance was observed with the use of sensible media [112]. In another study, [113] reasoned that there were no significant differences between the performance of the two and though PCM did not prove beneficial in terms of either the efficiency or the cost in exergy to be supplied to the store or thermal power characteristics, they could still be preferred due to their compactness. It was established by [114] through experimental analysis that latent systems were a viable option for solar heat energy storage and that it could be utilised as a substitute for domestic solar sensible applications.

2.2.2.3 Thermochemical medium

Chemical storage mechanisms rely on the phenomenon of chemical reactions (reversible reaction between two or more substances) or thermochemical sorption using endothermic and exothermic cycles [108]. The underlying principles of sorption are further based on adsorption, where gas bonds with the solid surface without creating new compounds, and

absorption, where a new material is formed due to interaction. In absorption, the energy storage density depends on the concentration of the solution whereas in adsorption, the solid/gas medium energy storage density is determined by density of the salt, composite porosity and additives. Generally, absorption couples such as $LiCl/H_2O$, $NaOH/H_2O$, $CaCl_2$/H2O, and $LiBr/H_2O$ are employed for absorption while Hydrates and Ammoniates are used for adsorption [108]. Thermochemical energy storage offer high energy storage, low heat losses, capability to conserve energy at ambient temperature as long as desired and they seldom suffer from heat loss problems [108]. For the purpose of this thesis, only latent media are described in detail.

2.2.3 Micro-fins

Micro-fins, intended as extended surfaces for improving heat transfer, have at least one micro-scaled dimension. They have been effectively integrated with optoelectronic systems [115, 116], with condensers or evaporators for cooling systems and air conditioning devices [117] and with tubes in brine coolers [118] etc. to enhance heat transfer rate. Micro-fins have proven to offer better thermal performance as well as higher mass specific power. Indeed, they have been found to provide up to 50 % higher power to mass ratio in contrast with the conventional heat sinks [92]. Fins also provide larger heat dissipation capability which means the size of heat exchangers could be more compact entailing less refrigerant load in a cooling system. Use of micro-fins has been preferred to relying on forced convection as they are noiseless, require no power for operation and offer less expensive alternative [119]. Even though they may not always increase the heat transfer substantially, micro-fins prove beneficial in terms of material usage and can be considered useful for the applications dependent on weight minimisation of heat sinks [120], such as with BICPV systems.

The fundamental mode of heat transfer in a micro-fin is via convection but it has already been demonstrated that the contribution of radiation should not be neglected [121, 122]. While numerous studies have been undertaken for natural convection around fins and micro-fins, the existing heat transfer correlations appear insufficient for emerging technologies such as micro-fluidics, nanostructured devices etc. [119]. However the authors of [123] have extensively analysed the correlation between fin geometries and heat transfer coefficients, effects of fin orientation, and influence of fin thickness and

proposed a modified correlation based on their experimental investigation. The effect of micro-fin height (between 0.25 and 1.0 mm) and micro-fin spacing (from 0.5 to 1.0 mm) on heat transfer coefficient under steady state natural convection are published in [124]. Another experimental investigation carried out on a horizontally mounted heat sink revealed the direct proportionality relationship between convective heat transfer coefficient and micro-fin spacing while inverse proportionality with respect to the fin height. Highest value of heat transfer coefficient (h) was recorded at the lowest fin height of 0.25 mm and spacing of 1.0 mm. The value of h reduced by a maximum of 34.8 % due to fin height increase from 0.25 mm to 1.0 mm for 1.0 mm fin spacing. The computational fluid dynamics modelling results were found to agree with the experimentally obtained correlations. In their work, the authors of [125] applied microscale heat sinks to a processor chip of micrometer scale. The authors of [126] reported the advantages of micro-structured roughness on heat transfer performance of heat sinks, cooled by forced air and showed that 20% enhancement is observed for finned heat sinks compared to milled ones. The application of micro-fins for thermal management of electronic systems has been studied in [119, 127, 128] as well as micro-channel heat sinks for reducing thermal resistance for power electronics cooling [129-131]. Application of fins [51, 132] and micro-fins [92, 133] for high CPV system passive cooling have been already proposed. However, for this work, the notion has been extended to potentially use micro-fins with PCM/n-PCM for the thermal regulation of low concentration BICPV systems.

2.3 Combined usage of passive-passive cooling

In their review on solar cell performance enhancement with the use of various cooling methods, the authors of [134] summarised that PCM layer was found to effectively increase the electrical efficiency of the PV cells and fins on back side of the module have similar effect, with the heat transfer rate determined by the exposed area and wind velocity. The authors of [75], numerically characterized the PCM melting in a plate fin type heat sink focussing on parameters such as aspect ratio, Nusselt number (Nu), Rayleigh number (Ra), Stefan number (Ste) and Fourier number (Fo). They established that Nu with Ra depend on the PCM containment aspect ratios and melt convection. The authors of [135] performed numerical investigation on melting, solidification and heat transfer rates of PCM (using n-eicosane) and studied the effect of mixing PCM with different volume fractions of 80 nm Copper nanoparticles. Results demonstrated that

using 2 % and 4 % volume fractions of Cu nanoparticles led to a respective reduction in full melting time by 25 % and 46 % while full solidification time by 9 % and 16 %. Similarly, by mounting 4, 10, 15 and 20 fins, respective solidification time reduced by 28 %, 62 %, 75 % and 85 % while full melting time reduced by 39 %, 73 %, 78 % and 82 % respectively. Adding nanoparticles accelerated the melting and solidification rate via enhanced heat conduction of the mixture and that the top section melting rate was higher than at bottom owing to natural convection. Having fins led to more significant improvements, especially while solidification, because of restrained natural convection during melting. The authors of [96] experimentally examined PCM based heat sinks for electronic equipment cooling using n-eicosane PCM and pin fins as the TCE. A number of 33, 72 and 120 pin fins were packed with PCM. With 72 pin fins, the enhancement factor was found to be 21, which was maximum, but as the number of fins increased beyond this, heat transfer showed reduced effects. Clearly, fins contributed to the enhanced operational duration for the electronic devices and heat transfer performance was determined by the PCM mass as well as the fin volume fraction.

In another series of studies, Huang et al, 2003 [136] demonstrated the substantial effect of temperature regulation on PV efficiency improvement. Three configurations were tested: (i) Single flat Aluminium plate system, (ii) PV–PCM without internal fins and (iii) PV–PCM with internal fins using PCM RT25. A 0.0045 m thick Aluminium plate was used to fabricate PCM containment with inner dimensions (L=0.300 m, W=0.040 m, H=0.132 m) and two full-length 0.030m wide fins. The system (iii) maintained front surface temperature below 36.4 °C for 80 min with one PCM (T_m-32 °C, depth 20 mm) under 1000 Wm^{-2} irradiance, (T_{amb}-20°C), while it was below 33 °C for 150 min with another PCM (T_m-26.6 °C, depth 40 mm) under 750 Wm^{-2} irradiance. Provision of metal fins within the PCM containment also showed significant thermal performance improvement. Another experiment by the same author [137], evaluated the performance of two PCM (paraffin wax based RT25, granulated; GR40) for limiting temperature elevation of PV systems achieved temperature reduction of over 30 °C using RT25 with internal fins. Four sets of systems were characterised at 750 Wm^{-2} (T_{amb} 23 ± 1 °C), namely; (i) Flat Aluminium plate, (ii) Flat Aluminium plate with eleven fins at (width 27 mm, thickness 0.5 mm thick and 12 mm pitch), (iii) PV–PCM system and (iv) PV–PCM system with thirty one Aluminium fins (40 mm inside the PCM) with RT25. The effect of fin parameters on temperature control could be summarised as:

(i) Fin spacing – five fin spacings (4, 8, 12, 16, 20 mm were studied) in vertical orientation and the results showed that fins with 8 mm spacing nearly halved the number of fins required for controlling the temperature under 28 °C as compared to 4 mm spacing. The 4 mm spaced systems were the quickest to melt lowering the front surface temperature due to higher heat transfer rate. The temperature difference between fin spacing of 12 and 4 mm was only 0.9 °C. The best configuration was with 8–12 mm space, which not only used smaller amount of fin material but also sustained lower temperature for extended periods.

(ii) Fin width-out of the five studied widths (27, 30, 33, 36, 40 mm), 40 mm performed the best in maintaining PV frontal surface at 28 °C for the longest duration (125 minutes). The relation between the fin width and temperature retaining time was almost linear exception being the widths of 30 and 33 mm that displayed insignificant effect.

(iii) Fin types – three types of fins (strip Aluminium matrix, uncoated soft-iron wire matrix and straight fins of 36 mm width) were chosen to study the effect of fin types and the lattermost reached the least temperature with fastest phase change completion.

To analyse the impact of fin geometry (fin-length, fin-ratio and the angle between adjacent fins) and outer tube thermal conductivity on PCM melting process in a sleeve tube with internal fins, [138] carried out a detailed numerical study, with 2D assumptions. The produced numerical model fairly agreed with other published experimental and numerical results. The results indicated that the PCM melting time could be decreased with small fin-ratio to a certain extent and the angle between adjacent fins had only slight effect on the melting, while the outer tube conductivity proved to greatly impact the melting process whether or not natural convection was taken into consideration. Further, reducing fin-ratio to increase melting speed did not show any notable effect while the presence of natural convection had highly significant influence. Also, 60–90° angle between neighbouring fins in natural convection condition exhibited the highest effectiveness. The authors of [139] illustrated a new cooling technique for low concentrated photovoltaic–thermal system, using a micro channel heat sink with different volume fractions of Al_2O_3–water and SiC–water nano-fluids. At different concentration ratios, the effect of cooling mass flow rate and nanoparticles volume fractions, system performance was investigated. Results from the numerical simulation of the thermal model showed significant decrease of solar cell temperature at higher concentration ratio

by using nano-fluids compared to using water. SiC based nano-fluid performed better in terms of temperature reduction compared to Al_2O_3 based, and nanoparticle volume fraction was found to be directly proportional to the achieved temperature reduction and hence electrical power increment. Consequently nano-fluids contributed towards higher electrical efficiency at higher concentration ratio, compared to water. For instance, for high solar concentration ratios where the cell temperature reduces to 38 °C, and electrical efficiency improves up to 19 %. It was surmised that nano-fluids increase thermal efficiency for low (less than 17.8) concentration ratios, while reduce efficiency for higher concentration.

From the literature survey, it has become quite evident that the combined use of passive-passive thermal management techniques has proven effective for solar cells and with BIPV systems. However, no mention has been found on their applications for BICPV systems in literature so far. The higher temperature and concentration of temperature around smaller areas makes the thermal management in BICPV designs different from BIPV .Therefore, one of the knowledge gaps that is addressed during this research work is proposing a combined (micro-fins with PCM and n-PCM) passive cooling technique for the temperature regulation of low concentration BICPV systems.

2.4 Phase Change Materials

PCM, as latent heat storage systems absorb and release thermal energy while undergoing reversible phase transformations over a narrow temperature range or at nearly constant temperature [140] thus, their heats of fusion can buffer temperature variations [141]. A schematic (Fig. 20) shows the working of PCM in a solid-liquid-solid type of phase transformation using the exothermic/endothermic cycle. Within the last few decades, a number for authors have reviewed the importance, uses, and challenges, encountered with PCM use [141-149]. The authors of [107], with their broad review of energy storage methods, investigated and analysed latent heat storage materials (thermal, physical, kinetic and chemical properties and economics) such as PCM. They categorised PCM as group I (most promising), group II (promising) and group III (less promising; with insufficient data) based on properties such as the T_m and the H and the number of carbon atoms. Measurement techniques for T_m and H, based on differential thermal analysis (DTA) and differential scanning calorimetry (DSC) using alumina as the reference material were also discussed in brief.

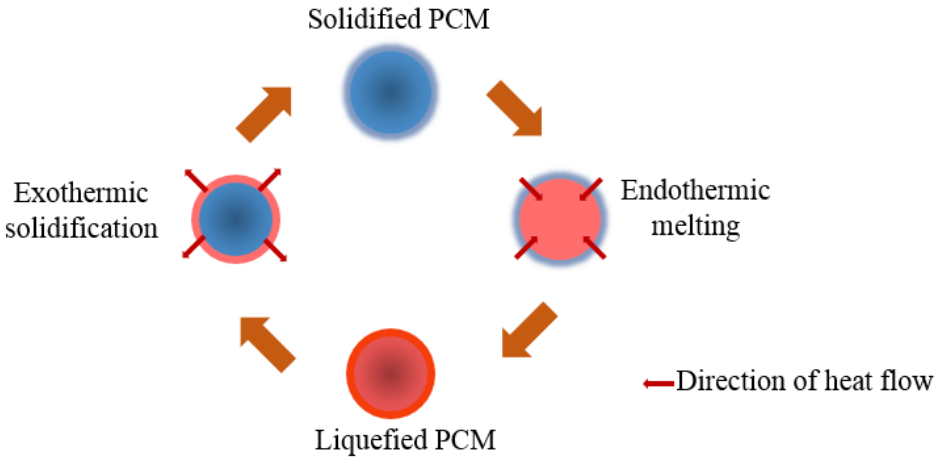

Figure 20: Schematic of the working of a PCM.

Thermo-physical properties (thermal conductivity, density and specific heat) of several PCM containment materials such as aluminium, copper, glass, stainless steel etc. were presented. Numerical simulation of latent heat storage systems, enthalpy formulation and numerical solution for the moving boundary or *Stefan problem* was suggested and solved using algebraic equations using the control volume technique developed by Voller [150] and Patankar [151]. An interesting concept of off-peak electricity storage was proposed in [152] wherein PCM were melted to stock surplus electricity as latent heat energy providing hotness/coldness when required, which can reduce peak load requirements and uniformalise electricity demand, thereby achieving cost reduction.

Selection of PCM could be broadly based on the following criterion, (a) phase change temperature range falling within the desired range [153]; b) high latent heat, specific heat and thermal conductivity; c) low volume expansion and low/no subcooling during freezing [153], d) non-poisonousness, non-corrosiveness, non-flammable, non-explosive and chemically stable [153]; and e) low-cost. It also includes parameters such as full or partial storage availability, freezing and melting heat transfer characteristics, cyclic duty and reliability [154]. PCM are also selected by their charging/discharging rates, heat exchanging surface, thermal conductivity (k) of heat exchange container material and effective k of the PCM [149].

2.4.1 PCM types

- Based on their initial and final states during phase change or physical/chemical transformation with absorption or release of heat PCM can be classified as solid-solid,

solid-liquid, liquid-gas and solid-gas types (Fig. 21). Typically, solid-liquid or crystalline solid-liquid solution types are mostly used due to the ease of working and functionality. The liquid-gas and solid-gas types of PCM are not preferred because of their dependence on compression and low volumetric heat capacity [155, 156].

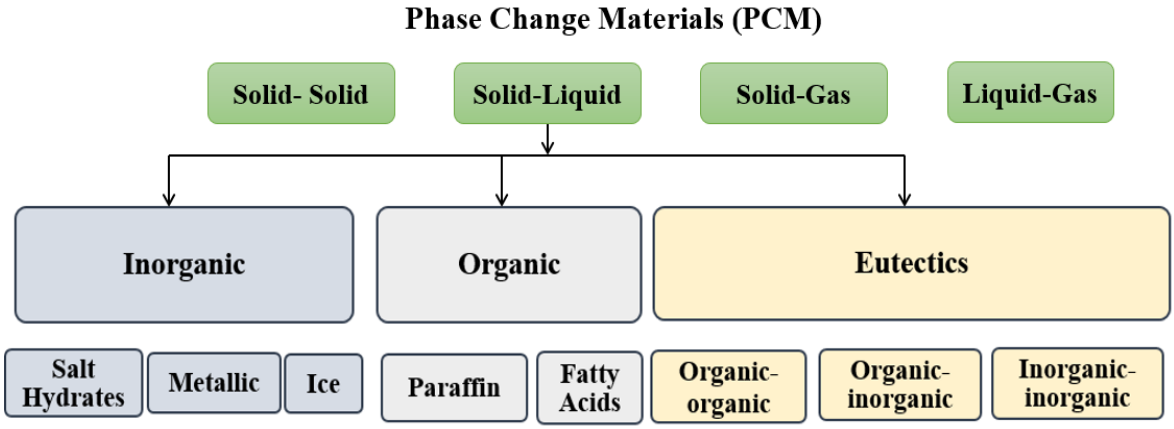

Figure 21*:* Classification of PCM types.

- Depending on the constituents, PCM may be broadly classified as Organic, Inorganic and Eutectics mixtures (Fig. 21, Table 5). Organic PCM comprise of either fatty acids or paraffin waxes (n-alkanes with the general chemical formula $C_nH_{2n+2;}$ n = number of molecules). They are more commonly used due to their high heat of fusion, availability in large temperature ranges, low super-cooling, inertness, stability, non-toxicity and relatively low cost [157-159]. However, on the flipside, they are flammable, exhibit low thermal conductivity and volumetric latent heat capacity and practically cause leakage issues in molten state due to thermal expansion. Commercially available organic PCM have phase change temperature ranging from -9 ºC to 150 ºC. Inorganic PCM, on the other hand, are based on salt hydrates (general chemical formula $AB.nH_2O;$ n = number of water molecules) and they have high volumetric latent heat capacity, higher k than organic PCM and higher heat of fusion [160]. Their limitations, however, are super cooling, easy and quicker decomposition and highly corrosive nature. Commercially available salt hydrate based PCM can be applied for applications with -21 ºC to 120 ºC phase change temperature. In their extensive review, [161] have shown that organic solid–liquid PCM have much more advantages and capabilities than inorganic PCM but do possess low k and density as well as being flammable. Eutectic mixtures are made of organic or inorganic compounds [162] and are capable of changing phase between (-114

ºC to 0 ºC). Table 5 highlights the advantages and disadvantages of PCM under these classification categories.

Table 5. Classification of PCM highlighting their advantages and limitations.

• Advantages ○ Limitations

Organic PCM	Inorganic PCM	Eutectics
Polymers with long chain of C, H molecules. Exhibit high orders of crystallinity when freezing and mostly change phase above 0°C • Availability in large temp ranges • Congruent melting • Chemical & Physical stability • High heat of fusion • Self nucleating properties • Safe, non-reactive, recyclable ○ Low thermal conductivity ○ Low volumetric latent heat storage capacity ○ Flammable	General formula: AB.nH2O (A-acid; B-base, n- no. of water molecules).Incorporate water of crystallisation while freezing, tend to change phase above 0°C • High volumetric latent heat storage capacity • High heat of fusion • High thermal conductivity • Sharp melting point • Non-flammable ○ Corrosive nature ○ Decompose quickly ○ Incongruent melting ○ Super-cooling	Solutions of salts in water with a phase change temperature below 0°C. Binary and tertiary eutectics of organic, inorganic compounds • Sharp melting point (range of pure substances) • Volumetric heat storage density higher than organic compounds ○ Lack of extensive research and knowledge gap

- Based on encapsulation size, PCM areclassified as macro (> 1 mm), micro (0–1000 μm) and nano (0–1000 nm) encapsulated [156]. Classification can also be based on the encapsulation container geometry (spherical, cylindrical, rectangular etc.).

Last five decades have seen the utilisation of paraffin waxes, hydrated salts, fatty acids and eutectics of organic/inorganic compound as PCM in a widespread range of applications and Farid et al [153] reason that the availability of PCM in with widely varying melting and solidification temperatures enable their use in extensive applications. Fig. 22 (a) draws the comparison of the melting point of various PCM types and Fig. 22 (b) shows the associated latent heats for the respective materials.

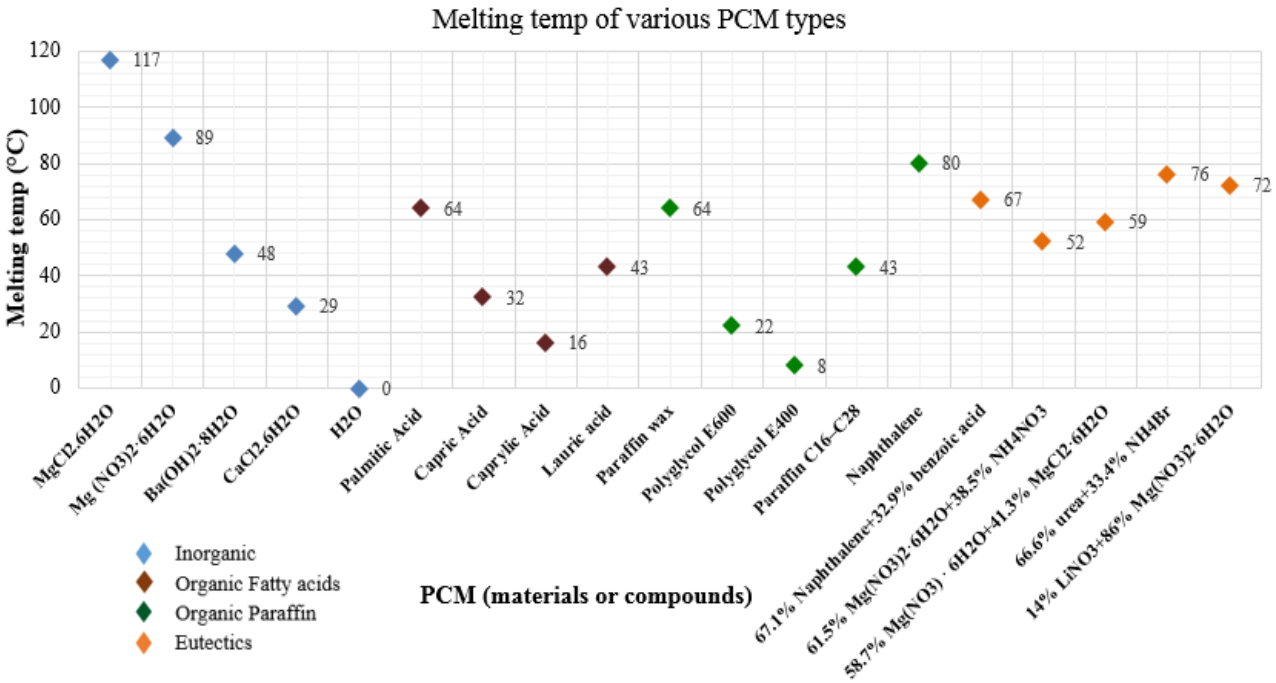

(a)

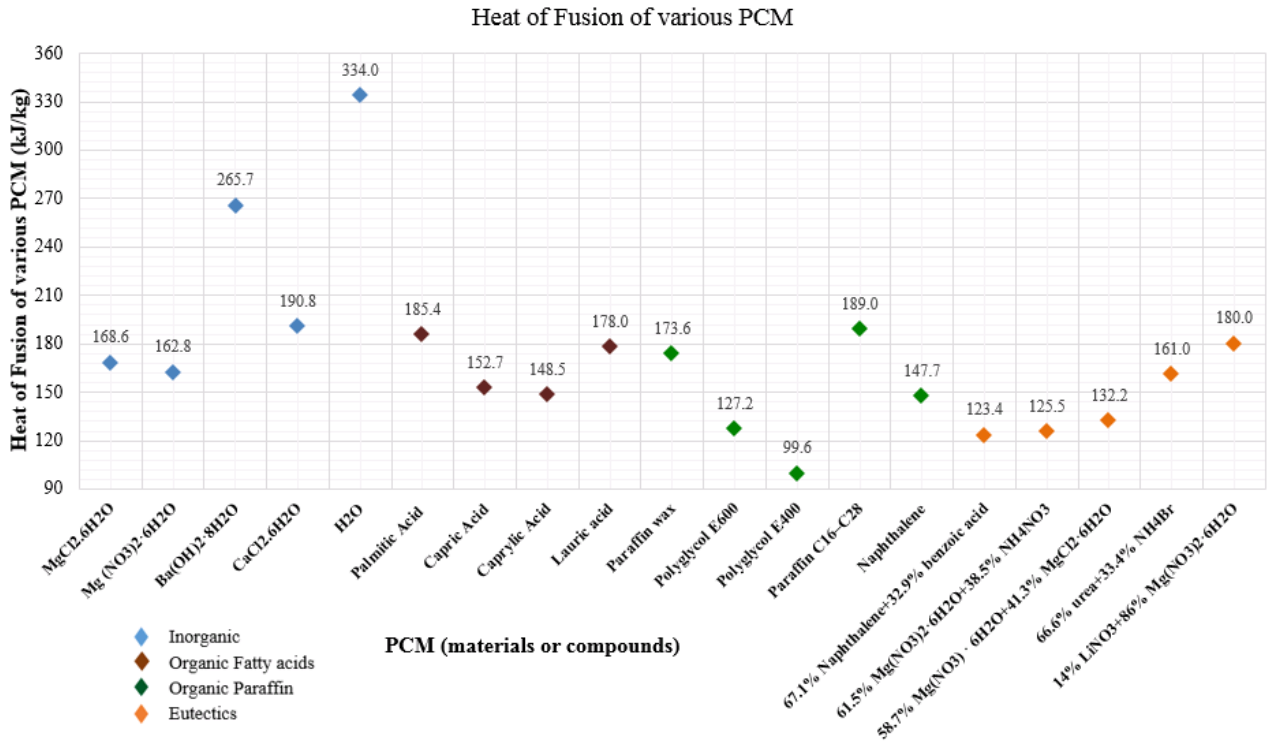

(b)

Figure 22: A comparative assessment of (a) melting temperature and (b) heat of fusion for various PCM types. (Data source: [141, 163]).

The important thermo-physical properties of a PCM such as the melting temperature (T_m), latent heat (H), and thermal conductivity (k), vary depending on the type of PCM (paraffin-wax, fatty acids, inorganic salt hydrates and eutectics). The former two are

discussed more in detail due to close relevance with the experimental work carried out in this thesis.

The details on synthesis, characterisation, and their thermal and chemical properties are elaborated within the publications for fatty acids based PCM [164-167] and paraffin based PCM [168-171]. Environment friendly and biodegradable bio-based PCM such as soybean, palm and coconut oil [172] etc. they are and owing to their substantially less inflammable nature, are becoming a preferred option to paraffin based PCM which are generally more inflammable.

2.4.2 PCM applications in literature

The wide-spread practical applications of PCM include residential buildings [173, 174], under concrete pavements [175], air conditioning systems [176, 177], thermo-regulated textiles [178, 179], PV panel cooling [134, 180], solar dryers [181, 182], solar chimneys [183, 184], smartphone and electronic device cooling [185-187], internal combustion engines [188], electrical super-cooling mitigation, battery thermal management [189] vehicle component thermal buffering [190] etc. Looking into specific PCM applications for thermal management of buildings, intended for higher energy efficiency via integration with building masonry [191], PCM are used as follows: inside buildings walls [192, 193], for under floor heating, they may be used in macro-encapsulated form into the ventilated façade in its air cavity for day lighting and room heating [194], for low energy and free cooling of buildings [89, 195], as lightweight thermally activated ceiling panels [196], as moving PCM curtains integrated with thermally effective windows [197], to impart improvement in hot water heat stores with stratification [198], as tiles for building use [199], floor supply air conditioning system using granulated PCM [200] etc. PCM were also used for capacitance in the air conditioning systems for reducing fluctuations in the daily cooling load, which later developed into direct integration with the refrigeration systems to save energy and for better control [201] and thermal energy storage for solar water heating applications [202].

2.4.3 PCM for BIPV cooling

Recently emerging concept of PV-PCM system integration for temperature control offers an opportunity for extending its usage to BIPV and BICPV systems. Employing PCM passively can retain BICPV temperatures within safe operating limit and can collect the

rejected heat for possible regeneration. Literature mentions hundreds of theoretical and experimental evidences and investigations to ascertain the effectiveness of BIPV-PCM and BICPV-PCM systems, a gist of which is presented here.

In their extensive review on PV-PCM, [203] suggested that researches have established the technical viability of PCM use for PV temperature control only if challenges such as thermal conductivity and phase stability are addressed. The authors of [204] used a commercial organic PCM to increase the PV electrical efficiency and output power using experimental setup and TRNSYS software for simulating the heat extraction. The experimental results demonstrated that the PV panel maximum temperature was reduced by 35.6 °C using PCM in a one day period. Simulation results showed that the PV-PCM panel output was higher by 7.3 % for one-year period. In a study on BIPV-PCM system, [205] developed a 1-D dynamic simulation program with MATLAB/SIMULINK® and solved it using control-volume based finite-difference scheme, where the electrical and thermal efficiency showed an increase of 10 % and 12 % respectively, with the experimental and the numerical results in agreement. The authors of [206] reviewed PCM utilisation for thermal management of concentrating and non-concentrating PV modules. The effect of temperature rise on different PV systems, comparison between hybrid photovoltaic thermal (PV/T)-PCM and PV-PCM systems, commercialisation, practical use, economics of incorporating PCM with PV systems, various experimental set-up of PV-PCM systems and results as given in literature and number of studies reported since 1978 through to 2014 have been discussed. PCM cooling techniques for PV systems could assume passive or active mode with heat regeneration achieved by natural cooling and active heat removal respectively. They concluded that by and large, the use of PCM contributes to performance improvement of such systems. However, the studies were performed for short durations and require testing for extended periods of time to understand the discharging and re-charging of PCM, as full discharge becomes indispensable for its maximum heat storage capacity during the next charging cycle.

PCM use for thermal regulation of BIPV has been experimentally reported [207], for a PV-PCM system that achieved maximum temperature reduction of 18 °C for 30 min and of 10 °C for 300 min at 1000 Wm^{-2}. A selection of five different PCM types (commercially available paraffin wax; RT20, eutectic mixture of Capric–Lauric acid and Capric–Palmitic acid, a pure salt hydrate; $CaCl_2 \cdot 6H_2O$, and a commercial blend; SP22

(T_m, 21-29 °C and H, 140–213 kJ/kg) were used for experiment at three irradiance levels of 500, 750 and 1000 Wm^{-2} to evaluate the performance of each PCM. Variable parameters for the experiment were thermal conductivity and mass of the PCM. It was achieved by altering container materials, dimensions (only width) and quantity. Four types of PCM containments were fabricated using aluminium and Perspex with 3 cm and 5 cm width. In general, all PCM containments made with aluminium (5 cm) performed better than Perspex for all irradiance levels. For warm climates (T_{amb} around 34 °C, I = 1000 Wm^{-2}), PV–PCM systems with Capric–Palmitic acid and $CaCl_2•6H_2O$ were found economically viable. The results from [207] could be summarised (Table 6) in terms of temperature difference (degree) and duration of deviation (time difference) between the BIPV surface temperature without and with PCM.

Table 6. Temperature difference and deviation in a 4-hour period for various PCM applied to BIPV.

Irradiance	**PCM →**	**RT20**	**Capric–Lauric acid**	**Capric–Palmitic acid**	**$CaCl_2•6H_2O$**	**SP22**
500 Wm^{-2}	Degree	4.6	7	7.5	8	6.5
	Duration	6.5	9	11.0	13	9.5
750 Wm^{-2}	Degree	7.5	8	9.0	10	7.5
	Duration	6.0	8	10.0	12	9.0
1000 Wm^{-2}	Degree	3.5	4	11.0	12	7.5
	Duration	5.5	6	9.5	11	9.0

In another relevant work, [208] investigated the commercial PCM's potential for the annual outdoor performance enhancement of a BIPV module outdoors using a simplified heat balance model to calculate the extra energy gain. They inferred from the theoretical study that an increase of up to 3 % of the total energy output with the use of PCM can be expected, however, the additional material and peripheral costs made the system seem economically unviable. They argued that for realising the standard payback period of 10-20 years, the PCM heat capacity may need to be increased by about one order of magnitude; an unrealistic task. Nonetheless, the double role-played by the PCM in controlling BIPV temperature as well as the building temperature made it a more feasible option. In order to investigate the temperature regulation effect of PCM on a rack-mounted PV panels [209] experimentally evaluated the heat dissipation in PCM containments with four different configurations.

2.4.4 PCM heat utilisation

As with any other technology, the future of BICPV-PCM integration depends on its technical feasibility, which is proven from the experimental and simulation results already published and the financial viability, in terms of costs incurred versus financial benefits realised. One factor that could support the viability factor, would be the possible utilisation of waste heat from PCM or enhanced thermal energy harvesting. As suggested by *Enibe* et al. [210], PCM can be utilised for passive solar powered air heating system. Another way of utilising the heat energy stored in PCM could be to combine a BICPV-PCM system with a solid-state thermoelectric (TE) technology based on either *Peltier* (cooling) or *Seebeck* (power generation) mode, which has been reported by [211] for low concentrator photovoltaic. The authors used a novel integrated CPV-TE PCB-based receiver based on Peltier module, which reduced the operational CPV cell temperature by 66.4 °C and increased the absolute cell efficiency by 2.38 %. They concluded that the TE technology proved convenient, reproducible with the capability to almost instantaneously control the operational steady-state cell temperature for different irradiance levels. In a study conducted on the direct cost benefit of the PV-PCM systems by the authors of [212], it was found that the investment costs for mass production of such systems were higher than the financial benefits, thereby reducing appeal in terms of cost effectiveness in cold European countries such as Ireland. However, the results were contradictory and positive when analysed for the warm Asian countries because of the benefit exceeding the costs almost two times, which reassured the feasibility and attractiveness of PV-PCM technologies. The experimental results, numerical simulation and reviews discussed in this section underline the effectiveness of PCM in electronic components cooling, for regulating PV and BIPV temperatures and pave a way for further introductory application into BICPV systems.

2.4.5 Challenges with PCM

The drawbacks of using PCM include low thermal conductivity (of the order of 0.2 W/m.K) [213] in organic PCM, high volumetric changes associated with the solid to gas and liquid to gas phase transformations [214], undesirable change in material properties due to cycling, phase segregation and sub-cooling [215] and corrosive effects [216-218] of inorganic PCM. The challenges mainly faced by the organic and inorganic PCM are discussed here.

2.4.5.1 Thermal conductivity

One of the main challenges with organic PCM as heat removal medium is their low k, which causes delay in PCM phase transformation, leading to slow charging and discharging rates and consequentially challenges in temperature control [219]. A possible solution to address this issue is the incorporation of thermal conductivity enhancers (TCE) [220, 221] by adopting following methods: PCM additives like carbon-fibre chips, aluminium powder, metal screens, metal spheres or utilizing metal fins and PCM absorption in porous metal foam or expanded graphite matrix to form composites which is an ideal choice [222]. Possible remedy to address it includes improved heat transfer techniques to increase charging, discharging rates and addition of high thermal conductivity materials. Traditionally used metal inserts with paraffin wax (reported since 1966) are Aluminium (forms such as honeycomb, powder, gauze, fins, alumina foam and powder etc.), Copper (Cu foam, plates used as circular and longitudinal fin etc.), stainless steel (screens, spheres, fin etc.), carbon fibre (woven sheets and brushes etc.) and graphite (powder, expanded, exfoliated, matrix etc.) [223]. TCE are of the form of fixed, stationary high conductivity inserts or structures such as fins [224, 225], honeycomb, wool, brush, powder additives, foam, woven sheets, screens, gauze, etc. traditionally made of metals such as Cu, Al, Ni, stainless steel and in the more recent years carbon fibres, graphite, graphene [226-230], single and multi-walled carbon nano-tubes [231-235]. In addition, graphite in the form of powder, expanded, exfoliated; matrix etc. has also been cited [236-238]. Composite PCM with fillers also prove to be very thermally conductive [239]. Experimentally, composite PCM thermal conductivity improvement of 14 % (with T_m=42-44 °C) and 24 % (T_m=56-58 °C) have been achieved using expanded, exfoliated graphite (EG) (ratio of 3% by mass) owing to the thermally conductive network of the EG pore structure [240]. Further, the thermal conductivities of composite PCM varied linearly (with a high correlation of 0.9986) with mass fraction of the TCE material, EG in this case. An increase of 81.2 %, 136.3 %, 209.1 %, and 272.7 % thermal conductivity in composite PCM was noticed using 2%, 4%, 7%, and 10 % mass fraction respectively compared to plain paraffin wax [241]. Preparation and properties of TCE based on Mg and Ca can be found in [242], while thermal performance of PCM with porous media as TCE has been mentioned in [243]. TCE use with PCM for cooling of electronic components has been reviewed extensively in [220] while experimentally studied in [244]. The authors of [245] experimentally analysed TCE for solar chimney applications

[246]. Review on TCE specifically for paraffin waxes can be found in [247]. Nanomaterials as TCE is proposed useful by several authors [230, 248-256].

2.4.5.2 Leakage issues: PCM Encapsulation

A critical issue with solid-liquid organic PCM is leakage [257, 258] in liquid phase due to volumetric changes in expansion. Encapsulation or shape-stabilisation is the process to integrate PCM into supporting material as macro or microencapsulating PCM could potentially avoid PCM leakage. The shape-stabilised PCM can be categorised as composite PCM or microencapsulated PCM (MEPCM) [259] and in both the cases, the shell stays stable during PCM phase change (Fig. 23). High-density polyethylene (HDPE) material, formed stable via cross-linking, has been frequently employed as a PCM supporting material due to its high structural strength. MEPCM comprises of a PCM core and polymer or inorganic shell to maintain the shape and prevent PCM from leakage during the phase transformation [260]. This allows greater heat exchange ability because of high amount of heat storage by MEPCM particles [261].

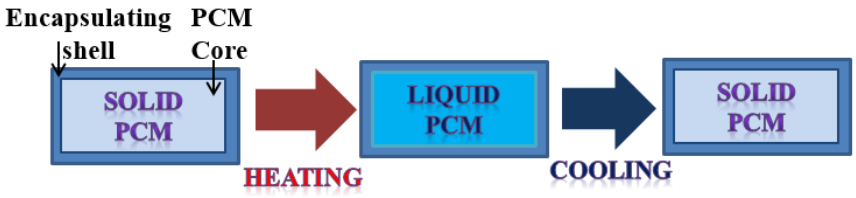

Figure 23: Structure and working of PCM in encapsulated form, Note that the encapsulating material undergoes no change during PCM phase transformation.

Encapsulation of PCM in a matrix on nano-scale has attracted attention in the recent times because it leads to more stabilised and tuned properties of active material [262]. The advantages of PCM encapsulation are availability of large heat transfer area, reduction of PCM reactivity towards outside environment and controlling the changes in volume of the storage materials during phase change [153]. To ensure higher mechanical strength and leak proof characteristics, high PCM encapsulation efficiency is considered desirable and the enthalpy of phase change of the encapsulated PCM is a strong function of encapsulation ratio and encapsulation efficiency [261]. Various forms of commercial encapsulated PCM are shown in Fig. 24: (a) Flat containers for building temperature regulation, (b) Ball containers for heat storage (solar, waste heat, hot water etc.), (c) Tubes for stacking in tanks with minimal void space, (d) Flexible metallic/non-metallic pouches

for temperature critical transport use, (e) Eutectic plates for temperature controlled shipment and (f) Hot/cold plates for food transportation.

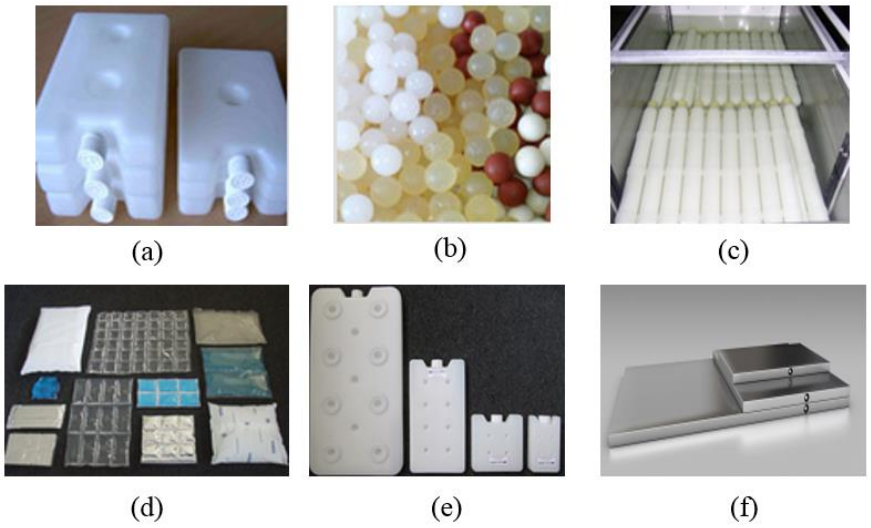

Figure 24: Commercial encapsulated PCM (courtesy: PCM Products Ltd. UK).

An important parameter, core-to-coating ratio affects mechanical and thermal stability while thermal conductivity of the shell material decides the heat transfer rate. Though encapsulation of metallic shells is difficult, they offer high heat endurance and HT rates, for e.g. silver nanoparticles show substantial improvement in thermal and structural stability of microcapsules on addition with the shell surface [261]. A technique proposed for using PCM as thermal system comprised of forming a two-phase fluid by mixing with another fluid, most commonly, water with PCM.

The five main types of these mixtures [263] are: (i) Ice slurries, (ii) micro emulsions (dispersion of PCM, water using an emulsifier), (iii) Microencapsulated PCM slurries (microencapsulation of PCM in polymeric capsule, dispersed in water), (iv) Clathrate hydrate PCM slurries (clathrate hydrates composed of water as a host molecule, forming a weaved structure where the molecules of other substances are accommodated as guest molecule). The accompanied heat exchange due to the chemical reaction of formation and dissociation of clathrate hydrate amounted higher greater compared to melting of ice into water) and (v) Shape-stabilized PCM slurries (organic PCM infiltrated in high density polyethylene, with a melting temperature higher than of the paraffin). This way paraffin is retained inside the structure of high-density polyethylene, avoiding leakage.

The authors of [264] proposed a BIPV integrated with MEPCM and performed the parametric numerical simulations for thermal and electrical characterisation of the BIPV-

PCM system. The results showed that after operating for a day in summer, more than half the m-PCM layer remained in liquid phase while increasing the minimum efficiency by 0.13 %. In winters, a portion of m-PCM did not freeze in the middle, increasing minimum efficiency by 0.42 %. During the normal conditions, the respective increase and decrease in the minimum efficiency was 0.09 % and 0.18 %, respectively for aspect ratios of 0.277 and 1. They concluded that employing appropriate m-PCM layer improved both, the thermal and electrical performances of BIPV and that the performance also relied on the melting temperature and aspect ratio of the panel. Studies in [203] show the potential of the emerging PV/T technology with MEPCM.

2.4.5.3 Corrosion

Another challenge with organic PCM as thermal energy storage is the corrosion of metal pipes, plates and PCM enclosures or containments; anything that remains in contact with salt hydrates under temperature. Farrell and co-workers [216] experimentally investigated the corrosion rates of aluminium alloys and copper as utilized in heat exchangers in air conditioning industry and found that copper experienced the maximum mass loss, while with aluminium had very insignificant mass loss in contact with PCM. In a study on salt hydrates used for LHS, Porisini [265] experimented with the corrosion of metals used for storing PCM and their reliability of thermal performance. LHS components with salt hydrates such as $Na_2SO_4.10H_2O$, $CaCl_2.6H_2O$, $Na_2SO_4.1/2NaCI.10H_20$ with 15 °C $<T_m$ < 32 °C were considered while enclosing materials such as stainless steel, carbon steel, AI alloys, and Cu were tested. Stainless steel was tested as the most corrosion-resistant alloy to all the hydrated salts tested. It was also concluded that copper had a corrosion zone that did not increase after extended periods of time [265]. An image of a corroded stainless steel container encountered during high temperature inorganic PCM is shown in Fig. 25.

Figure 25: Corrosion of a stainless steel based PCM container.

2.4.5.4 Phase segregation and sub-cooling

Ideally, the latent heat of fusion and crystallization are constant over cyclic uses for a perfectly reversible PCM. However, differences arises due to subcooling or incongruent melting [261]. Inorganic PCM tend to lose their high storage density after repeated use due to incongruent melting and hydrated salt formation, making the process irreversible and leading to the continuous decline in their storage efficiency [153]. The salt hydrates do not change their phase straightaway, around their phase change temperatures, due to subcooling, wherein the PCM remain in a metastable state; not in a thermodynamic equilibrium, to reduce which, nucleating agents are added to PCM [75, 266].

2.5 Thermal Conductivity Enhancers: Nanomaterials

In order to overcome the inherent low thermal conductivity of PCM, nanomaterial based TCE can be added to a base PCM. Nanoscopic properties differ significantly from their corresponding macroscopic properties; the extremely minute particle size along with increased surface area display unique property creating vast potential for applications [267, 268]. Nanomaterials are defined as materials with one or more dimensions in the nanoscale (10^{-9} m) range, while nanoparticles are discrete entities with all three dimensions in the nanoscale [269]. The various nanoforms available for both nanomaterials and nanoparticles are nanotubes, nanofibres, nanorods, nanofilms, nanolayers, nanocoatings, nanosheets; these names stemming from their individual shapes and dimensions [270]. The term nanoparticle-enhanced PCM (NEPCM), referred to as n-PCM within this communication, was coined by the authors of [271] about a decade ago; they proposed the potential use of n-PCM for various thermal energy storage applications. Nanotechnology is proving attractive for many applications as nano-scaling tend to demonstrate significant change in the physical and chemical properties of the materials unique from their micro, macro or bulk equivalents. Similar to PCM classification, nanomaterials can be categorised as (i) organic, for example, fullerenes, carbon nanotubes (CNT); single-walled and multi-walled (SWCNT and MWCNT), graphite and nanofibers and (ii) inorganic such as metal and their oxides (aluminium, alumina, copper, cupric, cuprous oxide, iron, zinc, titanium, their oxides) and metalloid nanomaterials or Quantum dots, such as CdSe, ZnS, ZnO etc. [247]. Hybrid materials can be produced as different combinations of organic and inorganic nanomaterials via synthesis amalgamation (Fig. 26).

Kalaiselvam et al [154] conducted experiments and analytically investigated heat transfer characteristics and thermodynamic behaviour of spherically enclosed six different pure PCM and with dispersed nanoparticles for latent thermal energy storage system in buildings. It was observed that the solidification time was reduced by 12.97 % for PCMs dispersed with aluminium nano-particle of volume fraction of 0.07 (13820 s) as compared to (15880 s) for a pure 60 % n-tetradecane: 40 % n-hexadecane PCM.

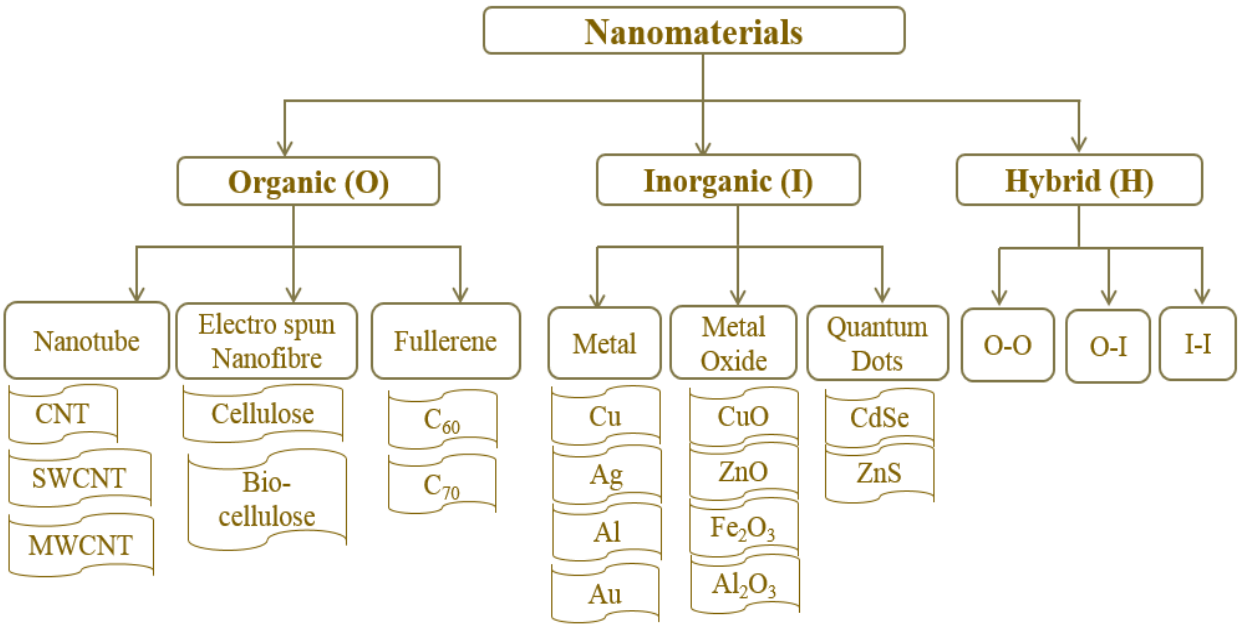

Figure 26: Classification of nanomaterials (adapted from [272]).

This further reinforces the argument that utilisation of nanomaterials are practically useful for overcoming poor PCM properties. As reported by Khodadadi et al [239], nano fluid (water with copper nanoparticles) addition to PCM showed improvement in k of PCM during heat release. For the experiment, three solid particle volume proportions of 0, 0.1, and 0.2 were used with Stefan no. 0.125, 0.136, and 0.50 respectively. Time was measured in 100, 500, 1000, 1500, sec and contours were generated for volume fraction of nano-fluid (λ=0 implies solid phase while λ=1 suggest liquid phase). The results indicated the sharp L-S interface improved functionality of NEPCM with respect to the base fluid. Jeong et al. [273] carried out experiments using exfoliated graphite nano platelets (xGnP), known for its chemical inertness and resistance to thermal degradation, seeking improvements in the thermal properties of bio-based PCM. xGnP comprises of several layers of graphene sheets with higher aspect ratio as compared to carbon nanotubes. Using thermal gravimetric analysis (TGA), differential scanning calorimetry

(DSC), Fourier-transform infrared (FTIR) spectroscopy and k analysis, they concluded that bio-based PCM, completely incorporated into the porous xGnP structure, resulted in 375% increment in k rendering thermally enhanced bio-based PCM (k=0.557 W/mK) more useful than its counterpart bio-based PCM (k=0.154 W/mK). In a study undertaken by [274], n-PCM were developed using pure paraffin waxes as the base PCM and alumina and carbon black as nanomaterials TCE. The resulting n-PCM with alumina showed the highest latent heat enhancement of more than 10%, while the one with carbon black showed high k improvement of above 25 %.

2.5.1 CuO nanostructures

An important class of transition metal oxides such as cupric oxide (CuO, a 3d metal oxide), has been found appealing due to interesting properties such as high thermal conductivity, critical temperature, semiconducting nature with a narrow band gap (1.4–1.7 eV) which make it useful for photoconductive and photo-thermal applications [275]. The crystal structure of Copper (II) Oxide is shown in Fig. 27 (a) and a Scanning Electron Microscope (SEM) image is given in Fig. 27 (b). CuO nanostructures offer excellent electrical, optical and catalytic properties and are available in many structures with different morphologies such as nanoribbons, nanowires, nanorods, nanotubes, nanoflowers, nanorings, nanosheets, nanoleaves, nanowhiskers, nanoplatelets, feather-like, urchin-like [276] and plate-like [75] structures. They are non-toxic, available at low cost and are chemically stable [277].

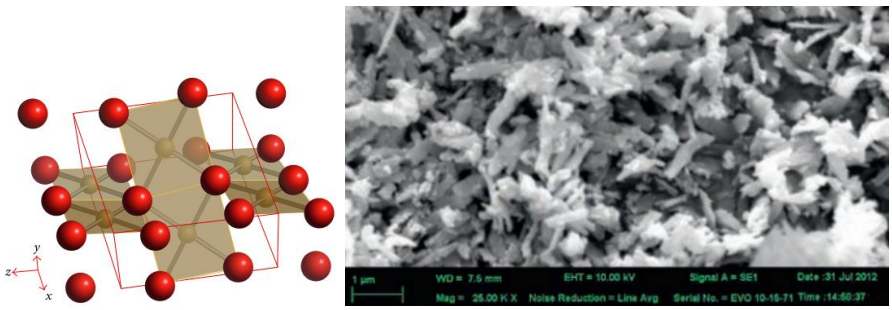

(a) (b)

Figure 27: CuO nanoparticles:(a) the crystal structure [278] and (b) SEM image [279].

CuO nanostructures are used in water chiller systems [234], antimicrobial applications against a range of bacterial pathogens [280], lithium ion storage [281] and CuO nanosheets as anode materials for electrochemical energy storage [282]. CuO nanostructures also find applications in supercapacitors, solar cells, gas sensors, bio

sensors, catalysis, photodetectors, energetic materials, field emissions, removal of arsenic and organic pollutants from waste water [283].

2.5.2 CuO nanomaterial based n- PCM as TCE

In [284], the authors experimentally and numerically investigated the constrained melting of n-octadecane as PCM dispersed with CuO nanoparticles as TCE in a horizontal cylindrical vessel under a constant heat flux. They emulsified the PCM with varying mass fractions of CuO nanoparticle (1, 3 and 5 wt. %) and concluded that TCE increased the effective k and improved the melting process of the PCM; the rate of melting process being higher at lower value of nano-additives, but this rate decreased for higher values of nanoparticle concentration because of growing effects of viscosity, agglomeration and sedimentation. In addition, it was deduced that the lower concentrations of TCE displayed higher energy storage capacity and involved less costs compared to higher concentrations [284]. Experimental results from [234] revealed that nano-fluids with low concentration of Cu or CuO showed significantly higher thermal conductivity. For the case of CuO-ethylene glycol suspensions at 5 vol. % and Cu-water at 0.1 vol. %, k increased by 22.4 %, and 23.8 % respectively. It was concluded that the volume fraction had an approximately linear relation with TCE in case of CuO nano-fluids. The experimental work in [285] suggested that TCE were almost two times as effective in RT25 (lower melting temperature range) than in RT42 (higher melting temperature range) during melting process, and five times in solidification. Further, studies using RT42 (the PCM used for the experiments within this publication) showed that addition of metal based TCE, even in low volume fraction (< 4%), greatly improved the heat transfer characteristics of the PCM. They also concluded that higher volume fractions of TCE do not always lead to better thermal regulation and also that the distribution of the TCE within the PCM mix has considerable effect on heat transfer.

A n-PCM was prepared using RT42 (50 % by mass) mixed with (15%, 200μm) graphite platelets (expanded graphite or EG) acting as TCE within HDPE matrix [286]. The composite so formed displayed fine dispersions of EG, improved mechanical properties, with unchanged melting and solidification temperatures, enhanced thermal stability of the composite and increased k (from 82.7 % to 207.4 %) with increased mass fractions of EG (5–15 %). It was also deduced that along with the increase in thermal conductivity, the lowering of latent heat of fusion gave rise to higher heat release rate of the n-PCM. The

results from [287], a study on the effect of CuO nanoparticles (average size 30-40 nm) on the k of paraffin, revealed the direct correlation between the nanoparticles volume fraction in the suspension and the effective k of the nanofluid and that a decrease in nanoparticle size initiated increased Brownian motion of the particles, leading to more particle-to-particle interactions. The various underlying phenomenon considered were the lowering of fluid viscosities and the interaction of fluid with the nanoparticle surface, which produced a shell of ordered liquid molecules on the particle surface that transmitted energy (via phonons), to the bulk of the fluid. This energy transmission resulted in greater k of the suspension so formed, which was measured experimentally to compare with a variety of models. However, the models could not predict the thermal conductivities of the nanoparticle suspensions effectively.

The authors of [288] experimented on beeswax/CuO nano-PCM using DSC to measure the melting temperature and heat capacity and inferred that the melting temperatures with 0.05, 0.1, 0.15, 0.2, and 0.25 wt % were of 63.62 °C, 63.59 °C, 63.66 °C, 63.19°C, and 62.45 °C respectively. Furthermore, there were no chemical interactions between CuO and wax as found with the FTIR testing and though k increased, the heat capacity decreased, which apparently did not affect the nano-PCM performance. Thus, the resultant heat transfer of nano-PCM was faster than the base PCM. In another relevant study, [289] examined the effect of alumina and cupric oxide nanoparticles on the thermal performance of paraffin wax (dispersed with 0 %, 1 %, 3 %, 5 % and 10 % by volume of nanoparticles) and concluded that both the TCE only marginally increased the thermal conductivity. However, alumina performed slightly better due to the lesser magnitude of dynamic viscosity increase and also because the k of alumina was higher, an underlying reason for the ease in melting for conduction dominated solidification process. The authors argued that the economically viability for the technology due to stability and cyclic durability was still questionable [289].

2.5.3 CNT

CNT belong to the structural family of fullerene and are carbon allotropes of seamless cylindrical structure with diameter ranging from one to a few nanometers [290]; some pictures are shown in Fig. 28 (a-d) and SEM images in Fig. 28 (e-g). CNT length size in the range of 100 nm to several cm [291] and they may be open or close ended. Their thermal conductivity depends on the nature of helix and they are good conductors of heat

in axial direction while behaving as heat insulator in lateral direction [292]. The span of usage is due to their unique thermal, mechanical, chemical and electrical properties such as extremely high electron mobility (100,000 cm^2/Vs) [293] leading to high current carrying capacity, high electrical conductivity (104 S/cm) [294], high k (3500 W/mK) [295], hardness equivalent to that of diamond, and high thermal stability. However, CNT as bulk composite materials and thin films based on unorganized CNT architectures have lesser values for these properties than their organized counterparts such as yarns and sheets [291]. Exceptionally high k makes it the most likely choice as filler for composite material. Han et al [296] discussed the effect of nanofiller addition to polymers to increase k. In another study on molecular dynamics simulation carried out by Berber et al [297] an unusually high value of k (equivalent to 6600 W/mK), equivalent of an isolated graphene monolayer or diamond was observed. The reason was large phonon mean free paths in the system. CNT can be classified based on the layers of graphene and their structures [290], as (a) Single-walled nanotube (SWNT-diameter ≈ 1 nm; tube length ≈ several thousand times diameter); (b) Multi-walled (MWNT); (c) Polymerized SWNT (solid-state manifestation of fullerenes and related compounds with diamond-like hardness); (d) Nanotorus (carbon nanotube with very high magnetic moments) and (e) Nanobuds (combine CNT and fullerenes with *buds* covalently bonded to the outer sidewalls of the underlying CNT).

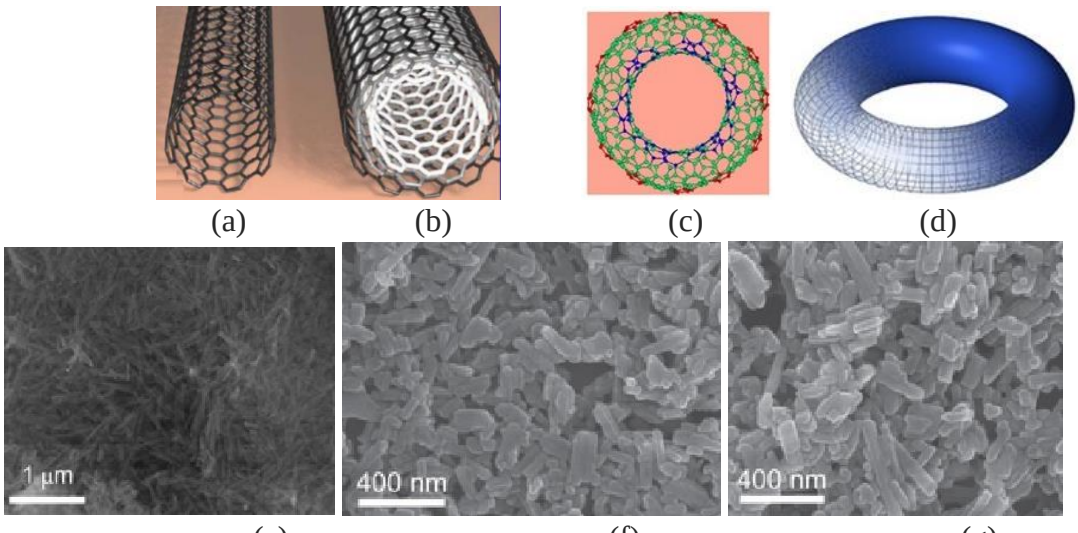

Figure 28: (a) SWCNT, (b) MWCNT [298], (c) a nanotorus and (d) its continuum model [299], (e), (f) and (g) SEM images of carbon nanorods from different areas (image courtesy Pradip Pachfule et al. [300]).

An experiment by Assael [301] investigated the effect of adding C-MWNT to water. Graphitic sheets were rolled in the form of C-MWNT with 20–100 annular layersAs dispersant, sodium dodecyl sulphate was used with a 0.6 % (v/v) suspension of C-MWNT in water. They concluded that a maximum of 38 % k enhancement was attained and that the k increase is directly proportional to the ratio of length/diameter which means longer the nanotubes for a given diameter, more is the enhancement recorded.

For the purpose of the experimental work undertaken within this thesis, nano-CuO was selected as a TCE in the preliminary investigation for which a brief literature survey is presented here. The rationale is described in the next chapter. Based on whether the resulting n-PCM improves the thermal performance of the PCM, more expensive TCE such as CNT could be utilised, which offer promising solutions.

2.6 Conclusions

There are several possible solutions to address the BICPV heating, out of which passive temperature regulation using PCM is primarily studied. Although apparently sensible media have been implemented in significantly more projects due to the maturity of technology and less expensive material, latent media are preferred for high energy density and nearly constant charging/discharging temperatures. PCM applied to BICPV can increase the overall system efficiency by two means. As a heat sink for dissipating heat, reducing the module temperature and minimising the reduction in BICPV efficiency. And, as a heat storage system for thermal applications (hot water, space heating and misc. agricultural use), thereby increasing overall system efficiency.

This chapter provides the fundamental evidence and influences the work produced in this thesis, as it introduces most of the theoretical and experimental information that form the foundation of the experimental work presented in the next chapters. The research questions and the knowledge gaps are acknowledged based on a thorough literature review. In addition, this chapter reveals two main important facts:

- Paraffin wax based PCM have been selected for low concentration BICPV as they are capable of desirable temperature control i.e. by keeping the BICPV temperature as close to the normal operating cell temperature. However, their low k needs addressing using TCE such as metal mesh/metallic oxide nanomaterial. The current research proposes to take the investigation further, develop solution for improving k

leading to synthesis of nanomaterial enhanced PCM (n-PCM). The effectiveness of PCM/ n-PCM for these low concentration BICPV have never been reported before.

- Micro-fins have been used in electronic cooling and light emitting diodes etc. but their application for a low concentration BICPV alongside PCM is also one of the novelties of this proposed research work.

After the literature survey on possible TCE, copper metal filler and nano-CuO were targeted for initial investigations due to availability, low cost and promising results. However, depending on how effective n-PCM proves for BICPV thermal management, CNT, though highly expensive may prove vastly beneficial. Passive-passive techniques seem to produce further enhancement in BICPV temperature control than the individual techniques applied in isolation. However, these are still in their nascent stage with regards to their application in low concentration BICPV systems. Their viability is only beneficial if the net profit exceeds the additional costs for PCM and micro finning. A suitable option to contribute towards increasing viability is thermal energy harvesting by adding a low temperature TE that has shown promising results in similar experimental proofs without PCM usage. The next chapter will focus on the available and selected materials for producing the BICPV and PCM system components; the methods, design and fabrication process for assembling. In addition, the instruments and techniques used during fabrication and for further experimental analysis are described.

Chapter 3. Materials, Methods and Designs

This chapter deals with the selection of materials, design, pre-fabrication, and engineered fabrication of the BICPV-PCM systems for experimental purposes. It also presents a list of the (i) key materials, (ii) instruments and (iii) analytical techniques, employed to carry out the experimental work contained within this thesis. The BICPV systems were attached with the appropriately designed PCM containments using various types of adhesives. Joining the internal and the external electrical circuitry followed this and attaching the peripheral devices for monitoring desired parameters. The original design of the BICPV, with top and bottom glass surfaces has been renovated using metallic back-plate. New approaches to manufacture PCM containments by selecting improved techniques, adequate thermally insulating materials, PCM with high latent heat capacity have been employed. The sections below are mainly divided into the categories of CPV, (BICPV/WICPV) system (acting as the heat source), PCM system (acting as the heat sink), the instruments (used for fabrication and assembling the components together as well as to run the measurements) and the software packages (used to design components, simulate experiments for validating the set-up and for thermal analysis) relevant to this research work. Analytical techniques using these instruments, based on software programs for material characterisation of PCM are briefly explained towards the end.

3.1 Methodology

The experimental work carried out within this thesis was focussed on BICPV-PCM systems, hence the material required for fabricating components of (BICPV/WICPV) system (heat source) and PCM system (heat sink) are described separately. Primarily, the BICPV system comprises of solar cells and concentrators with an optical transmission medium, whereas PCM systems are formed with various kinds of commercially available plastics and an organic PCM. The few thermal systems investigated within this thesis were: (i) a BICPV system based on LACPC, (ii) a BICPV system based on SEH concentrator, (iii) a Window-integrated (WICPV) system based on SEH and (iv) a small prototype of a thermal system without the PV component to study the effect of micro-fins as an auxiliary passive cooling mechanism. One test prototype module was fabricated for each type of BICPV-PCM system. The designs, materials and components of these aforementioned systems, and the rationale for material selection are described in the

subsequent sections. The model and make and the basic working principle of the instruments and devices used for: (i) fabricating and assembling the system components together (such as metal guillotine, solder and welder mentioned under miscellaneous devices), (ii) to run the measurements (such as solar simulator, DSC, SEM, XRD etc.) on the BICPV-PCM system and (ii) the software packages for material thermal analysis relevant to this research work are explained. The design and fabrication part of the thesis was based on the adopted fundamental research methodology as shown in Fig. 29.

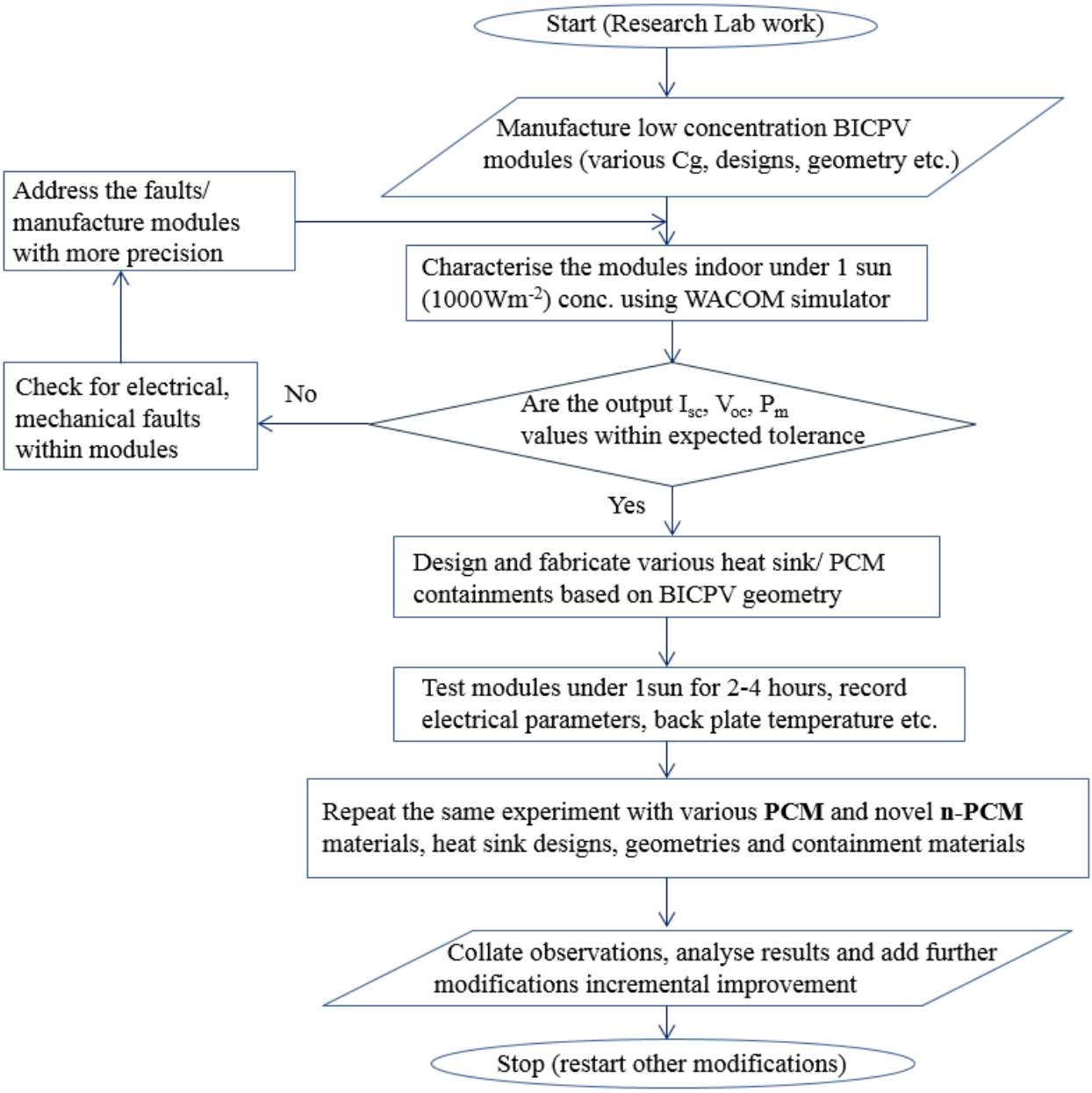

Figure 29: Process flow diagram for the research methodology followed for the thesis.

It describes the end-to-end experimental procedure in a methodical manner, from the fabrication of the BICPV system to characterisation, design and fabrication of the PCM systems and the use of the experimental methods such as testing procedure etc. for data collection. In order to determine the performance improvement imparted by passive cooling methods (micro-fins, PCM or n-PCM addition or a combination), the designed BICPV modules were tested for their thermal and electrical response, first without, and then with cooling. A highly collimated light provided illumination for electrical characterisation of the modules using a solar simulator. In cases where only thermal characterisation was the primary objective, a resistive heat source was used instead, along with a direct current based external power supply to emulate the temperature profile as obtained in BICPV modules under solar simulator. The output I-V curves and temperature data were obtained and compared for the cooled system against the baseline system with no cooling. Further, the BICPV-PCM experimental set-up was modified to investigate the effects of: (a) irradiance levels, (b) back-plate geometry, (c) PCM containment material, (d) PCM types, (e) passive cooling techniques such as micro-fins, water and PCM with different melting temperature ranges and (f) nanomaterial addition to PCM. In addition, some samples of PCM and nanomaterials were characterised and studied using scanning electron microscope (SEM), differential scanning calorimeter (DSC), and X-ray diffraction (XRD). Some of the thermophysical properties data from PCM suppliers and morphological data for nanomaterials were scrutinised for their validity and the observed deviations were reported.

3.2 BICPV Systems: Materials

A typical CPV (BICPV/WICPV) system consists of several elements; a dielectric optical solar concentrator at the light collection end, an encapsulant in between solar cells and concentrating element, soldered silicon solar cells at the absorbing or receiver end, a polyimide film for masking the metal, an aluminium (Al) base plate, soldering ribbons and insulating sleeves for electrical connections and the attached thermocouples for temperature measurements (Fig. 30). The key instruments employed during the fabrication processes were a metal guillotine machine, soldering station with soldering pencil and power supply, a vacuum oven and a thermocouple welder, detailed later.

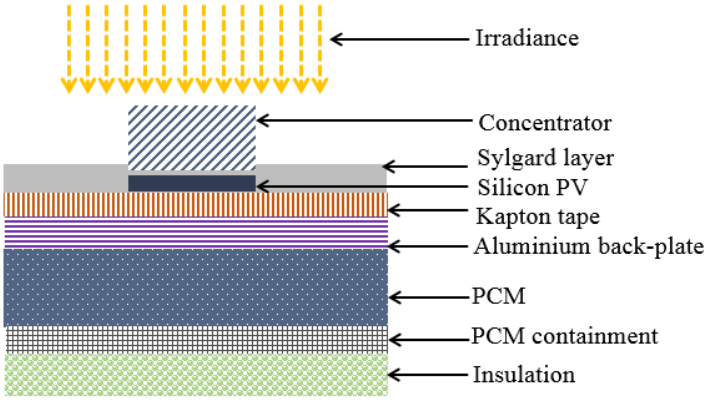

Figure 30: Components of a BICPV system.

3.2.1 Solar Cells

The solar cells used for this research work were crystalline Si-based LGBC (laser grooved buried contact) although there are provisions for utilising other kinds of solar cells with the same concentrators as in the original design. For low concentration modules, the selected solar cells are found suitable in literature because of their high efficiency, low cost, selective emitter structure and low contact shading [17]. The schematic of an LGBC solar cell (Fig. 31), with various layers of metals, alloys and doped metals is given for reference purposes, as there is no further research into this area within the thesis. Similar cells were employed in the original designs for LACPC [46, 302] and SEH [47, 74] based BICPV or WICPV respectively. It is to be noted that the due to the long-term storage of the solar cells used for this research work, their operational efficiency may have degraded. However, as the study undertaken within this research is relative or comparative in nature, this would not affect the final results.

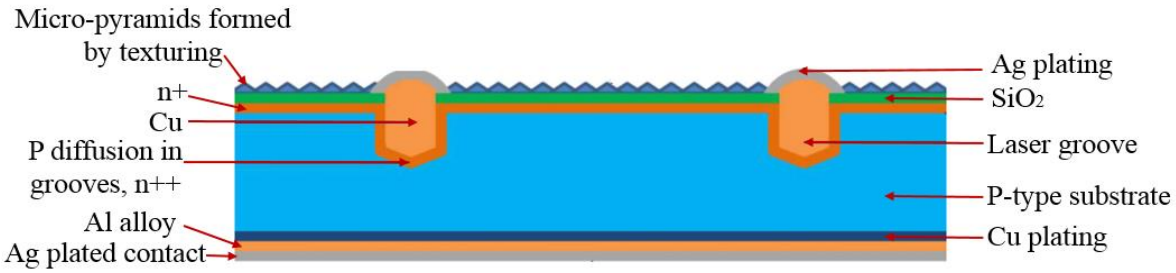

Figure 31: Schematic diagram of an LGBC solar cell structure; adapted from [48].

(i) Solar cells for LACPC

The 116 mm long, 6 mm wide *Saturn* solar cells with 6 fingers and 2.5mm bus bar width on the two ends were used with LACPC for BICPV (Fig. 32).

These cells have been optimised to perform under conditions of up to 10 x [75].

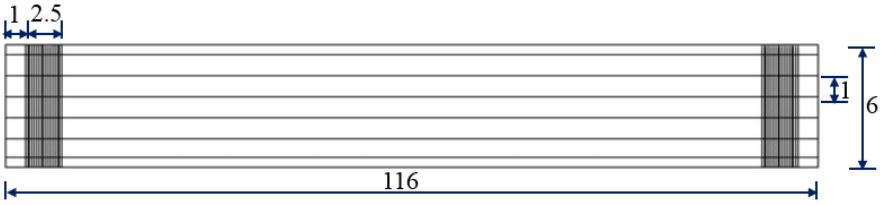

Figure 32: LACPC solar cell dimensions (in mm); adapted from [48].

(ii) Solar cells for SEH

With SEH concentrators, *NAREC* solar cells (11.5 mm long, 10 mm wide) were used with an effective area of (1 cm x 1 cm), hence, nearly square in shape (Fig. 33). Both, the 116 mm long and 11.5 mm long cells, had identical material composition, however, different dimensions. The technical data for both the types of cells are given in Table 7.

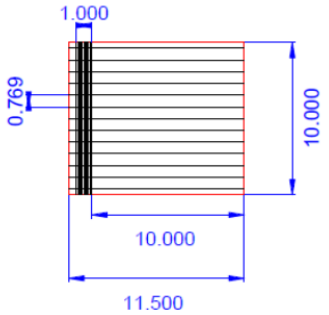

Figure 33: SEH solar cell dimensions (in mm)[43].

Table 7. Solar cell parameters.

Parameter	LACPC	SEH
Cell width (mm)	116	11.5
Cell length (mm)	6	10
Cell Thickness (mm)	0.3	0.3
No. of fingers	6	13
Busbar width (mm)	2.5	1
Finger width (μm)	35	35
Emitter sheet resistance (Ω)	100	100
Finger resistance per unit length (Ω/cm)	0.3	0.3
Conductivity (W/m/K)	148	148
Density (kg/m^3)	2330	2330
Specific heat (J/kg/K)	712	712

(iii) Micro-finned thermal system: Heating element

Whilst in a BICPV/WICPV system, solar cells are responsible for the heat generation during the electrical conversion, a heat source was used for the micro-finned thermal

system by means of a heating element equivalent to produce the combined heating effect of a solar cell and concentrator. *Omegalux® Kapton flexible heaters (Omega® KHLV-101/10-P)*, with 0.254 mm thickness and high flexibility, suitable for both flat and curved surfaces, were bonded to the plain and the micro-finned Al plate using an adhesive backing (Fig. 34). The rectangular heaters provided 28 V, 10.55 W/cm^2 and were supplied with 12 inches of Teflon insulated lead wire.

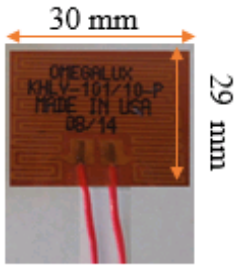

Figure 34*:* Omegalux® Kapton flexible heater.

3.2.2 Concentrators

The concentrators were manufactured using a dielectric clear polyurethane material, *Smooth-On Crystal Clear 200®*, selected due to its high transmission, low shrinkage, resistance to humidity and to solvent. Its low viscosity ensured ease of mixing and pouring and offered the benefit of resin curing at room temperature with negligible shrinkage. The resin is available as a 2-part mixture has part A, which is a modified aliphatic di-isocyanate (*4, 4´ Methylenedicyclohexyl diisocyanat*e) while part B comprises of *Phenylmercury neodecanoate*. Material properties are given in Table 8.

Table 8. Physical and electrical properties of Crystal Clear® 200.

Parameter	**Value**
Tensile Strength (psi)	2500
Compressive Strength (psi)	6385
Mixed Viscosity (cps)	600
Pot Life @ 23°C (Min)	20
Cure time at room temp(hour)	16
Specific gravity (g/cc)	1.036
Refractive Index	1.49962 at 20°C
	1.49894 at 25°C
Dielectric Strength (Volts/mil)	260
Dielectric Constant (at 100 Hz)	3.36
(at 1 kHz)	3.34
Vol. Resistivity (ohm-cm)	1.4 x 10^{15}
Dissipation Factor (100 Hz)	0
(at 1 kHz)	0.01
Shrinkage in./in.	0.001

Elongation at Break %	1000%
Mix Ratio	100A: 90B by weight
Heat Deflection Temp (°C)	50

3.2.3 Back-plate

The Aluminium back-plate, formed the base for mounting the skeleton solar cells with the following dimensions:

(i) LACPC based BICPV system– 169 mm x 160 mm x 0.6 mm

(ii) SEH based WICPV system with Copper tubes (strips)– 270 mm x 12 mm x 6.5 mm and acrylic back plate housing –270 mm x 220 mm x 8 mm

(iii) Micro-finned thermal system for BICPV application– 30 mm x 29 mm x 2.0 mm

(iv) SEH based BICPV system– 170 mm x 165 mm x 1.0 mm

3.2.4 Encapsulant

According to Merriam-Webster's Learner's Dictionary, an encapsulant is "*a material used to completely cover (something) especially so that it will not touch anything else or a material used for enclosing something in or as if in a capsule*." A solar cell encapsulant is used to bond the cell to the top covering (usually a transparent glass) and the backing sheet. The purpose is to avoid mechanical damage, provide optical coupling, electrical and physical insulation and protection against weather etc. An encapsulant also provides the necessary adhesion between the solar cells, the top surface and the rear surface of the PV module. Any degradation of the encapsulant can cause optical decoupling due to discolouration leading to loss in power and adhesion, delamination and even corrosion in metallic parts due to acetic acid production [303] in the generally used EVA (Ethyl Vinyl Acetate). The main desirable characteristics for solar cell encapsulant are: high adhesion strength, low thermal resistance, good optical transparency (with glass-alike transmission properties), resistance to UV-induced yellow-browning and moisture-induced delamination, stability at higher temperatures and with ultraviolet (UV) light and low cost [304], [305], [306]. A recent interesting report by NREL [307] provided useful information about the types of available encapsulants (Poly-Dimethyl Siloxane or PDMS, EVA, Poly-Vinyl Butyral or PVB, and Thermoplastic Poly-Olefins or TPO and Thermoplastic Poly-Urethane or TPU) and details their thermophysical and chemical properties.

For the experiments within this thesis, encapsulant refers to *Dow Corning® Sylgard® 184* Silicone Elastomer (data in Table 9), with the chemical name *Polydimethylsiloxane* elastomer. PDMS was preferred over EVA due to its exceptional intrinsic stability against thermal and UV light induced stress [308]. Other salient features of Sylgard® are high transparency, good dielectric properties, room temperature and rapid cure processing and easy flow-ability. It's supplied as a two-part (colourless silicone base and silicone resin solution curing agent), clear liquid component, to be mixed in a 10:1 ratio. As per [309], *Sylgard®* cures without exotherm at a constant rate regardless of sectional thickness or degree of confinement, requires no post cure and can be placed in service immediately following the completion of the cure schedule.

Table 9. Characteristics of Sylgard® 184 Silicone Encapsulant [309].

Parameter	**Value**
Tensile Strength (psi)	980
Dynamic Viscosity (cps)	3500
Pot Life @ 23°C (Min)	90
Cure time at room temp (hour)	48
Specific gravity (g/cc)	1.03
Refractive Index (at 589 nm)	1.4118
(at 632.8 nm)	1.4225
Dielectric Strength (Volts/mil)	500
Dielectric Constant (at 100 Hz)	2.72
(at 1 kHz)	2.68
Vol. Resistivity (ohm-cm)	2.9×10^{14}
Dissipation Factor (100 Hz)	0.00257
(at 1 kHz)	0.00133
Temperature Range (°C)	-45 - 200
Thermal Conductivity (W/m K)	0.27
Working Time (Min)	> 90
Mix Ratio	10:1 Base to Catalyst
Resistance	Oxidation, Thermal,
Compatibility	Ceramics, Plastics,
Stability	Low to High

3.2.5 Masking tape

A masking film made of a polyimide (registered as flexible *Kapton® type HN polyimide film*, by DuPont™) was used to create an electrical insulation between the cells and the metallic back plate. The polyimide films exhibit good mechanical toughness, balance of electrical, chemical and physical properties over high temperature ranges. The layered structure of the material is given in Fig. 35. For the set-ups within this thesis, high bond,

anti-static Kapton HN insulating film, 304 mm x 200 mm x 0.025 mm and adhesive tapes of various widths were used, the properties for which are listed in Table 10.

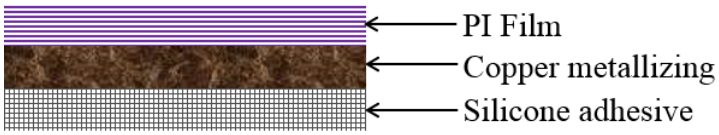

Figure 35: Structure of anti-static Polyimide film Silicone tape (not to scale).

Table 10. Properties of Polyimide insulating film.

Parameters	Values
Material	Kapton HN
Maximum Operating Temperature	+400 °C
Length	304 mm
Width	200 mm
Thickness	0.025 mm
Density	1.42 g/cm³
Thermal Conductivity	0.16 W/m.K
Thermal Coefficient of Linear Expansion	20 ppm/°C
Dielectric Strength	118 kV/mm
Peel Strength	630 g/in
Tensile Strength	> 3.5 kg/mm²

3.2.6 Thermocouples

K-type thermocouple (Ni-Cr (+) & Ni-Al (-)), made of one core *Polytetrafluoroethylene* (PTFE) sheath for optimum accuracy, with fine twin twist, were used for the temperature measurements. With tolerance class 1, temperature range of -75 to 250 °C, the thermocouples proved suitable for the experimental set-up also due to flexibility. The thermocouples were fabricated in the laboratory for cost economy. A ready-made 1 m long, 1.2 mm probe diameter, K-type thermocouple cable costs £10 while less than £2 excluding labour costs to fabricate in the laboratory thereby saving a massive 4/5th costs. They exhibit mechanical strength, resistant to oils, acids and adverse fluids and are colour coded to IEC-584-3. Table 11 lists the characteristics of the thermocouples.

Table 11. Characteristics of K-type thermocouple.

Parameter	Value
Minimum Operating Temperature	-75°C
Maximum Operating Temperature	+250°C
Core Strands	1/0.2 mm
Insulation Material	PTFE
Number of Strands	1
Size of Strands	0.2 mm

3.2.7 Miscellaneous materials

- *RS Quick Set* Epoxy Adhesive: is a rapid setting, pale yellow liquid adhesive with slight odour and cure time of 24 hours. It forms strong bonds within minutes of mixing with the resin hardener. The relative density of the adhesive is 1.17 at 20 °C, flash point, 150 °C and boiling point, 200 °C. It was used to glue the bottom Al plate with the Perspex walls of the PCM containment in the LACPC based module.
- *Geocel® Crystal Clear Seal & Fix*: an MS (*Silyl-Modified Polyether* based) polymer sealant and adhesive, was used to seal the top Al plate onto the PCM containment walls and to seal the holes within the PCM containment for the entry of the thermocouples. The sealant offers UV, weather-resistant and damp-tolerant properties and has clear colour. It doesn't shrink, is non-staining, solvent free and took about 20 minutes for setting in.
- *Loctite® hot melt glue gun:* a hot melt adhesive based on *Ethylene-Vinyl Acetate-copolymer*, and stable up to temperatures above 300 °C, proved better in sealing the ABS (*Acrylonitrile butadiene styrene*) plastic containment with the Al back-plate as it restrained leakage at high temperatures. It also formed the boundaries of the SEH based module. With a softening point 82 °C - 90 °C, mild distinctive odour and density 1g/cm^3 at 20 °C, the hot glue reached maximum bond strength in 2 minutes providing instant bonding.

3.3 BICPV system: Designs

The two key concentrators used within this thesis are: LACPC and SEH concentrators, the design of which are described here.

3.3.1 LACPC design

The design of the manufactured LACPC with a 2-D geometry (similar illumination profile along its length), is given in Fig. 36. The original concentrator design was first published by the authors of [46] in 2004, with the acceptance-half angles as 0° and 50°, offering up to 2.0 x concentration. This was further modified in the subsequent work by [15] in order to optimise the concentrator for building façade applications in the regions of northern latitude (>55° N). The modified design offered higher geometrical concentration of up to 2.82 x with 0° and 55° as acceptance-half angles.

3.3.2 SEH design

With an elliptical entry aperture, hyperbolic profile section and square exit aperture (hence the name *Square Elliptical Hyperboloid*), these are classified as non-imaging stationary 3-D solar concentrators and work on the principle of total internal reflection.

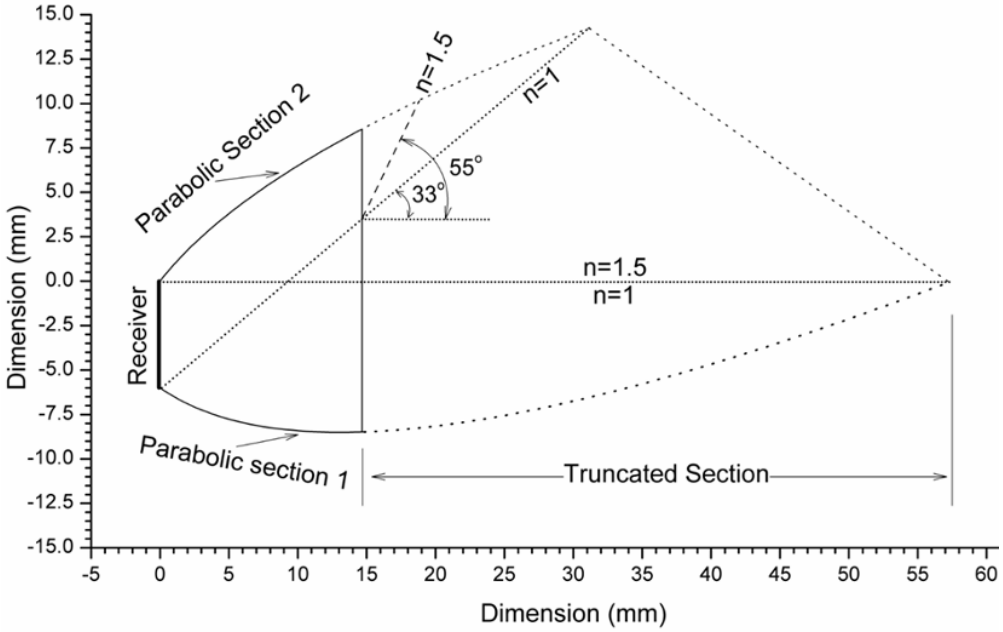

Figure 36: LACPC concentrator: geometrical design [46].

The selected SEH concentrator (Fig. 37 (a, b)), referred to as H3 in the original design [43, 47, 74] with 3 cm height (H), side of the exit square aperture (A) as 1 cm, major axis (b) as 3.2 cm and minor axis (a) as 2.4 cm, offered 3.29 optical concentration (maximum), $C_{opt\ max}$, and geometrical concentration ratio, $C_{g,}$ of 6 (Fig. 37 (c)). The Height Aspect Ratio (HAR), H/A for this concentrator was 3. Another important parameter, EAR or elliptical aperture ratio, is defined in Eqn. 12:

$$EAR = \frac{major\ axis}{minor\ axis} = \frac{b}{a} = 1.34 \quad \textbf{(12)}$$

The rationale behind selecting this particular height of the concentrator was that although H3 has the lowest acceptance angle of 40º (-20º, +20º), it has the highest optical efficiency of 68%. SEH concentrator design and fabrication process has been replicated from as given in [47, 74].

(a) (b) (c)

Figure 37: (a) SEH concentrator top view, (b) side profile and (c) design (in mm).

3.4 BICPV Systems: Fabrication Method

This section describes the basic processes involved in fabricating the different BICPV.

3.4.1 Metal cutting for the Back-plate

The metal back-plate, used as the skeleton solar cells base, was cut from a commercial plain Aluminium sheet roll (99 % pure) provided with a protective cover on both sides to avoid oxidation. The metal guillotine machine was used for cutting the sheets, which strongly held the sheet with the table preventing any lifting during shearing operation.

3.4.2 Wrapping the Masking tape

After the sheet was cut, polyimide based *Kapton*® tape was manually wrapped around the cut-to-size Al sheet for mounting the CPV assembly on top side. This was adopted to ensure appropriate electrical insulation between the solar cells and the conducting Al back-plate. The plate was set-aside after this.

3.4.3 Soldering the Solar cells

The solar cells were soldered in a series connection (with the front side of one cell connected to the back side to the subsequent cell and vice-versa) to ensure that the current through the connected strings of the solar cells remains the same. The total voltage, however, is the sum of the two voltages for a given current. In addition, series connection uses a single cable and handles larger voltages, hence preferred for connecting multiple solar cells in nearly all PV modules. The soldering process is briefly described here.

1. Using a soldering machine (power unit and soldering pencil) as discussed in previous section, five solar cells were connected in series for the LACPC (Fig. 38

(a)), eight cells for the SEH with Copper (Cu) tubes (six strings of which were soldered in parallel making 48 cells altogether as shown in Fig. 38 (b)) and six cells for the SEH based BICPV (four strings of which were connected in parallel configuration as shown in Fig. 38 (c)) module respectively. Lead-free, thin tin-plated Cu ribbons (0.1 mm thick, 1 mm wide) were used for the internal connections, while 3 mm wide ribbons for connections with the external measurement instruments.

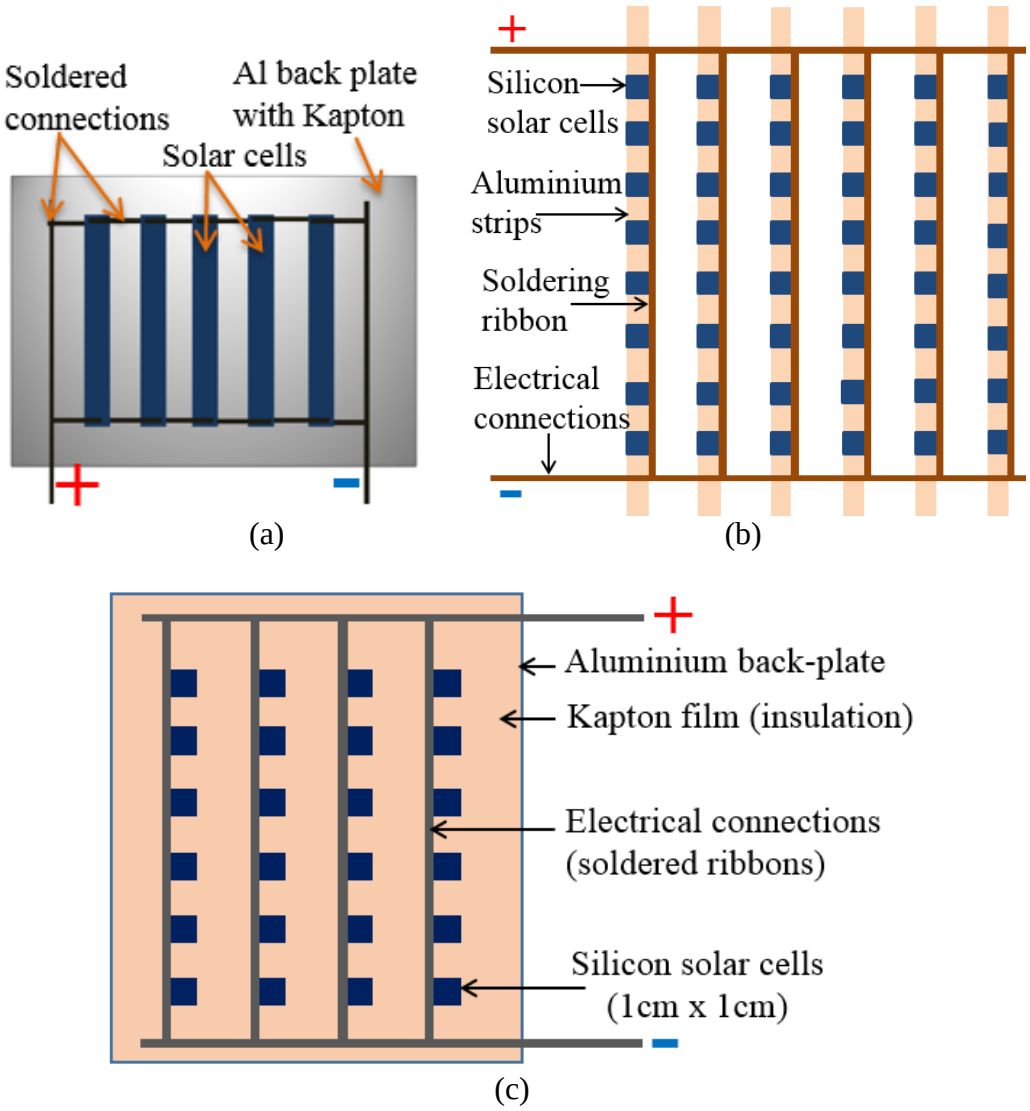

Figure 38: (a) Solar cells connections for (a) BICPV with LACPC, (b) WICPV with SEH and (c) BICPV with SEH concentrators.

2. The skeleton of these connected cells were wiped with a very light, even coating of *Dow Corning® 92-023 Primer* [310] to strengthen the bonding between cells and concentrator and to improve the inhibition resistance of cured silicones.

3.4.4 Casting the concentrators

The various BICPV modules were based on LACPC and SEH concentrating elements, providing low concentrations in two dimensions and three dimensions (2-D, 3-D) respectively. It is to be noted that both these concentrators were designed within the research group. An array of concentrating elements was fabricated via casting process using *Smooth-On Crystal Clear 200® in* the stainless steel casting moulds (Fig. 39 (a) for LACPC and Fig. 39 (b) for SEH).

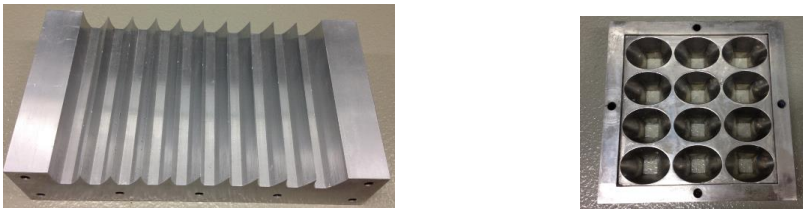

(a) (b)

Figure 39: Stainless steel casting moulds for (a) LACPC and (b) SEH concentrators.

The dielectric clear polyurethane material resin available as a 2-part mixture, was mixed to make the concentrators and the details on casting process based on in [74, 311] is synopsised here:

1. The stainless steel casting moulds were cleaned, dried and sprayed with a thin even coating of *Universal® mold release agent* to easily release the solidified dielectric concentrators from the metal moulds.
2. *Crystal Clear®200* casting resin (A: B mix ratio 10: 9) was manually weighed and mixed in glass beaker and stirred thoroughly to ensure proper mixing.
3. The mixture was degassed in the Vacuum oven at room temperature for 20 minutes for a few times.
4. The mixture was gently poured into the moulds to avoid trapped air bubbles.
5. The mould was left to cure for 24 hours at room temperature, after which the casted concentrating elements were removed using gentle tapping.

Using a single casting mould, 10 rows of individual linear concentrating elements and 3x4 arrays of 12 individual SEH elements were produced. Depending on the experiments, they were adjoined or cut to size using a band-saw for the module.

3.4.5 Encapsulating the solar cells

The solar cells were fixed on the back-plate, using silicone based Sylgard®, which also glued the concentrators on top of the cell assembly. The typical process consisted of:

1. Mixing: the two parts of Sylgard were poured in a clean glass beaker in the prescribed ratio (10:1), manually weighed on a micro-scale and then poured slowly in another beaker, thoroughly mixing using a clean glass rod.
2. De-Airing: the mixture in a vacuum oven to remove the trapped air bubbles for approximately 20 minutes.
3. Pouring: the de-aired liquid was gently poured over the back-plate wrapped in Kapton and with the soldered solar cells temporarily glued on it.
4. After leaving the encapsulant to cure for about 5 mins, the concentrators were fixed and pressed lightly with a uniform moderate weight for bonding the surfaces and providing optical coupling.
5. Sylgard® cures to a flexible elastomer requiring no post cure and can be placed in service immediately following 48 hours at room temperature.

3.4.6 Welding the thermocouples

The thermocouples were manually tip welded using a thermocouple welder at the medium level arc and medium level power (Fig. 40). No purge/argon gas was used. The thermocouple tips were attached at BICPV locations using a small piece of strongly adhesive aluminium tape and the twisted wires were reinforced using glue-gun.

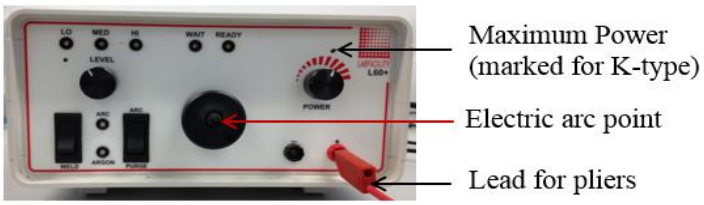

Figure 40: Thermocouple Welder with maximum power settings for thermocouple welding.

3.4.7 Module assembling process

As a general standardised method for assembling the module, the concentrators were attached on top of the series connected silicon cells skeleton using optically clear *Sylgard®*, poured over in a uniform layer, left for 24 hours to cure at room temperature. This ensured an appropriate optical coupling between the concentrators and the soldered cells assembly, as an adhesive as well as a protective coating from mechanical damages. Another thin layer over cured silicone ensured prevention against delamination at higher temperatures. The assembled LACPC module, with 11.9 cm x 8.4 cm concentrator top dimensions is given in Fig. 41 (a). The WICPV module, made of the dielectric material

based SEH concentrator (detailed in [47]), had the profile designed using a continuous union between an elliptic entry aperture and square exit aperture where the solar cells were placed. Each SEH concentrator assembly measured 10.2 cm x 10.1 cm considering shrinkage and manufacturing allowance, which was assembled on Al metal strips (1.2 cm wide). Four concentrator assemblies with 12 SEH elements were required to cover the 48 solar cells used within the designed system. (Fig. 41 (b)). For the SEH based BICPV module (Fig. 41 (c)), one casted 4 x 3 concentrator assembly, along with strips of 4 x 1, 2 x 3 and 2 x 1 SEH concentrators (cut from the other casted 4 x 3 concentrator assemblies using a band saw) were attached on the 24 solar cells (six series connected cells and four such strings connected in parallel) using *Sylgard*®.

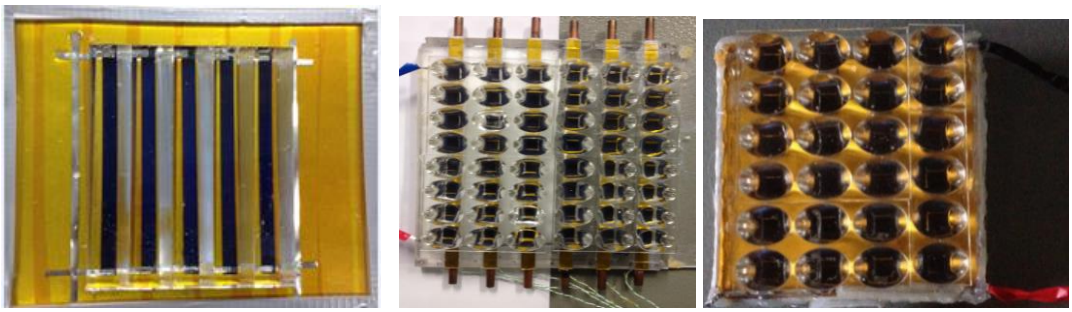

(a) (b) (c)

Figure 41: The assembled modules: (a) BICPV based on LACPC, (b) WICPV based on SEH concentrators, showing the semi-transparency effect and (c) BICPV based on SEH.

For the micro-finned thermal module, a 30 mm x 29 mm x 2 mm Al plate was used as the heat sink and mounting *Omegalux® Kapton flexible heater* (Fig. 42 (a)). Micro-fins were manufactured using micro-milling facilities at the University of Strathclyde (UK) (Fig. 42 (b)). Al metal was selected to emulate the experiment performed in [311], however, the plate thickness of almost 1.5 times higher than in [311] was selected due to practical challenges on down-scaling. The aspect ratio of 1.1 contributed to the robustness and durability of the component against bending. The shape and dimensions of micro-fins can be found in Fig. 43.

(a) (b)

Figure 42: (a) Heating element on top of unfinned Al plate and (b) micro-finned plate.

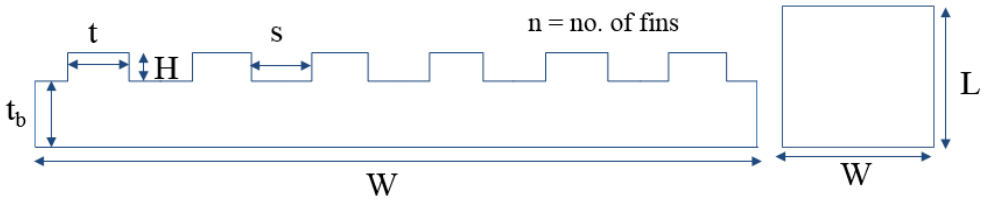

Abbreviation (units)	t (mm)	t_b (mm)	s (mm)	H (mm)	W(mm)	L (mm)	N
Nomenclature	Micro-fin thickness	Plate thickness	Spacing between micro-fins	Micro-fin height	Plate width	Plate length	No. of fins
Magnitude	1	2	0.5	0.5	30	29	20

Figure 43: Enlarged view of the micro-fins and the table with nomenclature used and the actual dimensions: Micro-fins form the secondary passive cooling mechanism.

3.5 PCM Systems: Materials

This section details the various PCM used as well as the PCM containment designs and their fabrication processes. Costs have been given for reference purpose.

3.5.1 PCM Materials

The PCM were outsourced from *Rubitherm® Gmbh*, Berlin, Germany. Mostly, the focus has been on organic paraffin wax based PCM due to the reasons discussed in the previous chapter. Table 12 enlists the supplier's thermophysical properties of the PCM. Due to much higher temperature than ambient within laboratory, working with lower melting PCM (with phase change temperature < 30°C) did not prove practical.

3.5.1.1 RT28HC

Rubitherm® RT28 HC (melting range: 27-29 °C), was used in SEH system with Cu tubes as lower melting PCM. This is a solid-liquid type organic PCM with higher heat capacity, and supplied as a white, odourless solid with costs at (US $ 11.5/kg).

Table 12. Characteristics of the various PCM used within this thesis.

PCM	Melt peak (°C)	Congeal peak (°C)	Flash point (°C)	Max. Operating temp. (°C)	Latent Heat capacity ± 7.5% (kJ/kg)	Latent + sensible heat (kJ/kg)	Density (at 15°C) (kg/l)	Density (at > 40°C) (kg/l)	Vol. expansion (%)
RT28 HC	28	27	165	50	245	241.2	0.88	0.77	12.50
RT42	41	42	186	72	174	172.8	0.88	0.76	12.50

GR42	41	42	190	70	55	57.6	0.80*		NA
RT50	49	50	200	70	168	169.2	0.88	0.76	13.63
RT55	55	55	200	90	172	172.8	0.88	0.77	14.00

* Bulk density (g/cm^3)

k for all RT PCM is 0.2 W/m.K and for GR PCM is 0.1 W/m.K

3.5.1.2 RT50

Rubitherm® RT50, (melting range: 45-51 °C) was selected to test the effect of melting range of a PCM on its thermal regulation capability. A solid to liquid type PCM, it was used with the SEH system with Cu tubes as a higher melting PCM. RT50 is a white transparent paraffin supplied as small tear-drop pellets form at a cost of (US $ 6.5/kg).

3.5.1.3 RT42

Rubitherm® RT42, (melting range: 38–43°C) was used with BICPV and micro-finned systems. It is an organic, paraffin wax material. RT42 was used with also further treated with nanomaterials to investigate the effect on thermal conductivity for another study. A translucent material supplied as blocks, it has a high latent heat of fusion, low super-cooling, chemical non-reactiveness, and low vapour pressure, self-nucleating properties, non-toxicity, environmentally friendly attributes and relatively cheaper costs (US $ 6.5/kg). It should be noted that the PCM was recycled for a few studies, which theoretically doesn't change any properties until it exceeds to thousands of cycles.

3.5.1.4 GR42

Rubitherm® GR 42, a solid-solid PCM (melting range: 38-43°C), is a granulate which contains PCM within a secondary supporting structure, such as a natural porous mineral particle. Its cost was comparable to other PCM used within this research (US $ 6.8/kg). Since it doesn't undergo any change in its form, it was used in the micro-finned thermal system study to take advantage of its shape-stabilised property.

3.5.1.5 RT55

Rubitherm® RT55, (melting range: 51-57 °C) was selected to test the effect of melting range of PCM in the LACPC first with respect to another lower melting PCM system and then against an insulated back. A solid to liquid type PCM, RT55 is a white transparent paraffin supplied as a block at a cost of (US $ 6.5/kg).

3.5.2 Thermal conductivity enhancers

The thermal conductivity of organic PCM was enhanced using Copper mesh in stage 1 and with a copper nanomaterial in the stage 2 for the initial instances of investigations.

3.5.2.1 Copper mesh

The woven Cu (purity of 99.98 %) wire mesh, 125 mm wide, 0.25 mm thick and weighing 58 gm/m, designed like a tube sock and supplied by *The Crazywire Company*, Cheshire, UK was used as the TCE in the first instance. Many authors [312] have found that metallic meshes reduce the complete melting time of PCM and that melting initiates from the corner region of meshes. The woven Cu wire mesh designed like a tube sock (Fig. 44 (a)) was cut using scissors and washed before first use to remove contaminants accumulated during production process. This was then filled in the PCM containment in layers so as to fill the entire volume of the containment as shown in Fig. 44 (b). Approximately 170 gm of mesh was used for the set up. They were layered in a parallel arrangement as studies have found [313] layering without interlayer gap resulted in 80% melting reduction time. The mesh was filled with the poured over liquid PCM, which solidified within the containment, causing the mesh to stay fixed within.

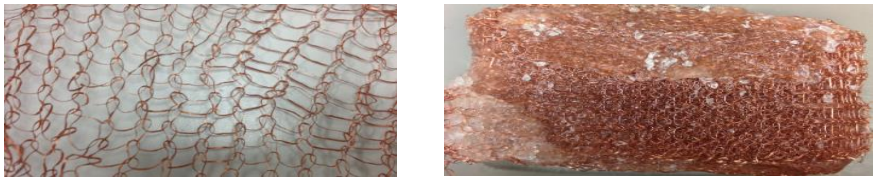

(a) (b)

Figure 44: Copper mesh (a) single layer and (b) multi-layered with PCM incorporated.

3.5.2.2 Nano-CuO

Copper (Cupric) Oxide Nanoparticle or Nano CuO with an average particle size of 60 nm was selected as the stage 2 TCE for organic PCM, (properties in Table 13). It was sourced from *EPRUI Nanoparticles & Microspheres Co. Ltd*, China.

Table 13. Manufacturer-supplied physical and chemical properties for Nano-CuO.

Parameter	**Value**
Average Particle Size (nm)	60
Purity (ICP Test) (%)	> 99.8
Specific Surface Area (m^2/g)	13.08
Colour	Black
Morphology	Nearly spherical
Bulk Density (g/cm^3)*	0.3-0.45

True Density (g/cm³)	6.31
Components (contents; μg/g)	Ba (0.79), Cd (2.37), Co (6.32), Fe (86.9), Mg (71.1), Mn (3.16), Sr (2.37)
Components (contents) (%)	Ca (0.04), K (0.03), P (0.03), Pb (0.01), Zn (0.02)
Components (others)	Al, Cr, Li, Mo ,Ni, Ti not tested

* True density-of particles that make up the material; bulk density- average material density of a large volume.

The additive nanomaterial, nano-CuO for the base PCM was outsources and used as it is without much further treatment. The rationale for selecting CuO are given below:

- Appreciable thermal conductivity (33 W/m·K) compared to Silica (0.02 W/m·K) and TiO_2 nanoparticles (0.7 W/m·K) which have comparable costs.
- Low cost (US $59/100g) as compared to Cu nanoparticles (US $399/100g), 60 nm silicon nanoparticles (US $399/100g), 30 nm silver nanoparticles (US $450/100g).
- Safe for use, non-toxic [280], whereas Alumina (Al_2O_3) nanoparticles are proven to exhibit environmental toxicity effect [75] and Ease of availability.
- Non-oxidising and non-reactive with paraffin wax based materials.

3.5.2.3 n-PCM Ultra sonication

Hilsonic ultrasonic cleaner with the attached ultrasonic bath was used for mixing and dispersing the nano-CuO particles within the paraffin wax based PCM. The principle is using the ultrasonic energy for agitating the particles. The n-PCM was synthesised by mixing nano-CuO 0.5 % (by mass) with the required mass of PCM RT42 at a thermal bath temperature of 60° C to ensure the PCM was in a fully melted state. The mixture was then ultra-sonicated using Hilsonic® ultra-sonicator for 24 hours at 70 °C. Finer size of nano-material ensured higher mixing rate, proper dispersion within the PCM, ease of ultra-sonication and less settling of the particles under gravity in the molten state. The PCM and the resulting n-PCM are shown in Fig. 45.

Figure 45: Samples of PCM RT42 and nano-PCM (0.5%).

3.6 PCM Systems: Design

The containment for storing PCM also act as a heat sink for the BICPV system. It is to be noted, that the term PCM containment also incorporates n-PCM containments.

3.6.1 LACPC based BICPV

The inner and outer dimensions of the PCM containment used for the BICPV system with LACPC type concentrator are shown in Fig. 46. This design was based on heat transfer equations taken from literature based study [136, 137] and needed further mathematical treatment, which is explained here. This design was based on modified heat transfer equations as expressed in Eqn. 13 and Eqn. 14 given below.

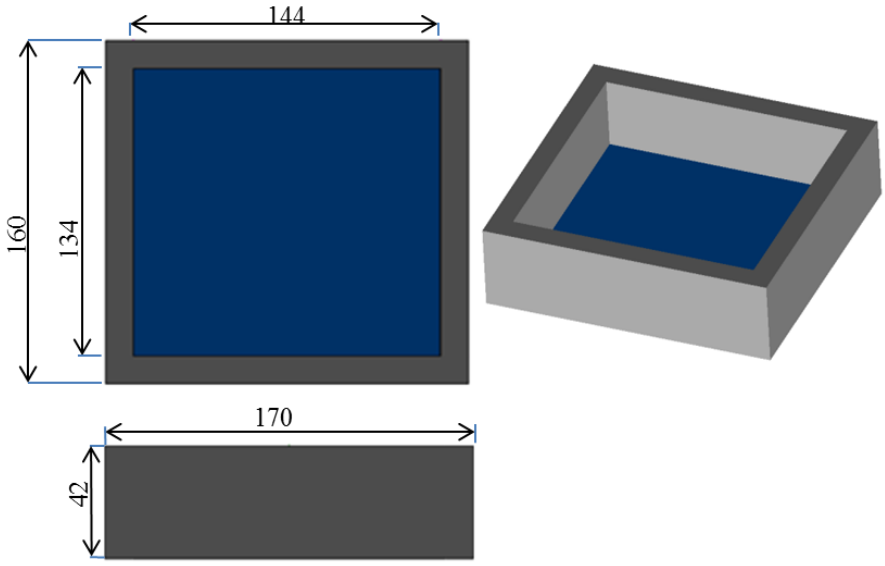

Figure 46: Design of the PCM containment for LACPC based BICPV (dim. in mm).

As per the available literature [136], the energy balance for a BIPV-PCM system is defined as follows:

(a) For $T_{PV,\,t} < T_m$, the relation is given by:

$$AI_r\Delta t = A(h_1+h_2)\left(T_{PV,t}-T_{amb}\right)\Delta t + \left(T_{PV,t+\Delta t}-T_{PV,t}\right)\rho C_P \Delta x A \qquad \textbf{(13)}$$

(b) The energy balance for the phase transition is:

$$AI_r \sum \Delta t = A(h_1+h_2)(T_m-T_{amb})\Delta t + H_L \Delta x A \qquad \textbf{(14)}$$

Where A-front surface area of the BIPV-PCM system (m^2), I_r-irradiance on photovoltaic (Wm^{-2}), Δt-time step (s), h_1, h_2-heat transfer coefficient at front, rear surfaces ($Wm^{-2}K^{-1}$), T_{amb}-ambient temperature (°C), T_m-PCM melting peak temperature (°C), $T_{PV,t}$- temperature

on PV at time t (°C), $T_{PV,\,t+\Delta t}$ - temperature on PV at time t + Δt (°C), ρ - density of PCM (kgm^{-3}), C_P - specific heat of PCM ($Jkg^{-1}K^{-1}$), Δx - depth of the PV/PCM system (m) and H_L - latent heat of PCM (Jkg^{-1}). The assumptions were that:

a. Initial thermal equilibrium between the PV and PCM
b. Constant values of h_1 and h_2
c. Top and bottom adiabatic boundaries of the system.

These equations seem mathematically inconsistent for the reasons stated below.

a. Eqn. 14 is dimensionally incorrect in its last term, which could be balanced by taking PCM density into consideration and the variable, area (A) could be eliminated, essentially meaning the equation could take the form of Eqn. 15 and Eqn. 16.

$$I_r\Delta t = (h_1+h_2)\left(T_{PV,t}-T_{amb}\right)\Delta t + \left(T_{PV,t+\Delta t}-T_{PV,t}\right)\rho C_P\Delta x \quad \textbf{(15)}$$

$$I_r \sum \Delta t = (h_1+h_2)(T_m-T_{amb})\Delta t + \rho H_L\Delta x \quad \textbf{(16)}$$

b. This energy transfer doesn't consider the electrical conversion efficiency of the solar cell (typically 16-20%), implying conversion of 100 % of the available solar irradiance into heat and no useful electrical conversion taking place within the BIPV system.An alternate energy balance equation for the BICPV system, considering it as a transient heat transfer case in a 1D domain, making an allowance for the geometrical concentration of the concentrator, could be written as Eqn. 17 and Eqn. 18. The term $(1–\eta_{elec})$ signifies that part of irradiance which is not converted to electricity, (typically 80% of the available irradiance). These are based on the assumptions as stated above (a, b and c) and also that

d. The PCM is immiscible, non-reactive and homogeneous.
e. The heat transfer occurs primarily by natural convection and heat conduction.
f. Radiation losses and thermal resistance between the PCM and walls are neglected.

Therefore, the modified equations are proposed as follows:

$$I_r(1-\eta_{elec})C_g\,\Delta t = (h_1+h_2)(T_{PV,t}-T_{amb})\Delta t + (T_{PV,t+\Delta t}-T_{PV,t})\rho C_P\Delta x \quad \textbf{(17)}$$

$$I_r\,(1-\eta_{elec})C_g \sum \Delta t = (h_1+h_2)\,(T_m-T_{amb})\Delta t + \rho H_L\Delta x \quad \textbf{(18)}$$

These heat transfer equations for BICPV–PCM systems are based on a 3D control volume based on heat flow perpendicular to irradiance assuming no heat transfer takes place in the walls due to low thermal conductivity (0.1875 $Wm^{-1}K^{-1}$) of Perspex.

For the initial experiments on the LACPC based BICPV modules, the PCM containment was assembled using 13 mm thick Perspex sheet (*cast Poly-methyl methacrylate*), which was cut to size using a band saw (described in 3.4.11) and finished using a grinding machine, to form the walls of the containment. The holes were drilled in the walls using an internal thread cutting tool for screwing the sides of the walls together using eight 6 mm screws. Al plate was glued to the bottom of the four walls and then sealed using *RS Quick Set Epoxy Adhesive*. *Geocel® Crystal Clear Seal & Fix* sealant was used to seal the top plate (with the BICPV module) onto the wall thickness. The back-plate of the BICPV module formed the top covering for PCM containment while the bottom one supported the containment base. Further, the screwed walls were also sealed using a sealant to ensure leak-proof bonding between the edges of the wall [311]. Once the sides and base was glued, it was set to cure at room temperature for 24 hours.

3.6.2 SEH based WICPV (with Copper tubes)

The PCM containments for individual Al strips were fabricated using six Cu tubes of length 32 cm, with 7 mm internal diameter and 8 mm outer diameter (Fig. 47). They were fitted at the bottom side of the Al strip (back-plate) which had solar cells and concentrator assembly on the top side. Cu was selected for making the tube containment due to its high thermal conductivity (between 301 $Wm^{-1}K^{-1}$-383 $Wm^{-1}K^{-1}$) [314] so they also serve as the thermal conductivity enhancer. The tubes were sealed on both the sides using detachable soft plastic stoppers, each 2.5 cm long, leaving at least 2 cm gap on each side to account for the volumetric expansion of the PCM in the molten state.

Figure 47*:* Cu tubes with filled PCM (a penny coin for size comparison).

3.6.3 Micro-finned thermal system

For the micro-finned thermal system, micro-fins acted as the secondary passive cooling mode, in addition to PCM cooling. The PCM containment for the micro-finned system was 3-D printed, using ABS plastic with the three-step process for model creation and printing [315] as described below:

1. **File preparation:** create the 3D model in CAD software (*Solidworks*), click "*print*." STL output is converted into 3D model print paths using Catalyst EX™ software including support structures that guide the uPrint SE 3D Printer extrusion head.
2. **Model printing:** using FDM Technology™, the 3D model is built with the support material layer by layer, from the bottom up on a removable modelling base.
3. **Support removal:** printed model is pulled, popping off the modelling base and dissolving the soluble support material using the *WaveWash Support Cleaning System.*

Once the 3D printed part was taken out, a 1.5 mm hole was drilled using drilling machine was allowing thermocouple entry within the containment. The design of the containment and the fabricated part are shown in Fig. 48 (a, b) respectively.

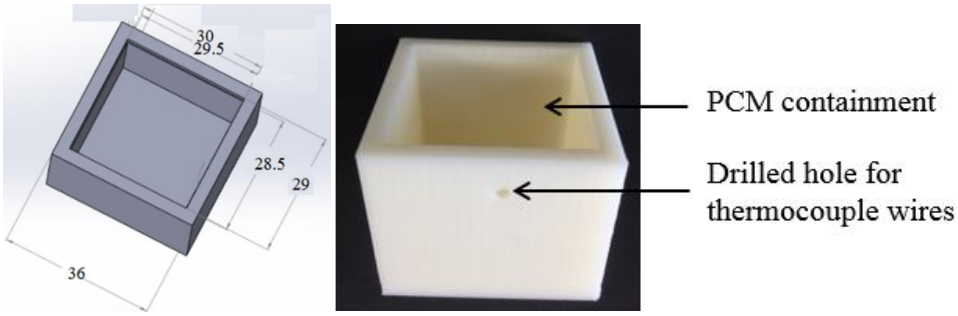

(a) (b)

Figure 48: The 3-D printed PCM containment (a) design and (b) fabricated part, for the micro-finned thermal system. Dimensions in mm.

3.6.4 SEH based BICPV

The PCM containment for SEH based BICPV was manufactured using the 3D printing process. The printed component was loaded into basket for a pre-set time and temperature (Fig. 49), and by gentle agitation of 3D printed part in the heated cleaning solution, support material was effortlessly dissolved away. *uPrint SE 3D* Printer powered by *Stratasys'* patented *FDM® (Fused Deposition Modelling™)* technology were used. The PCM containment is shown in Fig. 50 (a) and the design is given in Fig. 50 (b). One 3 mm hole was drilled on one side of the containment using the drilling machine, for accommodating thermocouples. All thermocouples were inserted through this hole, which was sealed using the glue gun for a leakage-proof assembly.

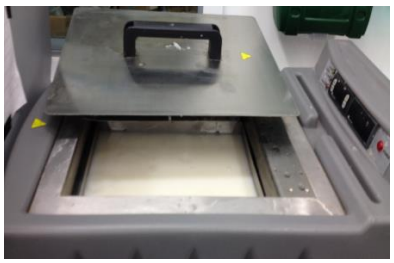

Figure 49*:* Support cleaning apparatus with the 3-D printed component inside the bath with the cleaning program running.

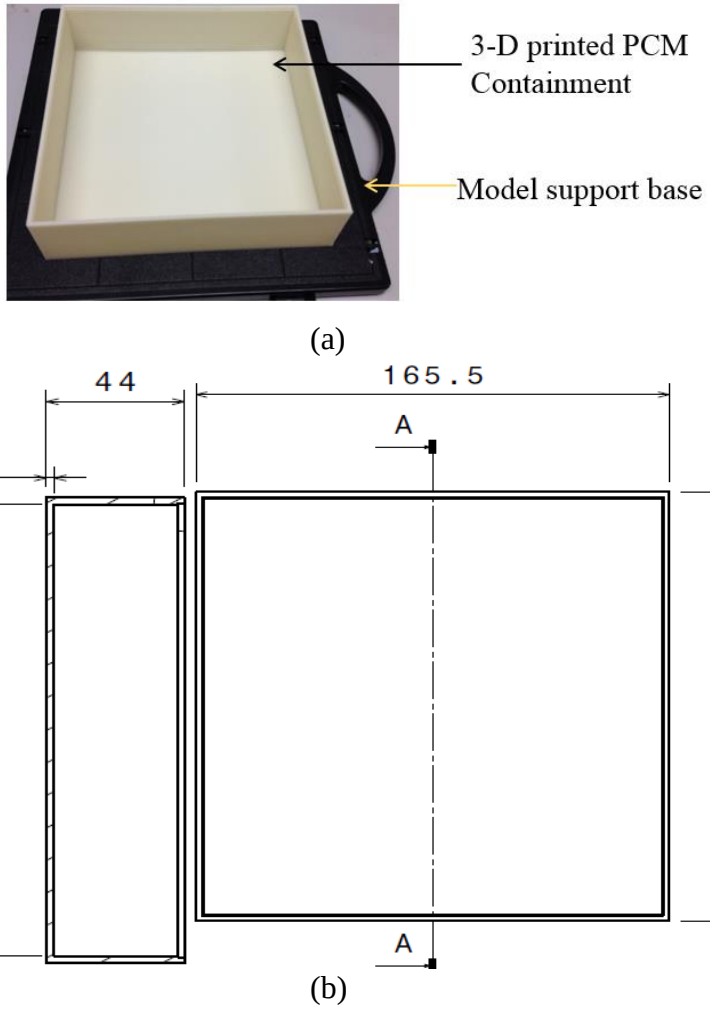

Figure 50: (a) 3-D printed PCM containment for the SEH based BICPV and (b) its design with dimensions in mm.

3.7 BICPV-PCM system assembly

The following sub-sections describe the assembly of the BICPV part (heat generating element) of the various systems with the PCM part (the heat absorbing elements) for the different module types, and details the applicable design data for these systems.

3.7.1 BICPV (LACPC)-PCM

The aim of designing and fabricating this module was to examine PCM effectiveness and the effect of varying irradiance on the BICPV electrical performance. The back-plate of BICPV was attached as the top covering for the PCM containment using acrylic glue. Thermocouples were attached at the rear side of the top Al plate, entering through the holes drilled in the containment walls, sufficient to accommodate the multiple wire thicknesses. The BICPV and BICPV-PCM system so assembled are shown in Fig. 51 (a, b) respectively while the properties of the individual key components are enlisted in Table 14. The design data for the mathematical analysis is given in Table 15.

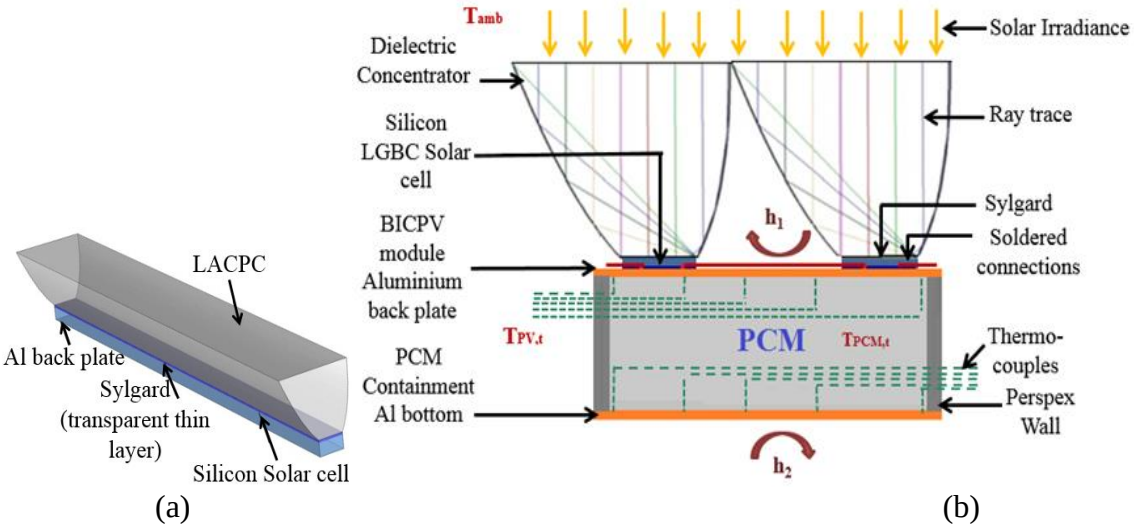

Figure 51: Schematics of the (a) LACPC based BICPV (b) cross-sectional view of the BICPV-PCM system.

Table 14. Thermo-physical properties of the BICPV component materials.

Component	Solar cell	Concentrator	Back-plate	Insulation	Encapsulant
Material	Silicon	Crystal Clear®	Aluminium	Kapton® tape	Sylgard® 184 Silicone
Width (mm)	6	136	169	25	169
Length (mm)	115	120	160	3300	160
Thickness (mm)	0.3	170	0.6	0.065	0.5
Density (kg/m^3)	2329	1036	2700	-	1030
Thermal conductivity (W/m/K)	149	-	205	-	0.27
Molar heat capacity (J/mol/K)	19.79	-	-	-	1030
Latent heat capacity (kJ/kg)	-	-	-	-	-

Melting temperature (°C)	-	-	660	-	-
Max. operation temperature (°C)	-	-	-	180	-
Volume expansion (%)	-	-	-	-	-
Volume resistivity (Ωm)	-	-	-	$1x10^{14}$	-
Dielectric breakdown voltage (V)	-	-	-	7500	-
Temperature range (°C)		-	-	-	- 45 to 200

Table 15. Design Data for the LACPC based BICPV.

Parameter	Definition	Value
θ	Inclination with the horizontal (°)	0
$L_{panel(o)}$	Outer length of the panel (cm)	17
$L_{panel(i)}$	Inner length of the panel (cm)	14.4
$W_{panel(o)}$	Outer width of the panel (cm)	16
$W_{panel(i)}$	Inner width of the panel (cm)	13.4
ΔX_{PCM}	PCM containment thickness (cm)	4.2
ΔX_{Al}	Aluminium plate thickness (mm)	0.6
L_{cell}	Solar cell length (mm)	116
W_{cell}	Solar cell width (mm)	6
A_{panel}	Area of PV/PCM system front surface (m^2)	0.0272
A_{cell}	Solar cell area (m^2)	0.0007
N	No. of solar cells in the system	5
$A_{cell\ total}$	Total area occupied by solar cells (m^2)	0.0035
I_T	Available irradiance (Wm^{-2})	1000
I_{PV}	Irradiance on PV panel (Wm^{-2})	1820
I_{Heat}	Irradiance after electrical conversion (Wm^{-2})	291.20
η_{Geo}	Concentration ratio (geometrical)	2.80
η_{Opt}	Optical efficiency of concentrator	0.65
η_{Cell}	PV electrical conversion efficiency	0.16
h_{rear}	Heat transfer coefficient rear surface ($W\ m^{-2}K^{-1}$)	5.00
h_{front}	Heat transfer coefficient front surface ($W\ m^{-2}K^{-1}$)	10.00
T_m	PCM melt temperature (°C)	41
T_{amb}	Ambient temperature (°C)	20.00
ρ	Density of RT42 ($kg\ m^{-3}$) at 15°C	880
C_P	Specific heat of RT42 ($J\ kg^{-1}K^{-1}$) solid	2000
H	Latent heat of RT42 ($J\ kg^{-1}K^{-1}$)	174000
k	Thermal conductivity of RT42 ($Wm^{-1}K^{-1}$)	0.20
α	Volumetric expansion (%)	12.50

3.7.2 BICPV (SEH)-n-PCM

The objective of fabricating this module was to examine the n-PCM effectiveness for BICPV performance. The system was assembled using the same process), but using SEH

instead of LACPC, 3-D printed containment sealed using *Loctite® hot melt glue gun* which provided better sealing properties quickly. The system is shown in Fig. 52.

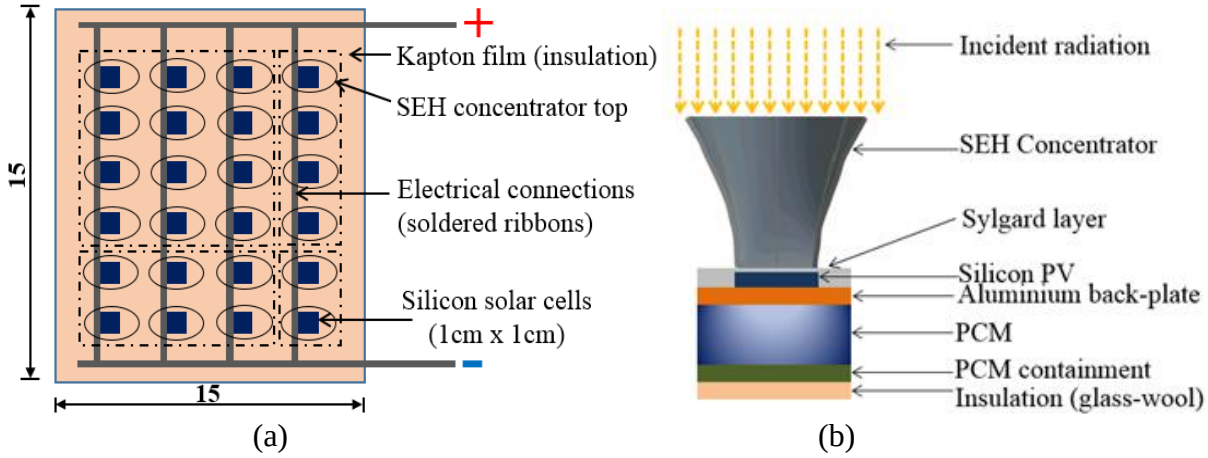

Figure 52: Schematics of the BICPV module based on SEH: (a) top view with dotted lines showing concentrator assemblies and (b) cross-sectional view (Dim. in cm).

3.7.3 WICPV (SEH)-PCM with Copper tubes

The WICPV-PCM module was designed to study the comparative effectiveness of latent (PCM) versus sensible (water) cooling towards improving electrical efficiency. The cooling media was contained within highly conductive metallic copper tubes, fitted at the rear side of the WICPV under Al back-plate with recesses, to ensure that the low k of PCM was overcome by the higher k of Al and Cu, for higher heat transfer. To ensure semi-transparency effect in the module compared to the original design, narrow strips of opaque metallic back-plates were used to mount the skeleton of the soldered solar cell assembly. The remaining structure was made of acrylic based clear plastic frame, so as to ensure provision of daylight penetration within the building. The top view (Fig. 53 (a)) and the cross-sectional view in (Fig. 53 (b)) can be used to visualise the overall module design. To measure the temperature under the back-plate, six K-type exposed welded tip thermocouples were placed between the Al strips and the Cu tubes using highly conducting thermal paste (thermal conductivity 3.4 $Wm^{-1}K^{-1}$). These tubes, primarily used as PCM containment, also acted as thermal conductivity enhancers and were insulated using a 3 mm thick glass wool strips between the recesses in the transparent acrylic frame that formed the foundation of the system. This transparency of the frame permits the use of the set-up as a building window or fenestration. Further, for water circulation within this system, a water circulation circuit was designed, using the same plastic pipes, which is described in the next chapter.

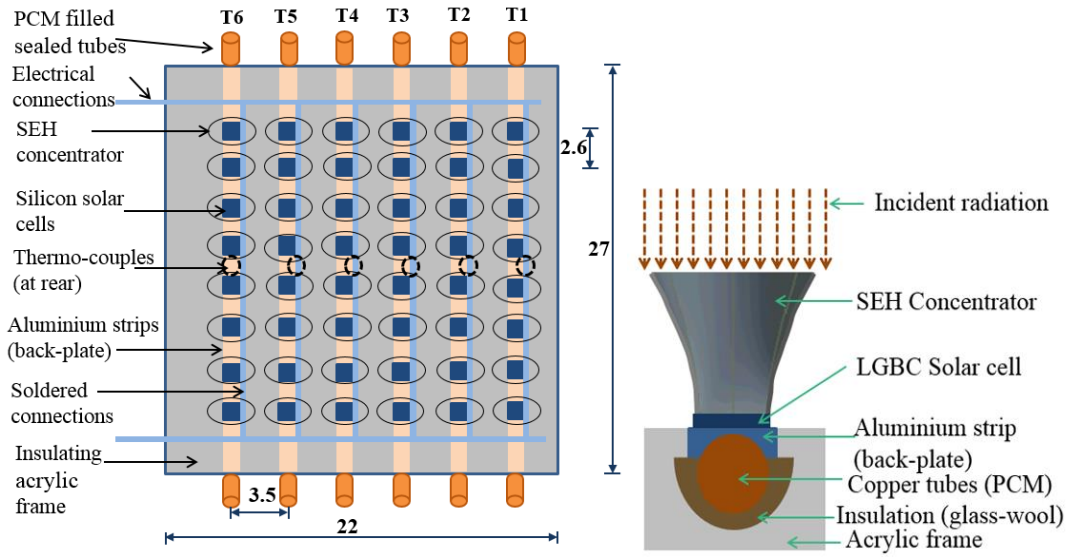

Figure 53: Schematics of WICPV with SEH concentrator: (a) top-view showing semi-transparency effect of acrylic frame (in grey) and (b) cross-sectional view (dim. in cm).

3.7.4 Micro-finned thermal system

For the micro-finned module, rectangular Al plates (either with or without the machined micro-fins) were snug fit on 3-D printed PCM containment which was insulated with a polystyrene layer (k = 0.03 W/m·K) on all sides. The system was sealed using silicone sealant to ensure added protection from PCM leakage upon phase change to liquid state. To ensure the fin contact with the PCM, it was tested after filling the containment for the first time with liquid PCM and upon solidification it was tested again. The heating elements were glued on the top flat surfaces of the plate, acting as a resistive heat source. The complete fabricated experimental set-up has been shown in Fig. 54 (a, b).

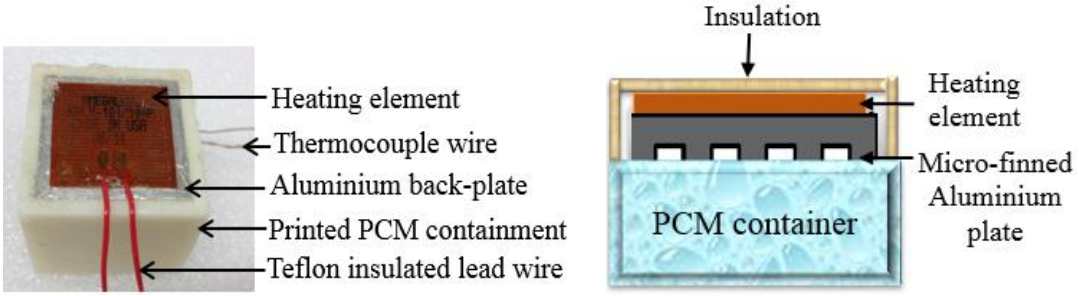

Figure 54: PCM system with micro-finned thermal systems (a) top-view and (b) cross-sectional view of the set-up with insulation layer.

The whole experimental set-up was enclosed within 200 mm × 200 mm × 200 mm insulated walls, covered on top, with only the front open, to shelter it from mechanical damages and temperature variations. The design data and the experimental parameters for the components used for the software based simulation are listed in Table 16.

Table 16. Design data for the micro-finned-PCM system.

Parameter	Definition	Value
V	Voltage applied (V)	8.0
I	Current applied (A)	0.101
v	Volume of PCM (m^3)	0.0000475
A	Area of the PCM containment wall (m^2)	0.087
T_m	PCM melting peak temperature (°C)	41.0
T_{amb}	Ambient temperature (°C)	26.0
σ	Stephan-Boltzmann constant ($Wm^{-2}K^{-4}$)	5.670367×10^{-8}
H_L	Latent heat of RT42 (Jkg^{-1})	174000
k	Thermal conductivity of RT42 ($Wm^{-1}K^{-1}$)	0.20
ρ_{PCM}	Density of RT42 at 15°C (kgm^{-3})	880
	Density of RT42 at 80°C (kgm^{-3})	760
	Density of RT42 at operating temp (kgm^{-3}) - Assumed	800
ρ_{CuO}	Bulk density of nano CuO (kgm^{-3})	300-450
	True Density of nano CuO (kgm^{-3})	6310
	Approximated density assumed for calculations	3380
ρ_{nano}	Density of RT42+0.5% nano-CuO; Calculated (kgm^{-3})	803.06
$C_{P,\ PCM}$	Specific heat of RT42 solid ($Jkg^{-1}K^{-1}$)	2000
$C_{P,\ CuO}$	Specific heat of nano-CuO; From literature ($Jkg^{-1}K^{-1}$)	2400
$C_{P,\ nano}$	Specific heat of RT42+0.5% nano-CuO; Calculated (Jkg^{-}	2002
χ_{PCM}	Mass percentage of RT42 (%)	99.5
χ_{CuO}	Mass percentage of CuO (%)	0.5
α	Volumetric expansion coefficient (%) of PCM RT42	12.50

3.8 Instruments and Devices

3.8.1 Solar Simulator

For providing highly collimated illumination for those experiments that require a controlled light source, *Wacom Super Solar Simulator* (*WXS-210S-20, AM1.5G* from *Wacom Electric Co. Ltd*., Japan), shown in Fig. 55 was used. With an irradiance area of 210 mm × 210 mm, and collimating angle within +/- 3°, it's a *Down-shine* type simulator with a 2000 W *Wacom* Xenon short arc lamp. Solar intensity fixed at 1000 Wm^{-2} provided constant irradiation for most of the experimental set-ups except when the effect of irradiance was studied.

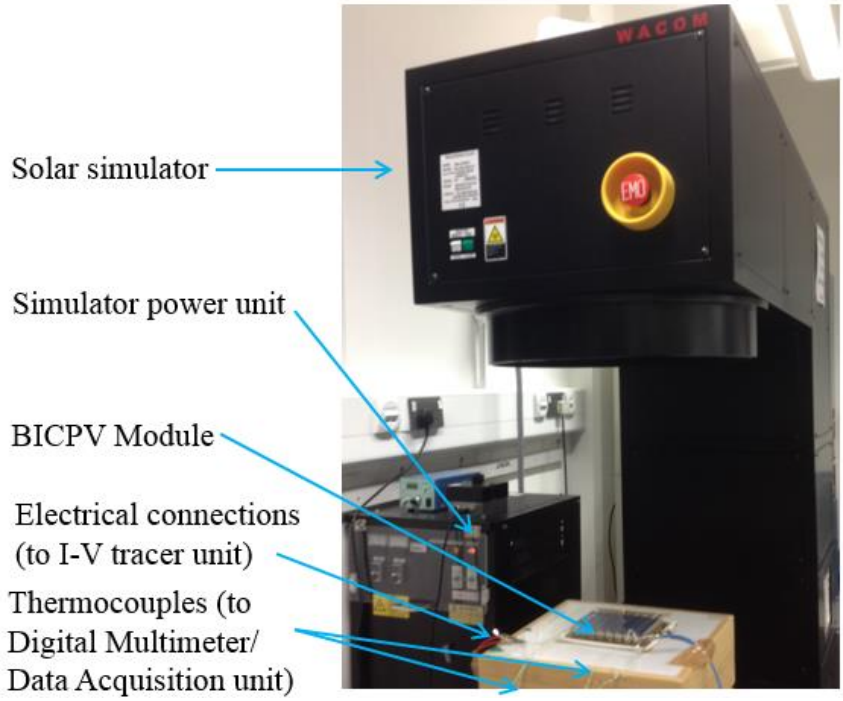

Figure 55: Wacom solar simulator front panel with BICPV for characterisation.

The simulator can vary irradiance level between 700-1200 W/m² and its classified as a *Class AAA* with positional non-uniformity within +/- 2 % at 1 sun, temporal instability of irradiance within +/- 1 % at 1 sun, spectral match approximating AM1.5G [316]. The simulator works on three-phase AC 200V, 50/60Hz, 15A with +/- 10 % tolerance, with diode full wave rectification in the circuit and stabilised irradiance by internal light monitor and feedback circuit. The lamp cooling fan and the propeller exhaust fan maintain the healthy operating temperature. The irradiance intensity was regulated using a *Voss electronic* GmbH *HelioCon* device, capable of controlling the Xenon lamp intensity using the *HelioCon* software. It can control the Xenon lamp intensity of the Wacom Simulator remotely or manually. With a high repetition rate from (0.1 W/m² per step), it offers high accuracy and repeatability of adjustment setting and is designed to work on 230V power supply [317]. The calibration constant for the device works on Eqn. 10, where He is the *Heliocon* value corresponding to the irradiance intensity, I.

$$He = -0.00000077I^3 + 0.001805947I^2 - 0.239755766I - 85.39340718 \quad \textbf{(10)}$$

For instance, the He values set on the device were 896.91, 710.80, 425.80 and 149.97 (rounded off to 2 decimal places) in order to receive an irradiance intensities of 1200 Wm^{-2}, 1000 $Wm^{-2,}$ 750 Wm^{-2} and 500 Wm^{-2} respectively.

3.8.2 Differential Scanning Calorimeter (DSC)

Differential scanning calorimetry is used to study the thermal transitions of materials such as melting temperatures and enthalpies (heats of fusion), crystallization and glass transition temperatures. The temperature difference between a sample and a reference substance of a fixed mass heated at a pre-defined rate is used to identify the chemical or physical changes in a material via exothermic and endothermic processes. A purge gas (usually Nitrogen, but also He and Ar) is circulated within the DSC cell to remove moisture, oxygen or dirt particles that may affect the measurements or damage the cell. Equipment manufacturers [318] advise that the balance chamber must continuously be purged with a pure, inert and dry protective gas. The purge gas also contributes to improved heat transfer, sensitivity and response and prevents the formation of localised hot-spots. Fig. 56 (a) sketches the basic outline of a DSC equipment. *Netzsch DSC 214 Polyma* was used for the purpose of thermal testing of the PCM and *Netzsch Proteus version 7.0.1* software was used for the analysis of the test results within the premises of this thesis. The DSC instrument comes with a special arena furnace, which is shown in Fig. 56 (b). Heating/cooling rates can be varied from 0.001 K/min to 500 K/min, at a temperature accuracy of 0.1 K/min and enthalpy accuracy of < 1 % [319]. The Indium response ratio is > 100 mW/K and the resolution is 0.25 µW [319]. The installation works on 230V, 50 Hz in dynamic, static, oxidizing and inert atmospheres.

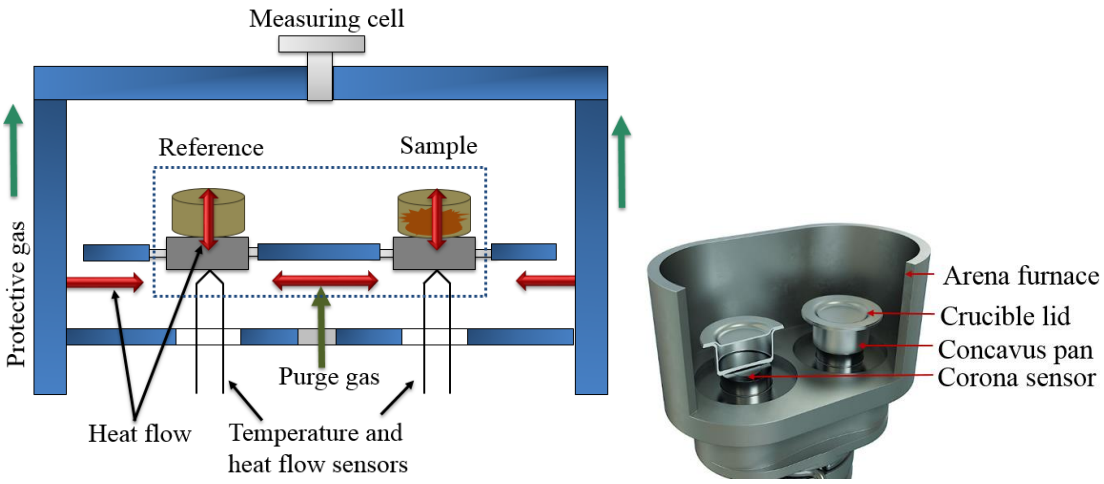

Figure 56: (a) Schematic of a DSC and (b) the cross-sectional view of Arena furnace (adapted from [318]).

The DSC instrumental set-up consists of the main equipment with the furnace, the nitrogen cylinder for providing the protective gas, a data acquisition system (computer running the *Proteus* software) attached to the DSC equipment and an auxiliary cooling accessory or intercooler unit IC70, which is capable of handling temperature as low as -70 °C and as high as 600 °C (Fig. 57 (a)). A set of standard samples (one sapphire disc each, Ø 4 mm, thickness 0.25, 0.5, 0.75, 1.0 mm) for calibration measurements (specific heat or sensitivity/enthalpy), with purity certificate was provided. The sample cutter and accessories such as a micro-spatula and a surgical blade were used to prepare PCM samples of masses 4-10 mg. The Al *Concavus* pans and lids had 30/40-µl capacity with outer bottom diameter of 5 mm (Fig. 57 (b)).

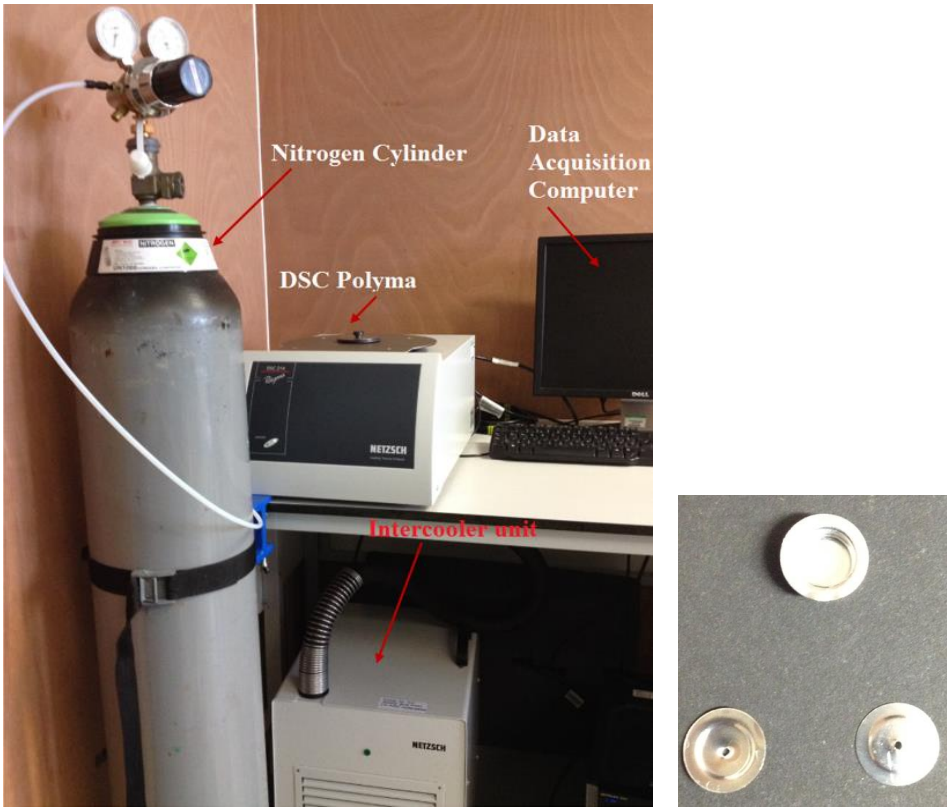

(a) (b)

Figure 57: (a) DSC unit with the Nitrogen cylinder and the intercooler unit IC 70 and (b) The sample crucible pan and pierced lids (from top and bottom).

Netzsch Proteus

Netzsch DSC Polyma supplied with the *Netzsch Proteus® version 7.0.1* software, was used for the thermal analysis and studying the thermophysical properties of the various PCM and n-PCM. The visual display and real-time data collection during the execution of the temperature program, was achieved using the expert mode measurement window. *Proteus*® analysis software programs are available as a 32-bit Unicode version, implying

that they support the settings which vary by location (decimal separators, data formats etc.). Other features include *curve evaluation* (added to the method for automatic evaluation of the measurement curve) and *specific heat* package (to determine C_p for solids, powders and liquids). The software can also be used for carrying out the heat-flow calibrations with sapphire as the standard material. Fig. 58 shows the GUI display, with the DSC curve obtained for a typical thermal analysis experimental run.

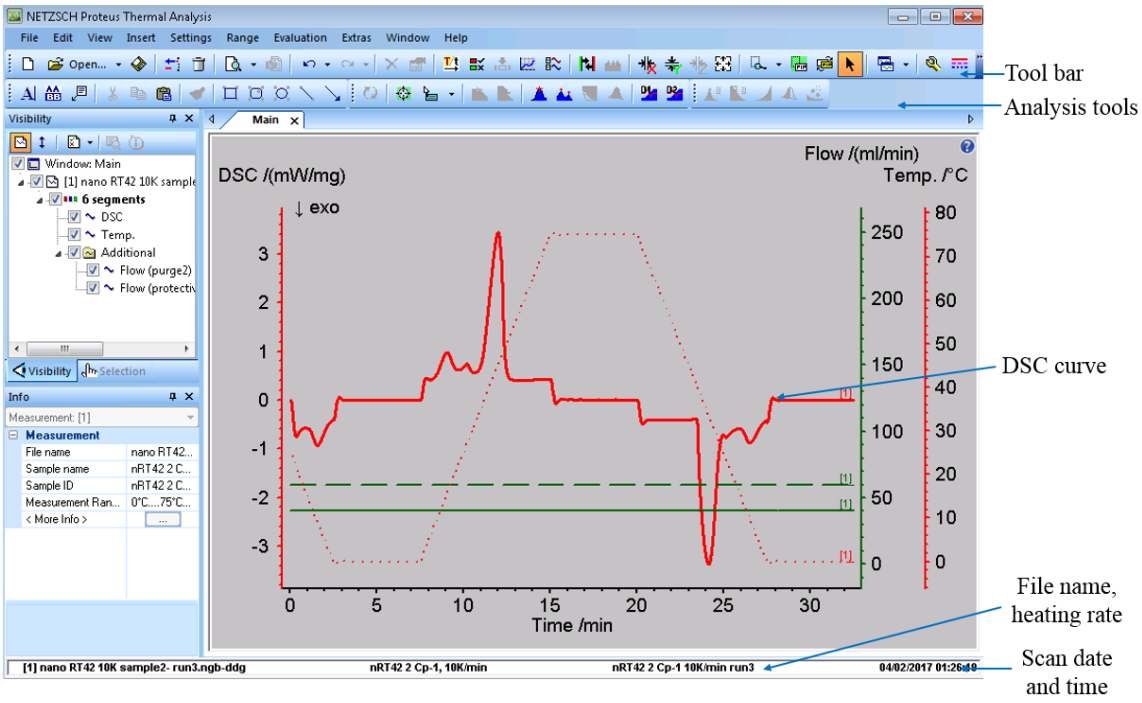

Figure 58: Netzsch Proteus® GUI with the DSC curve (solid red), flow rate (green line) and temperature program (dotted red) displayed.

3.8.3 Scanning Electron Microscope (SEM)

Optical microscopy is suitable for low-magnification (1000 X) analysis into colour, size and shape detection of samples but for higher resolutions, SEM is useful. The components and working of SEM used for PCM/n-PCM analysis are described here; the two SEM instruments used for the thesis are described as SEM-I and SEM-II. Basically, primary electrons striking specimen react with its surface producing the following beams [320]:

(i) Secondary electrons - lower energy electron beam (5-50 eV) produced from the samples after the SEM primary electron beam hits them.

(ii) Back-scattered electrons - same energy primary electrons reflected due to elastic scattering, providing good image contrast in the imaging field.

The key SEM instrumental elements are shown in Fig. 59 (a).

- Electron source or gun creates the electron beam discharged within a small volume with a slight angular spread and predefined energy.
- Lens system containing numerous electromagnetic or electrostatic lenses. It allows the beam from electron source to enter and upon exit, hit the sample surface.
- Scan unit produces onscreen image by modulating the detected system signal upon the beam movement in a raster pattern over the specimen area.
- Detection unit picks the backscattered electrons, secondary electrons and X-rays signals from the sample and transforms them into digital signals.

(i) SEM-I

FEI^{TM} Quanta FEG 650 SEM (Fig. 59 (b)) was used to characterise CuO nanoparticles as it can achieve magnifications of ~6 to 100,000 X, providing high resolution images in a digital format. The SEM works with a 200 V to 30 kV of accelerating voltage, up to 2 μA, continuously adjustable probe current and offers a 6.5 mm maximum horizontal field width at analytical working distance at 10 mm, 24.3 mm at 65 mm, 150 mm with Navigation Montage routine [321]. The samples were filled in the prescribed carbon coated stub and inserted in the holder within the main chamber. The vacuum pump was started for high vacuum and the beam is set on with a 2 kV signal; spot size 2.0. Using the control panel functionalities *(magnification, focus, stigmator, shift, image contrast and brightness)*, the required parameters were selected using the knobs for attuning. The tilt angle (10°), vertical (Z) distance, scan rate (2-30 μs) and pixel size were varied using the software options on the attached computer. The minimum working distance for this device was 10 mm, which is the OEM provided safety limit as well.

(ii) SEM-II

Hitachi S3200N SEM-EDS (Fig. 59 (c)) was used for high resolution imaging of n-PCM using gold sputtering. It can achieve a magnification of ~ 20 to 250,000 X, with a practical operational magnification of ~60,000 X. *BioRad Sputter Coater* (Fig. 59 (d)) from *BioRad Microscience Division* along with the *Polaron E5550* density thickness FTM unit (*Polaron equipment Ltd.,* UK, now *Quorum Technologies Ltd*.) was used to sputter coat the PCM and n-PCM samples in the specimen chamber using nano-layered gold coating. The thickness of coating was controlled using the Plasma current (electric kV) by means of turning the HV control knob.

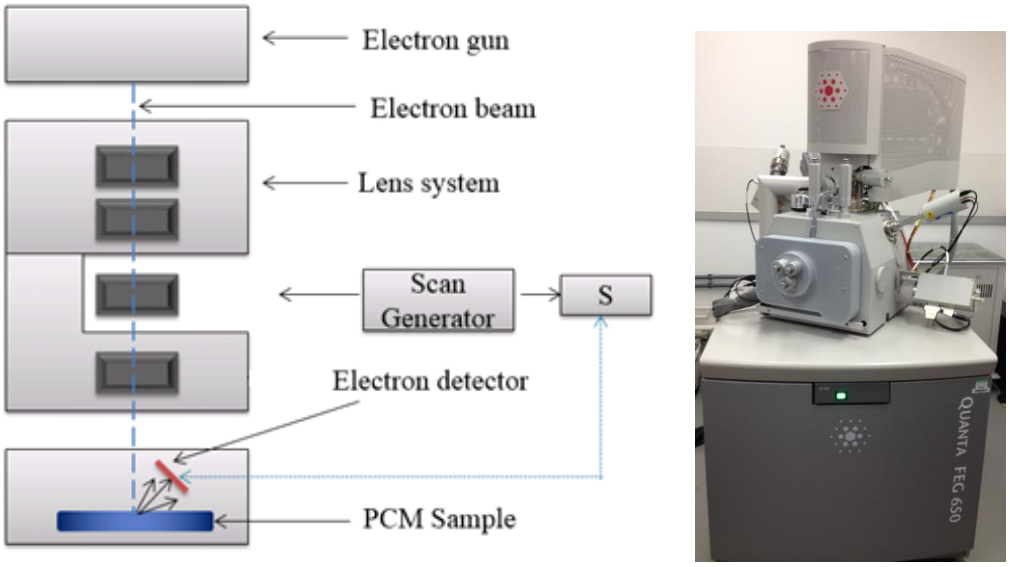

(a) (b)

(c)

(d)

Figure 59: SEM instrument (a) Schematics of a generic SEM, (b) FEI^{TM} Quanta FEG 650 SEM, (c) Hitachi S3200N SEM-EDS and (d) the Sputter Coater with the PCM samples in the specimen chamber being gold-coated to 60 nm.

3.8.4 X-Ray Diffractometer (XRD)

X-ray Diffraction, an example of X-ray wave interference, is used to produce the periodic atomic structure of crystals. It can be used for measuring the average spacing between the interatomic rows, determining the crystal or grain orientation, discovering the crystal structure for unknown materials and for defining the size, shape and internal stresses for small crystalline areas. The atomic planes of a crystal cause an incident beam of X-rays to interfere with one another as they leave the crystal. The phenomenon is called X-ray diffraction. It works on *Bragg's Law* as given by Eqn. 11.

$$n\lambda = 2dsin\theta \quad \textbf{(11)}$$

Where, θ is the angle of incidence at which the cleavage faces of crystals appear to reflect X-ray beams, d is the interatomic layers distance in a crystal, λ is the wavelength of the incident X-ray beam and n is an integer.

For detecting the purity of nanomaterials and PCM GR42, *Siemens D5000 Powder Diffractometer,* a bench-top X-ray Diffractometer, also configured as a reflectometer, was used for Control software allows automated data collection and visualisation. The specifications are given in Table 17. This XRD is used to examine mineral samples based on crystallography, with a lower detection limit of ~5 %.

Table 17. Siemens D5000 diffractometer Specification.

Parameter	Value
X-Ray Tube	1.5kW, Cu-anode
kV & mA	40kV, 30mA
Wavelength	1.5406/1.54439 (Cu Kα1/2)
Detector	Scintillation point detector
Div. Slit	V6 (variable, 6mm)
AntiScatter Slit	(same as above)
Scan Type	2θ/θ locked
Scan Range	2-70 °2θ
Step Size	0.02 °2θ
Scan time	1 sec/step
Scan Rotation	None
Interpretation software	EVA v.18.0.0.0.
PDF Database	JCPDS PDF-2 (2004) database

3.8.5 Temperature Data Acquisition System

For recording the thermocouple temperature of the BICPV modules functioning under the solar simulator, *Keithley Integra Series Model 2700 Multimeter / Data Acquisition*

System (Fig. 60) was used, as it is more useful for stationary testing. It can be used for measurement functions such as DC voltage, DC current, AC voltage, AC current, frequency or thermistors, period, event counter/totalizer, continuity and digital I/O etc.

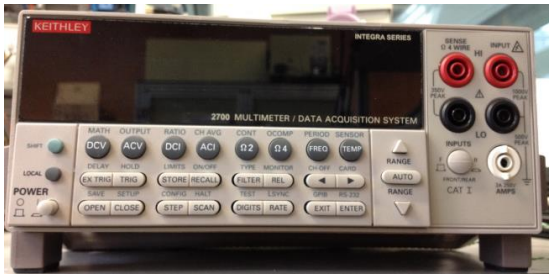

Figure 60: Keithley Integra Series Model 2700 Multimeter temperature recorder.

Each channel of the instrument has the ability to be configured separately for any of the 14 available measurement functions and provides built-in signal conditioning. ExceLINX-1A software was used to acquire data directly into an Excel spreadsheet format. The specifications for the instrument are given in Table 18.

Table 18. Technical specification for Keithley Integra Series Model 2700 Multimeter temperature recorder.

Parameter	Value
Power Supply	100V / 120V / 220V / 240V / ±10%
Range of temperatures (K-Accuracy	-200 to +1372°C ±0.2°C
Data logs storage format	as files with the .xls extension
Line Frequency	45Hz to 66Hz; 360Hz to 400Hz
Operating Environment	0°C to 50°C
Number of channel /slot	20
Thermistor	2.2kΩ, 5kΩ, and 10kΩ
Thermistor range	-200 to +600°C
Thermistor resolution	0.001°C
Scanning rate DCV	60/s - 185/s

3.8.6 I-V curve tracer

Eko I-V Curve Tracer (Fig. 61 (a)) was used in conjunction with *MP-160i software* (Fig. 61 (b)) for the CPV module testing and I-V characterisation in combination with the solar simulator, as determined by changing the electrical load during the I-V sweep (Fig. 61 (c)). *MP-160 I-V tracer* can be used for testing single or multiple solar cell or module characteristics in combination with a solar simulator or natural sun light. The radiant energy on the module can be measured with the voltage and current measurements. The technical specifications for the curve tracer are given in Table 19.

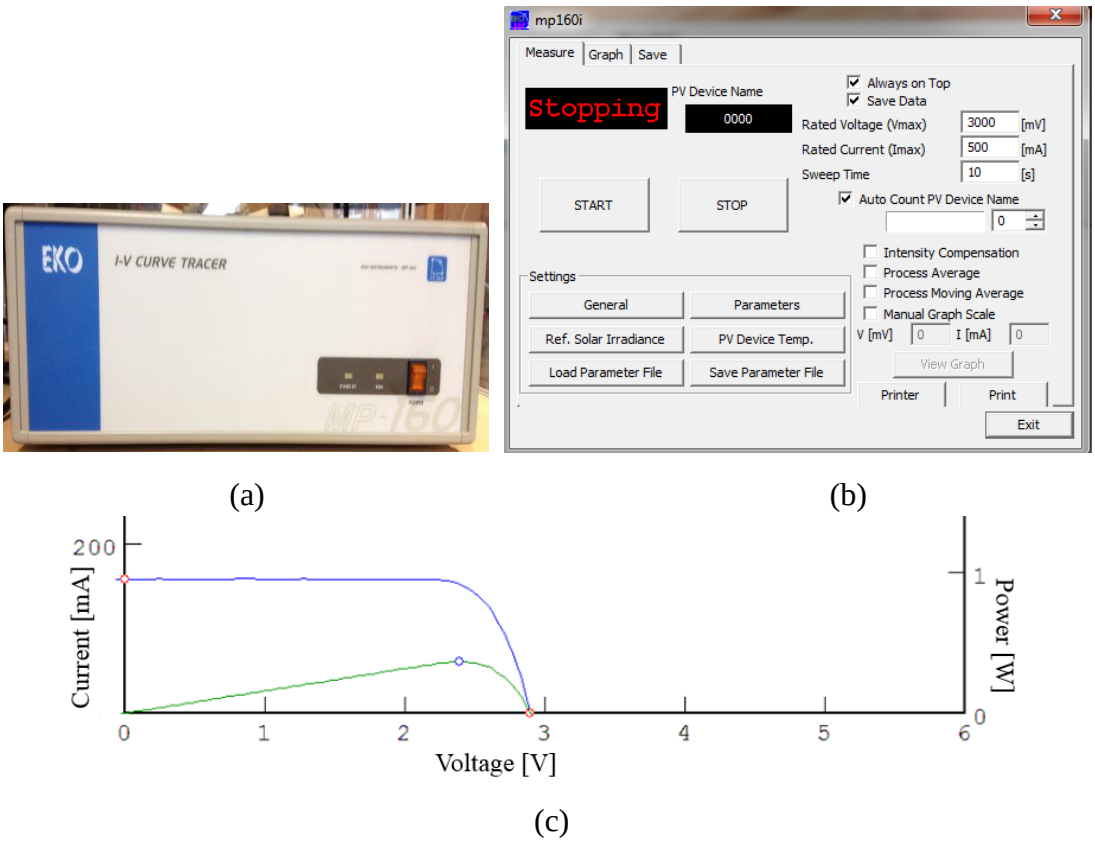

Figure 61: Eko MP-160 I-V curve tracer (a) front panel, (b) the mp 160i software console with the rated I-V settings and (c) a typical I-V curve.

Table 19. Eko MP-160 Specification.

Parameter	**Value**
Input Power	300W (Max. 360W)
Input Current	10A (Max. 11A)
Input Voltage	300V (Max. 320V)
Sweep Direction	V_{oc} to I_{sc} sweeping
Temperature Input	2 points; T-type or K-type thermocouple
Irradiance Input	1 point (30mV)
Operating	0 ℃ ~ 40 ℃, 20% ~ 90%RH
Power	AC100-240V, 50/60Hz, Stand-by 20VA,
Accuracy	+/- 0.5%FS
Resolution	1/1000FS
Sweep Time	2~330 seconds
Minimum Range	0.5 V, 5 mA
A/D Converter	16 bit (±15 bit)
Voltage Range	300V, 30V, 3V
Current Range	10A, 3A, 0.3A, 0.03A
I-V data points	256 sets (Voltage, Current, and Light amount, each
Communication	38400 bps

3.8.7 Temperature recorder

RDXL12SD 12-Channel Temperature Recorder (Fig. 62) with Excel-Formatted Data Logging SD Card was used for measuring and recording the temperature of the various points within the PCM system. As a hand held mobile device, it offers the flexibility for moving and placing, hence more suitable for the micro-finned thermal system, which didn't require a solar simulator. The technical specifications are highlighted in Table 20.

Figure 62: Omega® RDXL12SD 12-Channel temperature recorder front panel.

Table 20. Technical specification for Omega® temperature recorder.

Parameter	**Value**
Accuracy (%)	0.4
Read out temperatures	(-100º to 1300ºC)
(J-type)	(-100º to 1100°C)
Display	Backlit 3.9 in. diagonal
Powered by	8 AA-batteries or 9-VDC AC
Data logs storage format	as files with the .xls extension
Storage media	SD card
SD card memory limit	16 GB
Number of channels	Twelve
Temperature-	K, J, T, E, S and R

3.8.8 3-D printer

Stratasys' uPrint SE plus 3D Printer based on patented FDM® (Fused Deposition Modelling ™) technology was used (Fig. 63) to print the PCM containment using *ABSplus* plastic. The specifications for the printer are given in Table 21.

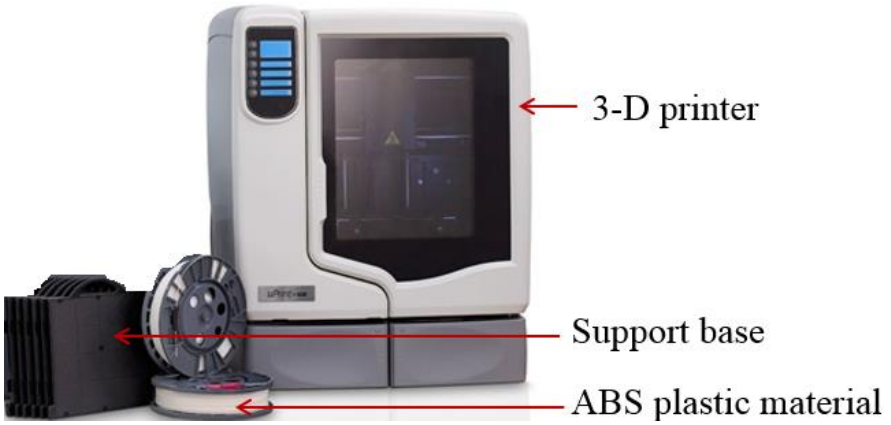

Figure 63: Stratasy's uPrint SE plus 3D Printer front panel and plastic material[315].

Table 21. Technical specification for uPrint SE 3D Printer [315].

Parameter	Value
Footprint	635 x 660 mm
layer thickness	.33 mm / .013
Model Material	ABS plus in ivory, white, blue, fluorescent
Build Size	203 x 203 x 152 mm
Workstation Compatibility	Windows® 7
Network Connectivity	Ethernet TCP/IP 10/100 base
WaveWash Support Cleaning System	48.33 (w) x 43.18 (d) x 43.85 (h) cm
Basket size	203 x 203 x 152 mm
uPrint SE 3D Printer Power	220–240 VAC 50/60 Hz, minimum 7A
WaveWash Support Cleaning System	100-240 VAC, 50/60Hz 1200W

3.8.9 Power supply

An external power supply (*Aim-TTi EX354RD*) was used to supply DC electrical power input to the resistive Kapton heaters. Temperature defining voltage and current were set to emulate the temperature rise in the BICPV system as experimentally determined in the literature. The power supply unit came with mixed-mode regulation (to combine HF switch-mode pre-regulation with linear final regulation) and two outputs (0 to 35V / 0 to 4A). The dual output DC bench power supply with digital V, I meters offered the option to work on constant voltage or constant current operation. The power rating was 280W, with minimum and maximum supply AC voltage of 110V and 240V. The calibration for V and I was performed using an external multimeter

3.8.10 Miscellaneous devices

1. **Multi-meter -** *Fluke® 117 true RMS digital mustimeter* was used to measure the instantaneous input current and voltage, which were then used to calculate the electrical power and heat for the micro-finned thermal system with micro-fins.
2. **Ultrasonicator -** Hilsonic ultrasonic cleaner with the attached ultrasonic bath was used for mixing and dispersing the nano-CuO particles within PCM. The principle is based on using the ultrasonic energy for agitating the particles.
3. **Support cleaning apparatus,** *SCA-1200* 220VAC manufactured by *PADT Phoenix Analysis & Design Technologies,* USA, was used to remove the support material from the 3-D printed parts. Working on 220-240 V, 50Hz, 10A, the equipment utilizes soluble support technology based on cleaning fluid containing a combination of *Sodium carbonate, Disodium carbonate,* compound with *hydrogen peroxide* and *anhydrous Citric acid.* Temperature ranges suitable for ABS, Polycarbonate and nylon are available.
4. **Metal Guillotine -** *Baileigh Industrial* hydraulic shear guillotine, *SH-5214*, with 52” shear, operating on 220 V, single phase power, with an adjustable back gauge for precise repeatability and table guides and front arm extensions was used for cutting Al sheets. It can cut 14-gauge mild steel over its full length and with the upper carriage built to minimise deformations while upper and lower blades with multiple shearing edges, gave a quick and smooth cut. The machine strongly held the sheet with the table preventing lifting during shearing**.**
5. **Band Saw -** *Record Power BS300E Premium 12" Band saw* was used to cut the concentrating elements to the required size as well as the walls of PCM containment from the Perspex sheets. With the ability to cut both curved and straight lines, the band saw table was dynamically balanced with its tilting tables and cast iron wheels for flywheel effect.
6. **Thermocouple Welder** - *Labfacility L60+* was used for welding thermocouples.
7. **Vacuum drying oven -** *MTI technologies* (250 °C, 215L, 22"x 25" x 24") *EQ-DZF-6210 Vacuum Oven* was used to degas the Sylgard and Polyurethane based mixtures for removing any trapped bubbles and to cure them.
8. **Soldering station** - For the solar cell soldering, *Weller WD1* soldering kit was used, with 120 V power unit WP80 soldering pencils, and *Xytronics 426 DLX* solder fume extractor.

3.9 Conclusions

The various materials employed for the BICPV-PCM system components and the rationale for their selection for the research work have been listed in this chapter. In a nutshell: (i) silicon based solar cells used for BICPV, (ii) *Polyurethane* material, with appropriate curing, used to cast the concentrators using the Stainless steel moulds, (iii) encapsulants, adhesives and epoxy glues, thermocouples, masking tapes, heating elements and (iv) PCM and nanomaterial types applicable for the thesis are discussed. No modifications were made to the original proposed design of concentrators or the type of the solar cells. However, the BICPV in this thesis were reformed using Al back-plate instead of glass plate used in the original designs. In addition, the top glass plate was removed from the system, so the available irradiance falls on the concentrator first before entering solar cells. The metal back plate was wrapped in a polyimide film for electrical insulation and a thin layer of clear silicone elastomer was used for encapsulating the solar cells. Various sized PCM containment were fabricated through either manual means or by printed them using a 3-D printer, which were then attached to the back of the BICPV through detachable adhesive means. The three main materials used are: (a) PCM, (b) nanomaterial and (c) n-PCM. The process of synthesising n-PCM has been discussed in brief. This chapter also contains the only BICPV-PCM analytical model for designing the system reported till date highlighted in Eqns. 17 and 18. Further, the model & make, and the working principles and technical specifications of the key instruments such as solar simulator, I-V tracer, multimeter/data acquisition, DSC, XRD and SEM are described. Miscellaneous devices such as thermocouples, temperature recorders and a number of other auxiliary tools such as for soldering, welding, ultra-sonication, vacuum drying and metal cutting are also explained.

PCM used were sourced from *Rubitherm Gmbh,* and nanomaterial was obtained from *EPRUI Nanoparticles & Microspheres Co. Ltd*, China. The facilities in Environment and Sustainability Institute, Penryn Campus (solar lab, chemical lab, research hall workshops and image-processing suite) provided the instruments and devices for fabrication. Micro-finning was performed at the University of Strathclyde. The next chapter will outline: (a) the processes followed to use the BICPV and BICPV-PCM systems shaped within this chapter and (b) the procedures for using the instruments for characterisation and measurements.

Chapter 4. Experimental Characterisation

The experimental characterisation provided a way to examine the influence of PCM/n-PCM on BICPV performance. The complete and final BICPV-PCM experimental set-up so arranged as explained in the previous chapter was capable of continuously measuring the output photoelectrical current, voltage and temperature firstly without, and then with the PCM/n-PCM. This chapter elucidates the procedures followed to investigate the electrical and thermal performances of the fabricated BICPV and the BICPV-PCM systems. The standard test procedure has been used for the indoor electrical characterisations using a solar simulator. A list of other PCM has also been tested for establishing their thermophysical properties as they are known to show deviations from the manufacturer data. Further, studies have been carried out to determine the material purity for the nanomaterial and granulated PCM. The specific techniques for characterising material samples were based on scanning electron microscopy (SEM), X-ray diffraction (XRD), and differential scanning calorimetry (DSC).

4.1 Introduction

In order to produce a fit-for-purpose BICPV module, it's vital to understand the electronic properties of the solar cells that it is composed of. A broad range of techniques is available for characterisation, mainly relying on different electronic structure and the different physical effects. To typify a solar cell's performance, electrical characterisation is performed. This is useful for research and development as well as during the manufacturing process of PV cells and involves measuring the output current or capacitance as a function of an applied DC voltage. Electrical characterisation is important in determining how to make the cells as efficient as possible with minimal losses and a range of key device parameters can be extracted from the DC and pulsed current-voltage (I-V) measurements [322]. I-V characteristics of a material provide information on the carrier concentration and the minority carrier diffusion length [323]. For comparing the different types of solar cells, they are rated on the basis of standardised measurements, usually conducted under standard test conditions (STC), which involves testing the cells using a vertical light source of 1000 Wm^{-2}, at 25° C ambient temperature and 1.5AM (air mass) spectral composition of the light [324]. The AM factor denotes the path length of the solar radiation passing through the Earth's atmosphere. An AM=1

signifies the shortest light path with vertical solar radiation, and a higher AM implies a small angle of incidence as the light travels longer through the atmosphere. The output measured under STC determines the solar element's rated module output that the manufacturer is obliged to state [12].

A comprehensive indoor electrical and thermal characterisation of BICPV was carried out to analyse the reliability of the designed systems. Both, the BICPV and the BICPV-PCM modules based on various concentrator designs providing different geometrical concentrations, were tested under the solar simulator. In general, the electrical characterisation consists of a series of steps investigating parameters of the module such as output short circuit current (I_{sc}), short circuit current density (J_{sc}), open circuit voltage (V_{oc}), maximum power (P_m), maximum power current (I_m), maximum power voltage (V_m), fill factor (FF), active area conversion efficiency (η_{in}), total area conversion efficiency (η_{pr}), solar cell efficiency (η) and temperature profiles under various constant levels of irradiance. Based on the results, the relative module electrical efficiencies were compared without and with the use of PCM/n-PCM. Fig. 64 summarises the features and aims for the planned experiments, including micro-finned thermal systems.

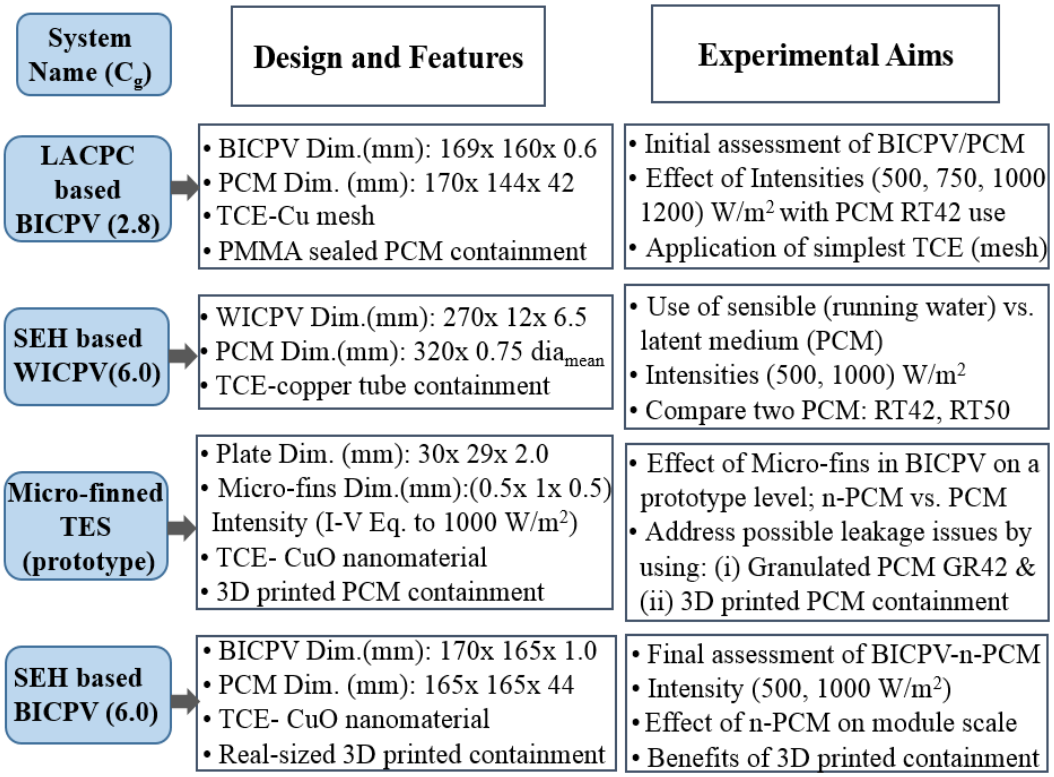

Figure 64: Various BICPV-PCM systems and the associated experimental aims.

It's also important to assess the thermo-physical properties and the phase transformation temperatures (both range and peak) of the PCM. Any inaccuracy in these data may affect the correct choice of PCM as well as the appropriate amount of material required for a particular application. The melting and congealing temperatures and the specific and latent heats of the materials have been validated using a DSC instrument. The morphology and orientation have been assessed using SEM while the purity and composition; using XRD techniques. The procedure for obtaining the DSC thermo grams and SEM micrographs has been detailed in subsequent sections of this chapter, which range from sample preparation to data acquisition and analysis.

4.2 BICPV-PCM system: Electrical Characterisation

The I-V characterisation of the modules were performed indoor, using highly collimated illumination at 0° (horizontal) under the class *AAA Wacom® Super Solar Simulator* and measured using *EKO MP-160i I-V Tracer*. The curve tracer, with a sweep time of 10 seconds (in V_{oc} ►I_{sc} direction), measured the instantaneous J_{sc}, V_{oc}, P_m, I_m, V_m, FF, η_{in} and η_{pr} for the BICPV systems under the simulator. In general, for all three experimental modules, the output electrical connections of the fabricated BICPV were joined with the current and voltage reading electric cables (shown by red and blue, live and neutral electrical cables in Fig. 65) of the curve tracer. In order to calibrate the simulator and to regulate the irradiance intensity for varying the available irradiance for the experiments, the following processes were followed:

Solar Simulator Calibration

The solar simulator lamp intensity was calibrated using a 20 mm x 20 mm reference solar cell made of monocrystalline Si, enclosed within 9 mm x 70 mm x 16mm anodized Al with a quartz window for protection and temperature sensor. Using a 100 ohm Pt RTD /Type K thermocouple as the temperature sensor, it was used to calibrate the 1 sun (1000 Wm^{-2}) irradiance of the solar simulator. The reference cell operated on < 200 mA, between 10°C- 40°C [325].

Solar Simulator Intensity Variation

With the *Voss electronic* GmbH *HelioCon* device, the simulator's Xenon lamp intensity was controlled based on *HelioCon* software. For running the device, communication port

8 was opened and turned on for operating the intensity regulator. For the intensities of 1200 Wm^{-2}, 1000 Wm^{-2}, 750 Wm^{-2} and 500 Wm^{-2}, the He values (He is the *HelioCon* value corresponding to the irradiance intensity, I; the parametric defining values on the *HelioCon* device) were set at 896.91, 710.80, 425.80 and 149.97 respectively.

4.2.1 LACPC

To study the effect of irradiance on the electrical parameters of the LACPC based BICPV system without and with the use of PCM within the same system, and ascertain the respective correlation, the radiation intensities of 1200 Wm^{-2}, 1000 Wm^{-2}, 750 Wm^{-2} and 500 Wm^{-2} were selected. The schematic of the experimental set-up along with the peripheral devices and the electrical parameters for the simulator are shown in Fig. 65. The data was recorded for over 2 hour-period at an interval of 5 minutes. The effect of intensity was studied using the *HelioCon* control box for regulating the Wacom solar simulator Xenon intensity for both the BICPV and the BICPV-PCM systems.

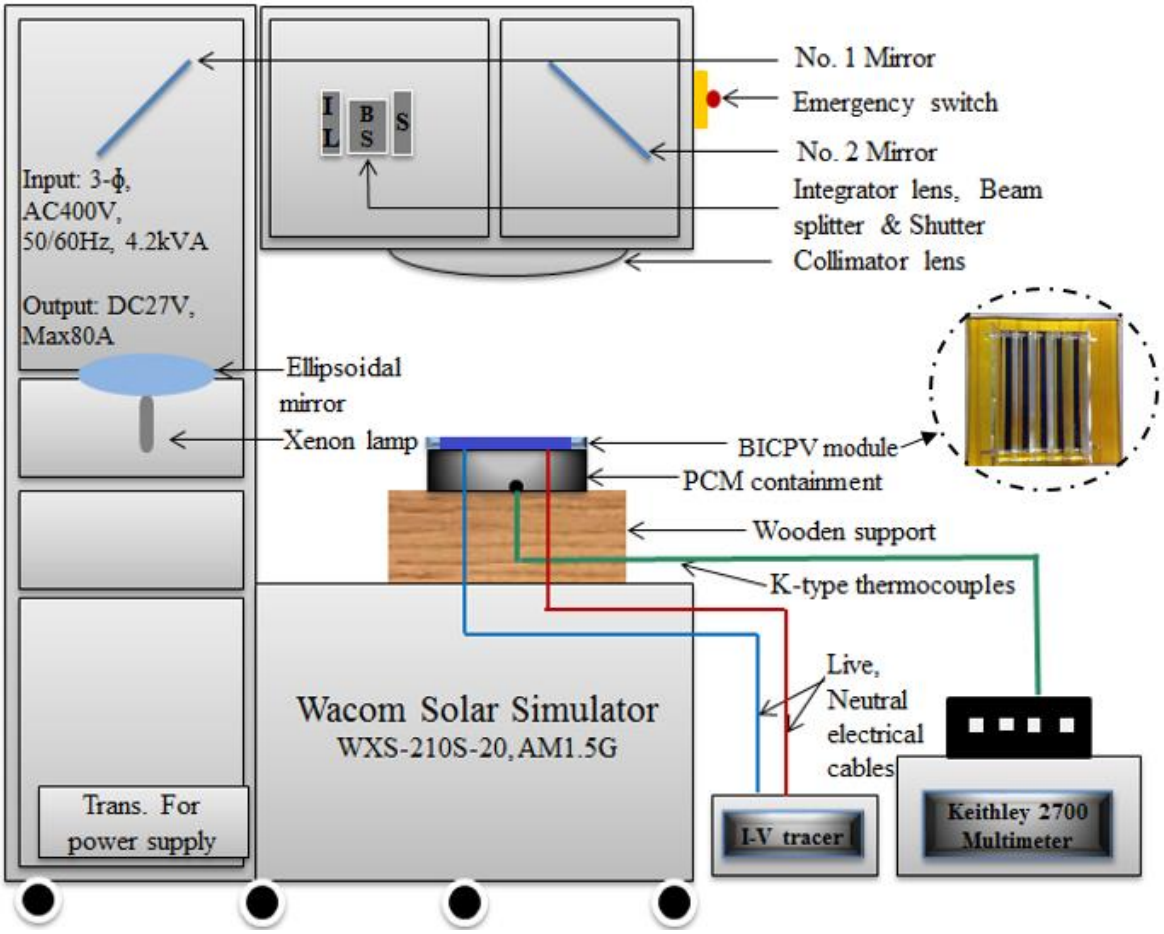

Figure 65: Schematic of the experimental set-up for characterising BICPV and BICPV–PCM systems, with the LACPC based BICPV in inset.

Similarly, for studying the effect of PCM thermal conductivity, the PCM (RT42) was replaced with the PCM and Cu-mesh combination. In order to do this, the PCM container was filled with the mesh, cut using standard scissors and then formed into layers, until the layers were thick enough to fill the entire volume of the containment. Liquefied PCM was then poured over the mesh to form a highly thermally conductive PCM system and PCM was allowed to cool down.

4.2.2 SEH with copper tubes

To test the WICPV system (with SEH concentrator and copper tubes) indoors with natural air convection, PCM and water-cooled options, the solar simulator was used to provide the irradiance. Intensities of 1000 Wm^{-2} and 500 Wm^{-2} normal to the horizontal surface were used for 1.5 hours. This limited time period was selected so as to focus on the heat absorption /melting phase of the PCM heating - cooling cycle. Eko® I-V curve tracer MP-160 was used to measure the output I_{sc}, V_{oc}, P_m, and overall system electrical efficiency η_{elec} was calculated from the obtained P_m data. Using the experimental set-up (Fig. 66) each experiment was repeated three times for repeatability and accuracy.

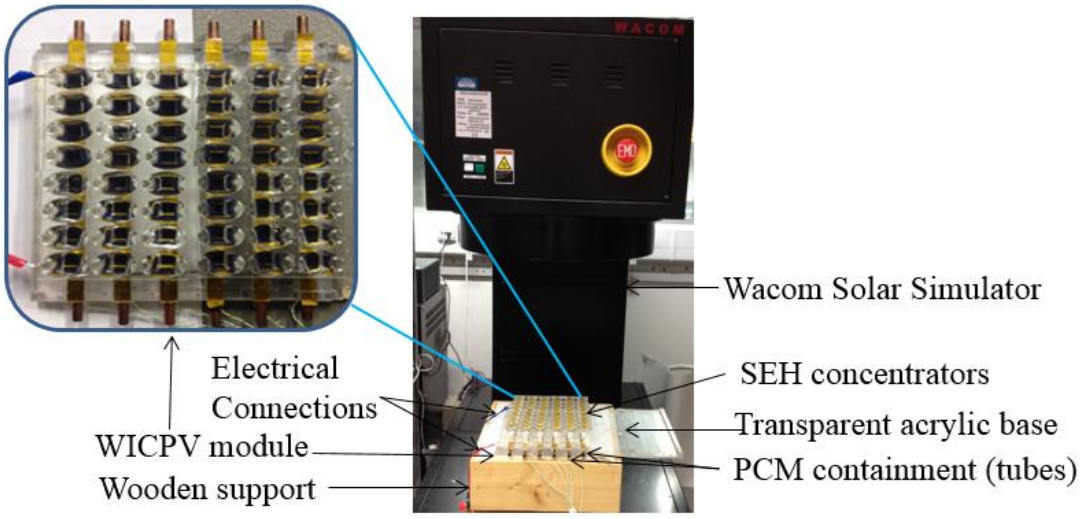

Figure 66: Experimental set-up of the WICPV system and the semi-transparency effect of the SEH system (in inset).

4.2.3 SEH

The SEH based BICPV-n-PCM system was illuminated with the solar simulator at 1000 Wm^{-2} and 500 Wm^{-2} for a period of 2.5 hours with applied n-PCM passive cooling and for 2 hours for characterising the module without any cooling (Fig. 67).

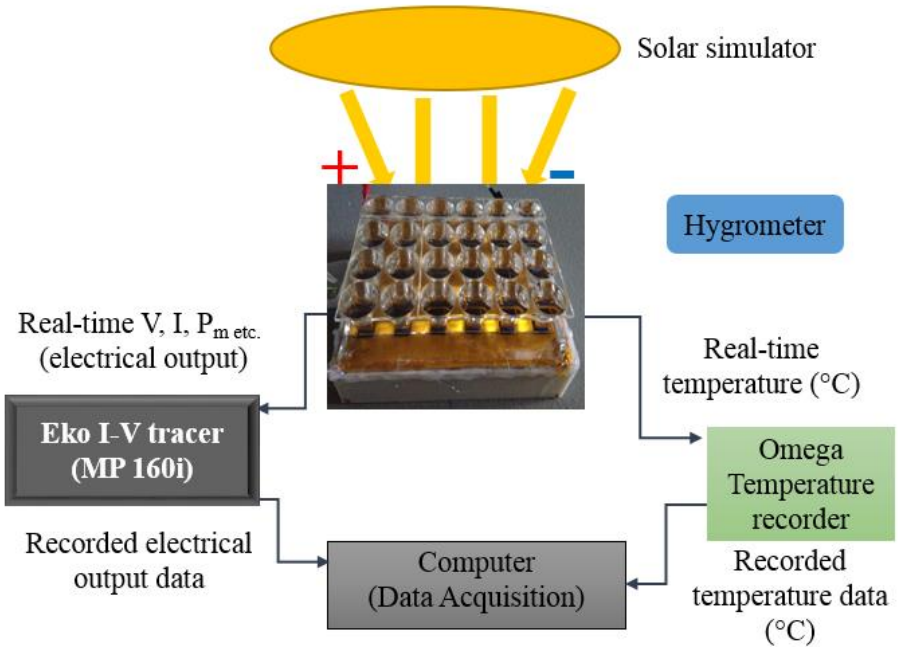

Figure 67: Experimental set-up for electrical characterisation of BICPV and BICPV–PCM system based on SEH concentrators.

There two types of n-PCM tested were with varying % by weight (0.5 % and 1.0 %) of nanomaterial (CuO with 60 nm average particle size) dispersed within PCM RT42. *EKO MP-160i* I-V Tracer was used for I-V characterisation of the module and the data was collected using *MP-160i* software intended for indoor use, every 10 minutes, on the attached computer. The experiments with same intensity and n-PCM type were repeated three times for repeatability and accuracy.

4.2.4 Micro-finned thermal system for BICPV applications

For this experiment, two rectangular aluminium plates without (for benchmarking) and with plate micro-fins geometries were considered. The aluminium plates (either with or without the machined micro-fins) were fitted on the 3-D printed PCM containment, which was then insulated with a 5 mm thick polystyrene layer (0.03 W/m·K) on all sides. The Kapton heaters were glued on the top flat surfaces of the plate, acting as a resistive heat source. The electrical power input was applied using *Aim-TTi EX354RD* dual DC power supply. Temperature defining voltage and current were set to emulate the temperature rise in the BICPV system as experimentally determined in the literature [311]. As the maximum temperature attained within the aluminium back plate under the highest solar irradiance (1200 Wm^{-2}) was 60 °C [311], for the tests within the present experiment, 70 °C was attained at the selected DC V, I combination (i.e. at P = 0.8W). This is because in

this case, the top surface had been insulated to avoid radiative and convective losses, contrary to the uninsulated reported BICPV system, so a higher temperature range was selected to account for the insulation effect. Fluke® 115 service engineers digital multi-meter was used to measure the instantaneous input current and voltage from the power supply, which were then used to calculate the produced electrical power and consequently, temperature rise. The experimental set up is shown in Fig. 68. A further study was undertaken to compare the effectiveness of two different (solid-solid and solid-liquid) PCM using the same set-up for thermal regulation of BICPV on a scaled down level. The reason behind using a solid-solid PCM was to overcome the challenges related to PCM leakage and study its suitability for BICPV applications. The temperature profile of the BICPV under solar simulator irradiance was emulated using an Aluminium plate with Kapton heaters for a period of 150 minutes. The melting temperature range for both the solid-solid PCM GR42 and solid-liquid PCM RT42 was similar as 38-43 °C.

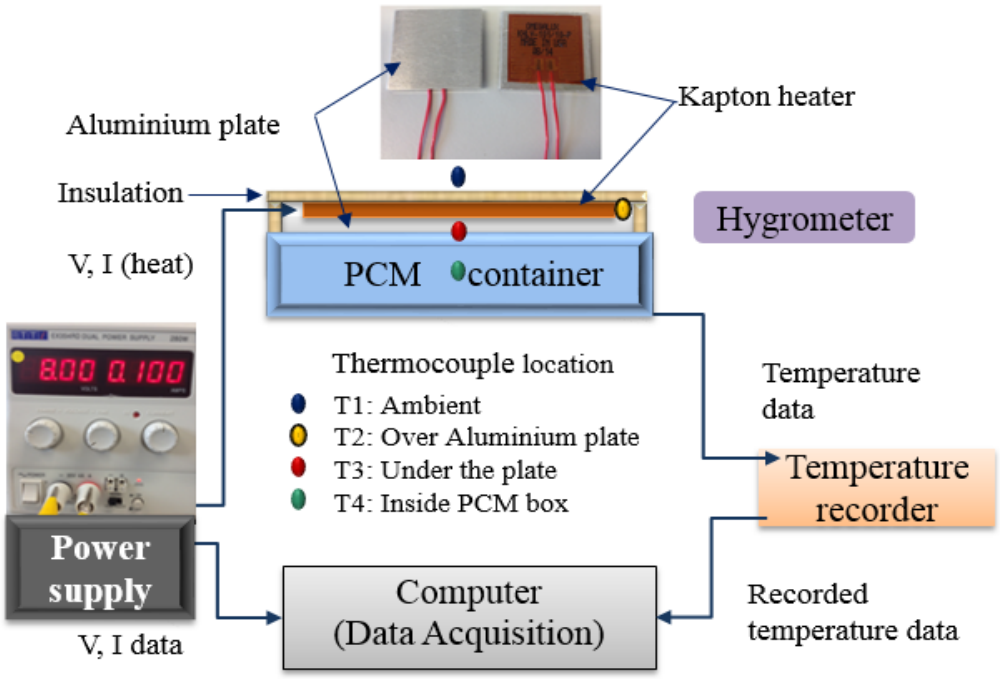

Figure 68: Schematic of the experimental system set-up with the highlighted thermocouple locations.

4.3 BICPV-PCM system: Thermal Characterisation

The thermal characterisation of the fabricated modules, without and with PCM, was based on the recorded temperatures using the K-type thermocouples. In general, for all the four experimental systems, welded thermocouple tips were attached to the location of

temperature monitoring. The other ends of the wires were either connected to the type k thermocouple plugs, to insert into hand-held temperature recorder or manually screwed inside the 20-slot channels of the temperature acquisition system. In order to calibrate the thermocouples, the standard procedure of using 0°C (ice point) and 100°C (steam point) as the reference points were used. By inserting the welded tip of the thermocouples in a bath, the output from each of them was noted down separately. Only the thermocouples that showed a stable and constant temperature at these fixed points, which also remained uniform, were selected for their suitability for the measurements. The thermocouples were re-calibrated each time before using them again for the experiments. The ambient temperature and relative humidity were monitored using Hygrometer *Testo 608-H1* placed in the vicinity of the modules.

4.3.1 LACPC-PCM

Five K-type thermocouples were attached to the back of BICPV using Aluminium adhesive tape for thermal conduction. Similarly, another 5 K-type thermocouples were attached to the inner side of the bottom Aluminium plate of the containment (Fig. 69).

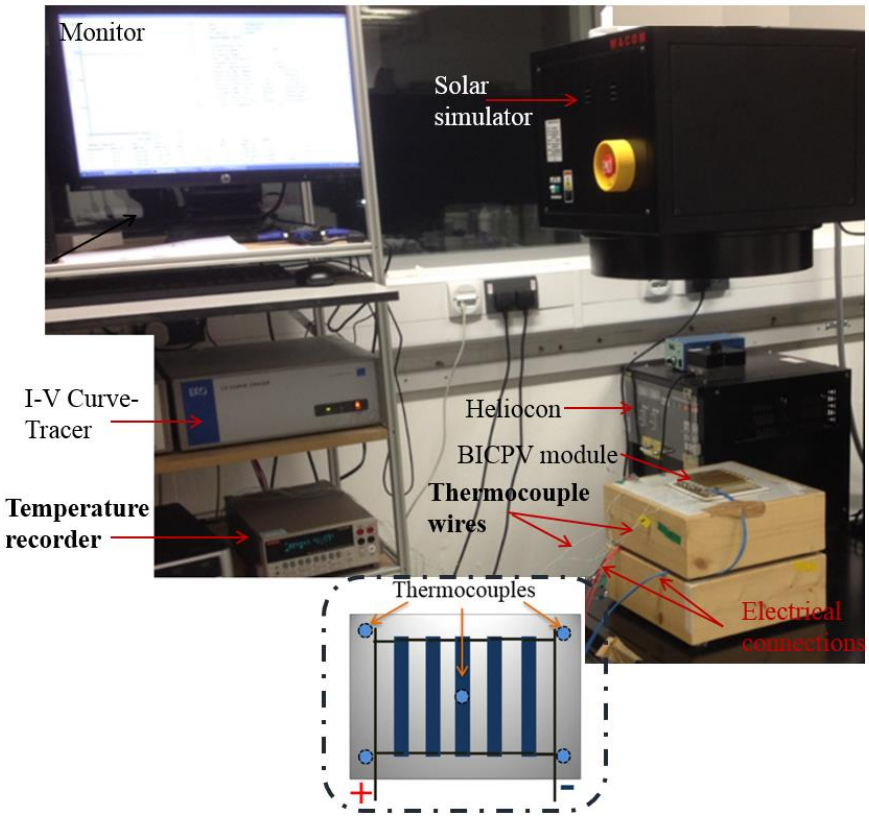

Figure 69: Thermal characterisation and the location of thermocouples (inset) for the LACPC based BICPV system.

The locations were chosen to study temperature variations across the centre and corners of the module and for examining the extent of temperature distribution within the underside of the back-plate. *Keithley Model 2700 Digital Multimeter* Data Acquisition and Data logging System were used to simultaneously measure temperature. The temperature data was recorded for over a 2 hour-period at intervals of 5 minutes and the ambient temperature was 25 °C - 29 °C.

4.3.2 SEH with copper tubes

For the SEH WICPV module, the temperature was recorded under the back-plate strips every 30 seconds for duration of 90 minutes using a *Keithley Model 2700 Multimeter Data Acquisition System*. All six K-type thermocouples were used to record the temperature at the centre of each solar cell skeleton under the aluminium strip on which they were mounted. The experiments were carried out indoors under ambient temperature conditions between 27 °C and 29 °C and relative humidity between 37 % and 46 %. For the experimental run with water, an arbitrary flow rate of 5 $mLsec^{-1}$ was selected, a rate at which the flow was visibly streamlined; below this rate, the flow in the pipes remained constricted and higher rates produced more turbulence, due to high Reynolds number. The water circuit for circulating water is illustrated in Fig. 70.

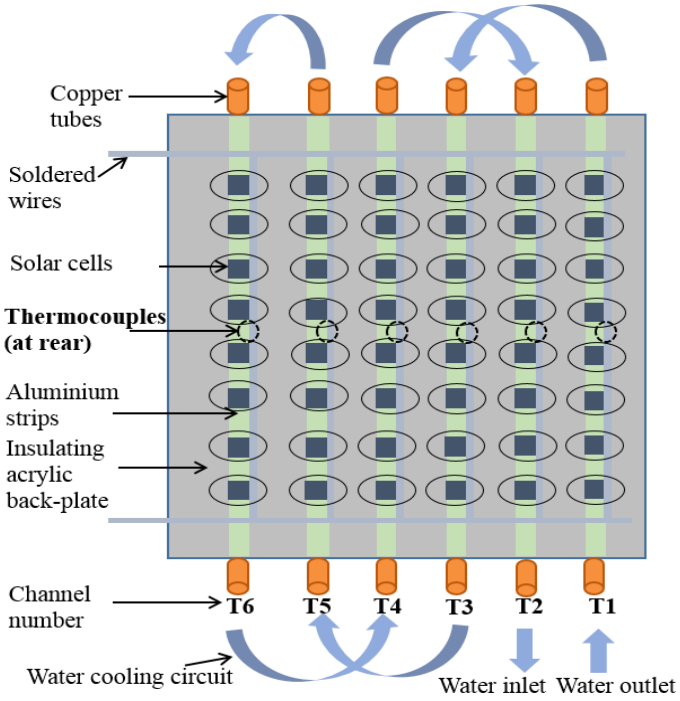

Figure 70: Water flow circuit for cooling the tubes behind the WICPV system and the thermocouple locations under the Aluminium strips.

Five clear soft plastic tubes on either side of the copper tubes were used as conduits for inter-channel flow. It is to be noted that for these experiments, the difference in heads (of water supply and the WICPV system) acted as the driving force for the water flow, doing away with the need for an electrical motor or pump thereby saving the active power loss. Hence, it may be argued that although water was continuously circulated for this experiment, it is still a passive cooling mechanism.

4.3.3 Micro-finned thermal system

The schematic of the experimental set-up has been shown in Fig. 68 above. The four K-type thermocouples, as shown by the coloured dots, were located vertically: above the insulation layer to record the nearest ambient temperature; at the central top of the plate; under the top plate; and in the mid-section of the PCM containment for different configurations, with the aim to study vertical temperature variations. The additional thermocouple placed outside the containment wall was used to detect how much heat was escaping through the sidewalls. Temperature measurements were recorded every 5 seconds for 2.5 hours using *Omega RDXL12SD* 12-channel temperature recorder. The entire experimental set-up was then enclosed within 200 mm × 200 mm × 200 mm insulated walls, covered on top, with an open front, to shelter it from mechanical and environmental damages. All experiments were carried out indoors under ambient temperature conditions between 26 °C and 27 °C and relative humidity between 21 % and 33 %. The following test cases or configurations were covered to justifiably use all possible combinations of micro-fins, PCM and n-PCM within the experiments: (i) flat (un-finned) plate, (ii) plate with PCM, (iii) plate with n-PCM, (iv) micro-finned plate, (v) micro-finned plate with PCM, and (vi) micro-finned plate with n-PCM.

4.3.4 SEH-n-PCM

For the SEH BICPV module, the temperature was recorded under the back-plate every 10 seconds for a duration of 3 hours, using a handheld *Omega RDXL12SD* 12-channel temperature recorder. Five K-type thermocouples were placed at horizontal locations; attached to the rear side of the top plate of the BICPV module using Aluminium adhesive tape and secured using the *Loctite glue gun* (Fig. 71) and five others were located on the bottom of the containment.

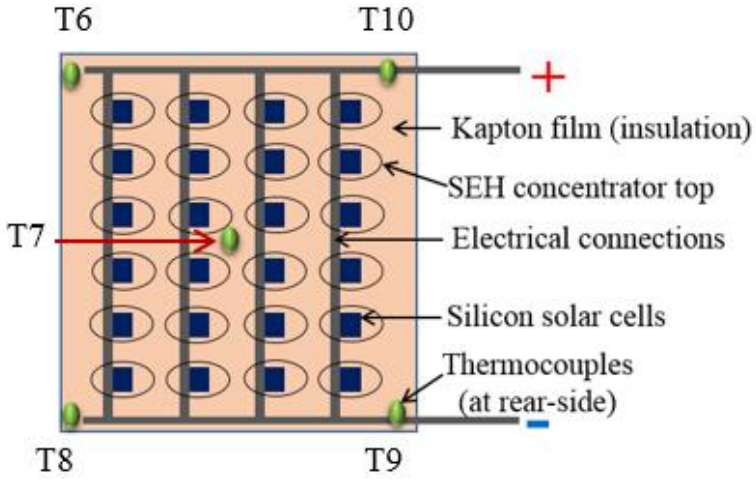

Figure 71: Experimental system set-up with the highlighted thermocouple locations at the rear side of the module.

4.4 DSC analysis of PCM

The working principle of the DSC is based on the measurement of the difference in the amount of heat used to increase the sample and the reference temperature as a function of either time or temperature. However, the results depend on the sample mass as well as the heating rate applied to the sample. It has been reported that the melting enthalpies measured experimentally by the authors of [326] for various PCM samples were lower than the manufacturer's values, with uncertainties ranging between 10 % - 47 %. Typically the data supplied by manufacturing companies are determined for a large amount of samples, which may be slightly or overwhelmingly different when the PCM is used in relatively smaller quantities such as, for the experiments within this thesis. Therefore, a DSC analysis becomes a necessity for detecting the magnitude of inaccuracy within the supplied PCM properties during phase change. The working on DSC involves a methodical process including sample preparation, calibration, evaluation and interpretation of the resulting curves, which are described below.

4.4.1 Samples

For the experimental work undertaken within this study, a wide variety of PCM including organic (RT series, based on paraffin wax), inorganic (SP series), granulated (GR series) and powdered PCM (PX series) were studied and analysed using DSC. This is done with a foresight of developing combination PCM from within the available different material types.

4.4.2 Sample preparation

The samples for DSC were prepared by sealing 10 ± 0.015mg sample of PCM in an aluminium (99.5 % purity) sample crucible. Known as c*oncavus* pans, (diameter: 5 mm, volume: 30/40 μL) these crucibles have a unique geometry with a concave bottom that allows a clearly defined ring-shaped contact zone. The lids were perforated using the standard perforation tool to avoid any pressure building in the sample during phase change. The pans were covered with pierced lids and cold-welded using a manual mechanical sealing press (Fig. 72) to avoid leakage of PCM in the liquid state that also maintains the furnace hygiene. As the samples for measurement were arbitrarily selected from the bulk supplied PCM, at least three samples were tested for each type of PCM in order to ensure accuracy and repeatability in the results.

Figure 72: A sealed, pierced lid DSC sample crucible (against a British 5 pence coin for size comparison).

4.4.3 DSC calibration

The DSC instrument was calibrated for temperature and heat flow/enthalpy/sensitivity measurements, with known reference standards (high purity reference materials with > 99.99 % purity). High purity metals exhibit sharp melting peaks, which make them popular for calibrating the instrumental response against accurate values. For purposes such as for organic materials and polymers, this may not be appropriate as there is an argument for calibrating *like with like*, however, indium, tin and lead are still widely used and will remain as convenient temperature and enthalpy standards for DSC in the time to come [75]. One empty reference crucible and the loaded sample crucible were placed in *Arena* Furnace. The reference crucible was always placed on the left furnace and the sample crucible on the right. The temperature program was set using the *Expert mode*. The tests were carried out under nitrogen gas as the purge and protective gas with a flow rate of 40.0 ml/min and 60.0 ml/min respectively. *Intracooler IC70* was used as the cooling device, as they offer an alternative to liquid nitrogen cooling.

(i) Temperature calibration

For temperature calibration pure metals were heated through their melting temperature range based on the exactly similar conditions (such as atmosphere and heating rate), which were to be used in subsequent measurement runs with the samples. A comparison was then drawn between the observed and the theoretically known melting points of the standard materials, to determine the resulting difference. The calibration shifting by a constant amount in the sample temperature is based on the number of points (one, two or more) and relies on a smooth curve through the calibration points. The DSC curve shows the melting of pure substances as they melt at an exactly defined temperature corresponding to their melting points. This temperature is taken as the onset or the start of the melting process which is defined as the temperature given by the intercept of the extrapolated slope of the melting curve and the continuation of the base line [327]. Fig. 73 shows the onset temperature calibration chart for the DSC equipment used within this thesis, using five substances ($C_{10}H_{16}$, Indium, Tin, Bismuth and Zinc). Table 22 represents the nominal and experimental temperature and the temperature correction.

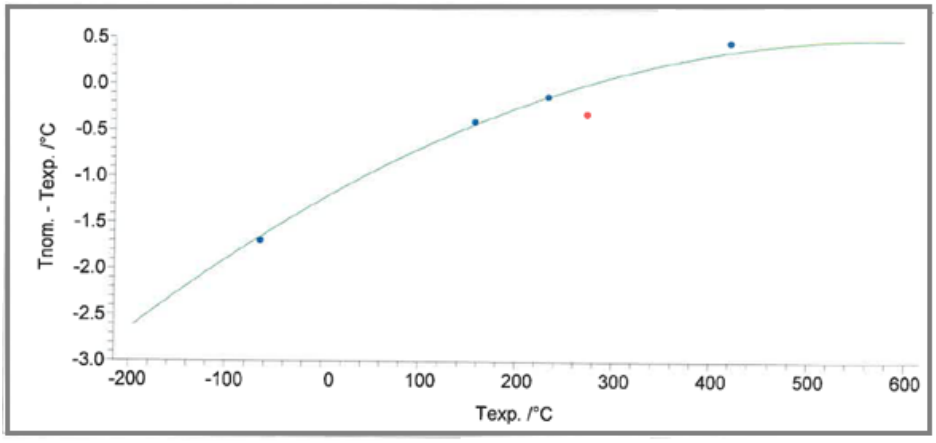

Figure 73: Temperature calibration chart for the DSC instrument.

Table 22. Nominal and Experimental melting temperatures for five calibration substances.

Substance	Temp. nom. (°C)	Temp. exp. (°C)	Mathematical weight	Temp. corr. (°C)
$C_{10}H_{16}$	-64.5	-62.8	1	-64.4
In	156.6	157	10	156.6
Sn	231.9	232	1	231.9
Bi	271.4	271.7	1	271.7
Zn	419.5	419	1	419.4

(ii) Sensitivity or Heat Flow calibration

As DSC instruments do not record the temperature directly at the sample, but through the crucibles via a thermocouple, this thermal resistance gives rise to a difference in the accuracy of measured and actual sample temperature, which affects the width of the measured peaks. A narrow peak and steep slope suggest proximity with the actual values [328]. The onset slope of the heat flow-temperature curve is used to calculate the value of thermal resistance [329]. Sensitivity calibration is carried out to determine the difference between the theoretically known and the observed values of heat or enthalpy of fusion for one or more standard materials. The ratio of these values is termed as a *Cell constant*. Fig. 74 shows the sensitivity calibration chart for the DSC equipment used within this thesis, using six substances ($C_{10}H_{16}$, Indium, Tin, Bismuth, Zinc and Caesium Chloride) as provided by the manufacturer while Fig. 75 demonstrates the physical usefulness of the calibration. Table 23 represents the heat of fusion, the experimental and calculated sensitivity of these substances.

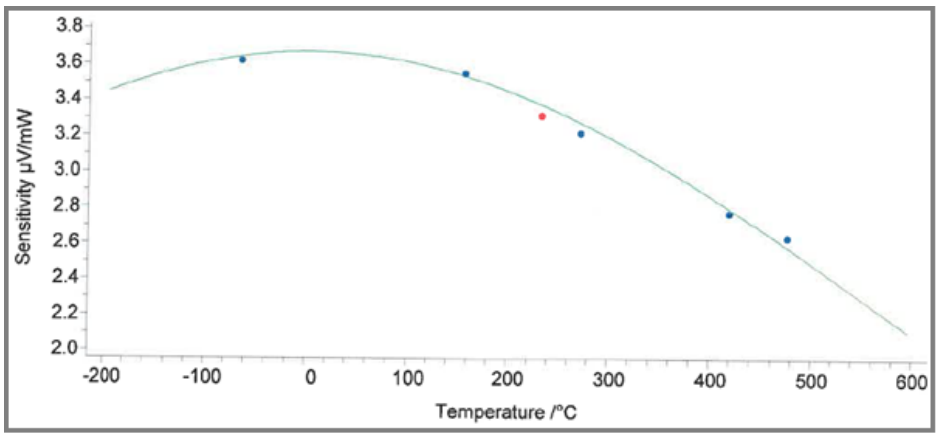

Figure 74: Sensitivity Calibration chart for the DSC instrument.

Table 23. Experimental and Calculated Sensitivity for six calibration substances.

Substance	Temp. (°C)	Enthalpy (J/g)	Peak Area (µV*s/mg)	Sensitivity Exp. (µV/mW)	Mathematical weight	Sensitivity Calc. (µV/mW)
$C_{10}H_{16}$	-64.5	22	79.577	3.617	1	3.642
In	156.6	28.6	101.53	3.55	10	3.537
Sn	231.9	60.5	200.451	3.313	1	3.382
Bi	271.4	53.1	170.987	3.22	1	3.28
Zn	419.5	107.5	298.048	2.773	1	2.801
CsCl	476	17.2	45.386	2.639	1	2.589

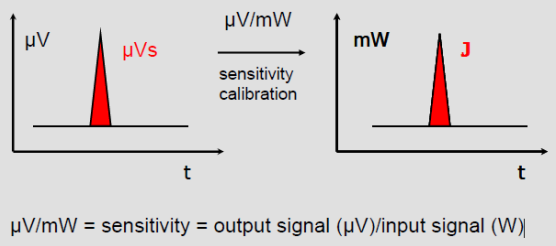

Figure 75: Schematic representation of sensitivity calibration [318].

4.4.4 Temperature program /thermal cycle

To ensure the samples underwent same thermal cycle of charging and discharging, the following generic thermal cycle was used: The samples cooled down to 0 °C from room temperature to standardise the beginning. After maintaining a 5 minute isotherm at 0 °C for achieving a uniform temperature distribution across, the samples were heated dynamically at the same rate to 75 °C followed by another 5 minute isothermal heating (Fig. 76). In the end, they were subjected to cooling cycle (75 °C to 0 °C) at the same rate. Emergency cut-off was set at 95 °C to avoid any accidental superheating failure.

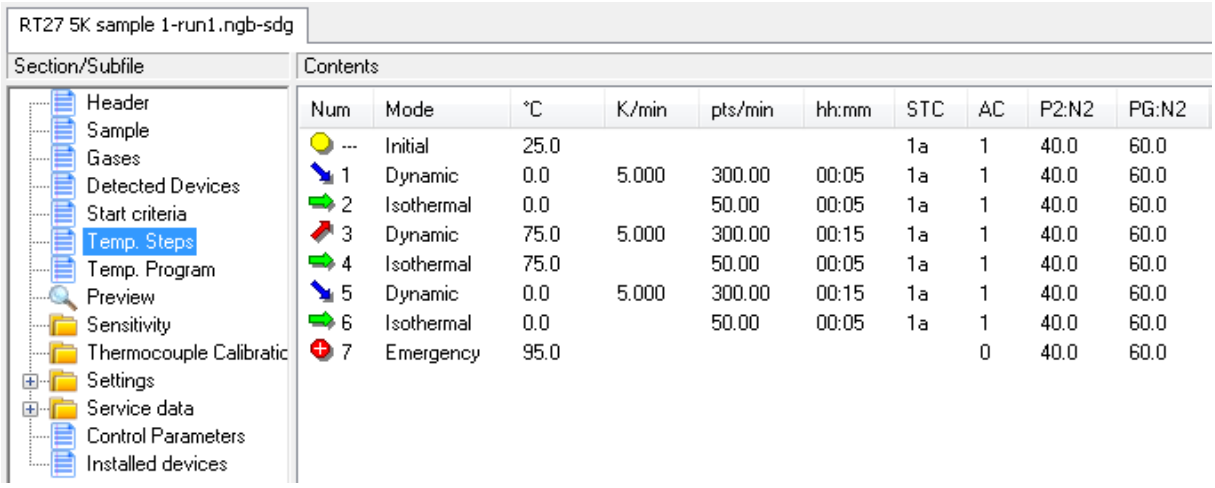

Figure 76: The set temperature program for the thermal cycle and the pictographically represented temperature steps.

The temperature range on the program was selected to ensure that the samples undergo complete phase change and their behaviour could be recorded for the entire range. Each sample underwent three heating and three cooling cycles using the same temperature program and the measurement data was averaged and tabulated. The first thermal cycle was used to ascertain more uniformity and homogeneity within the samples before characterisation. Therefore, the measured data, phase change behaviour and thermal analysis of the data obtained for this research work were based on the second thermal cycle onwards.

4.4.5 Measurement procedure

The *DSC 214 Polyma* instrument measurement window was opened in Expert mode and the desired measurement (baseline, sample + correction or sample) was selected. For running the measurements on the samples to determine melting temperature or heat of fusion, the following procedure was adopted (Fig 77):

(i) **Baseline run:** two empty crucibles of same mass, with one reference.

(ii) **Standard run:** one empty crucible and one with a standard material with known specific heat, of similar mass (a Sapphire disc) were used as a sample. However, the smallest Sapphire disc (Ø = 0.25 mm) with the least mass of 12.707 ± 0.005 mg, was selected for the experiments.

(iii) **Sample run:** one empty reference crucible and another with a known sample material and mass was used.

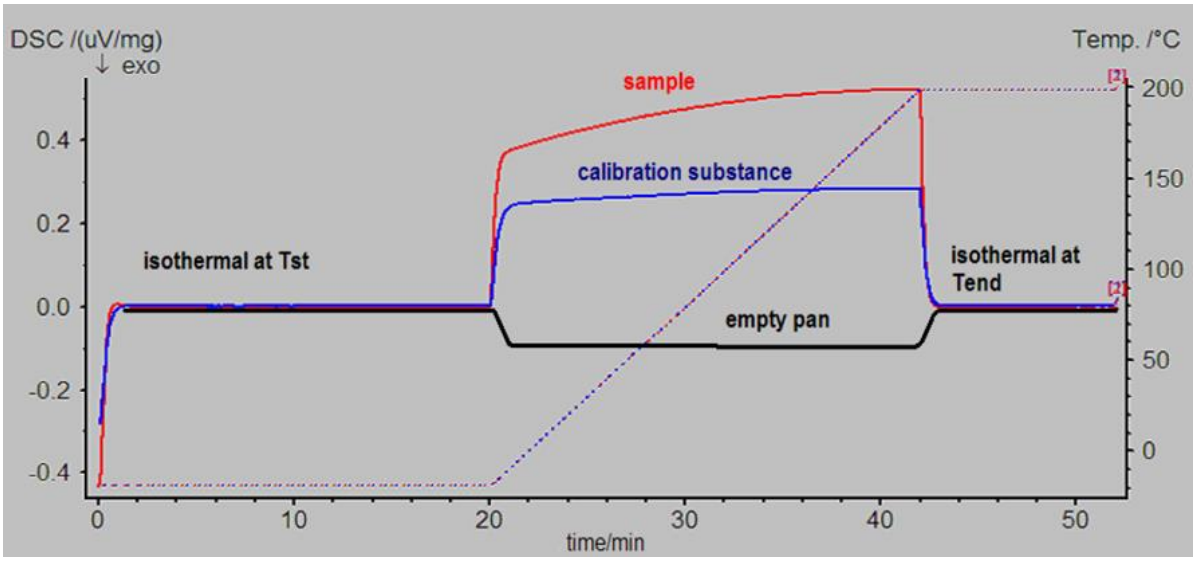

Figure 77*:* The various runs for sample measurement in a DSC [318].

4.4.6 Parameters

Material characterisation is imperative to correctly determine the thermophysical properties such as melting and congealing temperatures, and heat of fusion values for the PCM in use. Although within this thesis, only PCM charging side was employed for the experiments, which is mostly related to the melting characteristics, the PCM thermal analysis was carried out with an aim to determine both the melting and the solidification characteristics. Fig. 78 shows typical DSC thermograms for a PCM with the melting curve (in red) and the congealing or solidification curve (in blue). The signal (mW/mg) versus the corresponding temperature in °C is shown for the temperature range defined in the thermal cycle. The various important points on the curve, determining the material characteristics are highlighted by A, B, C, D, E and F. Once the curve is selected, options in the menu enable auto evaluation of Peaks, Onset, and Inflection and End temperatures.

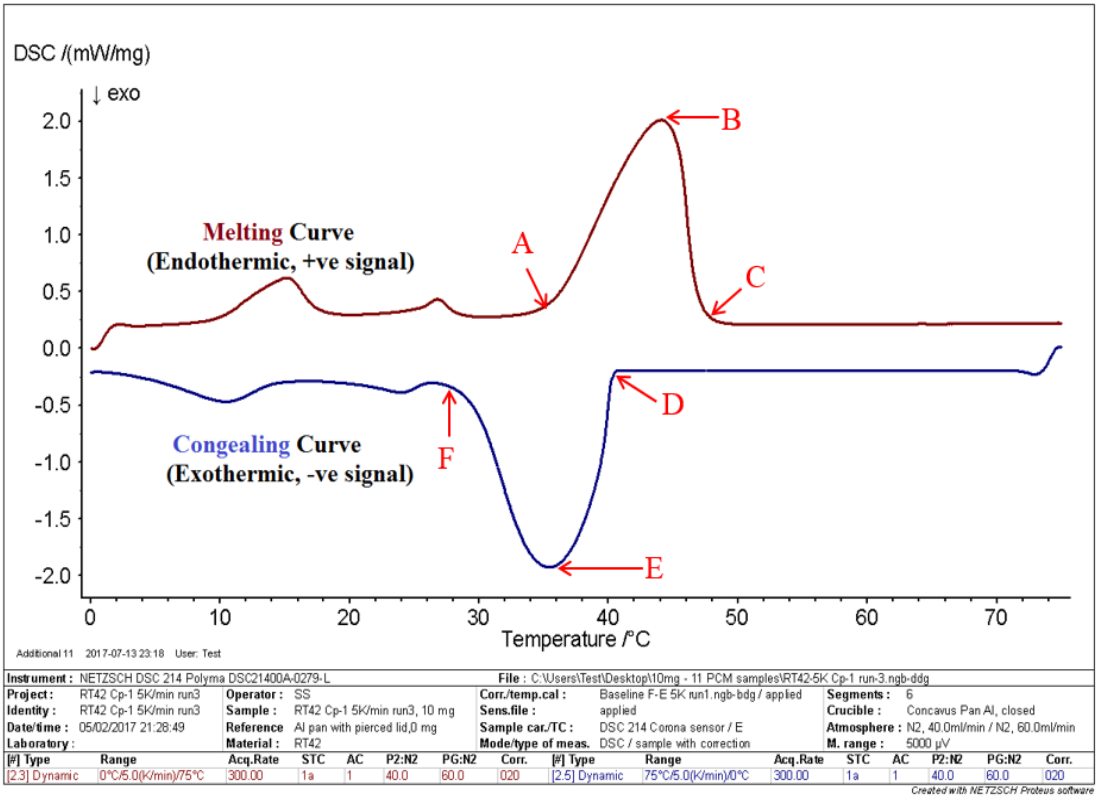

Figure 78: A typical DSC thermogram showing melting and the congealing/ solidification characteristic of a PCM. Highlighted by A, B, C, D, E and F are the various temperature points of importance.

The definition and measurement for the selected thermo-physical properties within this thesis are defined in the following paragraphs:

(i) **Melting Onset:** the onset temperature at which the phase of the material starts to change (point A in Fig. 78). It is also the intercept of the extrapolated slope of the melting curve and the continuation of the base line.

(ii) **Melting Peak:** highest point on the melting curve or the apex temperature of the solid-liquid transition, shown by point B in Fig. 78. Many authors [157] consider melting point as the peak temperature calculated from a DSC melting curve.

(iii) **Melting End:** the end point of the curve when it becomes a solid line again (point C). Some authors cite this as the real melting point of a substance, as melting phenomenon finishes here and all crystals turn to liquid from the solid state [330].

(iv) **Congealing/Solidification Onset:** the temperature during cooling cycle when the liquefied sample starts to solidify as given by Point D.

(v) **Solidification Peak:** this is the lowest point on the solidification curve or the apex temperature of the liquid-solid transition, shown by point E.

(vi) **Solidification End:** the end point of the curve when it starts to become fully solidified (Point F).

The following points were considered while taking these observations:

- For this thesis, the melting peak is the actual melting point of the substance.
- The width, i.e., the difference between the onset, and the end temperature of the solid-liquid transition indicate the carbon number distribution of the waxes [331], which are not studied. However, the temperature ranges for both melting and congealing cycles are studied to compare with the manufacturer data.
- The PCM temperature range was determined by the starting (Onset) and ending of melting/solidification throughout which the phase transition was in progress.
- The software of the temperature programme automatically determined the peak as the maximum (most positive) or minimum (most negative) values of the DSC signal during melting and solidification cycles respectively.

(vii) **Latent heat (L):** It is important to determine L of PCM because this determines the amount of heat that can be stored. On a specific heat -temperature curve, it is calculated as the area under the curve. Fig. 79 shows total latent heat capacity of the material between 10°C and 50°C (total cross-hatched area of 197.7 J/g) and the peak area (double cross-hatched area as 150.7 J/g).

(viii) Specific heat capacity (C_p): The C_p Ratio method was selected for evaluating C_p of the PCM samples. The two correction and sample runs were opened on the Proteus Analysis window using temperature scaling for the measurement (on X-axis). The appropriate dynamic heating segments on both runs were selected and sapp.nbs.cpe was highlighted. The three DSC curves, Baseline, Standard and Sample were selected and C_p curve was auto-calculated in a new window. As can be seen from Fig. 79, maximum or peak C_p was calculated as the value at the tallest peak (25.295 J/g/K). However, the baseline C_p for the material, which is provided by the manufacturers, can be given by the base C_p as highlighted in Fig. 79 (approx. 2.5 J/g/K).

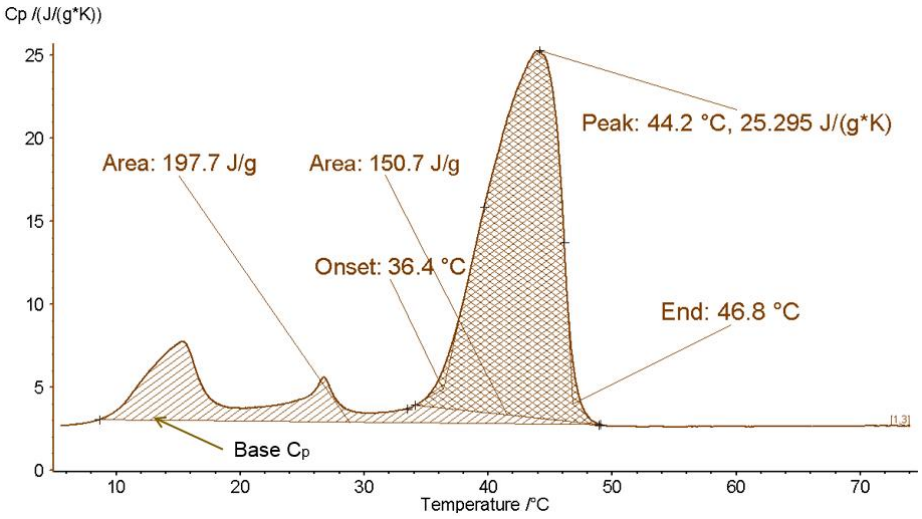

Figure 79: A typical DSC curve showing the L, Cp analysis for a PCM.

4.5 SEM analysis of PCM-I

To study the morphology of nanomaterial samples and to obtain the micrographs of n-PCM samples for studying the dispersion of nanomaterial within the PCM, *FEITM Quanta FEG 650* SEM was used. Samples of nanomaterial nano-CuO (60 nm) and n-PCM (RT42 enriched with 0.5 % w/w CuO) were tested. The nano-CuO samples were dispersed in 100% pure methanol magnetically stirred whereas the n-PCM samples were ultra-sonicated again before scanning them to enhance the dispersion and to avoid particle sedimentation thereby ensuring homogeneity in sample. The imaging process based on [320] is described here.

4.5.1 Sample preparation

The specimen was prepared on the stub that fits on top of the sample holder, using a carbon tape for adhering it. The stub was screwed into the end of the threaded rod (Fig. 80 (a)) after the specimens were filled on the prescribed carbon-coated stub (Fig. 80 (b)). The surfaces were blown using a nitrogen gun to remove any loose particles, which were then set-aside and inserted in the holder within the main chamber.

(a) (b)

Figure 80: (a) SEM sample stub in a sample holder and (b) carbon coated stub with n-CuO.

4.5.2 Venting and Loading

To minimize the time of exposure of the chamber to ambient air, it was vented while loading and unloading the sample as the contaminants and humidity can affect the quality of the sample images and increase the pump down times.

4.5.3 Imaging

The NavCam (navigation camera) was swung at 90° for activation and the stage was moved under the NavCam to capture the image. During images being taken, the WD was adjusted but a safe distance of 8 mm was ensured.

4.5.4 Venting and Unloading

The beam was turned off and the sample stage was lowered to the 10 mm mark before venting. The sample holder was removed and the chamber door was closed. The high vacuum button was clicked in order to pump the chamber again to high vacuum.

4.6 SEM analysis of PCM-II

Hitachi S3200N SEM-EDS by *Oxford Instruments* was used for high resolution imaging of PCM using gold sputtering in variable pressure mode. Capable of achieving a magnification of ~ 20 to 250000X, with a practical operational magnification of ~60,000X, it was selected as an alternative SEM equipment for overcoming electronic

charge accumulation observed in the PCM samples. At high voltages of the order of 1-5 keV, sufficiently high number of electrons are incident on the surface while at even higher voltages when the yield is lower, the excessive electrons are piled up on the sample (insulators like ceramics, polymers) surface, which if not conducted away, start to deflect the incoming beam, thereby producing distorted images [332]. Therefore, it is advised that the insulating samples be coated with extremely thin layers of a highly conducting material such as Gold or Platinum to improve their operation in high vacuum mode. Within this thesis, Gold-sputtering was performed as described below.

4.6.1 Gold-sputtering

On the *BioRad Sputter Coater*, using the *Polaron E5550* density thickness FTM unit the sputter coating of the n-PCM samples was performed with nano-layered gold coating. The PCM and n-PCM samples were inserted in the specimen chamber under vacuum. The pump pressure was set to slightly over 10^{-1} mbar, gold density to 19.3, and the thickness range to 10 nm. The input electrical current was set below 20-15 mA, while the voltage was set to 2 kV before pressed *start* on the FTM box. The thickness was displayed and when the required value was reached, the process was stopped using the *stop* button on the FTM box. The gold-sputtered n-PCM sample is shown in Fig. 81.

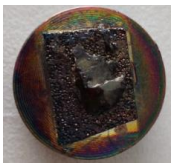

Figure 81: Gold sputtered n-PCM on the sample stub.

4.6.2 Imaging

The imaging process followed is described here [320]:

(i) Checking Initial Settings

Stage controls set to: X=30, Y=20, Z=exchange position, tilt=0, contrast and brightness (min), magnification (max), high Vacuum mode (yes) and no aperture.

(ii) Selecting a Vacuum Mode

The low vacuum mode was selected for the PCM samples and high vacuum mode for the nanomaterials due to the ease of imaging [333].

(iii) Preparing the Specimen

The sample preparation process was similar as above where in the specimen (sample holder holding the stub with the sample) was inserted into the sample stage and using the *ChamberScope* and detector was inserted following this to ascertain that it will not touch the detector. The height was adjusted as a 23 mm of WD.

(iv) Inserting the Samples

The Z-stage control was set to the exchange position and the chamber door was held tightly till the vacuum system started pumping. When the vacuum gauge displayed 9 x 10^{-5} Torr, the system was considered ready for use.

(v) Focussing the sample area and Image capturing

Using the focus knob, many hit and miss iterations for the optimal focus were required to produce the best possible imaging. For removing stretching effect in the images, astigmatism correction process was used as described in section 5.5.3. Using the X and the Y *stigmator* control knobs, the apparent focus in the image and the image details were improved. The contrast and the brightness were adjusted by means of the signal monitor *S*. The stigmator adjustment was checked for astigmatism correction every time the instrument focused was changed. The control panel on the image-capturing software is shown in Fig. 82. To save the digital micrographs from the samples, *Revolution* software was used in the Survey mode.

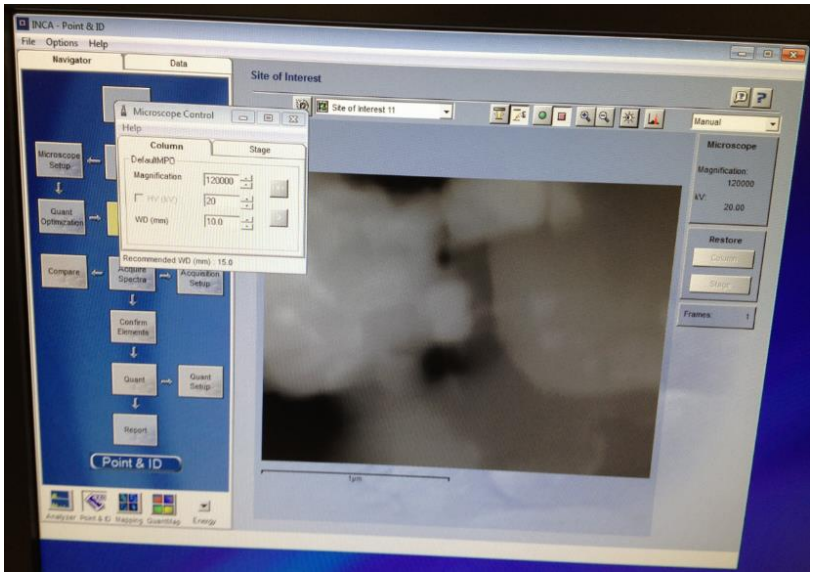

Figure 82: Control panel setting for micro graphing the gold-sputtered PCM samples.

4.7 XRD analysis of PCM/Nano-material

X-ray diffraction is used to determine the composition of the constituents in a sample semi-quantitatively by comparing the intensities of the diffraction peaks from the known phases [334]. Further, for complex mixtures with more than two phases (even if one amorphous), XRD can still be useful for determining the relative amount of each phase. The chemical composition of the PCM GR 42 and the purity of 60 nm nano-CuO were tested using XRD technology, based on crystallographic study of the material. Both these materials were outsourced and the manufacturers for PCM were unable to comment on the composition or the reactivity with PCM or nanomaterial. XRD proved a useful tool for identifying the constituents. Also, as it is considered as a good practice to verify the purity of the nanomaterial, XRD analysis of nano-CuO was performed, although manufacturer supplied data suggested > 99 % purity. *Siemens D5000 Powder Diffractometer* was set to work on a 40 kV, 30 mA, and 50 Hz electrical signals. The data output was in the form of spectra with identified phases representing minerals in the sample. The process for using the XRD is described below.

4.7.1 Sample preparation

As nano-CuO was supplied as 60 nm average particle size, it was used as it was while GR42 as uneven coarse material (Fig. 83 (a)) was grinded using a tungsten carbide ring mill. Using *Normal Mount* method, approximately 5 g of powdered sample was loaded into the XRD holder using a clean spatula to spread it evenly. The sample holder (Fig. 83 (b)) was numbered to ensure the location in the machine was tallied with the sample number. The powder was packed down while avoiding orientation using the narrow edge of the spatula. A glass plate was used to smoothen the powder surface until it became completely flattened and levelled with the top of the sample well (Fig. 83 (c)).

(a) (b) (c)

Figure 83: (a) Textures of Granular PCM GR42 compared to Organic PCM RT42, (b) annular sample holder marked with sample number and (c) glass on top for pressing.

The excess powder was brushed off gently from the sides to avoid contamination in the machine. The sample name and the grey sample holder number were logged in the book for reference.

4.7.2 Software program

The XRD commander program was opened and the default location to save the data files was added to the program before adding the input job title and the sample identification details using the *Create jobs* icon at the top of the screen.

4.7.3 Data interpretation and Analysis

The scanned file was opened on *EVA* software, and the profile was loaded. Using the search/match toolbar, the following path was followed *favour simple patterns → mineral*, to check the yellow quality marks and the *structure* selected. Then, also on the *main database* displaying *master*, search utility was used to process the peak-searching for matching the minerals in the samples and generating the list of probably matching mineral data. On the *toolbar*, the *pattern* tab displayed a list of minerals, from which each mineral was picked one by one to see if their peaks match on the sample profile. Non-matching samples were deleted and the steps were repeated to identify other peaks. The disturbances in the signals or noise in the profiles were removed by replacing the *background* and the analysed profile was saved as an *EVA* (or raw data) file**.**

4.8 Conclusions

While the manufacturing and fabrication processes have been discussed in the previous chapter, the experimental procedures for characterisation of BICPV and BICPV-PCM systems have been discussed here, focussed around thermal and electrical aspects. The three different BICPV-PCM systems, based on varying concentrator designs, were electrically and thermally characterised. The micro-finned-PCM system was only characterised for its thermal behaviour as the solar cells were replaced by an external electrical power supply emulating the BICPV temperature. A range of electrical parameters; short-circuit current, open circuit voltage and maximum power point were studied for the systems as well as the temperature under the PV back plate and other locations. For electrical characterisation, the collimated beam from the solar simulator at selected solar radiation intensities were used while the BICPV systems were set at a horizontal plane under the down shine type solar simulator. The electrical performances

were monitored using an I-V tracer and a multimeter/data acquisition system. The reference solar cell was used to calibrate the light flux of the simulator. For temperature measurements, K-type thermocouples were used in connection with either a handheld or stationary temperature recorder. The electrical conversion efficiency for the BICPV was calculated, first without and then with the use of PCM by incorporating them in the PCM containment at the rear of the BICPV. The thermocouples placed at the back-plate captured the temperature data.

The thermophysical properties of the PCM and n-PCM, were explored using DSC techniques to assess their melting and congealing temperature ranges, latent heat and specific heats in certain cases. For obtaining the micrographs of nanomaterial and n-PCM, SEM was used with the aim to explore surface morphology and distribution. The first images of n-PCM were of inadequate quality and clarity. To improve this, samples were sputtered with a gold metal nano-layer before imaging them for the second time using different facilities. The purity of the nano-material and the composition of a granulated PCM were analysed using XRD. The processes for operating these instruments; from sample preparation through to data collection and analysis has been discussed. The chemical imaging and mineralogical analysis department, Camborne School of Mines, a part of the University of Exeter, provided XRD facility. The next chapter will detail the observations and the outcomes, centred on the experimental results and based on the procedures explained in this chapter.

Chapter 5. Results and Discussion

This chapter presents the results of indoor electrical and thermal characterisation for each BICPV-PCM system. The results are presented in graphical or tabulated forms and include a comparison of the electrical parameters such as open circuit voltage (V_{OC}), short circuit current (I_{SC}), maximum output power (P_m), and electrical efficiency along with the temperature data. The plots for the measured data are plotted against the elapsed time that begins when the solar simulator was switched on. The results and benefits for introducing combined passive thermal management using micro-fins, PCM and n-PCM are discussed. The results of investigating the thermophysical analysis of the PCM using DSC, the material characteristics studied using SEM and the composition of granulated PCM discovered using XRD technology are also presented. Moreover, simultaneous minor investigations on the effects of irradiance, thermal conductivity and PCM type on thermal management of BICPV and the effect of using 3D printed PCM containment on leakage control are discussed. A very brief cost-benefit analysis, where appropriate, has been produced for the micro-finned PCM/n-PCM systems. A new analytical model for BICPV-PCM system was proposed as inaccuracies were found in the previously repeated PV-PCM model. In discussions, the major findings from the experimental results, their meaning, importance of the findings, and reasons are presented. This includes any extrinsic or intrinsic circumstances, features or limitations of the experimental set up.

5.1 Introduction

Extensive indoor characterisation was undertaken for the fabricated BICPV-PCM modules, using a range of incident solar radiation intensities supplied by the solar simulator. The electrical performance for the modules such as I-V and power curves were measured and compared. The investigated systems are discussed below:

(i) LACPC based BICPV system
(ii) SEH based WICPV system
(iii) Micro-finned thermal system
(iv) SEH based BICPV system

The systems were characterised for thermal behaviour in the horizontal direction across the back plate in cases (i), (ii) and (iv) while in vertical direction in (iii) to explore the distribution of heat across the system. The results were analysed both qualitatively and

quantitatively. In all cases PCM and n-PCM limited the temperature rise in BICPV to an appreciable degree. Other notable effects with PCM usage such as reduction in hot spot formation and more uniform temperature distribution across the back plate were discovered. The fundamental analytical model available in the literature for a PV-PCM system was challenged due to the detected incongruences in its dimensional analysis. Therefore, a revised model has been proposed for the BICPV-PCM system. Additionally, a brief cost analysis model for the system have been presented.

The opportunity of integrating a passive micro-cooling system with the back plate of a BICPV module was also investigated. After an initial investigation in case (iii), micro-fins were found to be beneficial in terms of heat transfer as well as reduced material usage. Experimental set-up was validated using simulation and uncertainty analysis has been reported for this case. The results from these original experimental investigations were analysed to understand their suitability on a real-world level. This chapter also presents the results from the evaluation of the thermophysical properties of various PCM and n-PCM, such as melting point (onset, peak and end), congealing/solidification point (onset, peak and end), Latent heat capacity, and Specific heat capacity using DSC. A list of different PCM types were analysed since they are envisaged as being useful for related future works. An attempt was made to study the morphological features such as shape and structure of the outsourced nanomaterial and n-PCM using SEM, the micrographs from which are added to this chapter. The particle purity based on material composition was assessed using XRD technology for granulated PCM, GR 42 and the metal oxide based TCE nanomaterial (nano-CuO) has been expressed as diffractograms.

5.2 Characterisation of BICPV-PCM system

(i) Electrical Characterisation

The short-circuit current (I_{SC}) and the open-circuit voltage (V_{OC}) are the two fundamental parameters of the I–V curve for a PV module. Both I_{SC} and V_{OC} are dependent on the incident irradiance and module temperature in such a way that change in I_{SC} and irradiance are almost directly proportional while change in V_{OC} is only nominally dependent. On the contrary, V_{OC} is inversely proportional to the module temperature causing significant reduction in electrical power at higher temperatures even though I_{SC} increases slightly with temperature [335]. The P_m and η are dependent on the I_{SC} and V_{OC}.

The following sub-sections detail the results derived from the I-V trace obtained for different BICPV modules with and without PCM.

(ii) Thermal Characterisation

The main aim of the work was to improve thermal management of BICPV, the results from the thermal characterisation are presented in the sub-sections below to display the behaviour of the system under different irradiances. The four different systems were characterised first without any cooling media and then passively using PCM, n-PCM or a combination of them with the micro-fins. In one case, tests were performed using water as a passive cooling means to compare the relative effectiveness of the latent and sensible media. In all systems, the thermocouples were attached at various locations under the back-plate and within the PCM containment. The curves represent the temperature obtained (in $^{\circ}$C) with respect to the time elapsed since illumination began.

5.2.1 LACPC BICPV-PCM system

(i) Electrical Characterisation:

The LACPC based BICPV-PCM module was illuminated under the solar simulator at 1000 Wm^{-2} irradiance for a period of 145 min. I_{SC}, V_{OC} and P_m curves versus elapsed time for the BICPV system under natural convention and with PCM, were obtained as shown in Fig. 84 (a), (b) and (c) respectively. With the use of PCM, less reduction in both V_{OC} and P_m were observed due to the inverse temperature relationship, while I_{SC} showed a proportional nominal decrease. The average V_{OC} increased by 5.6 % from 2.49 V without PCM to 2.63 V with PCM. At the start of the experiments, the voltage improvement was only slightly higher in the BICPV-PCM system, which continued to increase as time progressed and similar behaviour was observed for P_m. The value of P_m with PCM surpassed the value without PCM after 15 min from the start. Similar to fluctuations in Tc, P_m decreases sharply with PCM in the first 30 min (60 min without PCM) and stabilises later as the PCM starts absorbing excess heat. The melting temperature range of the PCM used for the experiment could effect this duration. After 70 min, P_m stabilised (fluctuation < 8 mW) for the rest of the duration with PCM while without PCM, P_m stabilised for a while after 70 min and then started reducing further after 110 min (Fig. 84 (c)). Overall, the average P_m without PCM was 581.7 mW while with

PCM, it was 626.4 mW showing a relative efficiency increase of 7.68 %. The absolute electrical efficiency for the module without PCM was 6.48 % whereas with the use of PCM in the system, it increased to 6.98 %. In Fig. 84 (d), a comparison has been made between the percentage changes in P_m at a frequency interval of 30 min, negative values indicates a decline over a period of time. As can be seen, during the first interval, the BICPV experienced an 18.6 % (10.0 % with PCM) electrical power loss. Similarly, during the second interval, the output power reduced by 4.6 % (1.2 % with PCM). In both the cases, power loss after 60 min was nominal, especially with the use of PCM. As can be observed from Table 24, the minimum output P_m using PCM was almost 17 % higher than that without PCM.

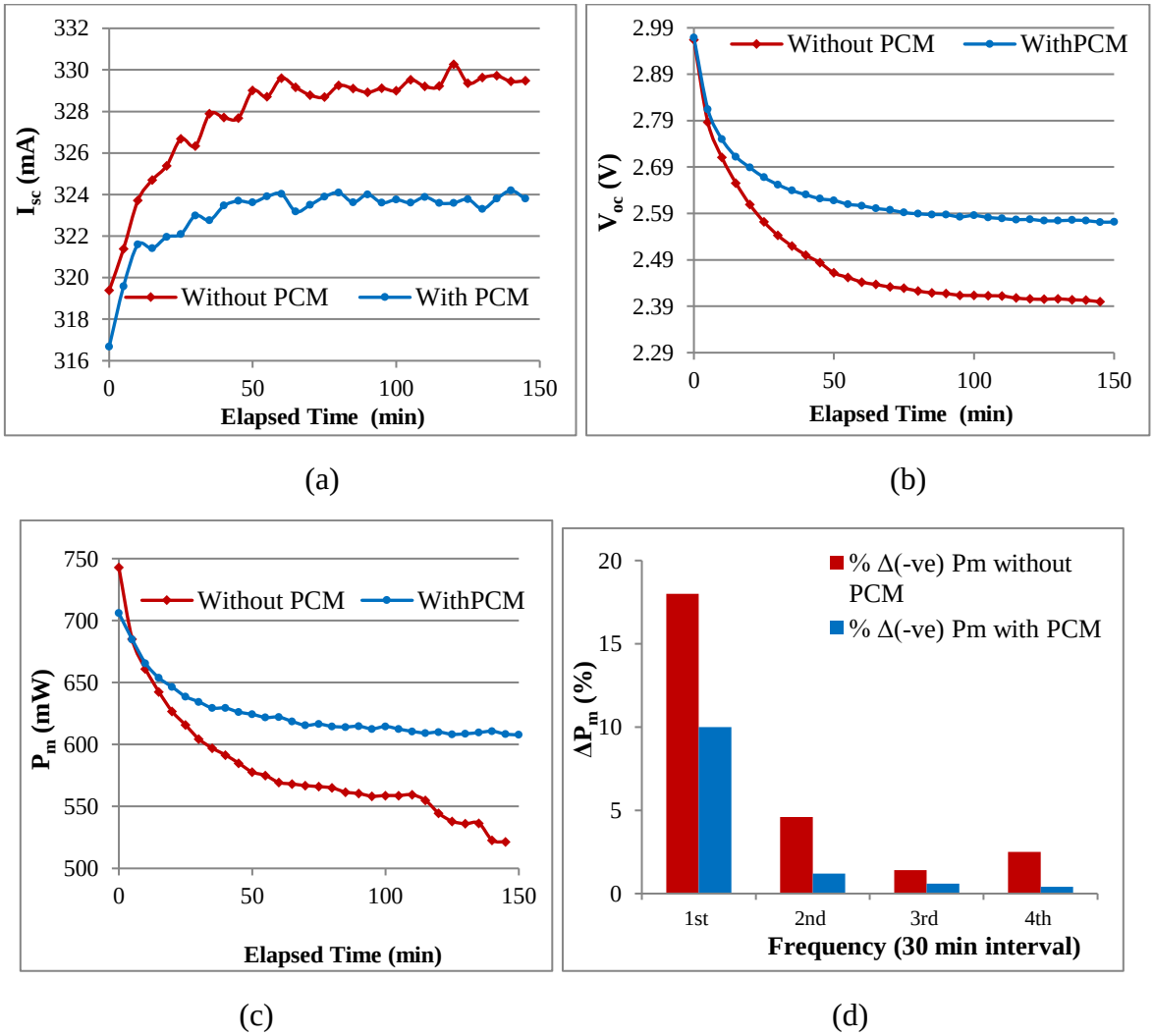

Figure 84: Comparison of BICPV parameters with and without PCM (RT42) versus time (a)I_{SC}, (b)V_{OC}, (c)P_m, (d) percent change in Pm at a frequency interval of 30 min, (Inclination: 0°, 1000 W m^{-2})

Table 24. Important experimental data from the BICPV-PCM system output at 1000 Wm^{-2}. (Negative sign indicates increase in the parameter value with the use of PCM).

	$I_{SC, Min}$ (mA)	$I_{SC, Max}$ (mA)	$V_{OC, Min}$ (V)	$V_{OC, Max}$ (V)	$P_{m, Min}$ (mW)	$P_{m, Max}$ (mW)
Without PCM	319.4	329.7	2.4	2.96	521.5	742.9
With PCM	316.6	324.2	2.6	2.97	608.4	706.0
Change (%)	0.9	1.7	-8.3	-0.3	-16.7	5.0

The maximum value of $P_{m,}$ was however higher for the non-PCM case (by 5 %) due to the lower ambient temperature at the start-up. There was a nominal decrease of less than 1 % and 2 % respectively in the minimum and the maximum $I_{SC.}$ Experimentally, it was verified that an increase in module temperature leads to decrement in (P_m) within the aluminium (thermal conductor) backed module.

5.2.1.1 Effect of irradiance

The effect of increased irradiance on the electrical output parameters and consequently the effectiveness of PCM for the LACPC based BICPV-PCM system was the focus of this study. The experiment as described in the previous section was repeated for 120 min at various intensities of 500 Wm^{-2}, 750 $Wm^{-2}$and 1200 Wm^{-2}. The effects of increasing irradiance on PCM effectiveness in terms of I_{SC}, V_{OC} and P_m profiles are illustrated in Fig. 85 (a), (b), (c) respectively. The relationship was almost linear between an increase in irradiance and the output Isc and P_m, however, this relationship wasn't directly proportional, especially at higher intensities with PCM. After an hour of running the experiment, P_m remained stable for the rest of the duration with PCM while without PCM, P_m stabilised for a while after 80 min but then started declining further (Fig. 85 (c)). The relative increase (calculated as a percentage figure) in electrical power using PCM with the BICPV system were 1.15 % at 500 Wm^{-2}, 4.20 % at 750 Wm^{-2} and 6.80 % at 1200 Wm^{-2}. Notably, at 1200 Wm^{-2}, the P_m increase with PCM was about 1 % lesser than that at 1000 Wm^{-2}, the reason for this could be inadequate PCM material thickness as well as the chosen PCM melting range. The absolute average comparisons of $P_{m,}$ I_{SC} and V_{OC} without and with PCM are plotted in Fig. 85 (d), (e), and (f). The percentage increase in V_{OC} (decrease in I_{SC}) with PCM were calculated as 1.6 % (-1.3 %) at 500 Wm^{-2}, 2.4 % (-0.5 %) at 750 Wm^{-2} and 3.9 % (-3.8 %) at 1200 Wm^{-2}.

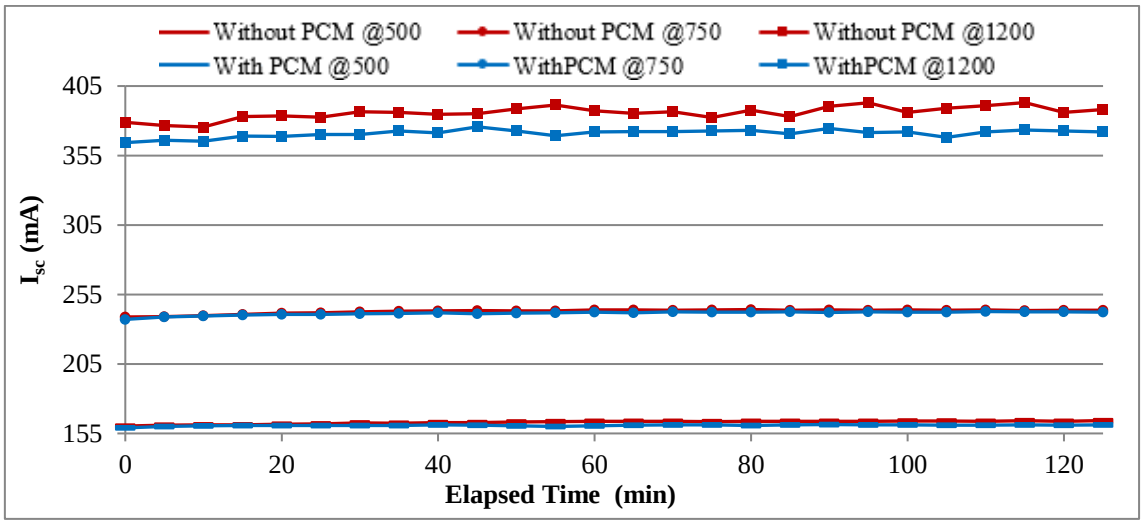
Without PCM @500
Without PCM @750
Without PCM @1200
With PCM @500
WithPCM @750
WithPCM @1200
405
355
305
255
205
155
I_{sc} (mA)
0
20
40
60
80
100
120
Elapsed Time (min)

(a)

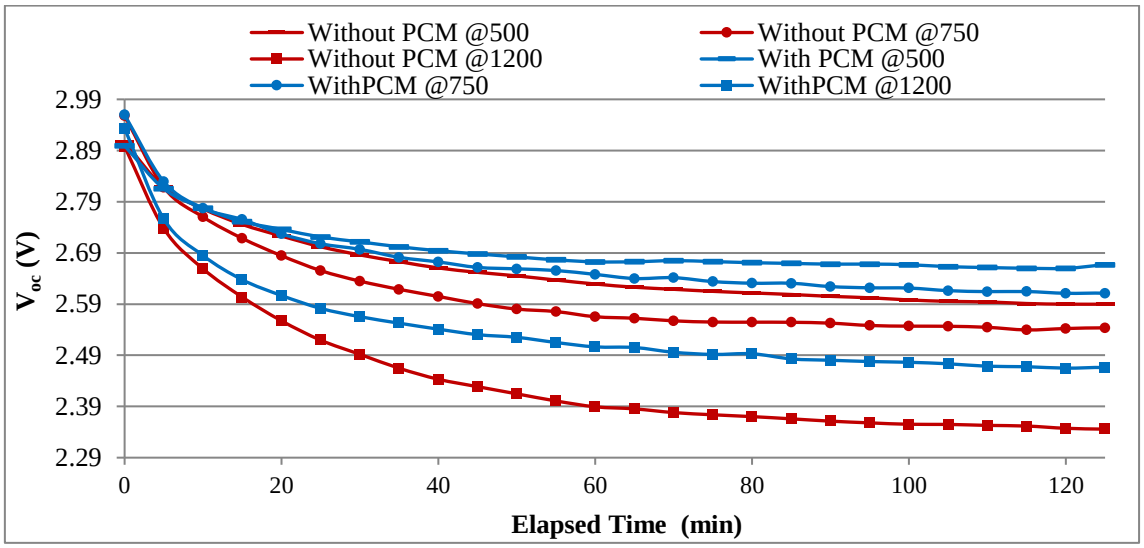
Without PCM @500
Without PCM @750
Without PCM @1200
With PCM @500
WithPCM @750
WithPCM @1200
2.99
2.89
2.79
2.69
2.59
2.49
2.39
2.29
V_{oc} (V)
0
20
40
60
80
100
120
Elapsed Time (min)

(b)

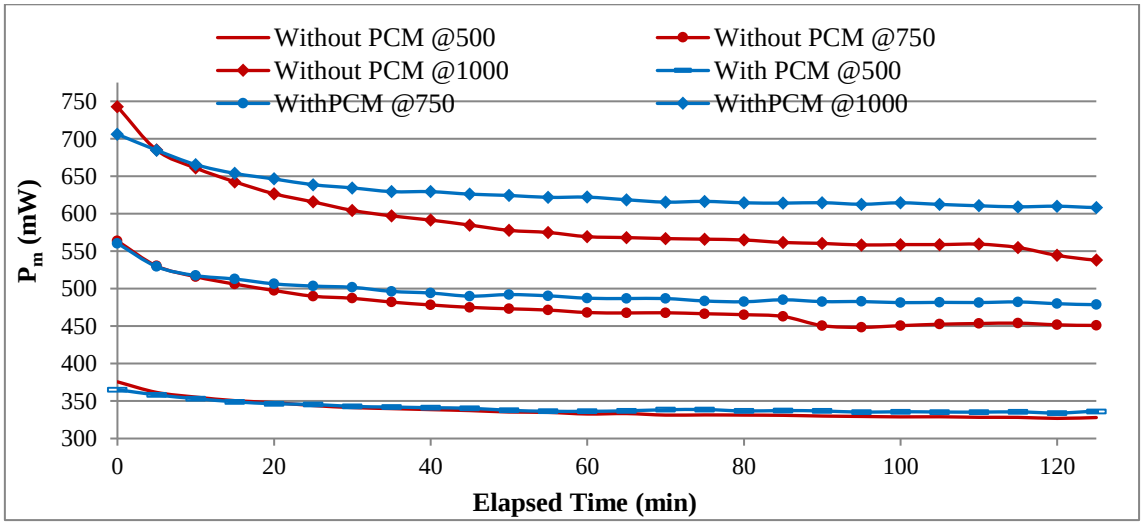
Without PCM @500
Without PCM @750
Without PCM @1000
With PCM @500
WithPCM @750
WithPCM @1000
750
700
650
600
550
500
450
400
350
300
P_m (mW)
0
20
40
60
80
100
120
Elapsed Time (min)

(c)

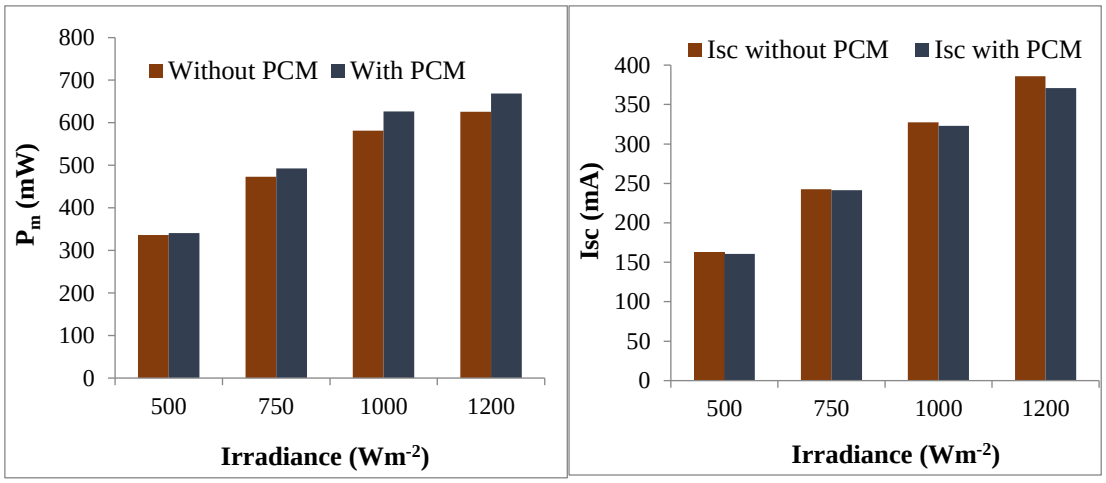

(d)

(e)

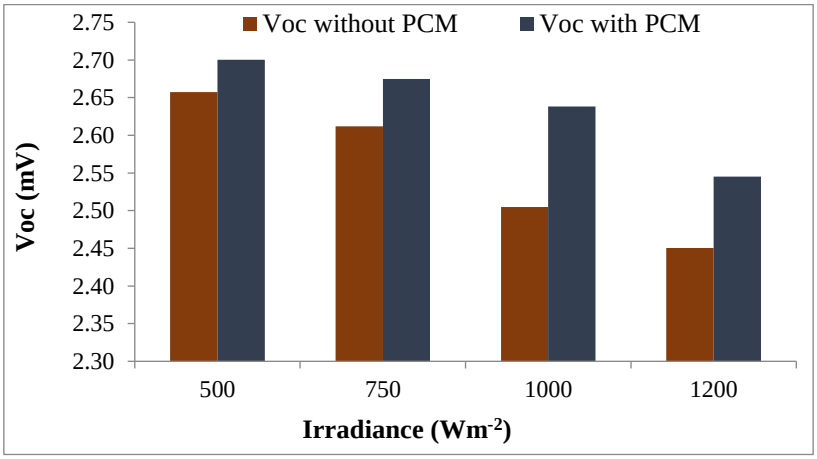

(f)

Figure 85: Comparison of electrical parameters at various intensities with and without PCM: (a) I_{SC}, (b) V_{OC}, (c) P_m at 500, 750, and 1200 W m-2 and average values in (d) P_m, (e) I_{SC} and (f) V_{OC} at Inclination: 0°and Intensities: 500, 750, 1000 and 1200 W m^{-2}.

The results indicated that this particular PCM had a more pronounced effect for lower to medium intensities and was comparatively less effective for higher levels of irradiance which may be due to lower melting temperature range of the PCM corresponding to heat generation in the BICPV panel at those intensities.

5.2.1.2 Effect of melting temperature range of PCM and insulation

To study the effect of melting temperature range, another PCM, RT55 was used in the set up. For the system, with 8 cells in series, it was found that the P_m without any heat sink/PCM arrangement was 625.8 mW, while with PCM RT55 it increased to 647.1 mW at 1000 Wm^{-2}, thereby showing an average increase by 4.1 %, (3.7 % lesser than a PCM

with lower melting temperature range, RT42). In addition, to examine the negative effects of inappropriate ventilation, the BICPV back plate was insulated with a glass wool of less than 1 cm thickness. The insulated system showed an average P_m of 611.7 mW, reducing the power output by 2.3 %. The profiles for P_m using different backing materials with the module is compared in (Fig. 86). As expected, the absence of thermal regulation (presence of insulation) proved detrimental to the efficiency of BICPV system, in this case by a small percentage for a small period of time.

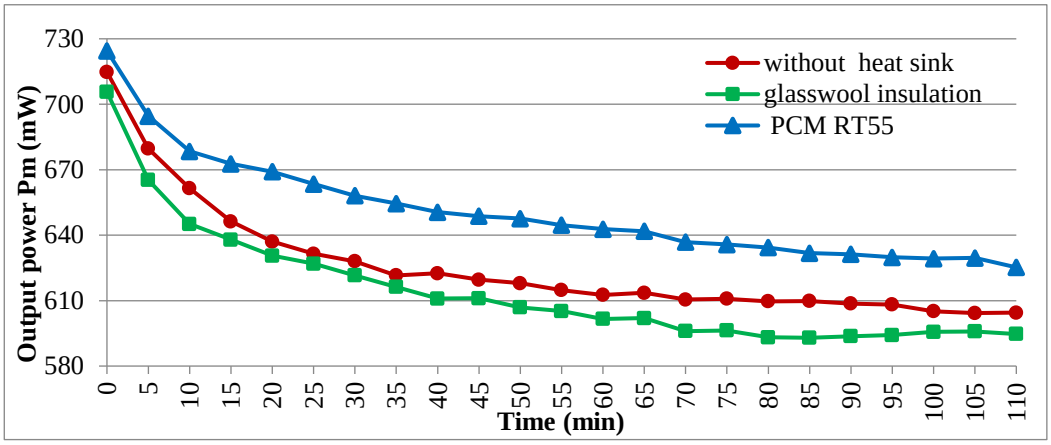

Figure 86: P_m profile at 1000 Wm^{-2} with and without PCM RT55 and insulated back.

5.2.1.3 Effect of thermal conductivity

Following the studies on the effect of thermal insulation, it was envisaged to study the benefits of enhancing the thermal conductivity of PCM. The simplest way to achieve this initially was by introducing a metallic (copper) mesh. The results obtained by comparing the maximum power output profiles at 1000 Wm^{-2} are presented in Fig. 87.

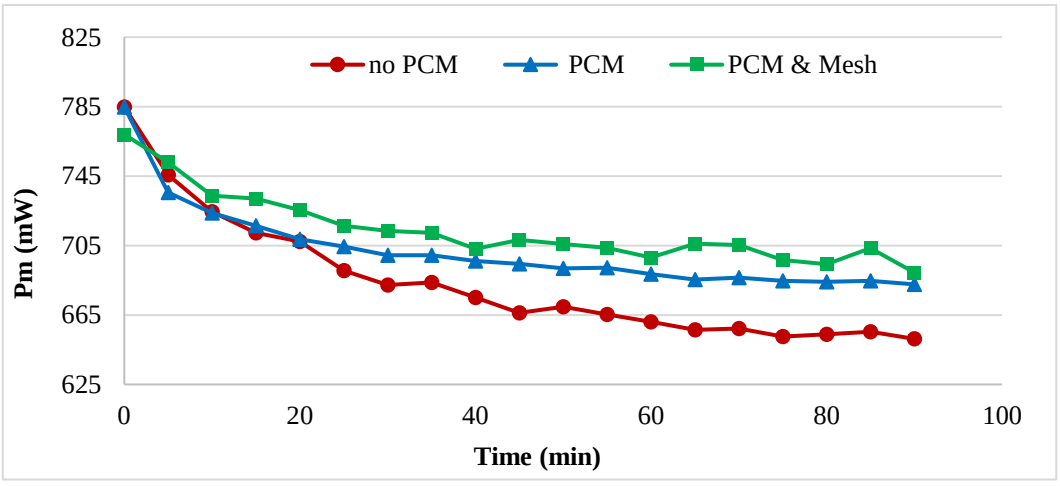

Figure 87: P_m profiles compared with PCM and enhanced PCM (1000 Wm^{-2}).

The initial values for P_m vary nominally due to a variation in ambient temperature which was outside of experimental control as well as slight degradation in module efficiency. Under 90 min of illumination, the presence of PCM increased the average P_m by 2.1 %, while PCM with copper mesh improved the average P_m by 3.9 % as compared to the case with no use of PCM. Hence, the effectiveness of the mesh was 1.8 % higher with respect to PCM. The respective V_{OC} decreased over this period as shown in Fig. 88. The system with PCM showed a 4.8 % increase in the average V_{OC} and a 4.1 % rise with PCM and copper mesh compared to no applied PCM. The Isc decreased by 15.5 % for PCM and 2.1 % with PCM and copper mesh. There was a 1.7 % increase in the average P_m by introducing the metallic copper mesh, so the initial experiment to determine the merits of TCE in BICPV proved successful.

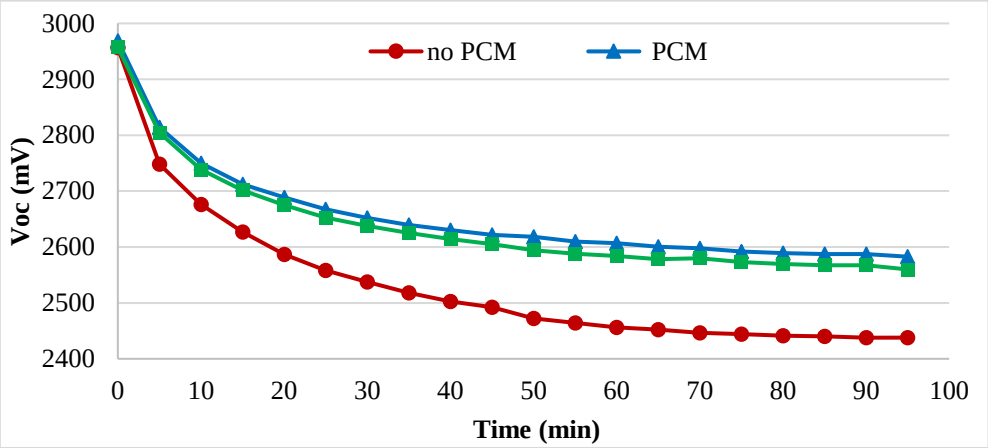

Figure 88: V_{OC} profiles compared with PCM and enhanced PCM (1000 Wm^{-2})

(ii) Thermal Characterisation:

In the LACPC based BICPV system, the temperature at the centre of the module (T_c) was recorded under the plate at an interval of 5 min for four levels of irradiances; 500 Wm^{-2}, 750 Wm^{-2}, 1000 Wm^{-2}, and 1200 Wm^{-2}.The temperature profiles for T_c and the average temperature at various irradiances is shown in Fig. 89 (a) & (b) resp. A comparison has been drawn between BICPV temperature without PCM (patterned red bar) and with PCM (solid blue bar) . Absolute average T_c at 500 Wm^{-2}, 750 Wm^{-2}, and 1200 Wm^{-2} showed a decrease from 36.3 ˚C to 31.5 ˚C (13.2 %), 43.8 ˚C to 33.7 ˚C (23.1 %) and from 54.2 ˚C to 47.6˚C (12.2 %) respectively with the use of PCM RT42. Comparing the average T_c reached at 1000 Wm^{-2} by the BICPV without PCM (50.1 ˚C) to that with PCM (46.3 ˚C), it was established that the use of PCM reduced the average temperature by 3.8 ˚C (7.6 %).

The maximum T_c (49.2 ˚C with PCM and 55.2 ˚C without PCM) was 3 ˚C higher than the average T_c with PCM and 5 ˚C without PCM suggesting more thermal disequilibrium in the system without PCM. The percentage change in T_c for every subsequent every 30-minute period of illumination is shown in Fig. 89 (c) to compare the relative temperature increase per quarter of the 2 hour experiment. It can be seen that during the first 30 min of starting the simulator, the temperature at the BICPV centre without PCM increased by 33 ˚C (24 ˚C with PCM) from the ambient. Similarly, during the second 30 minute interval, T_c increased by 4.5 ˚C without PCM (0.6 ˚C with PCM). In both the cases, the increase in temperature after 60 min was only nominal, more so with the use of the PCM.

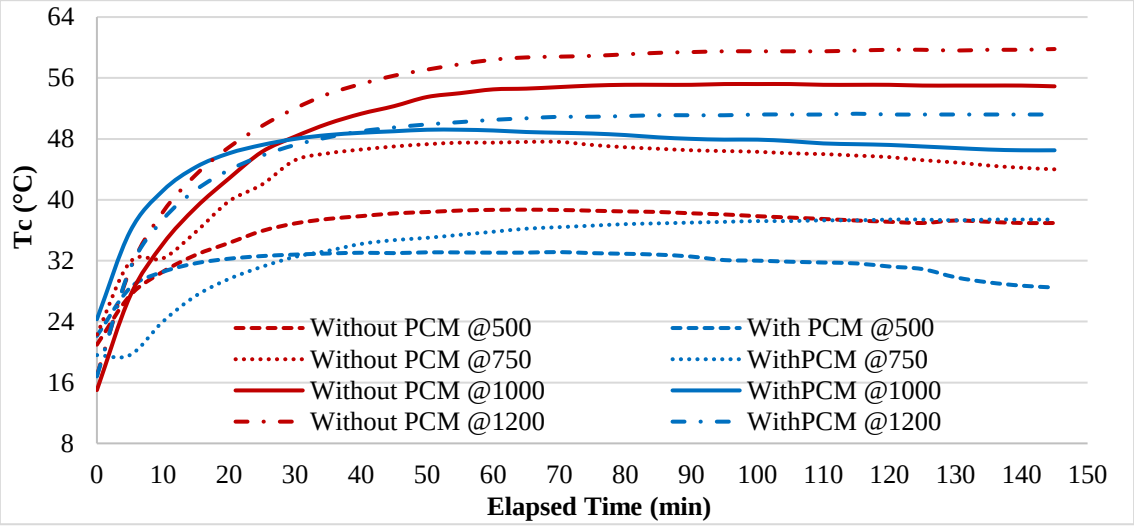

(a)

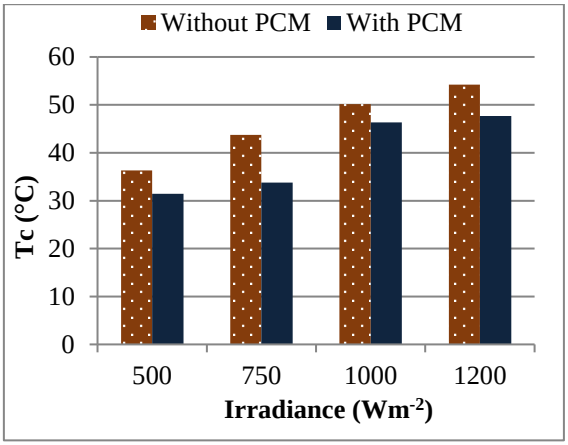

(b)

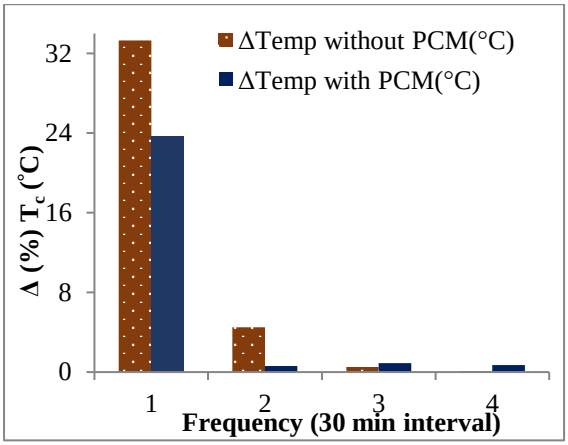

(c)

Figure 89: For the BICPV module with and without PCM RT42: (a) Temperature profile, (b) absolute average at 500, 750, 1000 and 1200 Wm^{-2} and (c) change in T_c (%) every 30-minute interval at 1000 Wm^{-2}.

The melting range of the PCM, 38-43 ˚C, which was slightly lower than the temperature at which the BICPV module temperature becomes nearly constant (46.5 ˚C) attained towards the end of the experiment. The bottom plate of PCM containment was fabricated with Aluminium to measure the extent of heat available after the complete melting of the PCM on the end opposite to the BICPV. This was aimed to gauge whether the heat could be used for other regeneration purpose such as domestic water heating. If successfully exploited, it could further improve the overall system efficiency by contributing in thermal processes in addition to the already realised electrical efficiency improvement. So far, a maximum temperature rise of 4 °C in the centre of the bottom plate with 24.4 °C as the average temperature could be realised which may be increased by running the experiments for longer than 2 hour. A highly non-uniform temperature distribution was also observed within the BICPV without PCM. Relatively higher temperatures were recorded under the centre while temperatures were lower towards the edges and lowest in the corners of the module. This could be attributed to the edge effect or end losses due to interfacing with the surroundings. This internal temperature gradient may lead to local high temperature or hot spots within the module leading to a loss in efficiency as well as possible permanent degradation in the long run. The silicon solar cells in the module were soldered in series and the cell with the smallest output limits the overall output current, hence the uniformity of temperature could again indirectly contribute to achieving higher overall electrical power output. It was thus deduced that PCM also aids in maintaining a uniform temperature throughout the BICPV module which may lead to prolonged module life.

5.2.2 SEH system with copper tubes

(i) Electrical Characterisation:

The experimental results presented here are based on the four test cases of: (a) without applied cooling/with natural convection as the baseline case, with latent cooling means, (b) PCM with lower melting temperature (RT28 HC), (c) PCM with higher melting temperature (RT50), and with a sensible medium (d) circulated water cooling. The electrical characterisation of the SEH based WICPV-PCM system was conducted for a duration of 150 min primarily at an irradiance of 1000 Wm^{-2}. However, the experiment was run with water only for 90 min as the electrical power output in this case remained fairly constant. Three runs were conducted and an average value is presented. A few

experiments were repeated at a lower intensity of 500 Wm^{-2} for testing the efficacy of PCM with respect to intensity in these systems. During the time period of the experimental run, both PCM were observed to undergo a complete phase change from solid to liquid state. The electrical characterisation is expressed in terms of the output I_{SC}, V_{OC} and P_m. These values were then used to calculate the absolute electrical efficiency (η_{elec}) and consequently, the relative electrical efficiency improvement in the WICPV using the different cooling options (cases b, c and d) compared to the output with no applied cooling (case a). The first exercise for these tests was to compare the effectiveness of PCM RT50 in the WICPV system at a lower irradiance of 500 Wm^{-2} and a higher irradiance of 1000 Wm^{-2}. The obtained profiles for V_{OC}, and P_m are illustrated in Fig. 90 and Fig. 91: (a) and (b) respectively without and with PCM RT50. As can be seen, there was a sharp and almost steady drop in V_{OC} at both intensities without and with PCM, although with the use of PCM, the decline was not as steep during the first 60 min due to the absorption of heat in the material. The I_{SC} curve showed an increasing trend with irregularities, possibly due to the effect of ambient cooling. The profile for P_m was relatively similar to V_{OC} at both irradiances. At higher irradiance, however, there was a sudden drop in P_m after about 30 min, possibly due to overheating caused by continuous operation at 1000 Wm^{-2}. The fluctuations in the beginning were possibly due to abrupt changes in the internal temperatures.

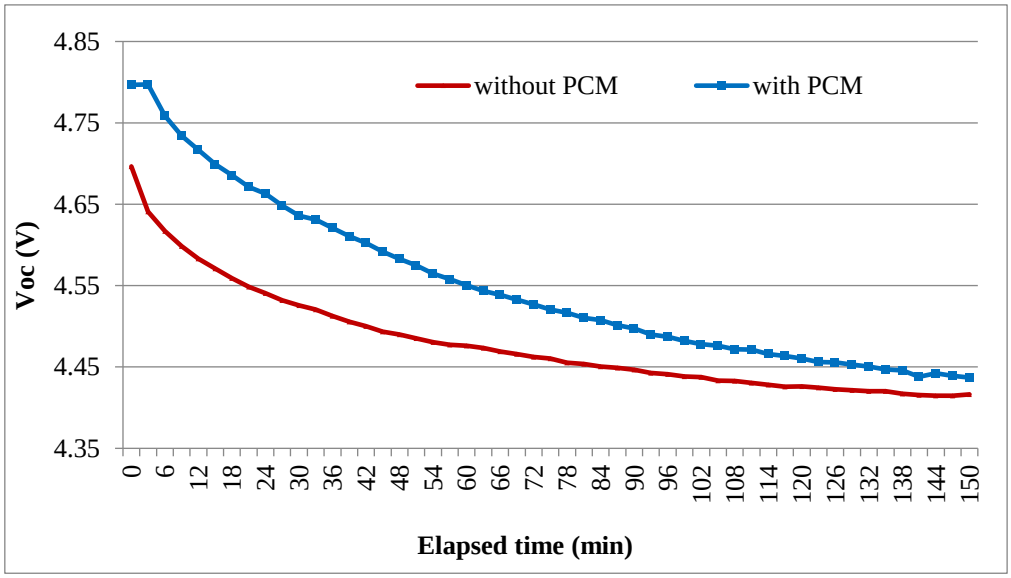

(a)

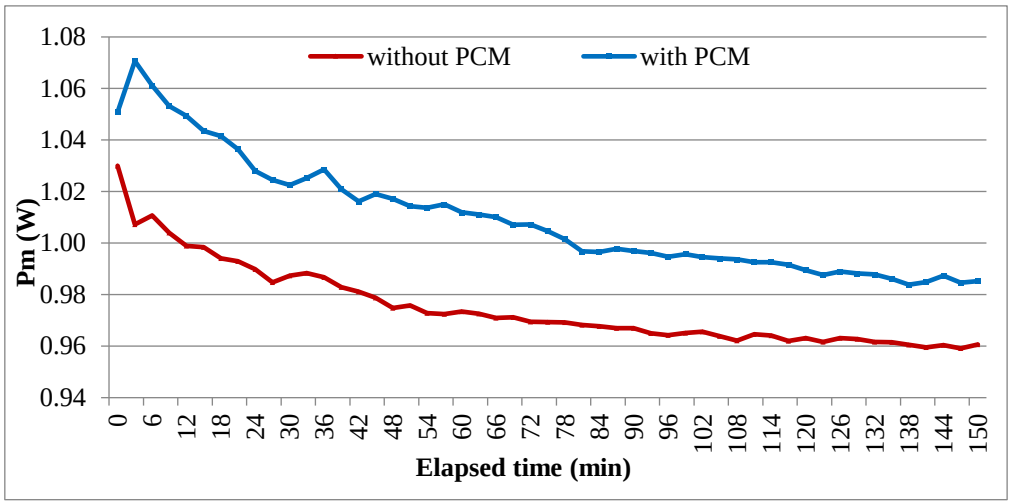

(b)

Figure 90 : Comparison of (a) open circuit voltage (V_{OC}), and (b) maximum power (P_m) without and with PCM RT®50 at a lower irradiance of 500 Wm^{-2}.

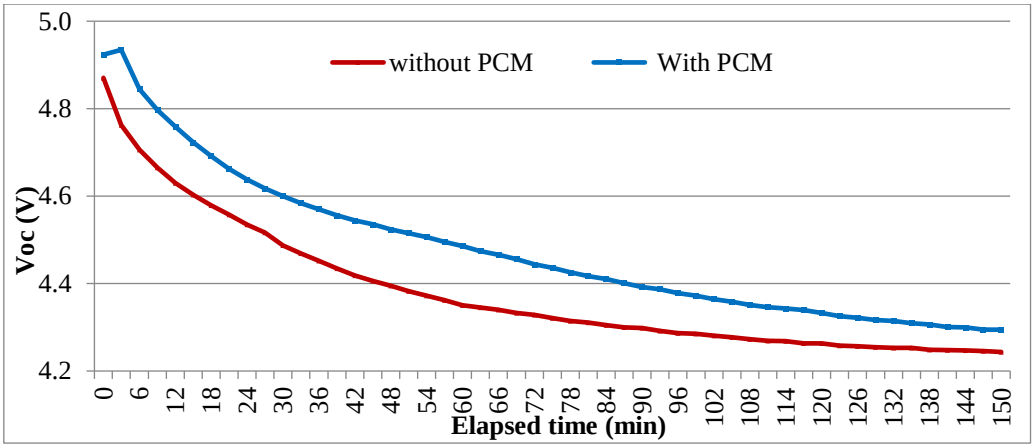

(a)

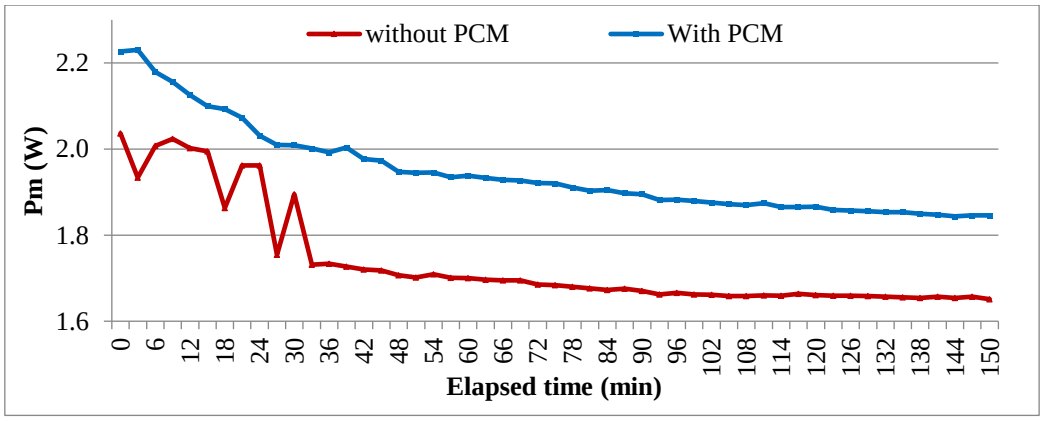

(b)

Figure 91: Comparison of (a) open circuit voltage (V_{OC}), and (b) maximum power (P_m) without and with PCM RT®50 at higher irradiance (1000 Wm^{-2}).

As can be observed from Table 25, the average values of electrical parameters increased with the use of PCM RT50 at both levels of irradiances. The unexpected increase in I_{SC} was possibly due to averaging of the data. The results demonstrated an average increase of 11.5 % in the output electrical power at 1000 Wm^{-2} and 5.2 % at 500 Wm^{-2} with RT50 incorporated as compared to a naturally ventilated system for 150 min.

Table 25. Experimental data for the photoelectrical parameters without and with PCM RT®50 for a duration of 150 min at both irradiances.

Irradiance (Wm^{-2})	**Parameter (average value)**	**Without PCM RT50**	**With PCM RT50**
1000	I_{sc} (A)	0.51	0.57
	V_{oc} (V)	4.39	4.48
	P_m (W)	1.74	1.94
500	I_{sc} (A)	0.28	0.28
	V_{oc} (V)	4.46	4.55
	P_m (W)	0.96	1.01

Following on from this, the next aim was to study the relative effectiveness of various cooling means at the standard irradiance of 1000 Wm^{-2}. To achieve this, the profile for the output power P_m (Fig. 92 (a)) and its linear trend (Fig. 92 (b)) for the WICPV-PCM system were compared with the three cooling means versus natural ventilation. The steady state change (increase or decrease) is shown by this linear trend. Although similar trends of decay in P_m were observed for the system in all cases; the decline was the steepest for the naturally ventilated system followed by the PCMs and it was the least for water cooling. With a higher melting temperature range, PCM RT50 exhibited higher effectiveness and the difference in the trend line compared to the uncooled system showed an increasing gap. As the melting temperature range of RT28 HC was lower than that of RT50, all the available material in the tubes melted earlier and the decline in the P_m started sooner. This indicate that for such systems, a PCM with a higher melting temperature range should be selected; roughly at least 25 °C above the room temperature. The average P_m for the duration of the experiment is shown in Fig. 92 (c). The average electrical power output with no applied cooling was 1.70 W, with RT28HC; 1.97 W, with RT50; 2.00 W and with circulating water cooling reached 2.11 W. The absolute electrical efficiency of the WICPV without additional cooling, with latent and sensible cooling is illustrated in Fig. 92 (d) and one can clearly see the gradual increase from 5.9 % with no cooling to 6.8 %, 6. 9 %, and 7.3 % with PCM RT28HC, RT50 and water respectively.

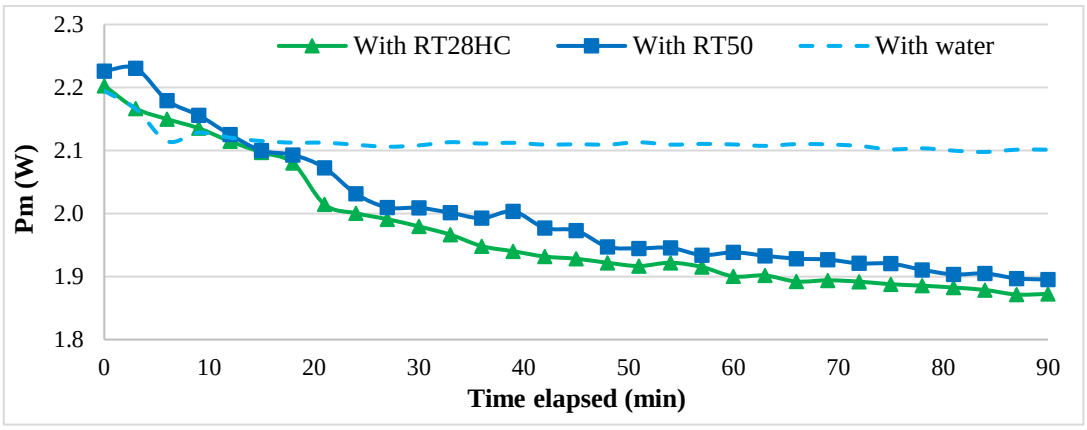

(a)

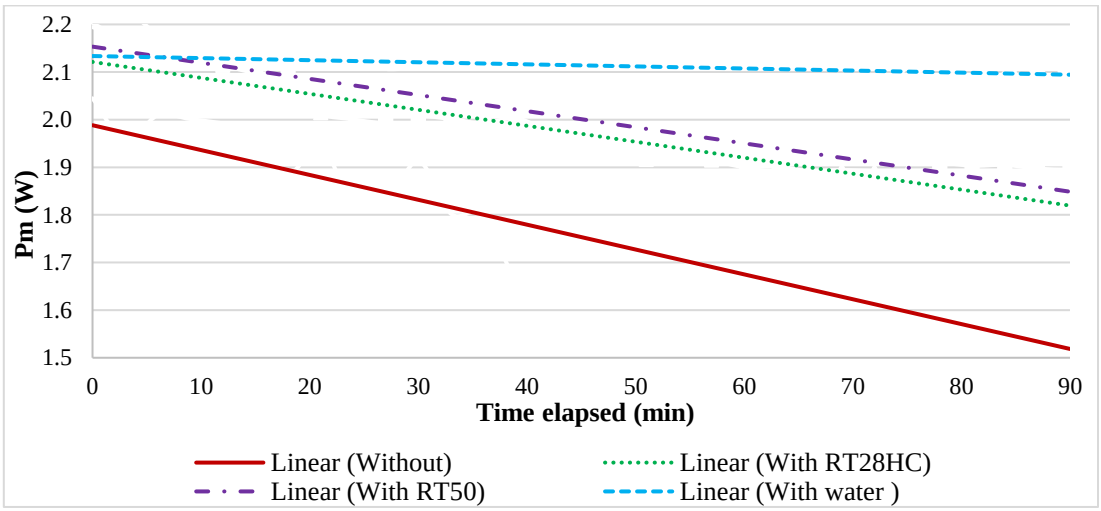

(b)

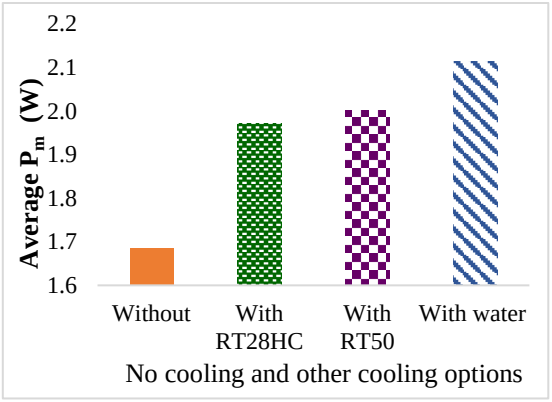

(c)

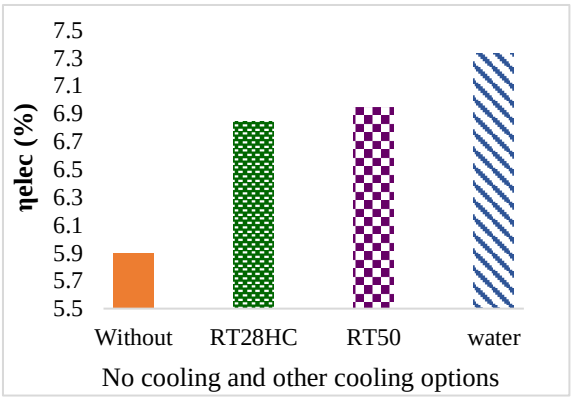

(d)

Figure 92: Comparison of the (a) profile of P_m, (b) linear trend of P_m, (c) average P_m and (d) absolute electrical efficiency for the WICPV with no applied cooling and using sensible (water) and latent (PCM RT28HC, RT50) cooling for 90 min at 1000 Wm^{-2}.

To quantify the relative effectiveness of each of these cooling options, the percentage change in the output electrical parameters of the WICPV with various applied cooling

means compared to no cooling were calculated at 1000 Wm^{-2} as demonstrated in Table 26. As the I-V data for the run with water was recorded for 90 min, the values from other cooling options were compared for the same duration. The output power was maximum with circulated water cooling (7.8 % increase in I_{SC}, 5.4 % in V_{OC}) followed by using RT50 (12.4 % increase in I_{SC}, 2.7 % in V_{OC}) and RT28HC (12 % increase in I_{SC}, 1.8 % in V_{OC}) against the naturally ventilated system at 1000 Wm^{-2}. The obtained curves from the I-V tracer and the measured data showed an output electrical power improvement of 16.9 % with the use of RT28HC, 18.7 % with RT50 and 25.5 % with circulating water at 1000 Wm^{-2} compared to the naturally ventilated set-up. With RT28HC, a 15.9 % relative increase in electrical efficiency was achieved, with RT50; 17.6 % and with water; 24.2 % respectively. Sensible cooling with circulated water proved more effective with 6.4 % and 8.0 % higher electrical efficiency achieved than with RT28HC and RT50 respectively.

Table 26. Relative change (% Δ) in output electrical parameters with PCM and water cooling compared to no cooling for a 90 min duration at 1000 Wm^{-2}.

Parameter	**% Δ**	**% Δ**	**% Δ**
	RT28HC	**RT50**	**Water**
I_{sc} (A)	12.05	12.37	7.81
V_{oc} (V)	1.81	2.66	5.40
P_m (W)	16.93	18.75	25.46
η_{elec} (%)	15.93	17.63	24.24

While the results demonstrated an average increase in the output electrical efficiency of over 17 % at 1000 Wm^{-2} with RT50, it halved to 6.5 % at 500 Wm^{-2} as compared to a naturally ventilated system, considering the first 90 min of the experimental data.

Water cooling produced higher improvements in spite of lower heat capacity due to continuous circulation effect. With Sensible cooling with water 6.4 % and 8.0 % higher electrical efficiencies were recorded than RT28HC and RT50 respectively. Water was circulated using water supply tank head as the driving force instead of electrical means, saving electrical expenses. However, in a real world scenario, power losses in running electric motor or pump for water circulation have to be taken into consideration, which may entail active power parasitic losses as well as a higher capital cost. In those cases, the overall efficiency with water systems may even become reduced. Hence, it could be concluded that PCM could still prove to be largely more effective in the long term.

(ii) Thermal Characterisation:

For the SEH system with six copper tubes under the six strings of solar cells, the temperature was recorded at the centre of and under each aluminium strip mounting solar cells. The effectiveness of latent passive cooling media, namely two PCM types; the lower melting RT28 HC and the higher melting RT50 was compared with the sensible passive medium, water, and was expressed in terms of the temperature reduction achieved by them at 1000 Wm^{-2}. A comparison of the obtained temperature profile for individual channels (channel 1 to 6, expressed as T1 to T6) is shown in Fig. 93 (a-f). As channel T1 was located on one edge of the panel experiencing maximum natural convection, the highest temperature (56.8 ˚C) reached there was less than 60 ˚C. Similarly for T6, which was located on the other edge but experienced slightly lesser natural convection due to its placement towards the solar simulator, the highest temperature (61.2 ˚C) reached there was only marginally higher than 60 ˚C. However, in the case of other channels, such as T2, T3 (one of the most centrally located channels), T4 (another centrally located channel) and T5, temperatures reached between 65 ˚C and 70 ˚C. The system with no applied cooling showed the highest temperature in all channels while, with water, the lowest temperatures were observed. Both the PCM showed approximately similar levels of effectiveness in achieving temperature reduction so further investigation is needed in bigger systems to test the respective performance of PCM with various melting points.

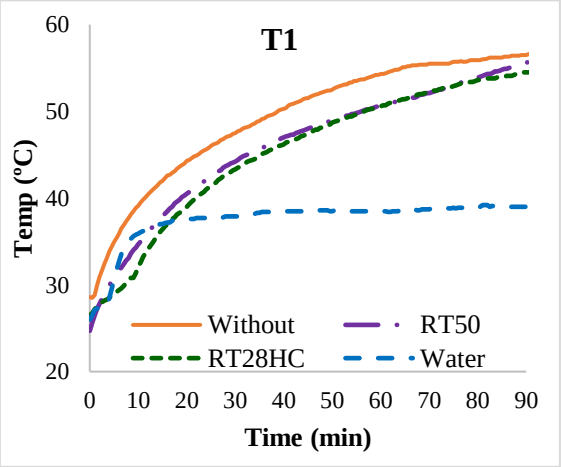

(a)

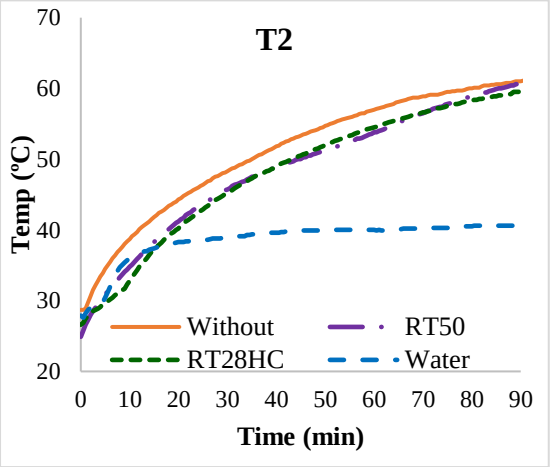

(b)

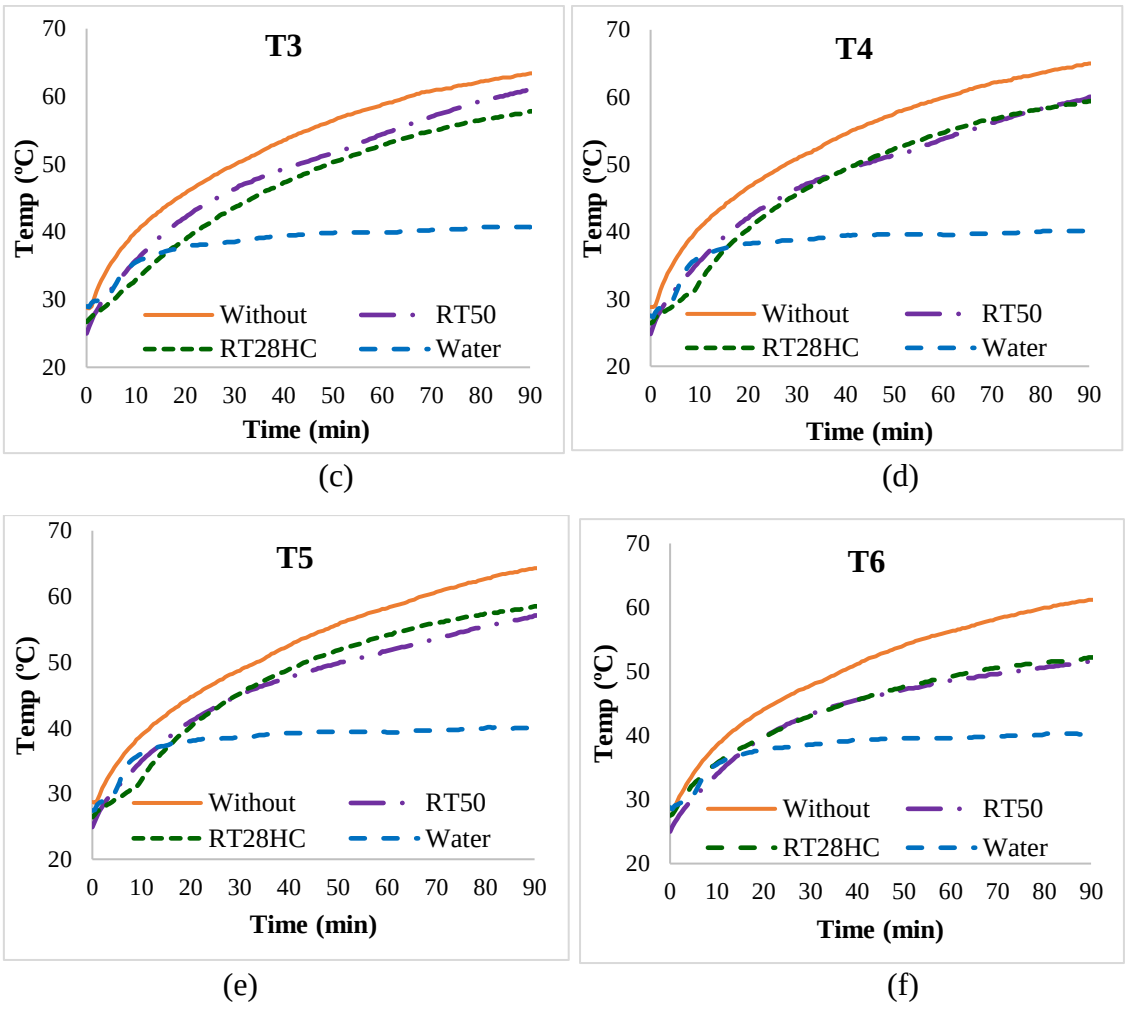

Figure 93: Comparison of channel temperature profile without applied cooling at 1000 Wm^{-2}, with RT28HC, RT50 and water cooling options. (a) T1 (on one edge), (b) T2, (c) T3 (centre), (d) T4 (centre), (e) T5 and (f) T6 (on another edge).

It was observed that towards the end, all the PCM in the channels melted to liquid form. The absolute temperature data at the end of the run (at 90 min), within channels T1 to T6 with PCM RT28HC, RT50 and water are arranged in Table 27. As can be seen, both PCM were in molten states as the end temperatures were well above the melting peak for each PCM; 28 °C and 49 °C respectively.

Table 27. Comparison of absolute temperature within each channel without applied cooling and with different passive cooling mechanisms at the end of experiment.

Media	T1 (°C)	T2 (°C)	T3 (°C)	T4 (°C)	T5 (°C)	T6 (°C)
Without	56.6	61.1	63.4	65.0	64.3	61.2
RT28HC	54.5	59.6	57.8	59.4	58.5	52.2
RT50	55.7	60.9	61.2	60.1	57.1	51.8
Water	38.5	40.1	40.2	39.6	39.4	39.9

The temperature data for the channels with all cooling options was averaged at 1000 Wm^{-2} and is shown in Fig. 94. It can be seen that for all channels the application of both sensible and latent cooling were beneficial, though in some channels, one PCM was slightly more effective than another, the reasons for which are unexplored at this stage.

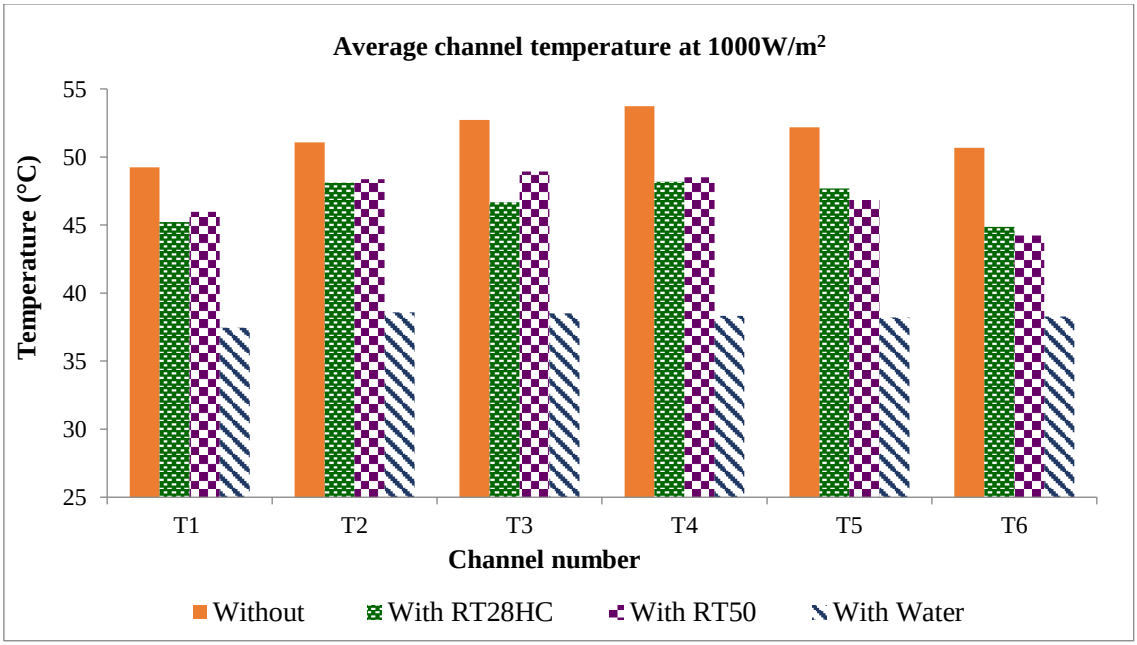

Figure 94: Comparison of average channel temperature, Ti (where i is the channel number) without applied cooling and with cooling (two different PCM and water).

The average temperature distribution within channels T1 to T6 for lower and higher irradiances with no PCM versus with PCM RT50 is demonstrated in Fig. 95. One can observe that RT50 was more effective at lower irradiance as the difference between the two graphs was higher. At 500 Wm^{-2}, the maximum average temperature without PCM was 46.1 °C (39.5 °C with PCM) while at 1000 Wm^{-2}, it was 59.7 °C without PCM (55.7 °C with PCM). Hence the difference was 6.6 °C at lower irradiance and 4.0 °C at higher irradiance. The highest temperature attained within the WICPV system without PCM was 53.7 °C while it was 48.2 °C with RT28HC, 48.9 °C with RT50 and 38.6 °C with water. Similarly, the lowest average temperature was recorded as 49.2 °C, 44.9 °C, 44.2 °C and 37.5 °C for the respective cases (details given in Table 28).

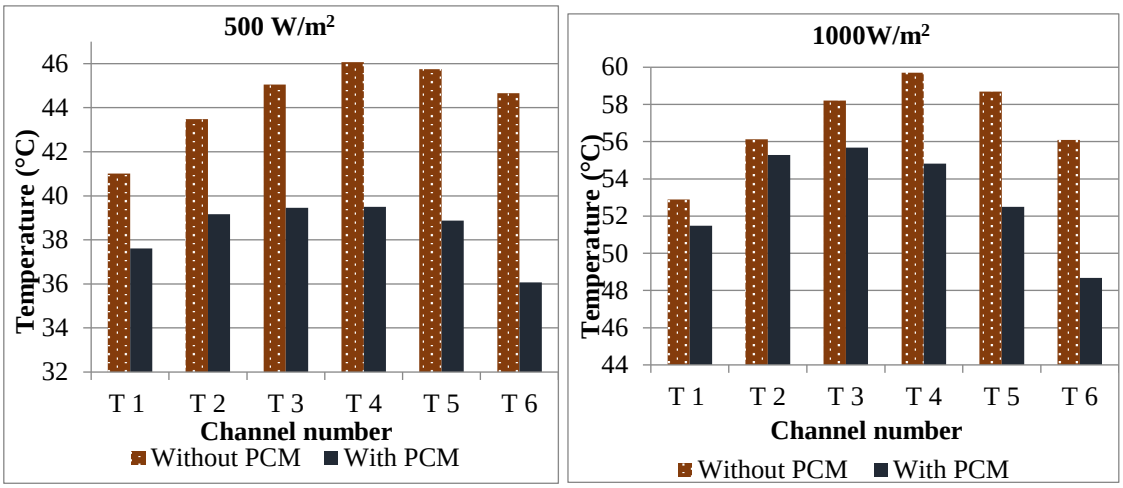

(a) (b)

Figure 95: Average temperature in channels: (a) 500 Wm^{-2} and (b) 1000 Wm^{-2}.

Table 28. Comparison of maximum, minimum and average temperatures across the channels with no cooling, PCM and water cooling options at the end of the experiment.

Media	T_{Min} (°C)	$T_{Avg,Min}$ (°C)	T_{Max} (°C)	$T_{Avg,Max}$ (°C)
Without cooling	56.6	49.2	65.0	53.7
With RT28HC	52.2	44.9	59.6	48.2
With RT50	51.8	44.2	61.2	48.9
With Water	38.5	37.5	40.2	38.6

There was only less than a degree of variation between the average highest and lowest temperatures obtained in the case of using both the PCM. It can also be seen that the average temperatures across all channels with water as a cooling medium was almost constant with a variation of ±0.4 °C. As an exception, T1 (inlet water channel) experienced the lowest average temperature of 37.5 °C in contrast to the highest 38.6 °C within T2 (outlet channel) due to the water circuit configuration. For the two cases of PCM cooling, the temperature at the central channels (T3 and T4) were comparatively higher due to their central location achieving lesser cooling via natural convection otherwise available to the channels on the sides or edges such as T1. The average temperature reduction achieved across channels 1 to 6 using different passive cooling media as compared to the case with no cooling for the duration of the experiment is highlighted in Table 29. As expected, the circulated water achieved the highest temperature reduction across all channels followed by RT28HC and RT50 respectively.

Table 29. Average temperature reduction achieved within each channel using various passive cooling media, compared to the case without applied cooling.

Channel/ Media	**ΔT1 (°C)**	**ΔT2 (°C)**	**ΔT3 (°C)**	**ΔT4 (°C)**	**ΔT5 (°C)**	**ΔT6 (°C)**
RT28HC	4.0	3.0	6.0	5.6	4.5	5.8
RT50	3.3	2.7	3.8	5.2	5.4	6.4
Water	11.8	12.5	14.2	15.4	14.0	12.4

It is to be noted, however, that since water was continuously circulated, despite lower heat capacity compared to PCMs, it was able to achieve greater cooling benefits. The rationale for choosing water circulation was that firstly, comparison of still water with PCM wouldn't have led to interesting conclusion in terms of quantitative difference in temperature control and secondly in practical situations, flowing water is used for heat removal applications, which required comparison with PCM. Also, it is easily achievable task in practice compared to circulation of PCM. The maximum average temperature reduction being higher by 9.6 °C and 10.3 °C and maximum temperature reduction by 19.4 °C and 21 °C in case of water cooled system as compared to RT28HC and RT50 respectively, essentially because of the circulation effect. Water has a specific capacity of 4.187 $kJkg^{-1}K^{-1}$ whereas both the PCM have reported specific heat values of 2 $kJ.kg^{-1}.K^{-1}$ in addition to the latent heat capacity of 245 $kJkg^{-1}$ and 168 $kJkg^{-1}$ for RT28 and RT50 respectively. This indicates that PCM circulation could give better results though it may incur additional costs in pumping and transportation. It may be worthwhile to highlight that for the experiments on SEH based WICPV system, water was circulated using the head of the water supply tank as the driving force instead of electrical means, thereby saving electrical expenses.

The use of PCM increased the uniformity in temperature distribution throughout the module, which is an important outcome for BICPV systems as a thermal disequilibrium leads to the formation of hot spots. The temperature distribution throughout the module was studied and it was found that the average temperature difference between the channels T3 and T4 (located in the centre of the module) and T1 (on the edge) was higher by 3.5 °C and 4.5 °C (without PCM), 1.4 °C and 2.9 °C (with RT28HC), 3.0 °C and 2.6 °C (with RT50). In terms of percentage change, the set-up with no external cooling showed a 6.6 %-8.4 % higher temperature in the centre than the edges while with PCM RT28HC, it was a 3.1 %-6.1 % difference and PCM RT50 showed a 5.3 %-6.1 % variation

in the temperature within the module. This implied that the PCM cooling almost halved the temperature variance within the module as compared to the natural ventilation case. This uniform spreading of heat across the module can reduce the formation of hot spots, which cause system degradation over a period of time.

The experimental data as obtained could provide an insight into designing heat sinks or PCM containments with variable dimensions within the same module. For instance, tubes with lesser diameter containing less material could be put to use for the sides of the panels while thicker tubes with more PCM could prove more effective for the central part of the panel, thereby saving on the material costs required to provide the uniform cooling effect throughout. This may be further helpful in maintaining a more uniform temperature across the CPV panel. The given copper tube configuration which could have been practically close-fitted within the system under narrow aluminium strips had a limited cooling contribution using lesser material and hence for lesser time. Therefore, the designs with bigger tube diameter may produce better results in terms of cooling and electrical efficiency of the WICPV.

5.2.3 SEH-n-PCM system

(i) Electrical Characterisation:

The SEH based BICPV system was characterised at a lower (500 Wm^{-2}) and a higher (1000 Wm^{-2}) irradiance for a duration of 150 min at 0° inclination. The system was then characterised by attaching the PCM containment filled with two n-PCMs; n-PCM 1 with 0.5 % and n-PCM 2 with 1.0 % of 60 nm nano-CuO dispersed in paraffin wax based PCM, RT 42. Two runs were conducted and an average value was obtained to take any environmental variations into account. For a qualitative analysis, the profiles of output power from the BICPV module at both intensities without and with n-PCM 1 and n-PCM 2 versus time are compared in Fig. 96: (a), (b) at 500 Wm^{-2} and 1000 Wm^{-2} respectively. As can be seen from the profiles, the system showed a substantial increase in P_m with n-PCM 1 from the beginning of both levels of illumination. The reason for abrupt trends with n-PCM 2 and the sudden decline in the values were unclear and may need further investigations which are beyond the range of this thesis as of now.

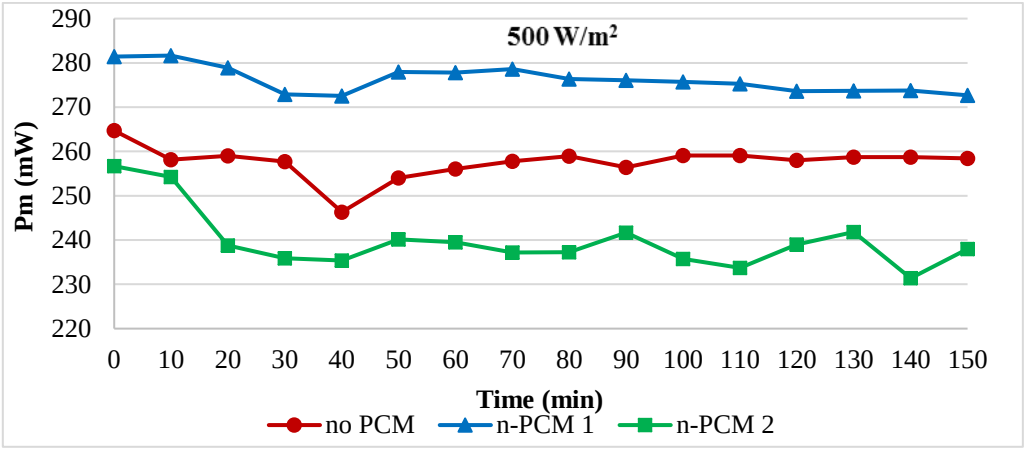

(a)

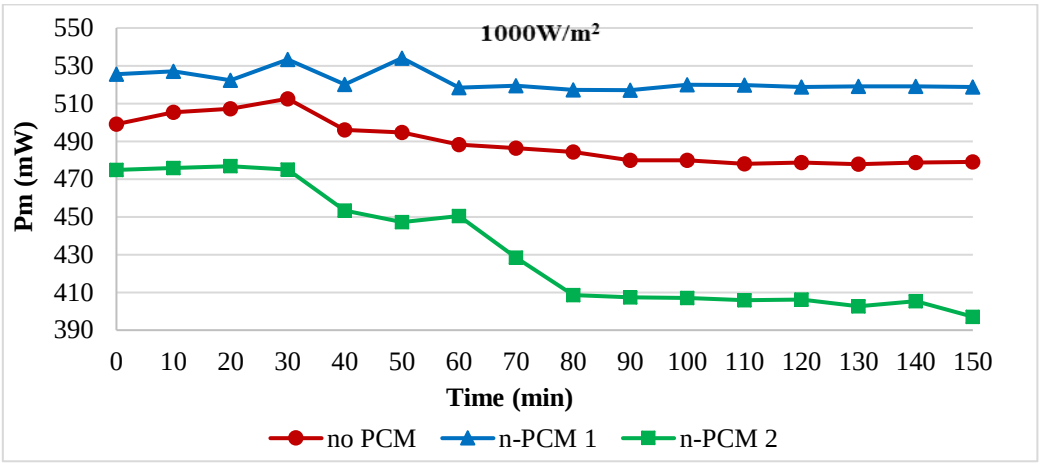

(b)

Figure 96: Comparison of P_m profiles for the SEH based BICPV at two irradiance levels without PCM, and with n-PCM 1 and n-PCM 2 versus time: (a) for irradiance of 500 Wm^{-2} and (b) for 1000 Wm^{-2} (Inclination: 0°).

One can see from the profiles that the values for P_m in all three cases almost stabilised after 80 min from the start at the lower irradiance while at the higher irradiance, P_m became stable for a while after 50 min but displayed a few variations with n-PCM 2. With no PCM, and with n-PCM 1 it mostly remained constant. For a quantitative comparison, the relative average P_m, I_{SC}, and V_{OC} with n-PCM 1 and n-PCM 2 media compared to the case with natural convective cooling are presented in Fig. 97 (a) at 500 Wm^{-2} and (b) at 1000 Wm^{-2}. As can be seen, at both lower and higher intensities, the use of n-PCM 1 exhibited higher improvement in performance for the system as compared to n-PCM 2. Though with n-PCM 1, V_{OC} was highest at lower irradiance, it was highest with n-PCM 2 at higher irradiance, although the disproportionate decrease in I_{SC} caused a decline in the overall P_m.

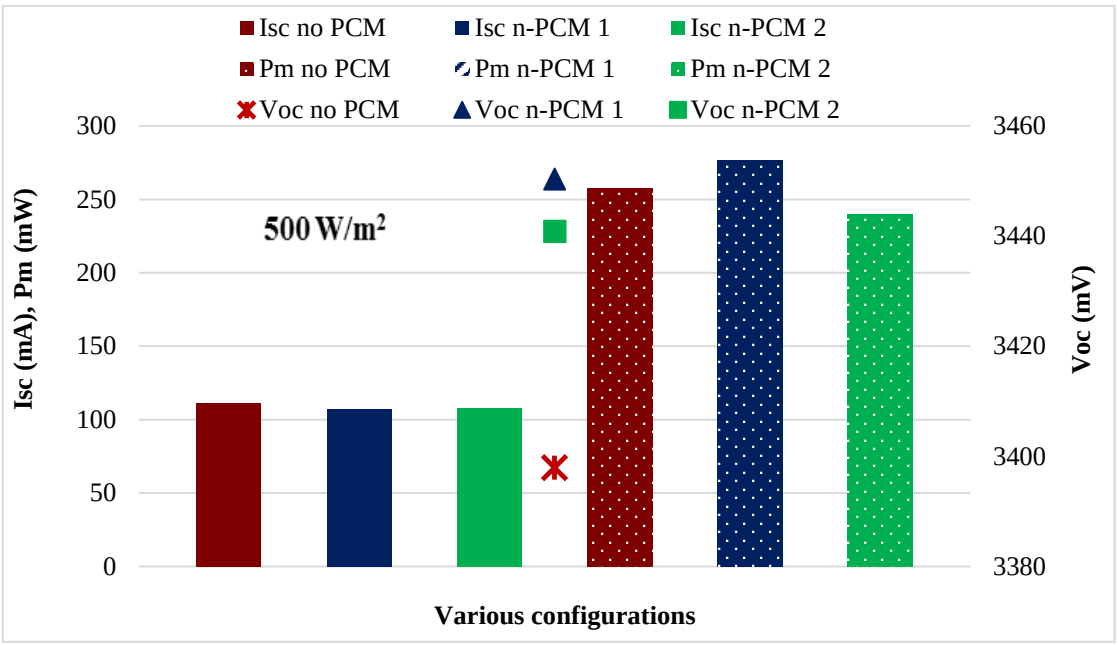

(a)

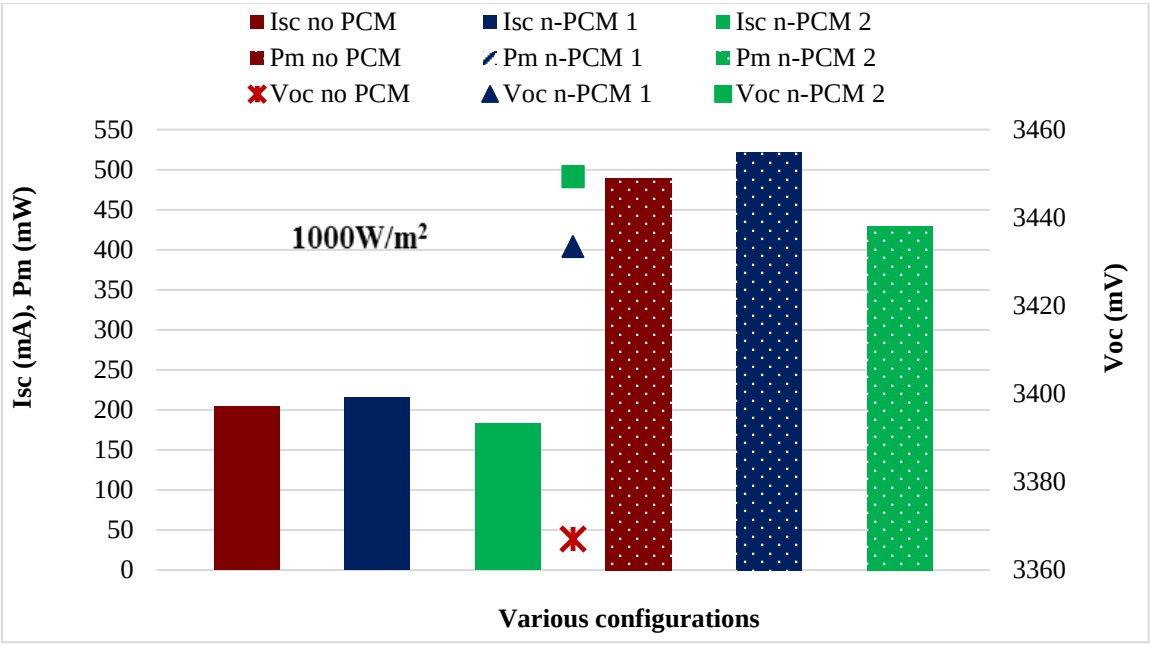

(b)

Figure 97: Comparison of relative average P_m, I_{SC}, and V_{OC} without and with n-PCM 1 and n-PCM 2 at: (a) 500 Wm^{-2} and (b) 1000 Wm^{-2}.

As shown in Table 30, the addition of n-PCM 1 resulted in a 7.2 % increase in P_m (1.5 % increase in V_{OC} and 4.0 % increase in I_{SC}) whereas with n-PCM 2 there was a decrease of 6.9 % in P_m (1.3 % increase in V_{OC} and 4.0 % decrease in I_{SC}) at 500 Wm^{-2}. Similarly, at 1000 Wm^{-2}, with n-PCM 1, there was a 6.7 % increase in P_m (2.0 % increase in V_{OC} and

5.5 % increase in I_{SC}) whereas with n-PCM 2 there was a decrease of 12.3 % in P_m (2.5 % increase in V_{OC} though 10.3 % decrease in I_{SC}).

Table 30. Change (% Δ) in the output electrical parameters with n-PCM 1 and n-PCM 2 compared to the no cooling. (Negative sign denotes a decrease from baseline).

Parameter	**% Δ at 500 Wm^{-2}**		**% Δ at 1000 Wm^{-2}**	
	n-PCM 1	**n-PCM 2**	**n-PCM 1**	**n-PCM 2**
I_{sc} (A)	4.01	-3.43	5.53	-10.31
V_{oc} (V)	1.54	1.26	1.97	2.44
P_m (W)	7.23	-6.91	6.68	-12.32

From the experimental data, it can be concluded that n-PCM 1 was more effective, with an increased electrical power output at both irradiance levels and n-PCM 2 performed relatively better at lower irradiance level of 500 Wm^{-2}.

(ii) Thermal Characterisation:

The SEH based BICPV system was thermally characterised without PCM (RT 42) cooling first and then the thermal performance was compared with n-PCM 1 and n-PCM 2 at 1000 Wm^{-2} and 500 Wm^{-2}. The temperatures were recorded at the points across the edges and at the centre of the module. While T6 to T10 were recorded just below the BICPV back-plate, T1 to T5 were the corresponding temperatures recorded at the base of the PCM containment. The temperature profiles for all the monitored points with both types on n-PCM are shown for 1000 Wm^{-2} in Fig. 98 (a) with n-PCM 1 and (b) with n-PCM 2, while at 500 Wm^{-2} with n-PCM 1 in Fig. 98 (c) and with n-PCM 2 in Fig. 98 (d). There have been minor fluctuations in the observation for the curves due to external environmental changes beyond control such as occurrence of day-night temperature difference as well as different temperatures (weather dependent) every day although every precaution was taken to minimise these effects and ensure that the working /operating conditions remained almost identical for all test cases. Apart from minor fluctuations, there was a common trend followed with the highest temperature monitored at the centre of the module. For comparing the temperature profiles with no-cooling, n-PCM 1 and n-PCM 2 at significant points under the BICPV back-plate for 1000 Wm^{-2} and 500 Wm^{-2}, Fig. 99 and Fig. 100 can be referred to, respectively. At most of the monitored points, n-PCM 1 proved to reduce the temperature better than or at least equal to as n-PCM 2, with a minor exception at 1000 Wm^{-2} (T7).

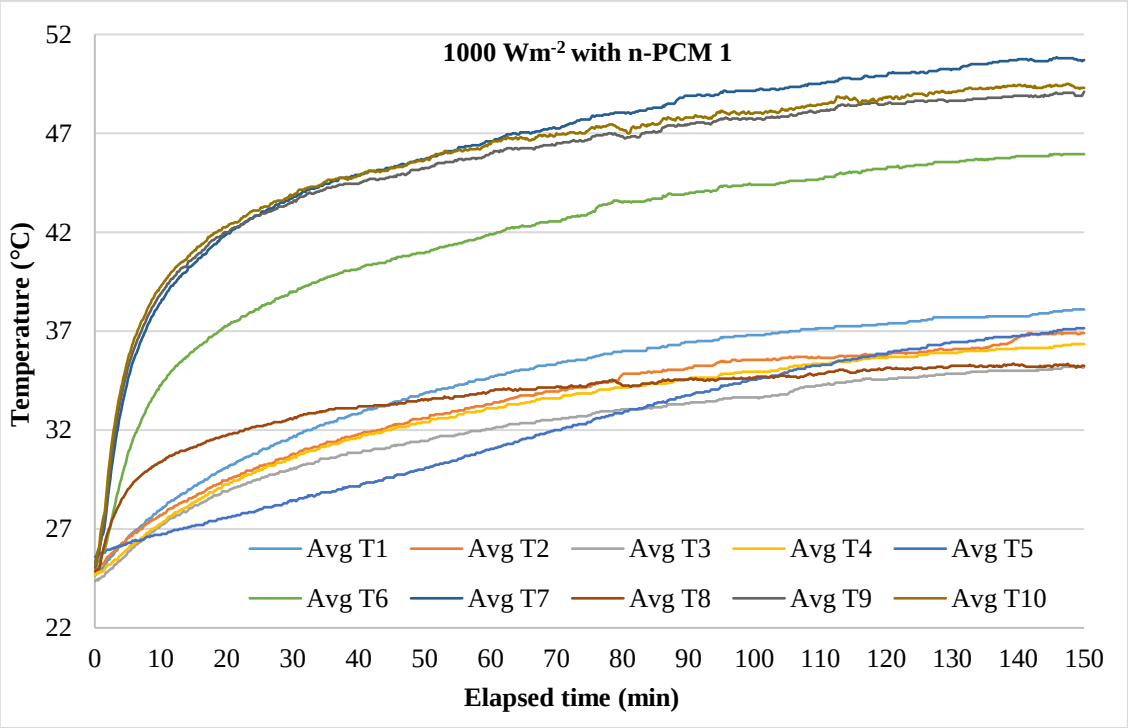
1000 Wm-2 with n-PCM 1
Temperature (°C)
52
47
42
37
32
27
22
0 10 20 30 40 50 60 70 80 90 100 110 120 130 140 150
Elapsed time (min)
Avg T1
Avg T2
Avg T3
Avg T4
Avg T5
Avg T6
Avg T7
Avg T8
Avg T9
Avg T10

(a)

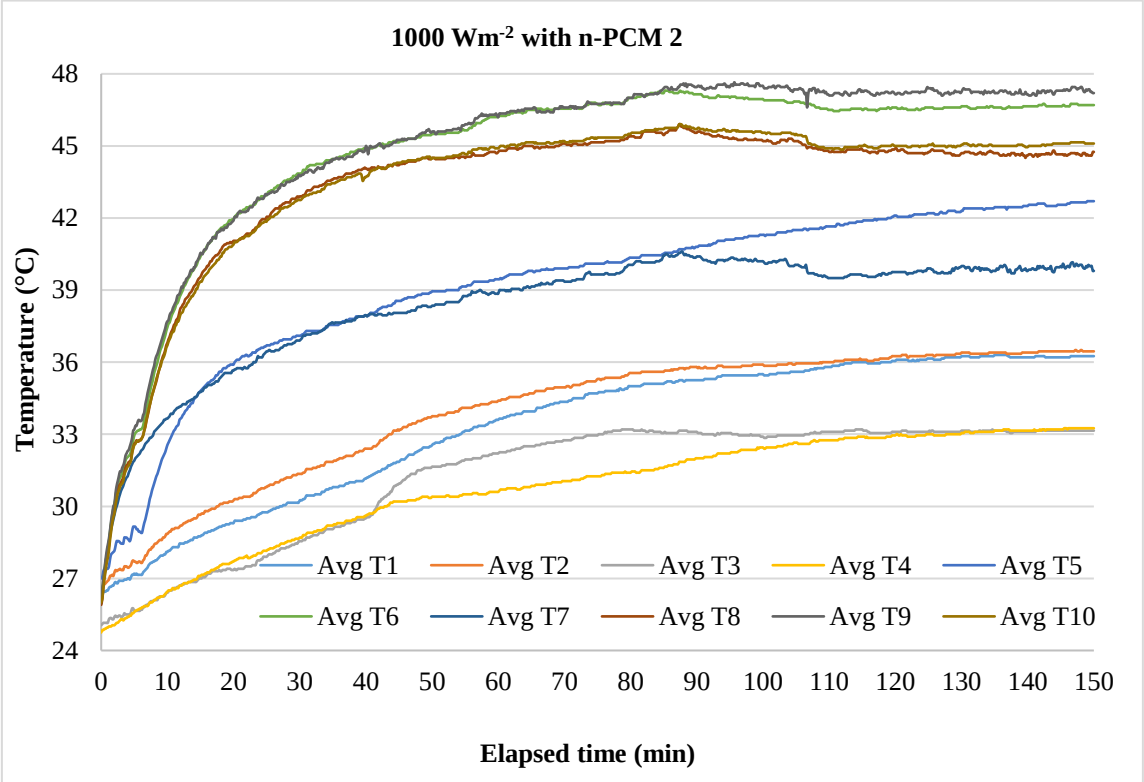
1000 Wm-2 with n-PCM 2
Temperature (°C)
48
45
42
39
36
33
30
27
24
0 10 20 30 40 50 60 70 80 90 100 110 120 130 140 150
Elapsed time (min)
Avg T1
Avg T2
Avg T3
Avg T4
Avg T5
Avg T6
Avg T7
Avg T8
Avg T9
Avg T10

(b)

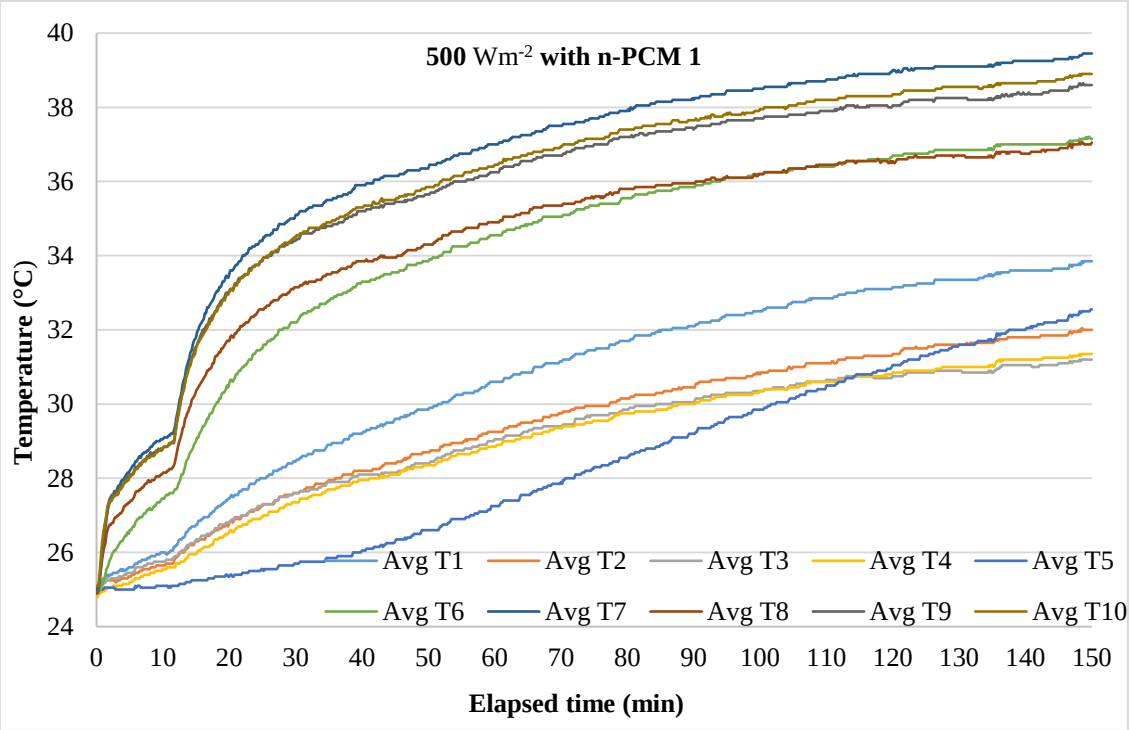

(c)

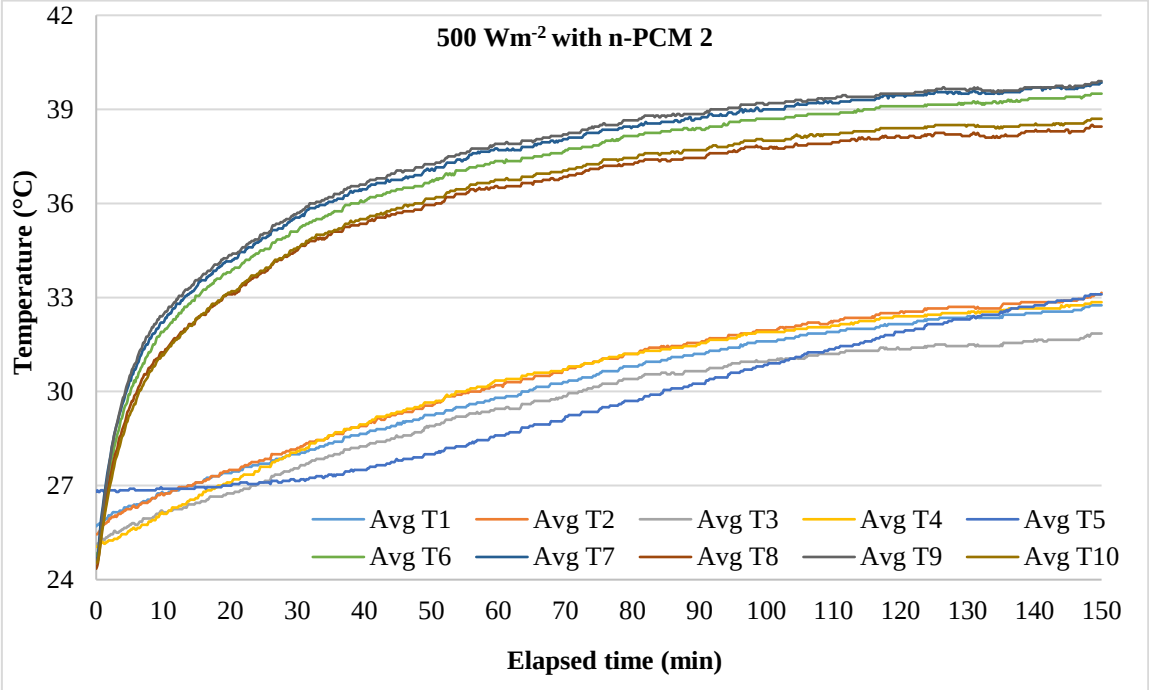

(d)

Figure 98: Temperature profiles for all the monitored points in the SEH based BIPCV system at: (a) 1000 Wm^{-2} with n-PCM 1, (b) 1000 Wm^{-2} with n-PCM 2, (c) 500 Wm^{-2} with n-PCM 1, and (d) 500 Wm^{-2} with n-PCM 2.

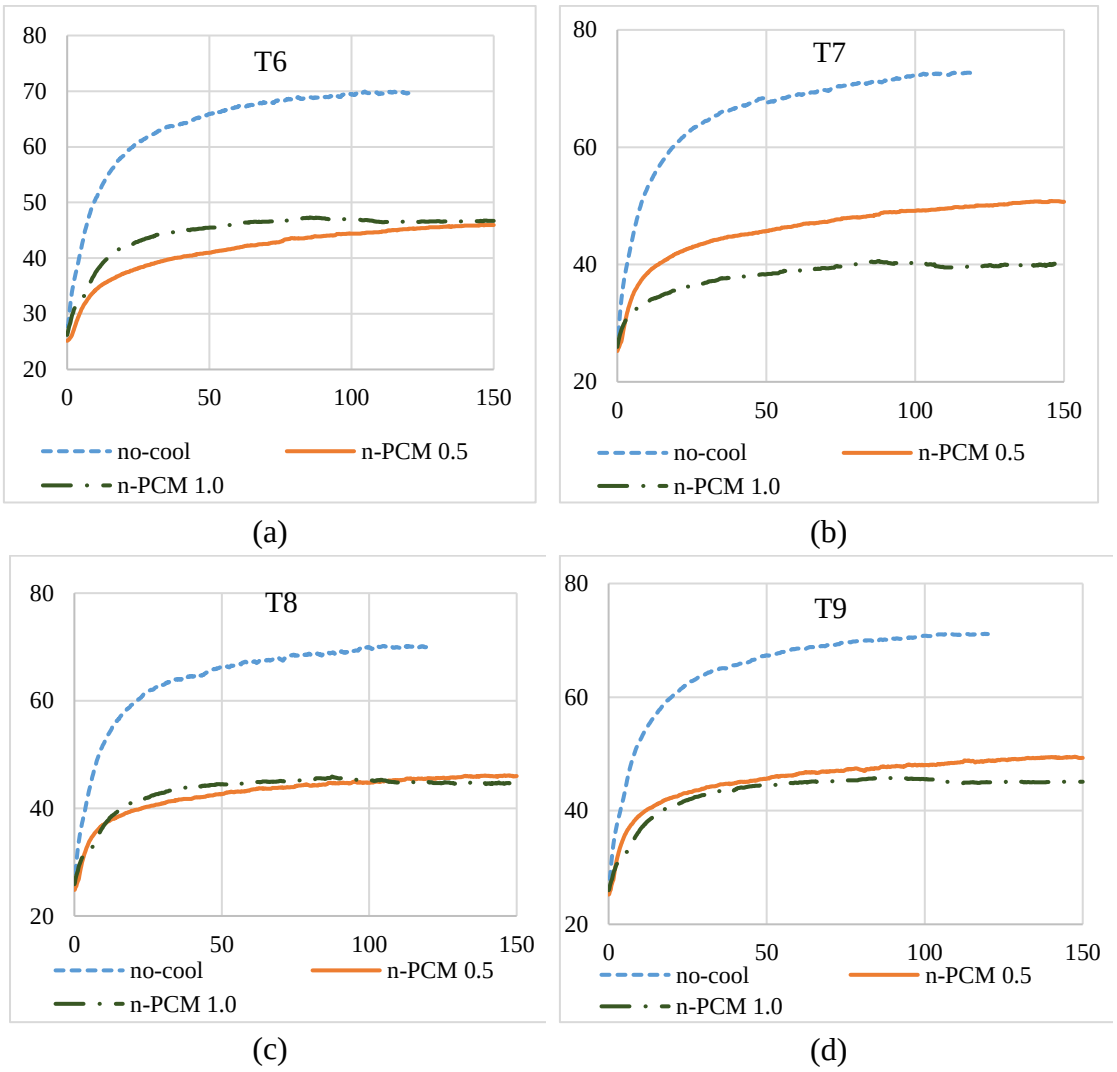

Figure 99: Temperature profiles under back-plate at 1000 Wm^{-2} with no-cooling, n-PCM 1 and n-PCM 2. Plotted on X-axes: temperature (°C), Y axes: time (min).

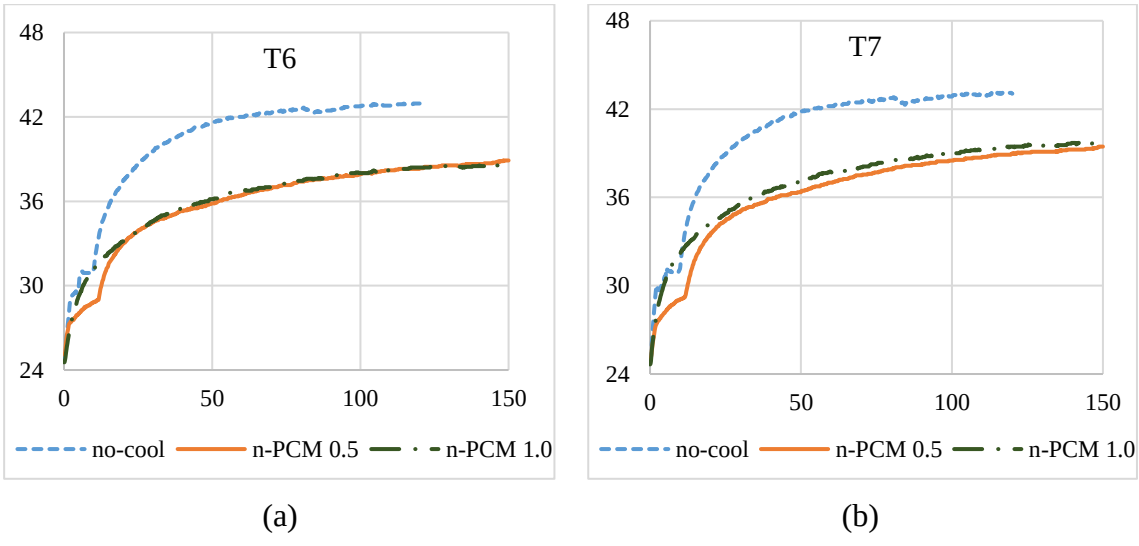

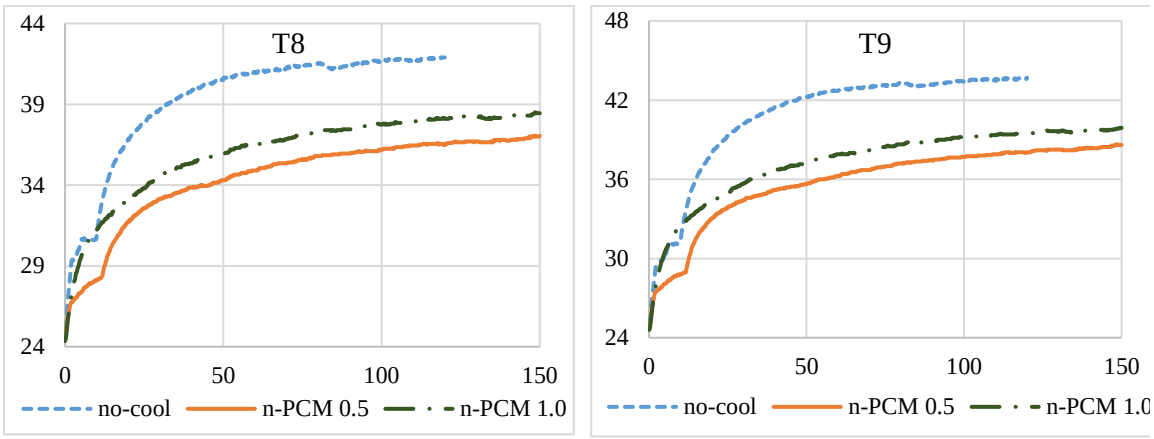

(c) (d)

Figure 100: Temperature profiles at significant points under BICPV back-plate at 500 Wm^{-2} with no-cooling, n-PCM 1 and n-PCM 2. Plotted on X-axes: temperature (°C) and Y axes: time (min).

The average and maximum temperatures recorded across the points of observation for both irradiance levels are shown in Fig. 101 (a) and (b) resp. for 1000 Wm^{-2} and 500 Wm^{-2}. As can be seen, the highest temperatures were detected at the centre of module (T7), followed by the sides with lesser exposure to the ambient air (T9 and T10).

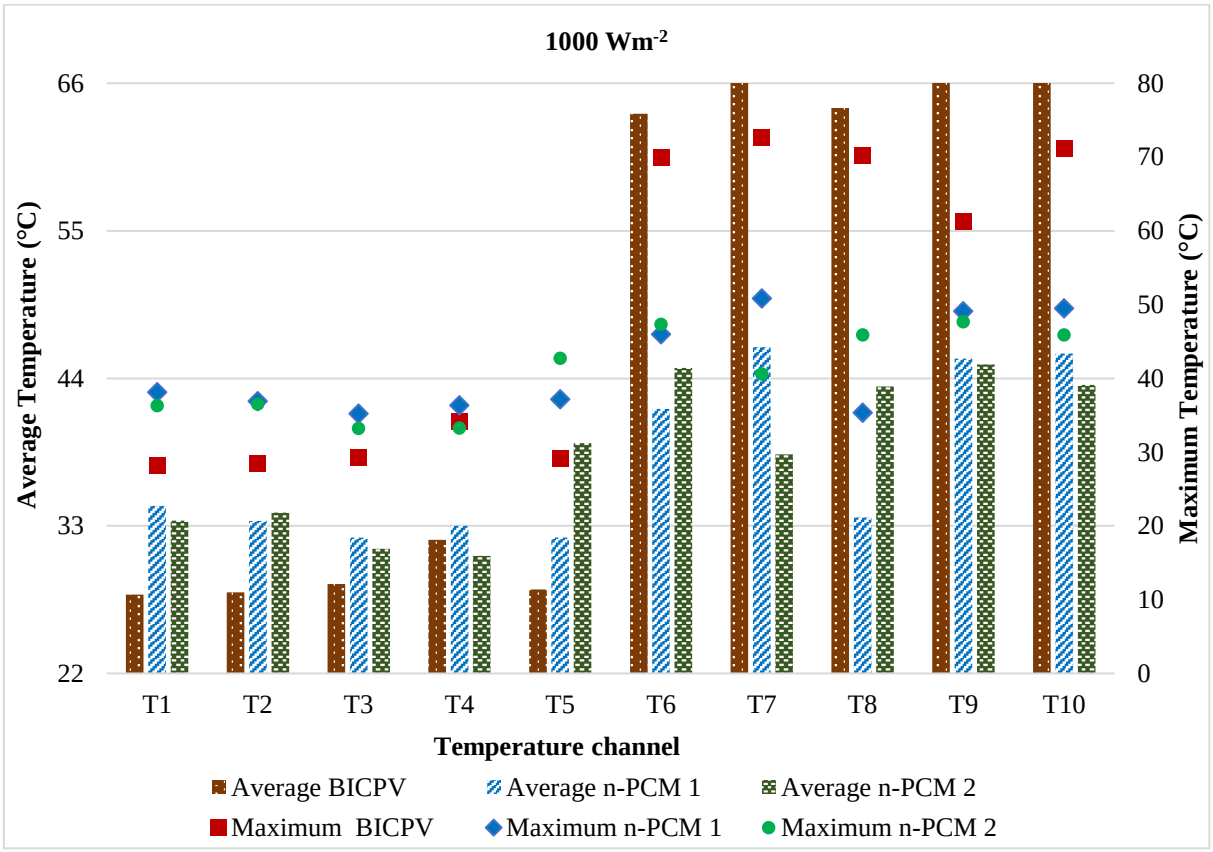

(a)

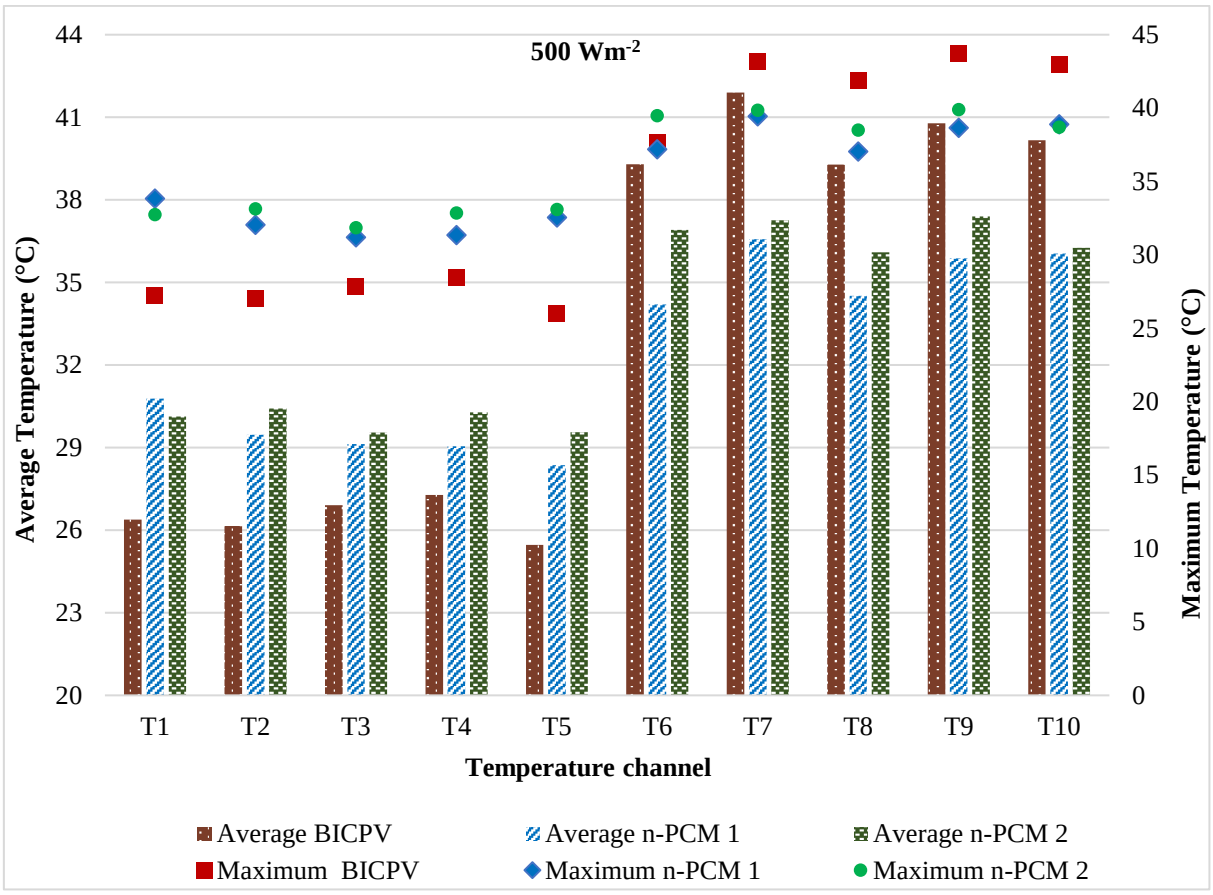

(b)

Figure 101: Average and maximum temperatures across points of observation in the SEH based BICPV at an irradiance of (a) 1000 Wm^{-2} and (b) 500 Wm^{-2}.

The sides near ambient (T6 and T8 located opposite to the solar simulator), showed the lowest average temperatures. At a higher irradiance of 1000 Wm^{-2}, the average temperature reductions across T6 to T10 with the use of n-PCM 1 were 22.0 °C (34.5 %), 19.7 °C (29.8 %), 30.5 °C (47.6 %), 20.8 °C (31.4 %), and 26.8 °C (36.9 %) while with n-PCM 2, they were 18.9 °C (29.7 %), 27.7 °C (41.9 %), 20.8 °C (32.4 %), 21.2 °C (32.0 %), and 29.2 °C (40.1 %) respectively. Using the lower irradiance of 500 Wm^{-2}, the average temperatures across T6 to T10 were reduced by 5.1 °C, 5.3 °C, 4.8 °C, 4.9 °C, and 4.1 °C with n-PCM 1; in terms of relative percentage drops, 13.0 %, 12.7 %, 12.1 %, 12.0 % and 10.3 %. With the use of n-PCM 2, the temperature reduced by 2.4 °C (6.1 %), 4.6 °C (11.1 %), 3.2 °C (8.1 %), 3.4 °C (8.3 %) and 3.9 °C (9.7 %). In conclusion it can be said that for the SEH based BICPV system, n-PCM 1 showed more improved thermal regulation as compared to n-PCM 2 especially at the lower irradiance.

5.2.4 Micro-finned thermal system

(i) Thermal Characterisation:

To emulate the temperature profile of the BICPV back-plate in the designed thermal system, insulated flexible heaters (resistive heating), were used. For understanding the thermal behaviour of the micro-finned thermal system, thermocouples were located at the top and rear side of the module, and within the PCM (RT 42) containment.. In order to select the appropriate values of the input voltage and current (V, I) to produce the output power required to produce similar thermal effects, the un-finned plate was characterised for various combinations of V, I input. The corresponding values of power and temperature were recorded for the experimental duration, at an interval of 30 min. The resulting data is presented in Table 31. It was found that out of P = 0.52 W (at V = 5.0 V), P = 0.62 W (at V = 6.5V) and P = 0.80 W (at V = 8.0 V), the latter values of V, I yielded the closest electrical power input required for producing the same thermal effect as reported for the BICPV in [311] at 1000 Wm^{-2}. Maximum temperature reached by the system (under the un-finned plate) with P = 0.52 W was under 46 ºC and with P = 0.62 W was under 57 ºC. However, with P = 0.80 W, the maximum temperature reached was over 70 ºC and hence, it proved to be the ideal power setting for emulation.

Table 31. Temperature profile attained by the un-finned aluminium plate for various Voltage settings for the Micro-finned plate for the duration of the experiment.

Temperature profile for various Voltage settings			
	V (V)	6.5	5.0
	P=V*I (W)	0.62	0.52
Under plate {T3} (ºC)	0th hour	25.6	26.6
	0.5th hour	54.8	44.2
	1st hour	56.2	45.2
	1.5th hour	56.3	45.5
	2nd hour	56.7	45.8
	2.5th hour	56.7	45.9
Centre of containment {T4} (ºC)	0th hour	25.6	26.6
	0.5th hour	36.7	33.1
	1st hour	38.3	34.2
	1.5th hour	38.5	34.4
	2nd hour	38.8	34.8
	2.5th hour	38.9	34.9

During the experimental run, the temperatures across the system were recorded at these points on a vertical section: (a) T1 or ambient temperature above the insulation layer, (b) T2 above the plate centre, (c) T3 below the plate centre, and (d) T4 at the centre of the PCM containment. A comparison of the average temperatures obtained across all the six configurations are given in Fig. 102. The bar graphs were plotted in such a way that the effect of introducing micro-fins on the un-finned surface can be easily compared for the three cases of using natural convection, PCM and n-PCM. As can be observed, the temperatures T2, T3 and T4 were recorded highest for the un-finned configuration, followed by the micro-finned configuration with only natural convection cooling. The same trend was followed for the configurations entailing the use of PCM and n-PCM respectively. It is to be noted that the ambient temperature closest to the shielded set-up, T1, remained relatively unchanged for all the configurations, which was desirable for ensuring a constant ambient temperature throughout each run. The magnitude of the reduction in T4, the temperature at the centre of the PCM containment, was appreciable for the case with PCM and n-PCM. However, if either the experiment was run for a longer duration or the set-up used a greater amount of PCM/n-PCM, this value would be expected to change. For the cases (i), (ii), (iii), (iv), (v) and (vi), the maximum values of the temperature above the plate, T2, were registered as 72.1 °C, 66.1 °C, 63.8 °C, 71.7 °C, 63.5 °C, and 62.6 °C respectively.

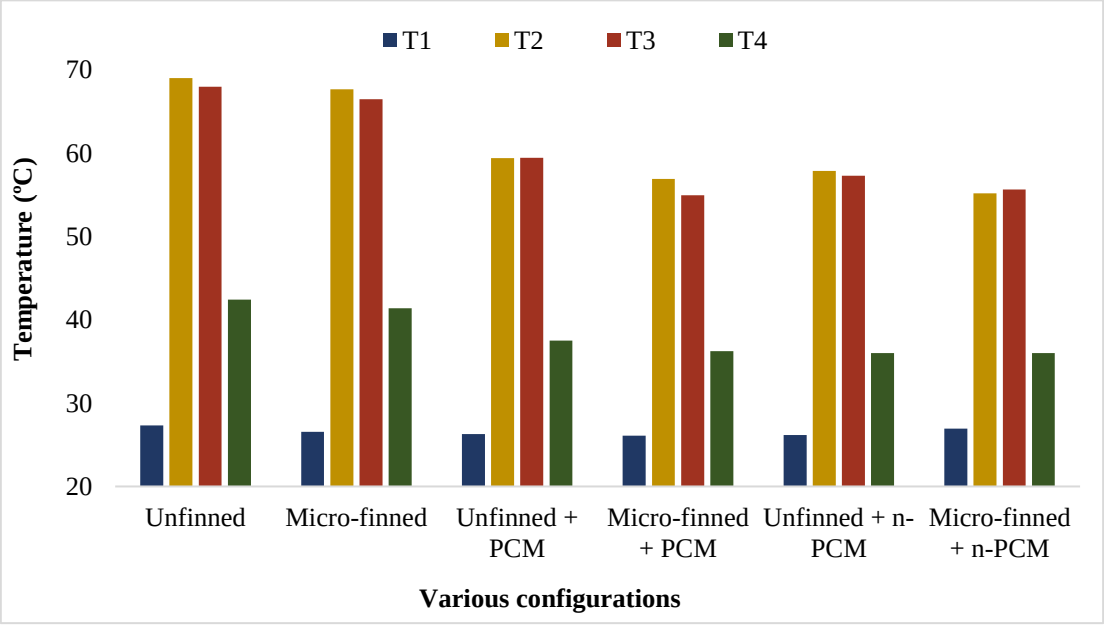

Figure 102: Comparison of average temperatures for all six configurations. (Thermocouple locations described in Figure 68).

Similarly, the maximum values of the temperature below the plate, T3, were recorded as 70.2 °C, 65.6 °C, 63.0 °C, 63.3 °C, 60.8 °C, 63.0 °C, and respectively. The maximum temperatures followed the same trend as the average temperature values. The average temperatures across all the four locations have been shown in Fig. 103 to present an alternative visual perspective for the reader.

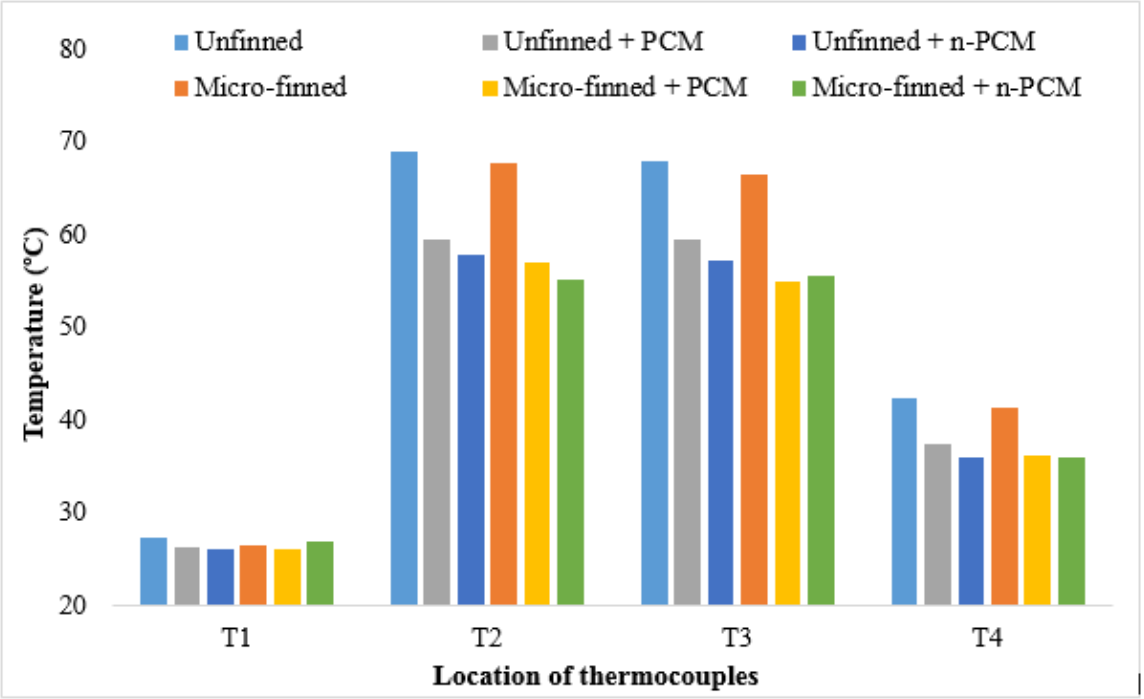

Figure 103: Comparison of average temperatures depending on the location of the thermocouple. (Thermocouple locations described in Figure 68).

As can be seen, T2, T3 and T4 were considerably higher in un-finned configurations compared to the micro-finned configurations. The use of both PCM and n-PCM, significantly reduced the average temperature. In the micro-finned systems, the average temperature at the plate centre was reduced by 10.7 °C (15.9 %) with the use of PCM and by 12.5 °C (18.5 %) with n-PCM. Similarly, in the un-finned system, PCM reduced the average temperature at the plate centre by 9.6 °C (13.9 %), and n-PCM by 11.2 °C (16.2 %). It was inferred from this data that micro-finned surfaces offered higher cooling potential compared to the un-finned surfaces, with at least 2 % greater improvement with PCM and 2.3 % with n-PCM. It can further be deduced that the sole use of micro-fins did little to reduce this temperature, while PCM provided a greater reduction in temperature both with and without fins. Furthermore, enrichment of PCM with nanoparticles yielded a small but noticeable decrease in temperature. On average, the steady temperature at the

centre of the plate measured below it, without any passive cooling provision, was reached within the first 100 min of the start-up. The temperature outside the PCM containment was measured to assess the extent of thermal insulation provided by the walls and for determining any radiative losses from the walls. It was observed that the walls were thermally insulated and only a small amount of heat could escape. The average temperatures below the plate, T3, for various configurations are plotted in Fig. 104. With natural convection, there was a rapid temperature rise in the beginning for both un-finned and micro-finned surfaces. The temperature reached 65 °C within the first 25 min of the start-up. However, with PCM, the temperature surpassed this value only for the un-finned configuration, after 120 min, thereby delaying the process by almost a factor of 5. For micro-finned surfaces with PCM, the temperature remained well below 64 °C for the duration of the experiment.

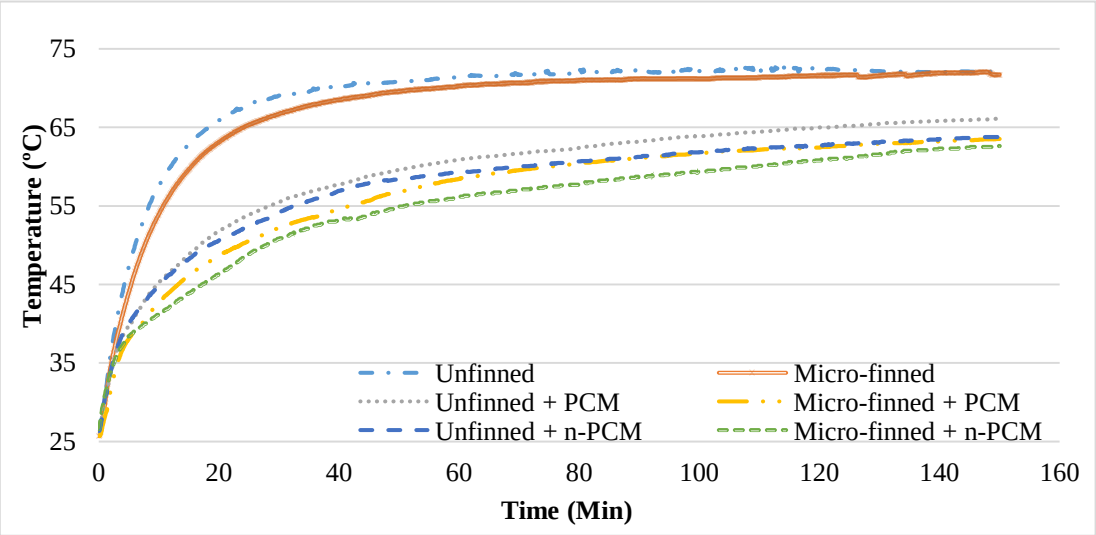

Figure 104: Temperature (average) profile obtained below the plate centre (T3) for six different configurations. (Thermocouple locations described in Figure 68).

The temperature in the PCM containment centre was another area of interest, as this ascertains the extent of PCM phase transformation. The average temperatures inside the centre of the PCM containment, T4, for all the configurations are plotted in Fig.105. As can be seen, both the surfaces, with and without micro-fins under natural convection, experienced a much higher temperature rise during the first 40 min and exceeded 45 °C before 140 min. With the use of PCM, the un-finned surface reached its peak at 43.6 °C and the micro-finned surface recorded 41.7 °C towards the end of the experiment. With the use of n-PCM, both the un-finned and the micro-finned surfaces remained below 41.5

°C throughout but there was very little difference in the temperatures for both the surfaces. The effect of nanomaterial addition seemed more pronounced with the un-finned surface as compared to the micro-finned surface because the difference between the two curves was greater than for un-finned surfaces. The reason behind this is unexplored so far, and may require further detailed analysis to confirm.

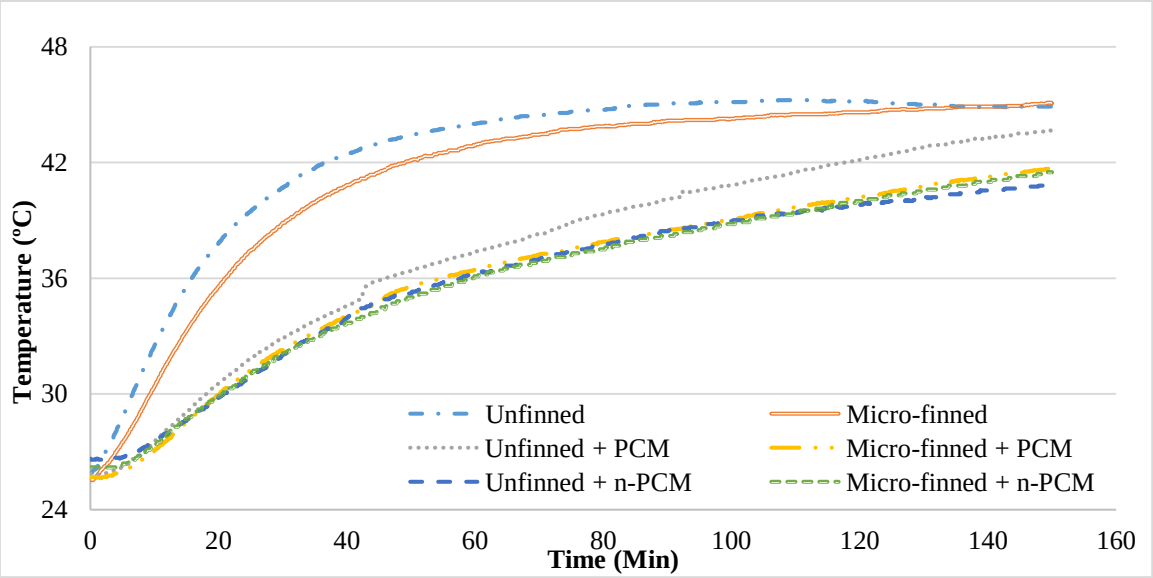

Figure 105: Temperature (average) profile obtained inside the PCM containment centre (T4) for six different configurations. (Thermocouple locations in Figure 68).

The results from the experiments as discussed above are presented below in terms of four key parameters for understanding the effectiveness of each individual passive cooling media in isolation as well as in combination. Their respective contribution to the thermal regulation of the system was defined in terms of the difference in the average temperature reduction (ΔT in °C) achieved by the system in their presence as compared to their absence. The two configurations were the un-finned and the micro-finned surfaces.

(i) **PCM effectiveness** -quantitatively determines the efficacy of PCM within the two configurations with respect to natural convection. Results showed that with the use of PCM, average temperature reduced by, ΔT = 9.6 °C (un-finned surface) versus ΔT = 10.7 °C (micro-finned surface).

(ii) **n-PCM effectiveness** -quantitatively determines the efficacy of n-PCM versus natural convection employed within the two configurations. The use of n-PCM

led to slightly higher temperature drop in the micro-finned surface, with ΔT = 12.5 °C compared to the un-finned surface, with ΔT = 11.2 °C.

(iii) **n-PCM effectiveness (versus PCM)** -compares the relative effectiveness of n-PCM to that of PCM in the two configurations. It was found that configurations with n-PCM achieved ΔT = 1.5 °C (un-finned surface) versus ΔT = 1.7 °C (micro-finned surface).

(iv) **Micro-Fin effectiveness** -quantitatively determines the effectiveness of micro-finned surface with respect to the un-finned (flat plate) with the three temperature regulation media (natural convection, PCM and n-PCM). Comparing the results, it was found that the micro-fins were capable of achieving ΔT = 1.3 °C (natural convection), ΔT = 2.5 °C (with PCM) and ΔT = 2.7 °C (with n-PCM) as compared to the un-finned plate under the similar conditions respectively.

As can be noticed, the micro-finned systems exhibited more effective thermal regulation as compared to the un-finned systems. In addition, the configurations using PCM demonstrated higher temperature reduction in comparison to non-PCM systems and consequently n-PCM performed better than PCM in thermal regulation. Another interesting theoretical aspect of this attained temperature reduction can be its correlation with the increase in the output electrical power. Based on an analytical method, the achieved temperature reduction could be converted to the increase in electrical efficiency and consequently power production for a BICPV. Assuming the temperature coefficient of maximum power point as -0.5 %/°C [52], which is a ball parked value for the BICPV panel, 12.5 °C decrease in its average operating temperature using n-PCM with micro-fins will theoretically lead to an increase of as high as 6.25 % in output power. Similarly, with the use of PCM and micro-fins, an 11.2 °C reduction in average temperature could increase the maximum output power by 5.6 %. Even in worst case scenarios of either using PCM with un-finned plate or PCM with micro-fins, a reduction of 10.7 °C and 9.6 °C will also result in 5.35 % and 4.80 % of electrical power gain respectively. It is worth noting the effect of each configuration on the heat transfer (Fig. 106). Indeed, both for the un-finned and the finned surfaces, replacing air with PCM leads to an increase in heat transfer coefficient between 16 % and 35 %. These results further confirm the advantages

of using PCM in heat transfer applications and its potential as an effective coolant in BICPV systems.

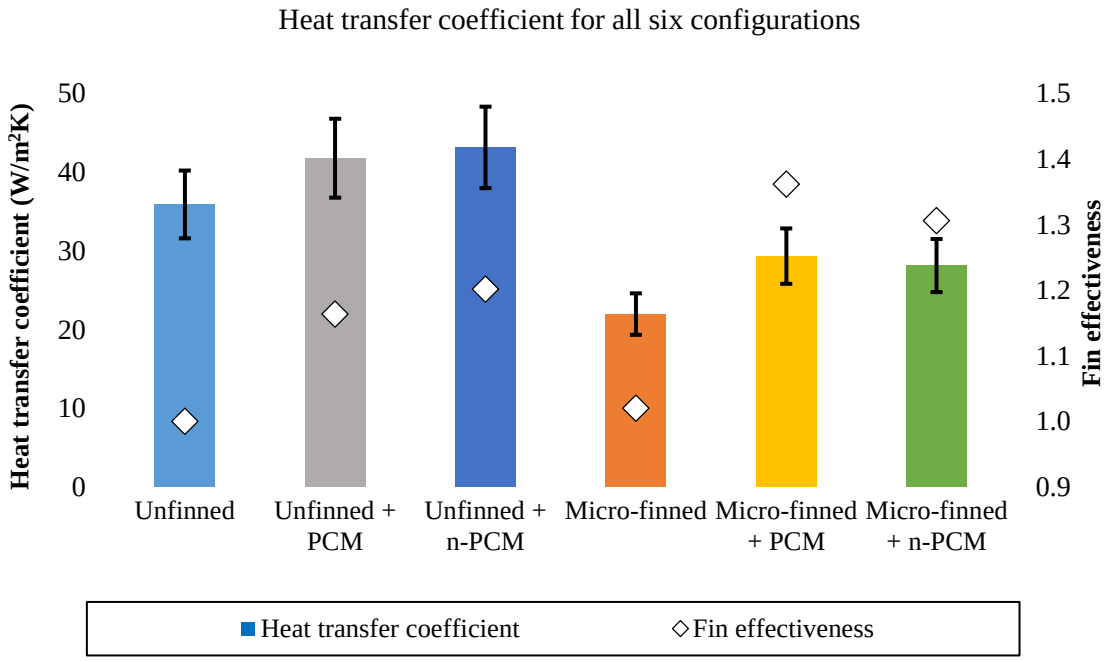

Figure 106: Heat transfer coefficients registered for the different configurations, with error bars. On the right axis, the overall fin effectiveness of each configuration compared to the un-finned surface exposed to air is reported. By definition, the effectiveness of the un-finned configuration is equal to 1.

On the other hand, in accordance with the previous literature [124], the introduction of fins causes a reduction in the heat transfer coefficient. A lower heat transfer coefficient should not be implied as a cause for reduction in thermal performance since it is mainly due to the fact that the heat transfer coefficient is calculated on the total surface area, which is larger when fins were added. Indeed, by analysing the overall fin effectiveness, defined as the ratio of the heat transfer rate for each configuration to that of the natural convection based un-finned case, it can be seen, that a combination of micro-fins and PCM can lead to an enhancement as high as 32 %. The thermal performance of the un-finned plate under the naturally convective condition was found to be superseded by the one with micro-fins, PCM, and n-PCM in increasing orders of effectiveness.

5.2.4.1 Effect of PCM type

To compare the effectiveness of two different (solid-solid and solid-liquid) types of PCM for the thermal regulation of a scaled down BICPV, their temperature profiles under constant heating were compared with a system with no applied PCM. The temperature profiles using no PCM, with a solid-solid PCM (GR42), and a solid-liquid PCM (RT42) are shown in Fig. 107. Although both GR42 and RT42 had similar melting temperature range of 38-43 °C, the steady state was reached at 147 min in non-PCM system, at 156 min with PCM GR42 and at 160 min with PCM RT42 incorporated system. The average temperature reduction achieved under the plate was 16.3 ºC with PCM RT42 and 7.6 ºC with GR42, and the maximum temperature was reduced by 12.5 ºC with RT42 and 5.6 ºC with GR42 for the duration of the experimental run (Table 32). As a result, RT42 was 9.7 % more effective than GR42 in reducing the maximum temperature and by 13.2 % in reducing the average temperature.

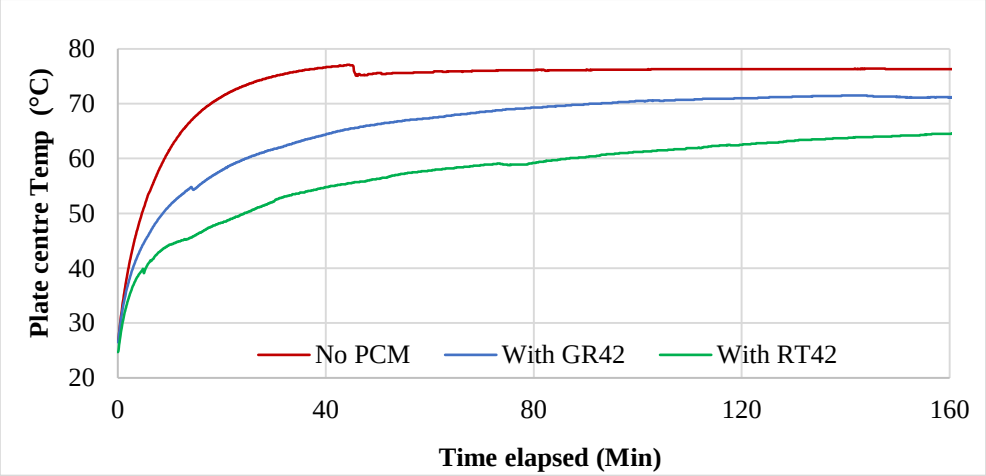

Figure 107: Temperature profile for the set up using no PCM, with a solid-solid PCM, GR42, and a solid-liquid PCM RT42.

Table 32. The average and maximum temperature reached in the system: using no cooling, with PCM RT42 and GR42.

Systems	Non PCM	RT42	GR42
Avg. Temp. (°C)	73.7	57.4	66.1
Max. Temp. (°C)	77.1	64.6	71.5

Various combinations of mass fractions can be used to produce a PCM mixture exploiting the non-leaking nature of GR42 while high utilising the higher heat capacity of RT42. The ideal fraction would contain GR42 saturated with RT42, but at which there is no visible leakage upon melting of the PCM.

5.3 DSC Analysis

For this part of the experiment, the results from the calorimetry studies are presented for PCM used within this thesis (RT42, RT28 HC, RT50 and GR 42) as well as a few additional PCM of different types (RT27, RT31, RT44 HC, PX25) which may be useful for future work. The experimentally obtained data for each specific thermophysical property is tabulated for individual runs at three different heating rates, a mean value was then obtained, and the standard deviation was calculated. In addition, the relative percentage difference between the manufacturer supplied values and the mean experimental values are also presented. The values were determined for three heating rates of 10 K/min, 5 K/min and 2 K/min. The standard deviation for each DSC run was calculated using the standard formula. The relative percentage change (% Δ) in the value of n-PCM from the value of base PCM was calculated as per Eqn. 19.

$$\% \Delta = \frac{\{(\text{Mean value of the property for PCM}) - (\text{Mean value of the property for n-PCM})\} * 100}{\text{Mean value of the property for PCM}} \quad \textbf{(19)}$$

The data obtained for two samples were prepared from the bulk material and three runs were performed on each sample. The thermograms obtained for a PCM sample with respect to Sapphire (standard material, shown by baseline) are given in Fig. 108 as an example. The three curves with different colours denote the different runs using the same samples. For pure materials, only single peak is expected to appear, however, the other smaller peaks in PCM appear as a result of polymeric nature of the material with different combinations of hydrocarbons present in it.

In order to interpret the DSC curves correctly, it is imperative to examine it for obvious artefacts, which are not caused by the samples, to avoid any misinterpretation of the results. Appendix-1 (Fig. 116) shows the examples of artefacts widely accepted [327]. The results for melting point (peak, range for onset and end), congealing point (peak, range for onset and end), specific and latent heat capacities for the many tested PCM and n-PCM samples are highlighted in Appendix-3 (Table 38-47 and Fig 117-120) .

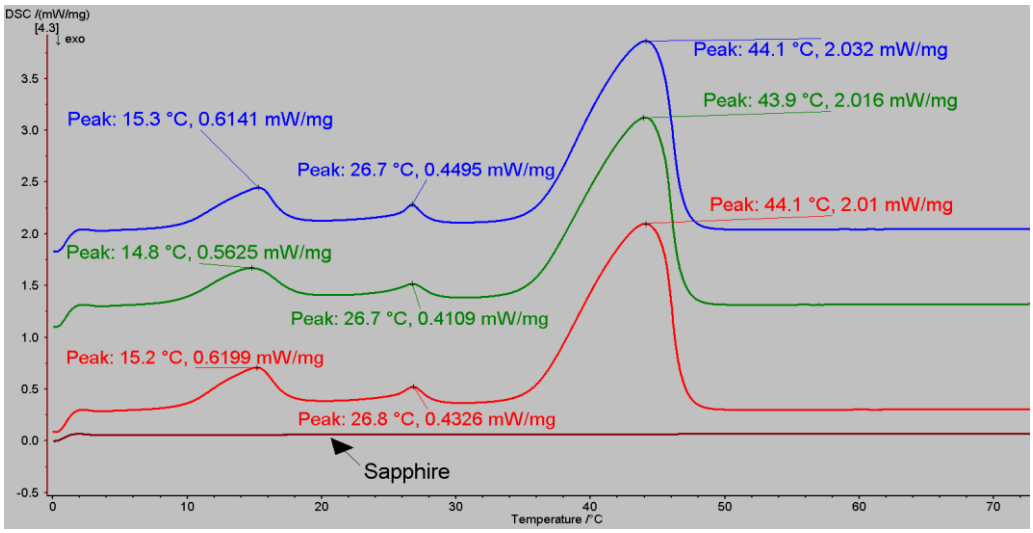

Figure 108: DSC calibration runs on a PCM sample and with Sapphire baseline.

5.4 Thermal Conductivity

For determining the thermal conductivity of n-PCM, the *Maxwell Garnett* Equation, Eqn. 20 [336] was used. The two n-PCMs tested for the experiments were: (a) n-PCM 1 (PCM RT42 + 0.5 % nano CuO by mass) and (b) n-PCM 2 (PCM RT42 + 1.0 % nano CuO by mass)

$$k_{n,PCM} = \frac{\{k_n+2k_p+2(k_n-k_p)\Phi\}.k_p}{k_n+2k_p-(k_n-k_p)\Phi} \quad \textbf{(20)}$$

where $k_{n,\,PCM}$ is the thermal conductivity of the resulting n-PCM, k_n is the thermal conductivity of the dispersed nanomaterial (for nano-CuO, k_n is 33 W/m·K), k_p is the thermal conductivity of the dispersion medium (for PCM RT42 k_p is 0.20 W/m·K) and Φ is the particle volumetric concentration (corresponding to a mass fraction of 0.5 % and 1.0 % respectively for n-PCM 1 and n-PCM 2). The effective thermal conductivity of the n-PCM 1 and n-PCM 2 using this analytical method were calculated as 0.2007 W/m·K and 0.2014 W/m·K respectively; an increase of 0.35 % and 0.70 % from the thermal conductivity values for the base PCM.

5.5 SEM analysis

The micro-structural analysis of, nano-CuO and the resulting n-PCM using SEM has been presented in this section. The morphological characterisation was carried with the aims to evaluate the degree of dispersion of the nanomaterial in the n-PCM after the

calorimetry cycle test. The purpose of carrying this exercise out was to assess if the structure of the material provided by manufacturers before shipping differed from them just before use, which may indicate any significant differences within the thermo-physical properties. As mentioned in the previous chapter, the quality of images for the n-PCM samples did not produce satisfactory results with the first SEM run, so a different route of gold sputter coating the samples was chosen before scanning using second SEM run. The images were still not of highly acceptable quality as paraffin wax samples started to charge (white appearance in dark background). The charging effect was observed due to their non-conducting nature. SEM imaging was performed for the nanomaterial CuO (60 nm) and an n-PCM (RT42 enriched with 1.0 % CuO).

5.5.1 Morphology of CuO

The surface morphology of the nano-CuO sample supplied by the manufacturer on a 1 micrometer (μm) scale (Fig. 121, Appendix-4). . It was cross-validated against the approximate particle size of a prepared layer of the nano-CuO sample. The nano-CuO micrographs are shown on different scales and resolutions in Fig. 122 (Appendix-4). The island growth of the tightly packed spherical arrangement can be clearly seen, the diameter of which varies between 65 and 150 nm. Although the supplied material sample was ground, milled and dispersed using solvents such as ethanol, agglomeration of nanomaterial can be clearly observed, showing a non-uniform distribution of the particle size, heterogeneous morphology and presence of other material.

5.5.2 Morphology of n-PCM

The n-PCM samples were first imaged without any metallic sputter coating on a scale of 200 μm and 10 μm respectively. However, to avoid the accumulation or build-up of static electric charges on the specimen surface that appear due to non-conducting nature of paraffin waxes, the samples were coated using gold sputtering. Appendix-4 shows the micrographs obtained on gold coated samples on a scale of (c) 400 μm, (d) 200 μm, (e) 20 μm and (f) 6 μm scales. One can clearly see from the figures that the charging of PCM continued to happen (bright patches seen in Fig. 123 (a) and (d)). The clarity of the images decreased with the increasing resolution and the dispersion of nanomaterial in the n-PCM could not be experimentally determined with the micrographs.

5.6 XRD analysis

Using X-Ray Diffraction, the samples were quantitatively analysed to determine the phase, structure and crystallinity. This was done by comparing the intensity of the diffraction peaks from each of the constituents to the intensity of the known phases of the pure material. Structural properties and crystalline structure of materials were also investigated using XRD technique. The rationale behind this exercise was that: (a) the nano-CuO sample didn't yield sufficiently satisfying results using SEM, possibly due to agglomeration, hence the supplier provided chemical properties had to be cross verified for the purity of nano CuO and (b) the composition of granulated PCM, GR42 wasn't known from the manufacturer's data. Further, they were unable to comment on the reactivity of its constituents upon treatment with other PCM or nanomaterial. The results from XRD analysis are described in this section.

5.6.1 Analysis of CuO

The XRD spectrum of nano-CuO nanoparticles provided by the manufacturer (though not very clear) is shown in Fig. 109 and it can be seen that the there are other constituents in a larger proportion in addition to some other materials in smaller ratios. The diffractogram image obtained experimentally is given in Fig. 110. Two reflections were observed in the diffraction patterns at $2\theta = 35.6$ and $2\theta = 38.8$ similar to [337], which attributes to the formation of the CuO as a monoclinic crystal. It was beyond the scope of the XRD programme to derive the weight fraction of the constituents in the samples. However, the presence of any common mineral or metal was easily gathered with the help of the analysis software. It was found from the diffractogram that the sample contained *Tenorite* (CuO), as well as *Cuprite* (Cu_2O) forms of copper oxides in addition to metallic copper (Cu). Tenorite occurs in the weathered or oxidized zone associated with deeper primary copper sulphide orebodies and Cuprite is an oxide mineral and a minor ore of copper, which can easily oxidise into other forms. As can be seen, there were some percentage of Cu_2O and metallic Cu present in the apparently pure sample of nano-CuO (inset of Fig. 110). It can be deduced that approximately 75 % of the material sample comprised of CuO while the rest was 17 % Cu_2O and 8 % metallic Cu.

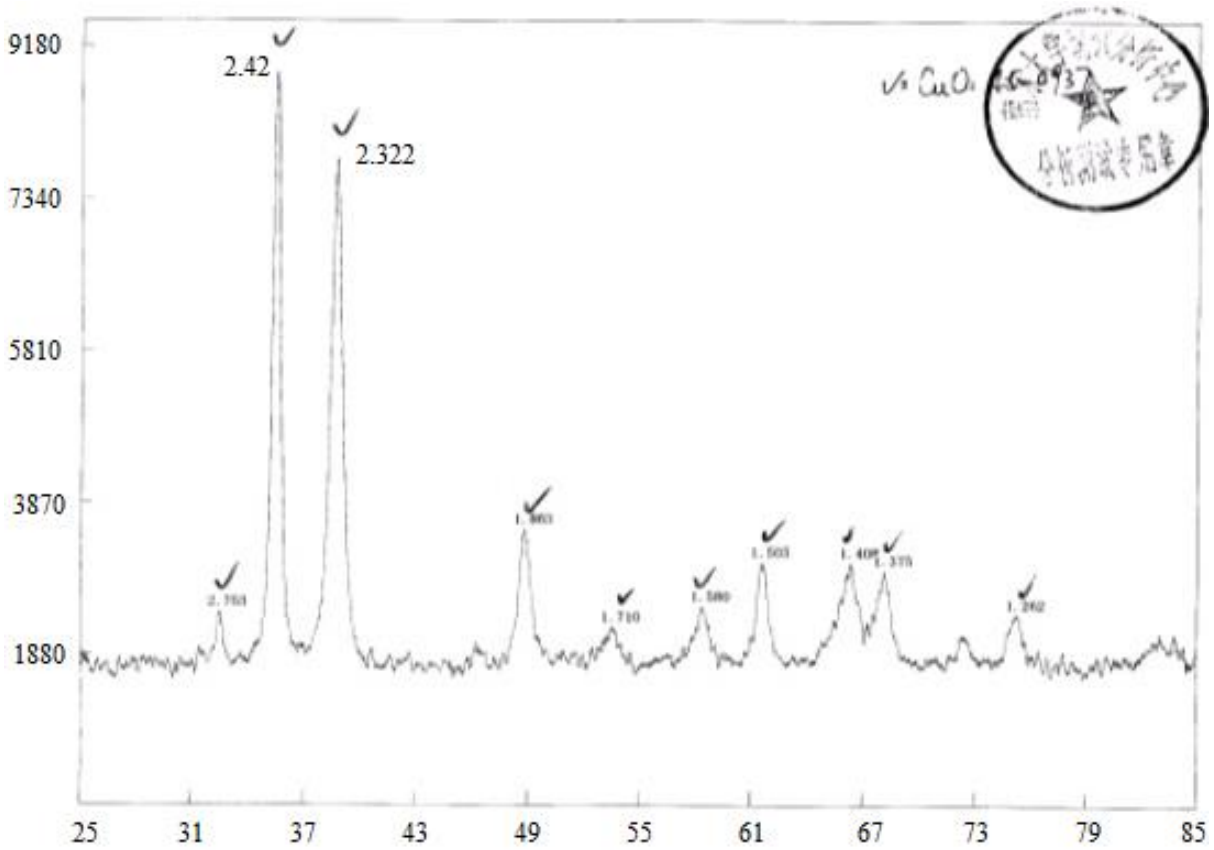

Figure 109: Manufacturer provided XRD image of the 60 nm Nano-CuO (Image was provided with an intrinsically low resolution, which can't be altered).

5.6.2 Analysis of GR42

For the granulated sample of PCM GR42, Fig. 111 displays the XRD spectrum. From the data it was found that the sample was composed of Paraffin wax in addition to Quartz and Haematite, all of which were non-reactive to other paraffin waxes as well as nanomaterials. The exact percentage composition wasn't required as this task was performed to detect the presence of any reactive constituents.

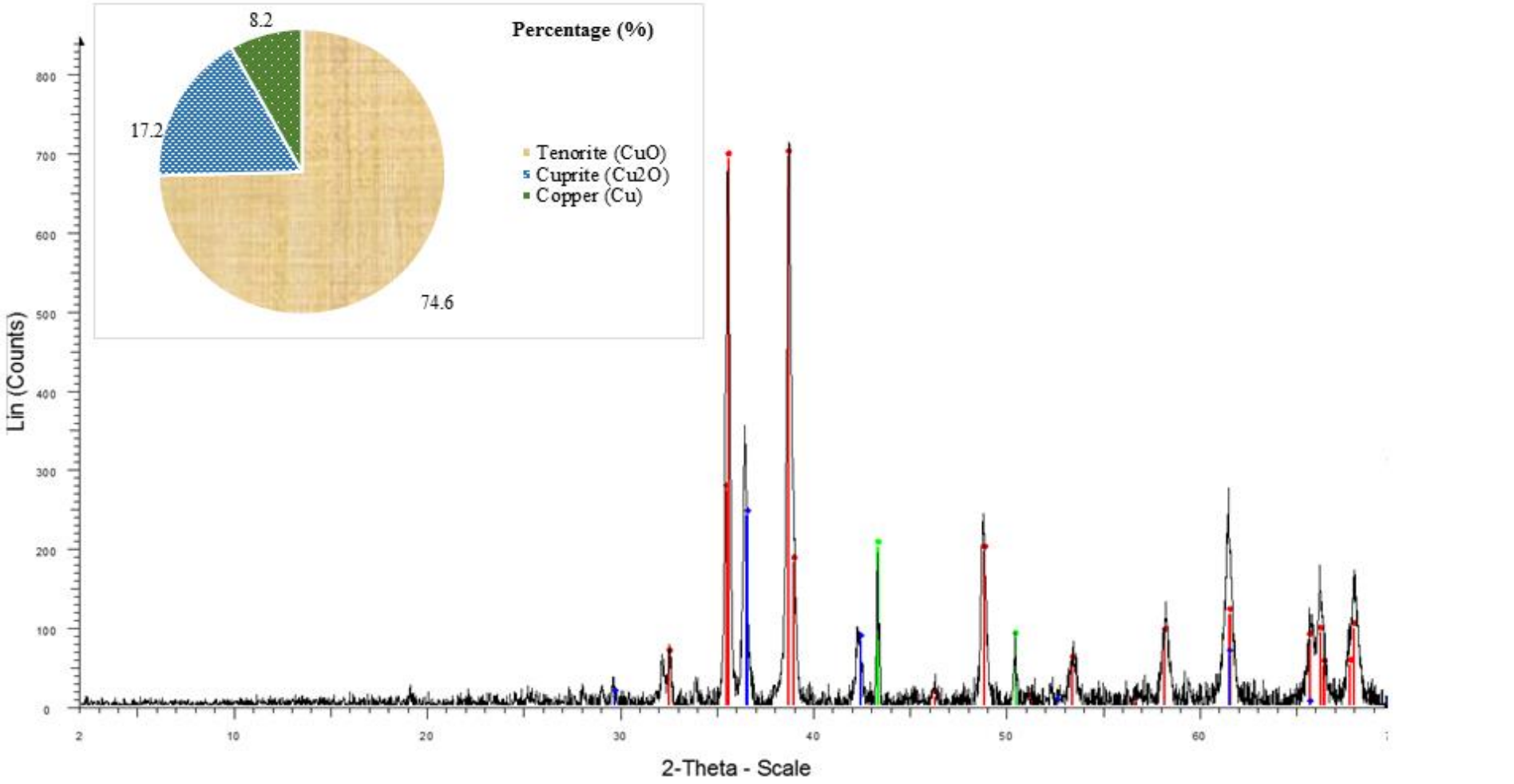

Figure 110: Diffractogram of copper oxide (CuO): Raw image with the explained colour coding below. S-Q (%) for the 60 nm Nano-CuO from the XRD diffractogram is shown in the inset.

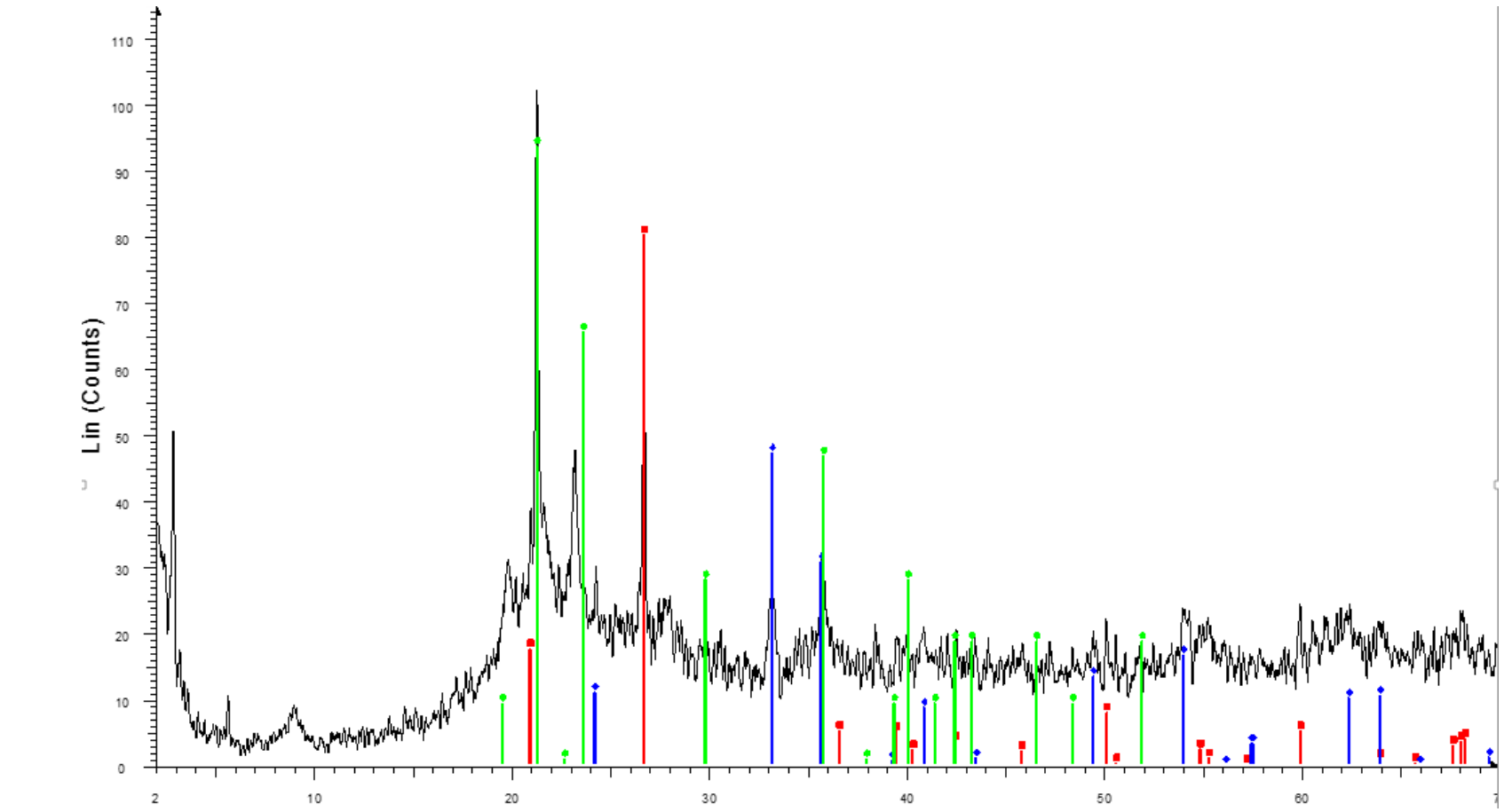

Figure 111: X-Ray diffractogram for a sample of PCM, GR42.

5.7 Experimental uncertainty and setup validation

The uncertainty of the experimental and the calculation processes was measured as described by the previous works in this field [124], by applying the formula on propagation of errors for independent variables [338]. In particular, the error occurring in determining the heat transfer coefficient of air in an un-finned configuration was calculated to determine the experimental uncertainty, where the heat transfer coefficient, h, is defined in Eqn. 21 [75]:

$$h = \frac{Q_{in}}{A_{fins} \cdot (T_{fins} - T_{air})} \quad \textbf{(21)}$$

Where Q_{in} is the input power, A_{fins} is the finned surface extension and T_{fins} and T_{air} are the steady state temperatures of the fins and of the air inside the containment respectively. Therefore, the uncertainty (Uh) was determined in Eqn. 22 [75]:

$$\frac{Uh}{h} = \sqrt{\left(\frac{UQ_{in}}{Q_{in}}\right)^2 + \left(\frac{UA_{fins}}{A_{fins}}\right)^2 + \left(\frac{UT_{fins}}{T_{fins} - T_{air}}\right)^2 + \left(\frac{UT_{air}}{T_{fins} - T_{air}}\right)^2} \quad \textbf{(22)}$$

Where the prefix U indicates the absolute uncertainty for each variable.

In accordance with [123], a conservative uncertainty of ±4 % was considered for the surface area of the micro-finned/un-finned plate. The applied electrical power was calculated from the supplied I, V measurements, which were measured in the proximity of the input connections to the heater. In accordance with the previous studies, no voltage drop was considered to have taken place in the wires between the power supply and the heater. All the uncertainties used in this analysis are shown in Table 33. Furthermore, an average deviation of 1.0 % was measured between the voltage readings and thus, taken into account for this calculation.

Table 33. Instruments' measurement uncertainties, as reported in the datasheets.

Instrument	Datasheet values in uncertainty
Fluke® 115 Service Engineers Digital Multi-meter	± (0.5 % + 2 digits) DC voltage from 0.001 V to 600 V DC current from 0.001 A to 10 A
RDXL12SD 12-Channel Temperature Recorder	± 0.4 % Measurement range (K-type): -100 ° C to 1300 °C Measurement resolution (K-type): 0.1 °C below 538 °C, 1 °C above 538 °C

Aim-TTi EX354RD dual DC power supply	Voltage: ± (0.3 % + 1 digit) Current: ± (0.6 % + 1 digit) (0 to 35 V / 0 to 4 A), P = 280W

Taking into account the steady state conditions, (8.0 V and 0.101 A of input, fin temperature of 68 °C and air temperature of 42 °C), an uncertainty of 12.6 % was found in the calculation of heat transfer coefficient. This value agrees with those reported in previous experimental micro-fins investigations [123] and is below the 20 % uncertainty span generally considered acceptable for natural convection correlations [339].

The quality of the experimental setup was then validated through a 2D model built in COMSOL Multiphysics® 5.2. Considering the simplest case for an initial investigation into validation modelling, it was based on a sufficiently appropriate 2D geometry. The behaviour of the flat surface when exposed to air within the containment, was modelled and then compared with the experimental results. The flat aluminium plate was reproduced on top of the setup (Fig. 112 (a)), the containment box (Fig. 112 (b)) was modelled using the built-in properties of acrylic plastic (1470 J/kg.K, 1190 kgm^{-3} and 0.18 $Wm^{-2}K$) and the centre of set-up is depicted in Fig. 112 (c). A 1.5 cm thick insulating layer made of polystyrene (1900 J/kg.K, 930 kgm^{-3}, 0.38 $Wm^{-2}K$) was placed on each side of the containment box. A heat flux of 0.8 W was applied to the aluminium plate and natural convection forces were simulated on the exterior surfaces of the polyethylene. The bottom surface of the setup was assumed to be mounted on a surface large enough to be at a constant temperature, such as a table. Under steady state conditions, the model returned the results as shown in Fig. 112, with a peak plate temperature of 70.9 °C, against the 68.0 °C experienced during the experiment. The temperature of the air at the centre of the box was found to be around 43.0 °C. The modelled setup returned a coefficient of heat transfer of 33 $Wm^{-2}K$, which was about 8 % lower than that registered in the experimental case. This difference falls within the experimental uncertainty calculated before, proving the reliability of the setup.

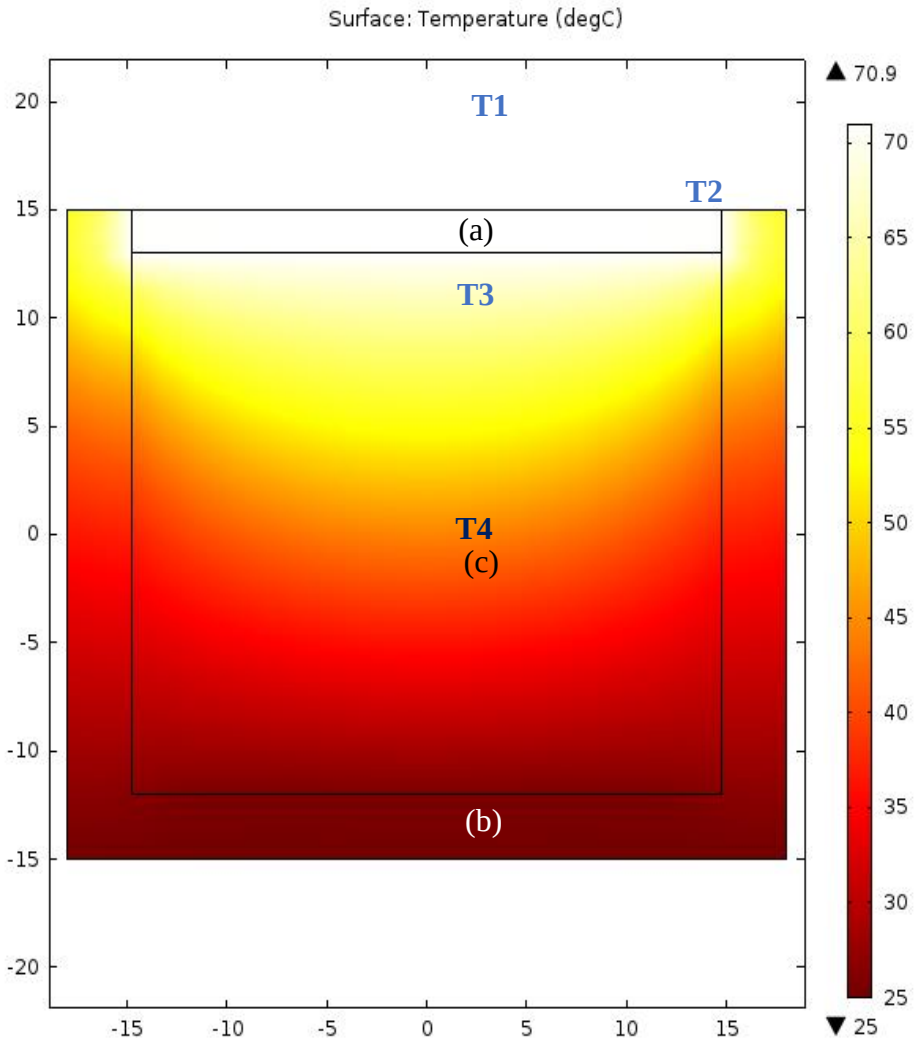

Figure 112: Results of COMSOL model for un-finned plate exposed to air under steady state conditions. The flat aluminium plate, containment and air are marked as (a), (b) and (c) resp.; the polyethylene layer is not reported. Temperature (°C), dimensions (mm). The locations of the thermocouples (T1, T2, T3 and T4) are represented too.

5.8 Other Important Observations

During the course of the experiments, a few important factors were noted which may either have internally affected the experimental outcomes to a minor extent or have appeared as an outcome of the experiments. These are listed and described below.

5.8.1 White spots/patches

Undergoing illumination for extended periods of time, white spots or patches between the encapsulant layer and the solar cells started to appear in the BICPV modules. Fig. 113 shows the white patches appearing between the soldered LACPC cells and Sylgard layer

after approximately 20 hours under the solar simulator at an intensity of 500-1200 Wm^{-2}. The effect of these could be sensed with the decrease in the output short circuit current from the module. There hasn't been much study on these patches, however, the authors of [340], who have used analogous systems for their research, described similar observations. They indicated that it may be due to uncured silicone material that gives rise to the white spots as the system is exposed to higher temperatures for elongated period of times. In addition, presence of certain materials or chemical interactions may inhibit complete curing of Sylgard such as the flux solvent used for soldering the solar cell with tabbing wire.

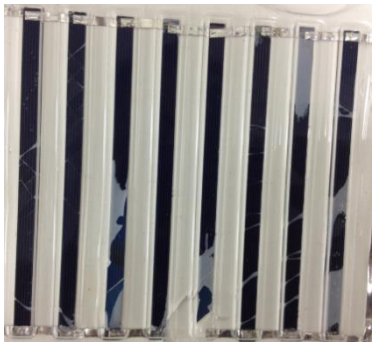

Figure 113: White spots in between solar cells and Encapsulant (Sylgard) layer.

5.8.2 Nanomaterial agglomeration

The n-PCM for the micro-finned systems was synthesised by mixing 0.5 % (by mass) nano-CuO with PCM RT42 at 60 °C to ensure the fully melted state of the PCM. The mixture was then ultra-sonicated using a Hilsonic® ultra-sonicator machine for 24 hours. The possibility of agglomeration within the nano-PCM was minimised by using the ultrasonic vibrator [250]. A low mass fraction of CuO was selected for the initial testing as the lower concentrations of TCE were found to show higher energy storage capacity with lesser costs involved [284] . Another important observation during the course of the experiment was the limitation of mixing nano-CuO with paraffin wax; namely the segregation, agglomeration and deposition of the metal oxide nanoparticles due to the difference in their densities (Fig. 114). After successive heating and melting cycles, the n-PCM showed visual signs of agglomeration and deposition of nano-CuO due to the difference in their densities. In future work, other forms of TCE or nano-particles with a density of the similar order as the base PCM could be used to overcome this. Though some tests have been performed with higher mass fraction of 1.0% for BICPV system and

DSC, it was envisaged to investigate the detailed effect of variation in mass fraction on performance in a future work, and hence this consideration does not fall in the immediate scope of this thesis.

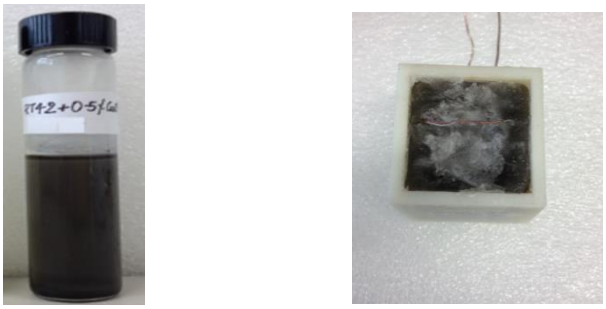

(a) (b)

Figure 114: n-PCM (RT42 dispersed with 0.5% nano-PCM): (a) homogeneous sample after ultrasonic mixing and (b) in agglomerated state after the experiments.

5.8.3 Leakage Analysis

Leakage is one the most challenging practical issues [257, 258] associated with the use of paraffin wax based PCM at temperatures exceeding than their melting range. A substantial amount of PCM leakage was observed in its melted form in those cases where the PCM containment was made using PMMA form of plastics, by sealing and joining the parts together. Every joined or screwed interface in the containment could be seen as a potential point of leakage at higher temperatures. As can be seen in the Fig. 115, there were 12 joined edges on the manually fabricated clear PCM containment while only 4 potential points of leakage in the opaque 3D printed containment. This shows that the leakage with the 3-D printed containment may have roughly reduced to one-third of its initial value quantitatively.

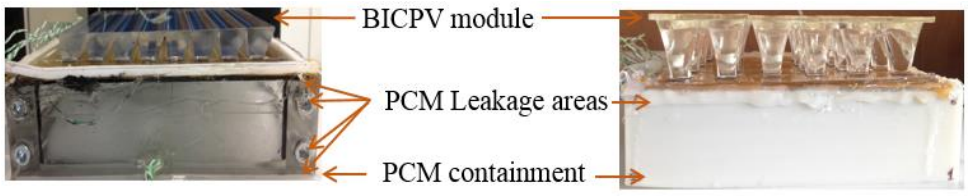

Figure 115: Leakage issues and addressing it through 3-D printing PCM containment.

Hence, the 3-D printed PCM containment, with no joined, screwed or glued parts showed significant improvement in terms of leakage control as opposed to the issues faced during previous similar works.

5.8.4 3-D printing

The PCM containments for latter studies were fabricated using 3-D print technology. This method not only contributed to substantial leakage control, but also reduced the high manufacturing turnaround time, and the associated labour plus material costs. This approach for manufacturing PCM containments using additive layer manufacturing technology has not been reported elsewhere and could pave the way for its future use.

5.8.5 Cost-Benefit Analysis

In order to analyse the cost effectiveness of the individual elements (PCM, n-PCM and micro-fins) forming the passively cooled system in tandem, a simple excel based cost-benefit model was produced. It compared the additional costs per degree temperature reduction (£/°C) for the system both individually and combined and was based on the amount of material used. The results from the cost-benefit analysis is shown in Table 3 and the details are given in Appendix-2. The assumptions are stated below:

1. It was assumed that the amount of base PCM did not change in n-PCM and that nanomaterial was just an add-on as the mass of the nanomaterial was negligible.
2. The costs of micro-finning per plate has been assumed as £ 2.0 as a ball-parked value.
3. The material costs are the actual costs per gram of the material used.

In this analysis the following were not considered:

1. The cost of 3-D printer and manual labour costs in designing the component.
2. The material cost saving due to micro-finning the surface instead of using thicker material section for producing the BICPV back plate.
3. The costs of micro-milling machine and other tools and accessories such as glues etc.

Table 34. Cost per degree temperature reduction in a micro-finned PCM/n-PCM system.

Cost/°C	**(£)**
PCM	0.044
n-PCM	0.042
Micro-fins	1.538
Micro-fins + PCM	0.226
Micro-fins + n-PCM	0.198

As can be observed from the Table 34, the cost of using n-PCM for every degree of temperature reduction was slightly lesser than the cost of using PCM. This was due to

higher temperature reduction achieved with n-PCM although the overall cost of the n-PCM was relatively higher by 45.4 % compared to the PCM costs. The cost of having micro-fins only was the highest for temperature reduction and the cost of micro-fins with n-PCM followed the one with micro-fins with PCM..

5.8.6 Module efficiency degradation

It was observed that the BICPV modules lost a part of their absolute electrical efficiencies over a period of time as they were constantly under intense irradiance levels during indoor characterisation. Though this constant high irradiance (750-1200 Wm-2) will definitely not be the case in real outdoor conditions, the lifespan of the modules must still be higher. However, with the analysis, it was found that on an average a module was degraded by almost 30 % after spending 12-15 hours under the solar simulator at intensities of 750 Wm-2 and above. At 1000 Wm-2, the BICPV modules were efficient and performed stably only during the first 10 hours of operation. This had been a deciding factor for selecting the experimental characterisation test run timing. Some of the reasons behind this reduced life expectancy over continuous use of BICPV module could be: (a) an increase in the cell's internal resistance because of the contaminants such as water vapour from the atmosphere, entering from the micro-cracks in the Sylgard layer, (b) UV exposure at higher temperatures and temperature cycling causing thermal stresses, (c) decrease in shunt resistance of the silicon cells at high temperatures, (d) the age of the solar cells (they had been stored previously for almost 7 years), (e) inefficient soldering of cells causing issues within the internal circuitry, and (f) the deterioration of the Sylgard layer causing white spots that prevent proper penetration of the irradiance.

5.9 Discussions

Going back to the research questions outlined initially (section 1.7), this section aims to describe whether and how have they been addressed. While the qualitative assessment has been detailed below, quantitative results are presented in the next section.

i. What will be the quantified electrical and thermal performance enhancement achieved by BICPV-PCM systems with respect to naturally ventilated BICPV. In other words, what benefits can be expected by introducing PCM for passive cooling of BICPV systems realised through experimental studies?

In all the four BICPV systems, addition of PCM achieved at least a 7 % increase in the output average electrical power. The heat absorption in PCM also reduced the overall average temperature of the BICPV panel. It may be concluded that these original experimental investigations to establish the PCM effectiveness for thermal management of BICPV were successful, a field which was unexplored before.

ii. Which combination materials can be synthesised via enriching PCM with nanomaterials? What will be the morphological and thermo-physical properties?

To address this, a low cost, relatively easily available, and non-toxic nanomaterial, nano CuO with an average particle size of 60 nm was dispersed in PCM RT42, in two mass ratios of 0.5 % (n-PCM 1) and 1.0 % (n-PCM 2). The morphology of nanomaterial was studied using a scanning electron microscope but it did not match with the manufacturer provided data for particle size. The reason for this was the agglomeration of the particles to form bigger lumps at a nanoscale. However, this did not affect the experimental results vastly on a macroscopic level. The dispersion of the n-PCM within PCM was also attempted to be studied using SEM, but could not yield meaningful results due to the charging of the PCM. The alternate solution, to sputter coat the sample with gold nano-layer, also did not prove effective. The inevitability of this issue was rooted in the non-conducting nature of the paraffin waxes. Nevertheless, the obtained images and micrographs are added within this thesis. The thermal conductivity enhancement provided by adding low proportions of nano-CuO (with k =33 W/m·K), was very little as the effective thermal conductivity of the n-PCM was calculated to have a 0.35 % increase. This could be increased with materials with higher thermal conductivity such as carbon nanotubes (with k of the order of 2000 W/m·K).

iii. What will be the expected performance enhancement realised within the mentioned BICPV system using laboratory synthesised n-PCM?

With respect to PCM, n-PCM proved effective by over 3 % in terms of improving electrical power output in one BICPV system. The n-PCM 1 proved more effective for temperature regulation in two experimental cases compared to n-PCM 2.

iv. How does variation in the following parameters affect the output power from, and the efficiency of, the BICPV in question?

- Levels of concentration - In order to study the effect of these parameters, various concentrators such as LACPC, SEH with different concentration ratios, were used

for fabricating the BICPV and no major differences were observed with regards to PCM application.

- Solar irradiance levels - A range of irradiance (500 Wm^{-2}, 750 Wm^{-2}, 1000 Wm^{-2}, and 1200 Wm^{-2}) were selected to repeat the experiments. It was found that PCM RT42 was more effective at higher intensities of over 750 Wm^{-2}, due to its melting range corresponding to the temperature rise in the BICPV.
- Heatsink designs - The heatsink design for PCM containments in all cases were based on a previously reported analytical model for flat-plate BIPV-PCM systems from literature. However, due to mathematical inadequacy, a new and refined BICPV-PCM model for designing was proposed.
- Material used for PCM containment - The two materials tested for fabricating the PCM containments were 13-mm thick Perspex sheet (cast *Poly-methyl methacrylate*) and 3-mm thick ABS plastic (*Acrylonitrile butadiene styrene*). It was easier to machine the latter and due to its lightness, the overall system bulk of the BICPV-PCM system wasn't increased, an important aspect for such systems. In addition, ABS based PCM containment was 3-D printed as a single part, exhibiting nominal PCM leakage upon melting into liquid form.
- Heat exchanging media - in addition to latent heat media (PCM), a sensible medium (water) was used to compare its effectiveness. Although water proved more effective, it was predominantly due to the circulation effect.

v. Can BICPV-PCM/n-PCM systems work in tandem with micro-finned back-plate, and if so, what will be the individual as well as the combined effectiveness of the elements constituting the passive-passive thermal management?

With micro-fins, PCM (and n-PCM) increased in effectiveness by 1.1 °C (and 1.3 °C), although micro-fins alone provided little cooling potential compared to the un-finned surface. Further, micro-finning the back plates were also envisaged to reduce the system bulk and reduce the mass specific power of BICPV systems.

vi. What will be the quantifiable effect of applying a sensible versus a latent heat media, to the thermal regulation of BICPV systems?

As expected, a sensible media has far more potential for temperature control as compared to a latent media. However, the experimental results revealed that the difference in the performance wasn't too great, with only 8 % and 6 % higher electrical efficiencies

compared to the two PCMs with a lower and a higher melting temperature range. This analysis did not consider any energy expenditure for the circulation of water since the natural supply head was the driver. If this was included, potentially the system may hardly reach a break-even for the cooling with water scenario or it may prove even more expensive or power consuming than the additional power produced

5.10 Conclusions

The detailed indoor experimental characterisation of the fabricated BICPV-PCM systems for electrical and thermal performances were performed using a highly collimated solar simulator at selected solar radiation intensities, and at a 0° angle of incidence. The four systems were first characterised in natural convective heat transfer conditions with no applied cooling. Passive cooling mechanisms, predominantly PCM and in later stages, n-PCM were used to investigate the extent of thermal regulation achieved as compared to natural cooling. The effect of PCM on temperature reduction and electrical performance was measured in absolute and relative terms. Further, other parameters were varied to assess their effect on BICPV temperature control using PCM such as: (a) operating parameters (irradiance), (b) design considerations (different types of concentrators, 3-D printing technology), and (c) material considerations (granulated solid-solid PCM, enhancing thermal conductivity with metal mesh and nanomaterials). A brief summary of results from electrical and thermal characterisation are given below.

- For BICPV-PCM systems, average panel temperature was significantly reduced by using a PCM and this effect was enhanced by adding passive means such as micro-fins and thermal conductivity enhancers using mesh and nano-CuO.
- A steep increase in temperature and corresponding reduction in maximum power was observed during the first 30 min using PCM.
- The module temperature increased linearly with the increase of irradiance. At 500 Wm^{-2}, 750 Wm^{-2}, 1000 Wm^{-2} and 1200 Wm^{-2}, the respective average back-plate temperature for LACPC system was reduced by 4.8 °C (13.2 %), 10.1 °C (23.1 %), 3.8 °C (7.6 %) and 6.6 °C (12.2 %) with RT42. The relative increase in maximum electrical power output was of 1.15 %, 4.20 %, 7.70 % and 6.80 %.

- For SEH system, average temperatures with PCM were reduced by 4.8 °C and 7.4 °C at 500 Wm^{-2} and 1000 Wm^{-2} respectively. An increase of 17 %, 19 % and 25 % in average P_m was observed with RT28HC, RT50 and circulated water.
- The thermal regulation improved when PCM was replaced by n-PCM. The average temperature with PCM was reduced by 9.6 °C (13.9 %) and 10.7 °C (15.9 %) in un-finned and micro-finned surfaces respectively while with n-PCM, it was 11.2 °C (16.2 %) and 12.5 °C (18.5 %) respectively.
- The average temperature reduction at 500 Wm^{-2} with n-PCM 1 were higher (5.1 °C, 5.3 °C, 4.8 °C, 4.9 °C, and 4.1 °C) than with n-PCM 2 (2.4 °C, 4.6 °C, 3.2 °C, 3.4 °C, and 3.9 °C). At 1000 Wm^{-2}, the respective reduction were (22.0 °C, 19.7 °C, 30.5 °C, and 20.8 °C) with n-PCM 1 and (18.9 °C, 27.7 °C, 20.8 °C, 21.2 °C, and 29.2 °C) with n-PCM 2. Higher concentrations of nanomaterials did not prove beneficial for improving the thermal management.

Some other conclusions from the perspectives of material characterisation, cost benefits, and design and running of the experiments are presented as follows:

- Using XRD analysis, GR42 was found to be composed of Paraffin wax, Quartz and Haematite, and nano-CuO sample contained Cuprite and metallic copper.
- Segregation, agglomeration and deposition of the metal oxide nanoparticles was observed in n-PCM due to the difference in their densities.
- White spots were formed in BICPV over a period of continuous use at high irradiances. These were responsible for the degradation of output efficiency.
- The cost per degree temperature reduction using n-PCM was slightly lesser than that using PCM. The cost (£/°C) of having micro-fins only was the highest at 1.54 for a unit temperature reduction and the cost of micro-fins with n-PCM (0.19) followed the one with micro-fins with PCM (0.23).

From the results obtained within this chapter, it could be concluded that the introduction of passive cooling mechanisms such as PCM, n-PCM and even producing micro-finned back-plate for BICPV systems have been highly effective in thermal management as well improving the electrical efficiencies. PCMs have also proved to improve the uniformity in BICPV average temperatures thereby offering a potential to increasing their lifespan.

Chapter 6. Conclusions and Recommendations

This final chapter draws conclusions from different aspects and phases involved in the experimental work carried out within the thesis; material selection, design, fabrication of components, assembling systems and characterisation. It presents an overall synopsis of the lessons learnt, limitations of the work, the achievements and future perspectives for the research area, with focus on adopting new materials, methods and approaches.

6.1 Summary

This thesis conducted experimental investigations on innovative solutions to improve the electrical performance of BICPV using passive temperature regulation. The research followed two directions: (a) the development of different BICPV-PCM assemblies based on low concentration CPV combined with mostly paraffin wax based organic PCM, to examine the effects of passive cooling on BICPV efficiencies and (b) the development of nanomaterial enhanced phase change material (n-PCM) for addressing low thermal conductivity of paraffin wax and analysis of thermophysical properties. In addition to this, a study on the applicability of micro-fins for the passive cooling of BICPV was also included in the first direction as an additional means of passive cooling. Both these studies have been conducted with the aim to contribute to the development of a low-cost and reliable BICPV thermal management method. The important outcomes of the work are resumed in the following paragraphs.

6.2 Selection of materials and components

Within this study, the solar receiver/BICPV is considered as the heat source. The PCM system, which acts as a heat sink, consists of PCM containment and organic PCM/n-PCM. A summary of the most common materials available for BICPV-PCM system and the suitability of the selections have been presented. Among the various available materials, most appropriate materials were selected on the basis of a literature survey.

- Organic PCM were used for latent heat removal as they are safe to use (non-toxic), cheaply available and are approved for building use in many countries.
- Finer nanomaterials with smaller average particle size (60 nm) were more efficient with prolonged dispersion in base PCM, increasing the effectiveness of the n-PCM in the long run.

- Despite adding nominally to the costs of machining, micro-finned plate was used to assess its effectiveness in possible applications as a BICPV back plate.
- In the first instance of testing the effects of k enhancement on PCM effectiveness, a copper mesh was selected due to low costs and availability.
- Nano CuO material was preferred due to higher thermal conductivity although metallic nanomaterials are more conductive, they cost 6-7 times more. In addition, the density of Cu is higher which leads to more particle segregation reducing its effectiveness over continuous charging/discharging cycles.
- Finer nanomaterials with smaller average particle size (60 nm) were more efficient with prolonged dispersion in base PCM, increasing the effectiveness of the n-PCM in the long run.

6.3 Conclusion from design and manufacturing aspect

One of each four different BICPV systems were fabricated using LACPC and SEH concentrators with a low concentration ratio (< 10x) as per the standard process in literature. However, the thick glass back-plate was replaced with a thin aluminium plate. The top glass cover was also removed and PCM containment was added at the back which reduced the bulk of the BICPV by more than 5 times.

- For same output power, the LACPC-BICPV system with a concentration ratio of 2.8 saved almost 50 % of the required number of solar cells and SEH based BI/WICPV required 60 % less PV material compared to a flat PV.
- The PCM containment was first produced by mechanical means and the components were manually picked-and-placed. However, PCM leakage indicated a need for improvement. PCM containments for latter studies were fabricated using 3-D printing, which controlled leakage substantially and in addition, reduced the high manufacturing turnaround time, and material costs.
- Micro-fins proved beneficial in terms of higher mass specific power or mass to power ratio. System bulk is an important consideration in BICPV.

6.4 Conclusion from electrical characterisation

Overall, PCM into BIPCV increased P_m by various percentages depending on melting temperature range of PCM and irradiances. The results for electrical characterisation have been concluded in Table 35.

PCM effectiveness is presented in terms of increase in the average output electrical power (P_m). The salient points are listed below:

- PCM proved more effective at higher (1000 Wm^{-2}) compared to lower intensities (500 Wm^{-2}). This was a direct result of PCM melting temperature (38 °C-43 °C). PCM with lower range may prove effective, but due to 30 °C ambient conditions in the laboratory it was not possible to select a lower melting PCM.
- Introduction of copper mesh as TCE showed a 1.7 % increase in the average P_m. The effect of using a higher melting PCM RT55 was found to increase P_m by 4.1 %, (3.7 % lesser than RT42). Insulating back plate with a lightly insulating material reduced the power output by 2.3 %.
- Introduction of nanomaterial (0.5 % mass fraction) into PCM proved beneficial in SEH system, by 7.2 % at 500 Wm^{-2} and 6.7 % at 1000 Wm^{-2}. However, increasing the mass fraction to 1.0 % did not yield expected positive results. The result for this could be the saturation of the available PCM, agglomeration of nanomaterials or attributed to the degradation in the overall module efficiency.

Table 35. PCM effectiveness in terms of increase in the average output electrical power (P_m) for all the experimentally tested systems.

			Average P_m (mW)		
Configuration	**PCM**	**Irradiance (Wm^{-2})**	**Without PCM**	**With PCM**	**Change (%)**
LACPC based BICPV	RT42	500	336.1	340.3	1.3
		750	472.7	492.5	4.2
		1000	581.7	626.4	7.7
		1200	625.7	668.4	6.8
	RT42+ mesh	1000	692.7	719.6	3.7
	RT55	1000	625.8	647.1	4.1
SEH based WICPV	RT50	500	960.0	1010.0	6.5
		1000	1740.0	1940.0	17.0
SEH based BICPV	n-PCM 1	500	257.6	276.2	7.2
		1000	489.2	521.9	6.7
	n-PCM 2	500	257.6	239.8	-6.9
		1000	489.2	428.9	-12.3

6.5 Conclusion from thermal characterisation

The thermal characterisation of the four different BICPV-PCM systems; (i), (ii), (iii) and (iv) the micro-finned PCM system are presented here. The effect of using PCM in terms

of maximum and minimum temperature reduction is given in Table 36 and the average values are compared in Table 37. It has been observed that PCM/n-PCM have been able to reduce the maximum system temperature between 6 % to 34 % depending on the configuration while the average temperature by at least 7.5 % and a maximum of 30 % compared to the systems with no PCM.

Table 36. Thermal regulation provided by PCM in terms of maximum and minimum temperature reduction for all the experimentally tested systems.

		Without PCM		**With PCM/n-PCM**			
Configuration	**Irradiance (Wm^{-2})**	**Max. Temp (°C)**	**Min. Temp (°C)**	**Max. Temp (°C)**	**Min. Temp (°C)**	**Max Change (%)**	**Min Change (%)**
LACPC based BICPV	500	38.7	36.0	33.2	31.0	14.3	13.7
	750	47.6	45.5	37.6	34.3	21.1	24.7
	1000	55.2	51.5	49.2	44.5	10.9	13.5
	1200	59.8	56.8	52.7	47.6	11.9	16.1
SEH based WICPV	500	51.9	45.1	46.5	41.5	10.4	8.0
	1000	65.0	56.5	61.1	55.6	6.0	1.6
SEH based BICPV	500	43.7	37.7	39.5	37.2	9.6	1.3
	1000	72.7	70.0	50.9	35.4	30.0	49.4
	500	43.7	37.7	39.9	33.1	8.7	12.2
	1000	72.7	70.0	47.7	40.6	34.4	42.0
Micro-finned system for BICPV	NA	72.1	70.2	63.8	63.0	11.5	10.3

Table 37. Thermal regulation provided by PCM in terms of average temperature reduction for all the experimentally tested systems.

		Average Temp (°C)		
Configuration	**Irradiance (Wm^{-2})**	**Without PCM**	**With PCM**	**Change (%)**
LACPC based BICPV	500	36.3	31.5	13.4
	750	43.8	33.8	22.9
	1000	50.1	46.4	7.5
	1200	54.2	47.7	12.1
SEH based WICPV	500	46.1	39.5	14.3
	1000	53.7	48.9	8.9
SEH based BICPV	500	40.8	36.6	10.3
	1000	66.2	46.3	30.1
	500	40.8	37.4	8.3
	1000	66.2	45.0	32.0
Micro-finned system for BICPV	NA	36.3	31.5	13.4

- Micro-finned systems with PCM reduced the average temperature at centre by 10.7 °C (15.9 %) and 12.5 °C (18.5 %) with n-PCM. Similarly, for the un-finned system, using PCM and n-PCM reduced the respective temperatures by 9.6 °C (13.9 %) and 11.2 °C (16.2 %), indicating higher micro-finned cooling potential.
- From the baseline comparisons on un-finned and finned heat sinks, the fin effectiveness in natural convection, with PCM, with n-PCM were demonstrated by decrease in average central plate temperature by 1.3 °C, 2.5 °C and 2.7 °C.
- PCM produced a clear enhancement in heat transfer for any investigated configuration. Indeed, enhancements as high as 35 % in heat transfer coefficient were registered when air was replaced with PCM. It was demonstrated that PCM and micro-fins can result in a fin effectiveness as high as 1.32.
- The module centre showed significantly higher temperatures than other parts. With the use of PCM, temperature variation was reduced for all cases and experimental conditions. It can be inferred that PCM can reduce thermal disequilibrium within the module, reduce hot spots formation and avoid untimely degradation of the modules.

6.6 Material characterisation

6.6.1 DSC

- A list of various types of PCMs either used within this thesis or are considered useful for future work were analysed for charging (melting)/ discharging cycles. At 10 K/min, measured values were substantially higher for almost all PCMs, while at 2 K/min, supplier's data proved closer to measured values.
- The melting onset temperature was slightly decreased at higher heating rates in n-PCM 1 and substantially increased in n-PCM 2. The change in experimental values for PCMs compared with supplier's data were 12 % on either side.
- Nanomaterial addition increased the solidification end temperature for most heating rates compared to the base PCM. The experimental means were lower than manufacturer's values, suggesting a higher degree of super cooling.
- The experimental values for latent heats were lower than the manufacturer's for the PCMs, indicating reduced heat storing capacity. They may prove 2-8 % less for certain PCMs and up to 44 % for others in both solidification and melting.

- The specific heat increased marginally for n-PCM 1 and further more for the n-PCM 2 compared with the base PCM for both melting and solidification.

In addition, the analytical method for calculating the effective thermal conductivity of n-PCM 1 and n-PCM 2 showed the respective values as 0.2007 W/m·K and 0.2014 W/m·K; an increase of 0.35 % and 0.70 % from thermal conductivity of base PCM.

6.6.2 SEM & XRD

- The micrographs were produced on different scales and resolutions (30 μm to 500 nm) without and with a micro-nano-layer of gold sputter coating of PCM samples. The island growth of the tightly packed spherical (diameter of 65-150 nm) arrangement, could be seen in nano-CuO in addition to agglomeration, non-uniform distribution of the particles and the presence of other material/s.
- The attempt to explore the morphology and dispersion of nano-CuO in n-PCM samples was held back by the accumulation of static electric charges on the surface due to the non-conducting nature of paraffin waxes.

6.6.3 XRD

- It was concluded that GR42 composed of Paraffin wax, Quartz and Haematite, all of which were non-reactive to other paraffin waxes as well as nanomaterials.
- The diffractogram confirmed the presence of Cuprite (Cu_2O) forms of copper oxides in addition to metallic copper (Cu) in the nano-CuO samples with approximate content of 17 % and 8 % respectively.

6.6.4 Cost-Benefits

- The cost per degree temperature reduction using n-PCM was lesser than PCM due to higher temperature reduction, although the material cost for n-PCM was higher by 45.4 %. The cost (in £/°C) of micro-fins only was the highest at 1.54 while for micro-fins with PCM, it was 0.23 and micro-fins with n-PCM at 0.19.

6.7 Limitations

The limitations of this thesis and the experimental work are discussed as follows:

- Characterisation: taken place indoors within the lab, so outdoor behaviours of the BICPV and BICPV-PCM systems are not included.

- PCM: except low k (associated with organic PCM), no other limitations (subcooling, flammability etc.) were addressed. Only charging of PCM was studied as experiments were conducted indoors using a solar simulator.
- Role of PCM: only PCM is used as heat removal media and not as a storage.
- This thesis is mostly based on experimental work with some mathematical analysis and an application of simulation.
- Micro-fins: the effect of varying micro-fins dimensions etc. are not covered.
- The BICPV life span was compromised due to degradation of Sylgard in almost 35-40 hours of running because of the decomposition of chemical compounds. The performance deterioration was also apparent due to overheating of cells for prolonged hours. Hence the system did not show high stability over time.
- While casting concentrators, some micro-bubbles were trapped inside the liquid. This may have affected the clarity as well as the effective concentration ratio.
- The solar cells were individually tested after soldering but a small minority of them failed during experiments, due to their ageing.
- The life expectancy of BICPV in continuous use reduced due to: (a) cell's internal resistance (increases because of contaminants such as atmospheric water vapour that seeps through the Sylgard micro-cracks), (b) thermal stresses (due to UV exposure at higher temperatures), (c) shunt resistance decrease in solar cells at high temperatures, (d) age of solar cells (stored for over 7 years before use), (e) internal circuitry issues (inefficient soldering) and (f) Sylgard degradation leading to the white spots formation that inhibited penetration of the light.
- n-PCM showed agglomeration, deposition of nanoparticles upon successive heating and melting, due to the difference in their densities. Although CNT, would suit best with thermal conductivity of 2000 W/m·K and bulk density almost four times lesser (maximum mass density of 1.6 g cm^{-3}) than CuO (6.3 g cm^{-3}), due to high material costs (30-130 times more expensive with C-grade: US$ 20.00, X-Long grade: US$ 75.00 per gm compared to US$ 0.59 per gm for CuO), they were not considered for the initial phase of TCE investigations.

6.8 Achievements

As part of the UK Department of Energy and Climate Change 2014 Solar PV Strategy [4], the emphasis as a key target is changing significantly towards increasing solar

PV rooftop installations. The present study was conceived as an incremental contribution towards those goals by helping unlock the huge potential for building-integration of PV across the UK. The salient points of achievements are given below:

- This thesis reports novel approach for enhancing electrical performance of the present day low-concentration BICPV passively with PCM which has not been reported before. This is the first instance of work relating thermal management of BICPV to efficiency increase. In previous studies on BIPV-PCM, primarily focus was on temperature regulation and melt fraction, i.e. the PCM containment part of the system. In this study, however, thorough investigation was carried on the effect on electrical parameters including efficiency, output I_{SC}, V_{OC} and P_m.
- As yet, the proposed mathematical model for BICPV-PCM systems is the only optimised analytical model for designing such systems. Previously used BIPV-PCM model was mathematically incongruent so, revised model was proposed.
- BICPV cooling using simple passive means such as micro-finned back-plate combined with PCM/n-PCM were developed. The low thermal conductivity of paraffin wax based PCM was successfully addressed using inexpensive TCE.
- The experimental investigation in this study has allowed identifying the most favourable passive cooling solution to BICPV temperature rise. The use of micro-fins with PCM and n-PCM for the passive cooling of BICPV have not been previously reported. The micro-fins showed dual benefits: reducing the system temperature and material and mass; enhancing the mass specific power.
- The use of PCM and n-PCM has proven to reduce the hot-spots in BICPV; a local overheating phenomenon leading to damaging effects such as failure of solar cells or cracking of encapsulating layer exposing the cells to environment.
- To address practical challenges such as leakage, high manufacturing turnaround time and associated costs, 3-D printing was used to fabricate PCM containments. This approach for containments manufacturing using additive layer manufacturing has not been found in literature and could pave way for the future use with market penetration.
- The specific knowledge accumulated on the issues and the challenges related to fabrication and long-term working of BICPV-PCM systems have been recorded, contributing to the development of more reliable and competitive systems.

6.9 Future Recommendations

The major objectives of the project were achieved and are reported in detail in the present thesis. However, a full scale outdoor characterisation of the BICPV-PCM systems would allow refining the presented design and material. A long term outdoor testing would also prove the durability of the developed BICPV-PCM systems and highlight any modifications that may need introducing. Moreover, BICPV with the micro-finned back plate with PCM and n-PCM in outdoor testing will lead to more accurate results on the PCM effectiveness as well as provide the data for studying their discharging. Finally, new ideas to be investigated have emerged during the current study. Hence, a list of recommendations for future works is reported here. They are categorised into component level, system level and application level:

(i) Component-level recommendations:

- Improve BICPV quality fabrication by automated processes for soldering solar cells and manufacturing concentrators. Use more appropriate soldering wires (material and dimensions) to avoid resistive losses within the internal circuitry.
- Other n-PCM such as CNT nanomaterial, in varying mass proportions, can be used. Inorganic PCM such as SP 31 or powdered PCM such as PX 25 can also be investigated, for which the thermal analysis are presented here.
- Composite PCM (varying mass proportions of granulated/organic PCM) such as GR42+RT42, can be treated with metallic nano-material for ideal combinations of leak-proofing and higher thermal conductivity.
- Finer nanomaterials (60 nm average particle size) helps in more efficient dispersion and for longer periods in the base PCM although CNT would be the best choice as their densities are almost a quarter of the density of nano-CuO.
- Encapsulation of PCM in Aluminium or HDPE shells for improved leakage control, ease of manufacturing, and fire safety of the system.

(ii) System-level recommendations:

- Investigate the relationship between micro-fin parameters (effectiveness, geometry etc.) for optimising heat sinks designs. Benefits for CPV cooling due to introduction of micro-pin fins instead of plate-fins should be studied.

- The stored thermal energy in the PCM can be used for potential building heating application either with thermoelectric devices or heat exchangers with other mediums such as water. The thermal energy extracted from modules can also be utilised for low temperature applications e.g. water and air heating [84].

(iii) Testing-level recommendations:

- Perform accelerated weather tests to enhance the stability and life time of BICPV-PCM assembly. On-field installation and continuous monitoring of the system to get more information on the long term performance and on the durability of the components.
- Analyse levelised cost of energy (LCOE) for various BICPV-PCM systems. It can include the costs of additional features (micro-finning, n-PCM synthesis).
- PCM discharge studies can assess the possible uses of heat and integration with a secondary power generator (Peltier or Seebeck devices).

These recommendations can improve the BICPV performance on one hand and reduce the overall costs of these systems on the other hand, by increasing BICPV lifetime. These investigations could not be conducted within this thesis because of (a) the time constraints, and (b) out of the main scope of PhD.

As a consolidated conclusion, it could be established that the research problem of determining the effectiveness of introducing micro-finned back-plate, PCM and n-PCM into BICPV systems has been answered to a substantial degree with the quantified outcome but further questions are raised concerning the long term stability of these systems. The experimental results presented within this thesis provide promising foundations on which to build the next stage of the work. By introducing micro-finned back-plate, PCM and n-PCM into a utility-scale BICPV system, it would be possible to test their effectiveness not only through temperature regulation, but also in terms of enhancing the output electrical efficiency of the BICPV systems. These types of investigations can contribute immensely to the future of the BICPV market, opening pathways for innovation and market penetration to increase its share in the competitive power generation industry.

Appendix-1

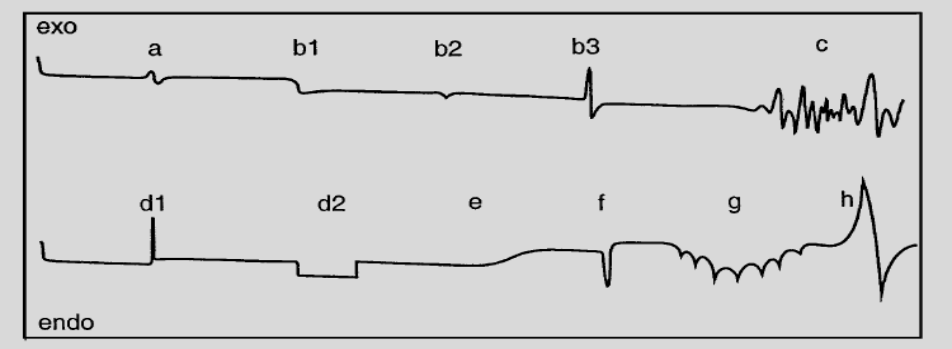

Figure 116: Artefacts caused by various sources, a-c for exotherms and d-h for endotherms [327].

a: a sudden change in the heat transfer between pans and samples either due to irregular sample forms toppling over in the pan or polymer films not pressed against the base of the pan.

b: a sudden change in the heat transfer between sensor and pan either due to the distortion of sealed pan because of vapour pressure of the sample, or small shift in the pan during dynamic temperature program as a result of the difference in coefficients of expansion (Al~24 ppm/K, sensor~9 ppm/K).

c: noisy signal caused by an entry of cool air into the cell due to misaligned cell lid

d: electrical effects either due to a possible discharge of static electricity in the metallic parts of the system, or disturbance in power supply (**d1**), or frequency interference caused due to the presence of radio emitters, such as a mobile phone in the vicinity (**d2**).

e: sudden change in the ambient temperature due to day-night cycle or presence of heat producing instruments.

f: if the increasing vapour pressure of the sample causes a burst of the lid, it produces an endothermic peak with a height proportional to the quantity of vapour.

g: periodic/intermittent closing of the hole in the lid due to the condensing droplets.

h: contamination of the sensors due to the presence of any residues from previous experiments

Appendix-2

The cost-benefit model of the micro-finned thermal management system for the BICPV.

Cost/°C	(£)
PCM	0.044
n-PCM	0.042
Micro-fins	1.538
Micro-fins+PCM	0.226
Micro-fins+ n-PCM	0.198

Cost /kg	US $	GBP	Amount	(£)	Comments
PCM	6.5	5.2	22.76	**0.118**	RT42
Nanomaterial	590.0	472.0	0.11	0.054	CuO nanomaterial
n-PCM			22.87	**0.172**	RT42 + CuO
Plastic costs	25.0	20.0	15.00	0.300	for 3D printing
Total PCM usage costs				0.418	PCM + plastic box
Total n-PCM usage costs				0.472	n-PCM + plastic box

Additional	Additional	Benefit (°C) temperature reduction		
PCM	0.418	10.7		9.6
Micro-fins	2.000		12.5	1.3
n-PCM	0.472			11.2

Appendix-3

1. Melting point (peak)

The melting peak determined as the maximum value of the DSC signal during the melting cycle is shown in Fig. 117 which is an example for RT42 at a heating rate of 5 K/min. Table 38 lists the melting peak temperatures (°C) for different PCM. A negative (-) sign indicates lower manufacturer value compared to experimental. Nanomaterial addition to PCM causes a nominal decrease in peak melting temperature, especially for higher heating rates. For most of the other PCM, the manufacturer provided values were closer to the measured value at the lowest heating rates of 2 K/min. At higher heating rates the measured values were substantially higher for almost all the PCM.

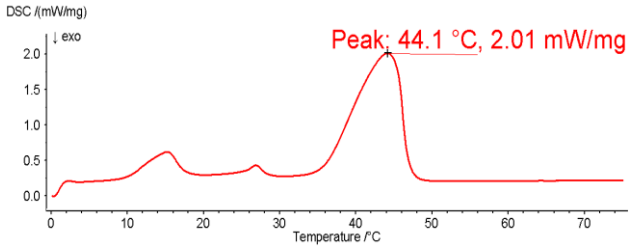

Figure 117: Example of melting point determination: RT42 heating cycle at 5K/min.

Table 38. Melting peak temperatures for different types of PCM. A negative value in the last column denotes a higher experimental value than the manufacturer given value.

Melting temperature (PEAK) °C								
PCM	**Rate [K/min]**	**Run 1.1**	**Run 1.2**	**Run 1.3**	**Mean**	**Std. Dev.**	**Manu. Value**	**% Diff.**
RT27	10	29.5	29.5	29.5	29.5	0.00	27.0	-9.3
	5	27.3	27.5	27.4	27.4	0.10	27.0	-1.5
	2	26.4	26.6	26.7	26.6	0.15	27.0	1.6
RT28HC	10	34.7	34.3	34.9	34.6	0.31	28.0	-23.7
	5	31.8	31.6	31.7	31.7	0.10	28.0	-13.2
	2	29.8	30.1	30.3	30.1	0.25	28.0	-7.4
RT31	10	31.7	31.5	31.5	31.6	0.12	31.0	-1.8
	5	29.6	29.7	29.7	29.7	0.06	31.0	4.3
	2	28.8	28.8	28.6	28.7	0.12	31.0	7.3
RT42	10	46.0	45.8	46.0	45.9	0.12	41.0	-12.0
	5	44.1	43.8	44.2	44.1	0.23	41.0	-7.5
	2	42.4	42.2	42.2	42.3	0.12	41.0	-3.1
RT44HC	10	48.8	48.3	48.4	48.5	0.26	43.0	-12.8
	5	46.6	46.8	46.8	46.7	0.12	43.0	-8.7
	2	45.3	45.3	45.5	45.4	0.12	43.0	-5.5
RT50	10	56.7	56.4	56.4	56.5	0.17	49.0	-15.3
	5	53.9	54.2	54.2	54.1	0.17	49.0	-10.4
	2	52.7	52.5	52.8	52.7	0.15	49.0	-7.5

PX25	10	29.9	30.0	30.0	30.0	0.06	25.0	-19.9
	5	28.5	28.5	28.5	28.5	0.00	25.0	-14.0
	2	27.3	27.3	27.4	27.3	0.06	25.0	-9.3
GR42	10	45.7	45.5	45.5	45.6	0.12	41.0	-11.1
	5	44.7	44.7	44.7	44.7	0.00	41.0	-9.0
	2	43.8	43.9	43.9	43.9	0.06	41.0	-7.0
nano-RT42-1	10	44.3	44.4	44.2	44.3	0.10	NA	NA
	5	43.1	43.1	43.2	43.1	0.06	NA	NA
	2	41.8	41.8	41.7	41.8	0.06	NA	NA
nano-RT42-2	10	45.1	45.1	45.1	45.1	0.00	NA	NA
	5	43.3	43.6	43.3	43.4	0.17	NA	NA
	2	41.2	41.7	41.8	41.6	0.32	NA	NA

2. Congealing/Solidification point (peak)

The solidification peak temperature was determined as the maximum negative DSC signal during the solidification process as shown in Fig. 118 as an example for RT42 at 5K/min. Table 39 lists the solidification peak temperatures for the PCMs investigated.

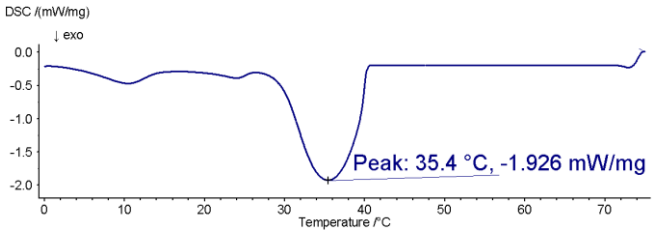

Figure 118: Solidification peak temperature: RT42 at 5K/min during cooling cycle.

Table 39. Solidification peak temperatures for different types of PCM.

Solidification temperature (PEAK) °C								
PCM	**Rate [K/min]**	**Run 1.1**	**Run 1.2**	**Run 1.3**	**Mean**	**Std. Dev.**	**Manu. Value**	**% Diff.**
RT27	10	19.9	19.9	22.3	20.7	1.39	27.0	23.3
	5	21.3	21.3	21.2	21.3	0.06	27.0	21.2
	2	22.7	22.7	22.6	22.7	0.06	27.0	16.0
RT28HC	10	17.8	17.8	17.8	17.8	0.00	27.0	34.1
	5	21.2	21.2	20.3	20.9	0.52	27.0	22.6
	2	23.0	22.3	22.7	22.7	0.35	27.0	16.0
RT31	10	21.2	21.1	21.2	21.2	0.06	31.0	31.7
	5	24.0	23.9	24.0	24.0	0.06	31.0	22.7
	2	25.8	25.6	25.6	25.7	0.12	31.0	17.2
RT42	10	32.5	32.5	32.5	32.5	0.00	42.0	22.6
	5	35.3	35.3	35.4	35.3	0.06	42.0	15.9
	2	37.9	37.9	37.9	37.9	0.00	42.0	9.8
RT44HC	10	33.0	33.6	33.9	33.5	0.46	43.0	22.1

	5	38.8	38.8	37.8	38.5	0.58	43.0	10.5
	2	35.0	34.9	34.9	34.9	0.06	43.0	18.8
RT50	10	43.1	43.2	42.9	43.1	0.15	50.0	13.9
	5	46.5	46.3	46.3	46.4	0.12	50.0	7.3
	2	48.5	48.6	48.3	48.5	0.15	50.0	3.1
PX25	10	17.8	17.9	17.9	17.9	0.06	25.0	28.5
	5	20.2	20.3	20.2	20.2	0.06	25.0	19.1
	2	22.4	22.3	22.3	22.3	0.06	25.0	10.7
GR42	10	37.1	37.3	37.2	37.2	0.10	42.0	11.4
	5	39.0	39.0	39.1	39.0	0.06	42.0	7.1
	2	40.9	40.8	40.8	40.8	0.06	42.0	2.8
nano-RT42-1	10	34.4	34.4	34.1	34.3	0.17	NA	NA
	5	36.9	36.9	36.9	36.9	0.00	NA	NA
	2	39.2	39.0	39.0	39.1	0.12	NA	NA
nano-RT42-2	10	33.7	33.7	33.7	33.7	0.00	NA	NA
	5	36.2	36.2	36.2	36.2	0.00	NA	NA
	2	38.7	38.6	38.6	38.6	0.06	NA	NA

It was evident from the data that nano-CuO addition increased congealing temperature. In general, for most other PCM, the manufacturer's values were closer to the measured values at the lowest heating rates of 2 K/min. At higher heating rates the measured values were substantially higher for almost all the PCM.

3. Melting Onset point

The PCM melting temperature range is based on the start and the end of the melting process throughout which the melting of PCM remains in progress. The onset point was determined as the intersection of the starting slope and the horizontal line (Fig. 119).

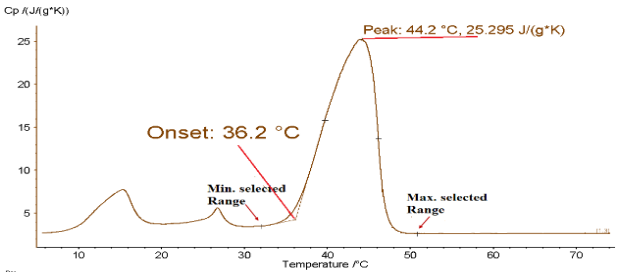

Figure 119: Example of melting onset temperature assessment: RT42 heated at 5K/min.

The melting onset temperatures for PCM (Table 40) show that addition of nanomaterial causes a slight decrease at higher heating rates in n-PCM 1 but a substantial increase in n-PCM 2. The experimentally obtained values for the other PCMs were either higher or lower by up to 12 % from the positive manufacturer's values.

Table 40. Melting Onset temperatures for different types of PCM.

Melting temperature (ONSET) °C								
PCM	**Rate [K/min]**	**Run 1.1**	**Run 1.2**	**Run 1.3**	**Mean**	**Std. Dev.**	**Manu. Value**	**% Diff.**
RT27	10	23.2	22.7	23.6	23.2	0.45	25.0	7.3
	5	22.7	22.7	22.8	22.7	0.06	25.0	9.1
	2	23.3	23.3	23.2	23.3	0.06	25.0	6.9
RT28HC	10	26.9	26.9	26.7	26.8	0.12	27.0	0.6
	5	26.6	26.6	26.5	26.6	0.06	27.0	1.6
	2	26.6	26.6	26.6	26.6	0.00	27.0	1.5
RT31	10	23.6	23.6	23.8	23.7	0.12	27.0	12.3
	5	24.1	24.1	24.3	24.2	0.12	27.0	10.5
	2	23.7	23.4	24.1	23.7	0.35	27.0	12.1
RT42	10	36.7	37.0	36.5	36.7	0.25	38.0	3.3
	5	36.7	35.8	36.0	36.2	0.47	38.0	4.8
	2	33.8	33.8	34.0	33.9	0.12	38.0	10.9
RT44HC	10	41.3	41.2	41.6	41.4	0.21	41.0	-0.9
	5	48.7	43.0	41.6	44.4	3.76	41.0	-8.4
	2	43.1	43.3	43.2	43.2	0.10	41.0	-5.4
RT50	10	48.6	48.6	48.4	48.5	0.12	45.0	-7.9
	5	47.0	46.7	46.9	46.9	0.15	45.0	-4.1
	2	45.8	45.6	46.9	46.1	0.70	45.0	-2.4
PX25	10	23.2	23.1	23.2	23.2	0.06	22.0	-5.3
	5	22.7	22.7	22.8	22.7	0.06	22.0	-3.3
	2	22.5	22.8	22.7	22.7	0.15	22.0	-3.0
GR42	10	39.1	39.2	39.2	39.2	0.06	38.0	-3.1
	5	39.0	39.6	39.4	39.3	0.31	38.0	-3.5
	2	39.5	39.5	35.0	38.0	2.60	38.0	0.0
nano-RT42-1	10	36.8	36.8	36.1	36.6	0.40	NA	NA
	5	36.0	35.9	35.9	35.9	0.06	NA	NA
	2	34.5	34.5	34.3	34.4	0.12	NA	NA
nano-RT42-2	10	45.0	45.2	45.7	45.3	0.36	NA	NA
	5	43.5	43.6	43.8	43.6	0.15	NA	NA
	2	42.2	42.3	42.1	42.2	0.10	NA	NA

4. Solidification onset point

The congealing or solidification temperature onset was determined in a similar way as melting onset, but on the opposite side of the curve. Solidification onset temperatures for different PCM are presented in Table 41. Nanomaterial addition increased the mean onset temperatures, especially at the lower heating rate of 2 K/min.

Table 41. Solidification Onset temperature determination for different types of PCM.

Solidification temperature (ONSET) °C								
PCM	**Rate [K/min]**	**Run 1.1**	**Run 1.2**	**Run 1.3**	**Mean**	**Std. Dev.**	**Manu. Value**	**% Diff.**

	10	25.6	25.6	25.6	25.6	0.00	27.0	5.2
RT27	5	21.3	21.3	21.2	21.3	0.06	27.0	21.2
	2	22.7	22.7	22.6	22.7	0.06	27.0	16.0
	10	19.7	19.4	18.8	19.3	0.46	27.0	28.5
RT28HC	5	21.2	21.2	20.3	20.9	0.52	27.0	22.6
	2	23.4	23.3	23.4	23.4	0.06	27.0	13.5
	10	21.2	21.1	21.2	21.2	0.06	31.0	31.7
RT31	5	24.0	23.9	24.0	24.0	0.06	31.0	22.7
	2	25.8	25.6	25.6	25.7	0.12	31.0	17.2
	10	32.8	32.8	32.7	32.8	0.06	42.0	22.0
RT42	5	36.1	36.1	36.2	36.1	0.06	42.0	14.0
	2	25.1	25.1	25.0	25.1	0.06	42.0	40.3
	10	33.0	33.6	33.9	33.5	0.46	43.0	22.1
RT44HC	5	38.8	38.8	37.8	38.5	0.58	43.0	10.5
	2	35.0	34.9	34.9	34.9	0.06	43.0	18.8
	10	43.1	43.2	42.9	43.1	0.15	50.0	13.9
RT50	5	46.5	46.3	46.3	46.4	0.12	50.0	7.3
	2	48.5	48.6	48.3	48.5	0.15	50.0	3.1
	10	17.8	17.9	17.9	17.9	0.06	25.0	28.5
PX25	5	20.2	20.3	20.2	20.2	0.06	25.0	19.1
	2	22.4	22.3	22.3	22.3	0.06	25.0	10.7
	10	37.1	37.3	37.2	37.2	0.10	42.0	11.4
GR42	5	39.0	39.0	39.1	39.0	0.06	42.0	7.1
	2	40.9	40.8	40.8	40.8	0.06	42.0	2.8
nano-RT42-1	10	34.4	34.4	34.1	34.3	0.17	NA	NA
	5	36.5	36.2	36.2	36.3	0.17	NA	NA
	2	39.0	38.8	38.7	38.8	0.15	NA	NA
nano-RT42-2	10	34.4	33.9	33.7	34.0	0.36	NA	NA
	5	36.6	36.6	36.3	36.5	0.17	NA	NA
	2	42.2	42.3	42.1	42.2	0.10	NA	NA

5. Melting End point

The PCM melting end point was determined as the intersection of the ending slope and horizontal line (Fig. 120) and the values obtained for the PCMs tested are listed in Table 42. Both the n-PCM exhibited lower melting end point temperatures than the base PCM.

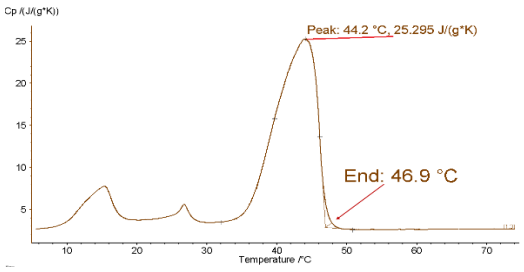

Figure 120: Example of melting end temperature assessment: RT42 heated at 5K/min.

Table 42. Melting End temperature for different types of PCM.

Melting temperature (END) °C								
PCM	**Rate [K/min]**	**Run 1.1**	**Run 1.2**	**Run 1.3**	**Mean**	**Std. Dev.**	**Manu. Value**	**% Diff.**
RT27	10	29.5	29.5	29.5	29.5	0.00	27.0	-9.3
	5	27.3	27.5	27.4	27.4	0.10	27.0	-1.5
	2	26.4	26.6	26.7	26.6	0.15	27.0	1.6
RT28HC	10	33.3	33.4	33.8	33.5	0.26	28.0	-19.6
	5	31.8	31.6	31.7	31.7	0.10	28.0	-13.2
	2	29.8	29.8	29.9	29.8	0.06	28.0	-6.5
RT31	10	31.7	31.5	31.5	31.6	0.12	31.0	-1.8
	5	29.6	29.7	29.7	29.7	0.06	31.0	4.3
	2	28.8	28.8	28.6	28.7	0.12	31.0	7.3
RT42	10	46.3	46.0	46.0	46.1	0.17	41.0	-12.4
	5	43.7	43.7	43.5	43.6	0.12	41.0	-6.4
	2	42.2	42.3	42.3	42.3	0.06	41.0	-3.1
RT44HC	10	48.8	48.3	48.4	48.5	0.26	43.0	-12.8
	5	46.6	46.8	46.8	46.7	0.12	43.0	-8.7
	2	45.3	45.3	45.5	45.4	0.12	43.0	-5.5
RT50	10	56.7	56.4	56.4	56.5	0.17	49.0	-15.3
	5	53.9	54.2	54.2	54.1	0.17	49.0	-10.4
	2	52.7	52.5	52.8	52.7	0.15	49.0	-7.5
PX25	10	29.9	30.0	30.0	30.0	0.06	25.0	-19.9
	5	28.5	28.5	28.5	28.5	0.00	25.0	-14.0
	2	27.3	27.3	27.4	27.3	0.06	25.0	-9.3
GR42	10	45.7	45.5	45.5	45.6	0.12	41.0	-11.1
	5	44.7	44.7	44.7	44.7	0.00	41.0	-9.0
	2	43.8	43.9	43.9	43.9	0.06	41.0	-7.0
nano-RT42-1	10	45.4	45.4	45.7	45.5	0.17	NA	NA
	5	43.9	44.4	44.3	44.2	0.26	NA	NA
	2	42.4	42.5	42.7	42.5	0.15	NA	NA
nano-RT42-2	10	45.0	45.2	45.7	45.3	0.36	NA	NA
	5	43.5	43.6	43.8	43.6	0.15	NA	NA
	2	42.2	42.3	42.1	42.2	0.10	NA	NA

6. Solidification End point

The solidification end point temperatures for the PCM were determined as the intersection of the ending slope and the horizontal line. The data for PCMs is tabulated in Table 43. For most cases, nanomaterial addition increased the solidification end temperature compared to the base PCM. For the other PCMs, the experimental means were lower than manufacturer's values, indicating the degree of super cooling would be higher during congealing cycle than expected.

Table 43. Solidification End temperature for different types of PCM.

Solidification temperature (END) °C								
PCM	**Rate [K/min]**	**Run 1.1**	**Run 1.2**	**Run 1.3**	**Mean**	**Std Dev.**	**Manu. value**	**% Diff.**
RT27	10	25.6	25.6	25.6	25.6	0.00	27.0	5.2
	5	21.3	21.3	21.2	21.3	0.06	27.0	21.2
	2	22.7	22.7	22.6	22.7	0.06	27.0	16.0
RT28HC	10	19.7	19.4	18.8	19.3	0.46	27.0	28.5
	5	21.2	21.2	20.3	20.9	0.52	27.0	22.6
	2	23.4	23.3	23.4	23.4	0.06	27.0	13.5
RT31	10	21.2	21.1	21.2	21.2	0.06	31.0	31.7
	5	24.0	23.9	24.0	24.0	0.06	31.0	22.7
	2	25.8	25.6	25.6	25.7	0.12	31.0	17.2
RT42	10	32.8	32.8	32.7	32.8	0.06	42.0	22.0
	5	36.1	36.1	36.2	36.1	0.06	42.0	14.0
	2	25.1	25.1	25.0	25.1	0.06	42.0	40.3
RT44HC	10	33.0	33.6	33.9	33.5	0.46	43.0	22.1
	5	38.8	38.8	37.8	38.5	0.58	43.0	10.5
	2	35.0	34.9	34.9	34.9	0.06	43.0	18.8
RT50	10	43.1	43.2	42.9	43.1	0.15	50.0	13.9
	5	46.5	46.3	46.3	46.4	0.12	50.0	7.3
	2	48.5	48.6	48.3	48.5	0.15	50.0	3.1
PX25	10	17.8	17.9	17.9	17.9	0.06	25.0	28.5
	5	20.2	20.3	20.2	20.2	0.06	25.0	19.1
	2	22.4	22.3	22.3	22.3	0.06	25.0	10.7
GR42	10	37.1	37.3	37.2	37.2	0.10	42.0	11.4
	5	39.0	39.0	39.1	39.0	0.06	42.0	7.1
	2	40.9	40.8	40.8	40.8	0.06	42.0	2.8
nano-RT42-1	10	34.4	34.4	34.1	34.3	0.17	NA	NA
	5	36.5	36.2	36.2	36.3	0.17	NA	NA
	2	39.0	38.8	38.7	38.8	0.15	NA	NA
nano-RT42-2	10	34.4	33.9	33.7	34.0	0.36	NA	NA
	5	36.6	36.6	36.3	36.5	0.17	NA	NA
	2	42.2	42.3	42.1	42.2	0.10	NA	NA

7. Latent heat capacity

The latent heat capacity was calculated as the area under the C_p curve and the temperature line and was determined on the basis of the highest peak area values. The data for melting and solidification cycles are in Table 44 and 45 resp. It can be observed that for n-PCM 1, the mean values were lower than the base PCM, they were higher for n-PCM 2 during both melting and solidification. For other PCMs, experimental values were lower than the manufacturer provided values, indicating PCM aren't as capable of storing heat as they

were advertised. They may be less efficient by a few percent for certain PCM and up to 44 % for others in both solidification and melting cycles.

Table 44. Latent heat capacity of PCM during melting.

Melting enthalpy (based on Highest Peak area) J g^{-1}								
PCM	**Rate [K/min]**	**Run 1.1**	**Run 1.2**	**Run 1.3**	**Mean**	**Std. Dev.**	**Manu. Value**	**% Diff.**
RT27	10	130.9	131.8	128.4	130.	1.76	179.0	27.2
	5	103.1	101.9	99.3	101.	1.95	179.0	43.3
	2	123.4	125.6	119.0	122.	3.36	179.0	31.5
RT28HC	10	235.4	236.8	236.2	213.	0.55	245.0	12.8
	5	229.6	227.5	228.9	228.	1.07	245.0	6.7
	2	213.1	214.2	213.7	213.	0.55	245.0	12.8
RT31	10	131.7	131.2	130.3	131.	0.71	165.0	20.6
	5	125.8	125.8	123.4	125.	1.39	165.0	24.2
	2	114.2	112.5	113.3	113.	0.85	165.0	31.3
RT42	10	150.7	150.6	146.4	149.	2.45	174.0	14.2
	5	150.7	153.3	152.6	152.	1.35	174.0	12.5
	2	142.4	142.4	142.8	142.	0.23	174.0	18.1
RT44HC	10	254.4	254.0	255.8	254.	0.95	255.0	0.1
	5	256.9	255.4	255.4	255.	0.87	255.0	-0.4
	2	245.7	236.9	234.4	239.	5.94	255.0	6.3
RT50	10	142.8	142.0	143.5	142.	0.75	168.0	15.0
	5	143.6	147.5	145.8	145.	1.96	168.0	13.3
	2	137.2	135.3	135.2	135.	1.13	168.0	19.1
PX25	10	69.7	68.4	68.7	68.9	0.66	95.0	27.4
	5	77.0	77.2	78.9	77.7	1.09	95.0	18.2
	2	74.0	75.8	75.7	75.2	1.02	95.0	20.9
GR42	10	40.7	22.2	31.3	31.4	9.28	55.0	42.9
	5	32.7	32.6	32.4	32.6	0.16	55.0	40.8
	2	30.5	31.3	31.2	31.0	0.40	55.0	43.7
nano-RT42-1	10	144.9	143.8	146.7	145.	1.46	NA	NA
	5	145.9	146.3	148.4	146.	1.34	NA	NA
	2	137.4	136.6	137.9	137.	0.66	NA	NA
nano-RT42-2	10	151.0	149.5	148.1	149.	1.45	NA	NA
	5	154.2	153.6	154.8	154.	0.60	NA	NA
	2	139.5	140.1	144.7	141.	2.84	NA	NA

Table 45. Latent heat capacity of PCM during solidification.

Solidification enthalpy (based on Highest Peak area) J g^{-1}								
PCM	**Rate [K/min]**	**Run 1.1**	**Run 1.2**	**Run 1.3**	**Mean**	**Std. Dev.**	**Manu. value**	**% Diff.**
RT27	10	-136.9	-137.3	-134.1	136.1	1.74	179.0	23.9
	5	-108.5	-107.8	-102.6	106.3	3.22	179.0	40.6
	2	-133.8	-132.8	-126.7	131.1	3.84	179.0	26.8

	10	-233.7	-234.7	-234.4	236.0	0.30	245.0	3.67
RT28HC	5	-236.3	-235.7	-235.9	236.0	0.31	245.0	3.69
	2	-236.3	-236.0	-235.7	236.0	0.30	245.0	3.67
	10	-130.3	-130.3	-130.2	130.3	0.06	165.0	21.05
RT31	5	-134.1	-135.1	-135.1	134.8	0.58	165.0	18.32
	2	-130.0	-130.7	-130.1	130.3	0.38	165.0	21.05
	10	-142.1	-147.6	-146.3	145.3	2.87	174.0	16.48
RT42	5	-158.1	-157.4	-157.5	157.7	0.38	174.0	9.39
	2	-160.3	-160.5	-159.8	160.2	0.36	174.0	7.93
	10	-257.1	-259.3	-267.9	261.4	5.71	255.0	-2.52
RT44HC	5	-264.1	-265.1	-263.8	264.3	0.68	255.0	-3.66
	2	-261.7	-262.1	-261.9	261.9	0.20	255.0	-2.71
	10	-148.9	-148.0	-148.0	148.3	0.52	168.0	11.73
RT50	5	-150.3	-149.6	-150.5	150.1	0.47	168.0	10.63
	2	-156.7	-156.9	-157.0	156.9	0.15	168.0	6.63
	10	-79.1	-80.0	-79.4	-79.5	0.44	95.0	183.67
PX25	5	-80.3	-82.3	-83.5	-82.0	1.62	95.0	186.36
	2	-86.0	-85.3	-85.9	-85.7	0.35	95.0	190.24
	10	-40.7	-40.3	-40.3	-40.4	0.23	55.0	173.54
GR42	5	-32.0	-31.4	-31.5	-31.6	0.30	55.0	157.49
	2	-34.2	-34.2	-32.6	-33.7	0.90	55.0	161.22
	10	-142.9	-147.8	-147.0	-145.9	2.63	NA	NA
nano-RT42-1	5	-153.0	-153.7	-155.5	-154.1	1.29	NA	NA
	2	-156.4	-156.6	-157.5	-156.8	0.59	NA	NA
	10	-152.8	-152.9	-152.3	-152.7	0.32	NA	NA
nano-RT42-2	5	-158.8	-158.7	-158.8	-158.8	0.06	NA	NA
	2	-145.8	-163.1	-159.1	-156.0	9.06	NA	NA

8. Specific heat capacity

The specific heat capacity of PCMs determined on the basis of highest peak values are displayed in Table 46 (melting), and Table 47 (solidification). It can be seen that C_p for both melting and solidification increased slightly from the values for the base PCM for n-PCM 1 and more for n-PCM 2. It is to be noted that C_p for all PCM was given at a constant value of 2 kJ/kg·K irrespective of the PCM type in the manufacturer data sheet.

Table 46. Cp of PCM during melting determined from highest peak.

Specific heat Peak during Melting $Jg^{-1}K^{-1}$						
PCM	**Rate [K/min]**	**Run 1.1**	**Run 1.2**	**Run 1.3**	**Mean**	**Std. Dev.**
	10	22.0	21.6	18.1	20.6	2.16
RT27	5	21.6	21.6	20.9	21.4	0.41
	2	35.0	35.5	33.2	34.6	1.20
RT28HC	10	32.4	31.0	31.2	64.8	1.12

	5	46.3	46.3	43.9	45.5	1.36
	2	66.0	64.5	63.8	64.8	1.12
RT31	10	17.9	17.8	17.7	17.8	0.10
	5	20.7	21.0	21.0	20.9	0.17
	2	22.2	20.8	22.5	21.8	0.89
RT42	10	20.4	20.7	20.6	20.6	0.15
	5	25.3	25.2	25.1	25.2	0.10
	2	27.6	27.8	27.8	27.7	0.13
RT44HC	10	34.9	34.1	32.6	33.9	1.18
	5	45.0	44.5	43.4	44.3	0.85
	2	59.7	60.6	60.6	60.3	0.50
RT50	10	20.5	20.2	20.3	20.3	0.15
	5	25.9	25.2	25.1	25.4	0.45
	2	28.1	29.3	29.4	28.9	0.73
GR42	10	6.5	6.4	6.4	6.4	0.04
	5	7.6	7.6	7.6	7.6	0.02
	2	8.5	8.6	8.6	8.6	0.05
nano-RT42-1	10	22.0	21.8	21.2	21.7	0.39
	5	25.8	25.2	25.4	25.5	0.31
	2	26.9	27.5	26.5	27.0	0.52
nano-RT42-2	10	21.8	21.2	21.8	21.6	0.36
	5	25.9	25.8	25.8	25.9	0.08
	2	26.7	27.8	28.2	27.6	0.81

Table 47. Cp of PCM during solidification on the basis of highest peak.

Specific heat Peak during Solidification $Jg^{-1}K^{-1}$						
PCM	**Rate [K/min]**	**Run 1.1**	**Run 1.2**	**Run 1.3**	**Mean**	**Std. Dev.**
RT27	10	22.1	22.1	18.1	20.8	2.31
	5	22.7	22.5	21.7	22.3	0.52
	2	38.8	38.8	37.4	38.3	0.84
RT28HC	10	35.8	38.2	36.1	36.7	1.32
	5	70.0	71.7	68.1	69.9	1.80
	2	91.2	115.5	89.1	98.6	14.68
RT31	10	17.0	16.9	16.7	16.9	0.15
	5	19.7	19.7	19.7	19.7	0.01
	2	23.0	22.7	23.0	22.9	0.12
RT42	10	20.2	20.1	20.1	20.1	0.05
	5	24.6	24.7	24.6	24.6	0.04
	2	31.1	31.2	31.2	31.2	0.03
RT44HC	10	39.0	32.9	35.3	35.7	3.06
	5	49.2	52.5	52.4	51.4	1.88
	2	86.3	119.5	120.6	108.8	19.46
RT50	10	19.8	19.7	19.6	19.7	0.09
	5	25.1	25.8	24.7	25.2	0.58
	2	33.2	32.4	32.5	32.7	0.41

GR42	10	5.9	6.0	6.0	6.0	0.02
	5	7.3	7.3	7.3	7.3	0.01
	2	9.1	9.1	9.1	9.1	0.01
nano-RT42-1	10	21.7	21.4	21.4	21.5	0.16
	5	25.7	25.8	25.9	25.8	0.10
	2	32.3	32.2	32.1	32.2	0.08
nano-RT42-2	10	21.3	21.3	21.3	21.3	0.01
	5	25.9	25.8	25.9	25.9	0.03
	2	31.9	32.4	32.4	32.2	0.30

From this exercise, a more appropriate value for the thermo-physical properties of the PCMs have been experimentally obtained especially for different heating rates. At this juncture, this may not seem very useful but for planning future experiments, these differences will have to be taken into consideration especially for highly sophisticated thermal regulation systems.

Appendix-4

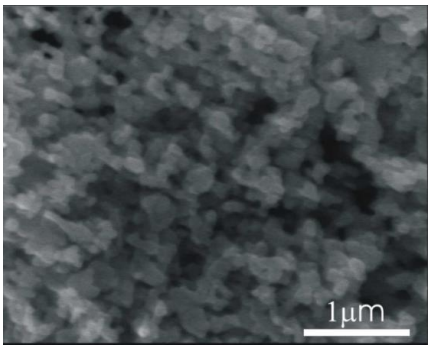

Figure 121: Manufacturer provided SEM image of the 60 nm Nano-CuO.

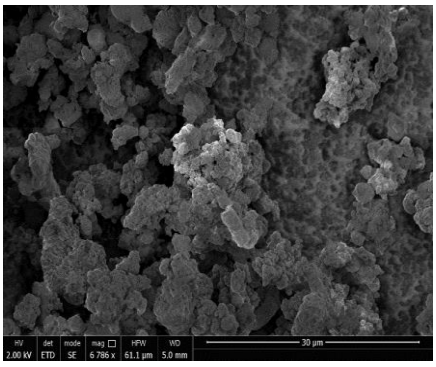

(a)

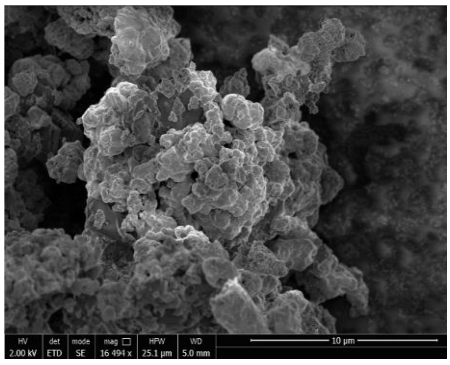

(b)

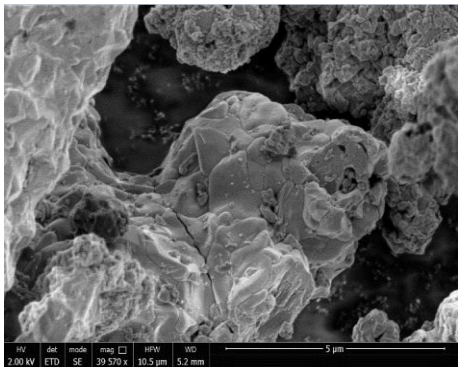

(c)

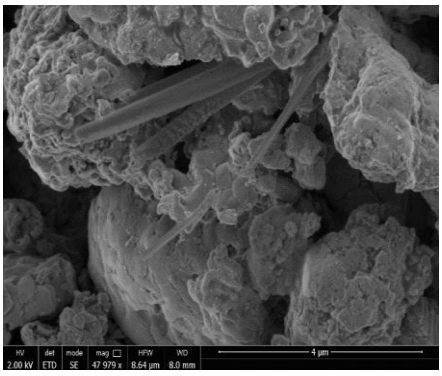

(d)

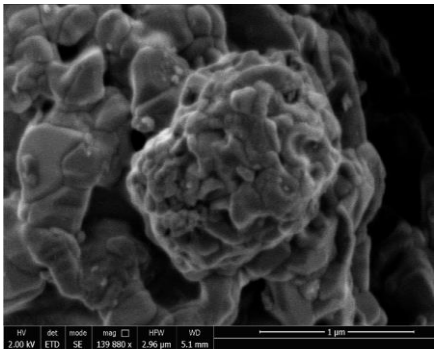

(e)

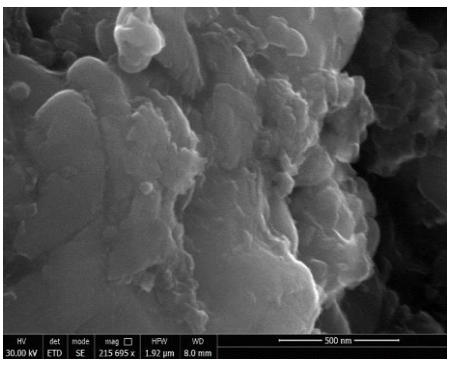

(f)

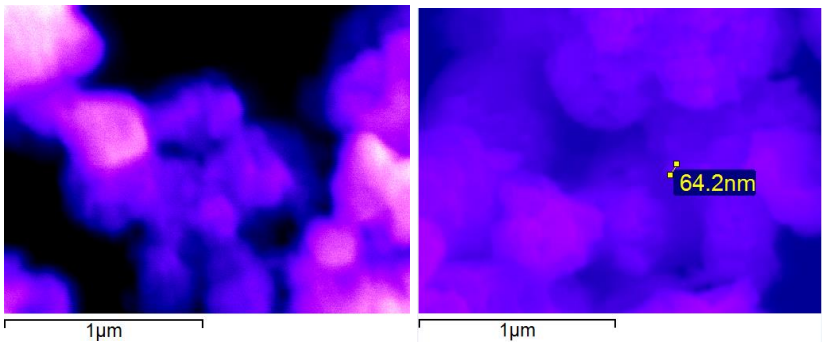

(g) (h)

Figure 122: Micrographs of nano-CuO at a scale of: (a) 30 µm, (b) 10 µm, (c) 5 µm, (d) 4 µm, (e) 1 µm, (f) 500 nm, and with gold sputter coating: (g) 1 µm and (h) 500 nm.

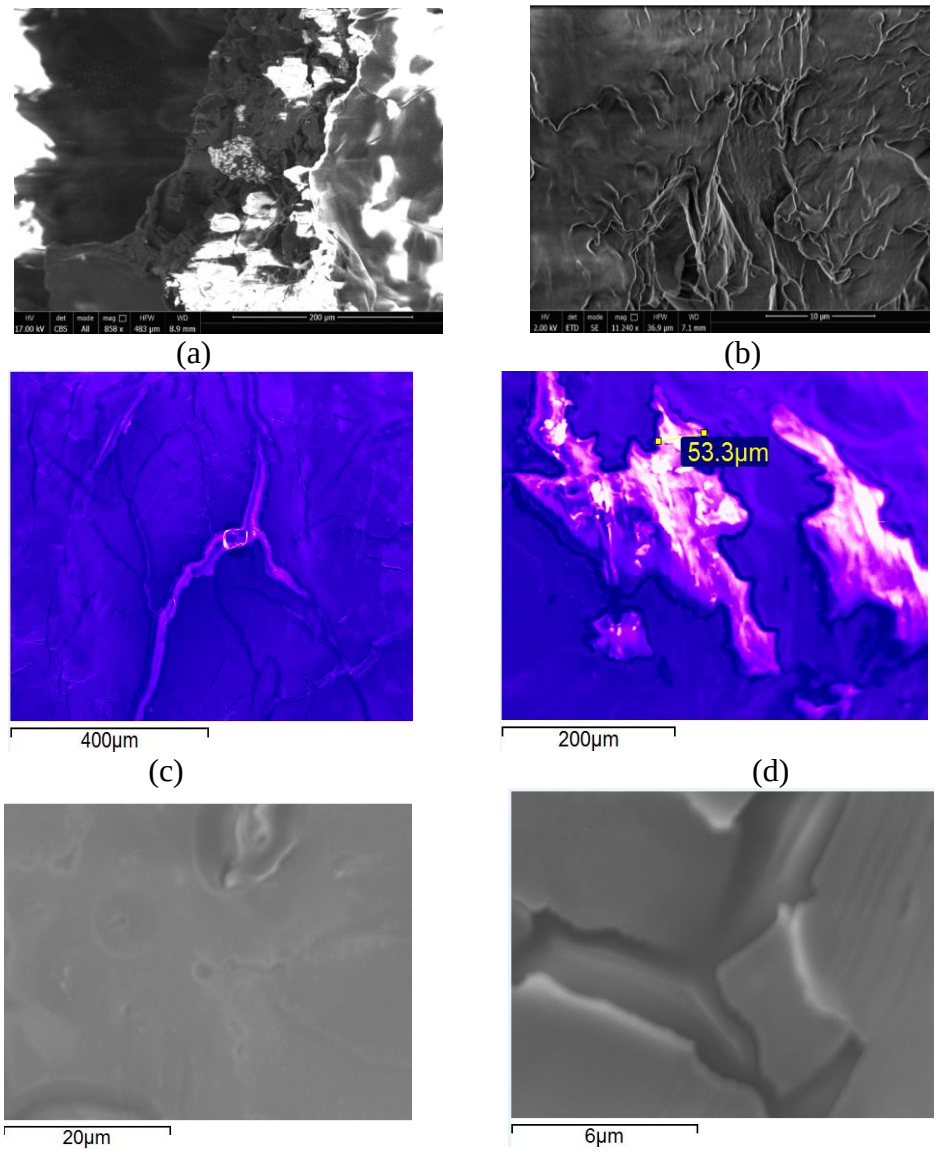

(a) (b)

(c) (d)

(e) (f)

Figure 123: Micrographs of n-PCM (RT 42 with nano-CuO) without gold coating at a scale of (a) 200 µm, (b) 10 µm, and gold sputtered samples at (c) 400 µm, (d) 200 µm, (e) 20 µm and (f) 6 µm scales.

Bibliography

1. EIA, U.S., *International Energy Outlook 2016 With Projections to 2040*, in *International Energy Outlook* U.S.E.I. Administration, Editor. 2016, U.S. Department of Energy, Energy Information Administration Washington, DC p. 276.
2. ISE, F., *Photovoltaics report*. 2016, Fraunhofer Institute for Solar Energy Systems, ISE: Freiburg, Germany.
3. REN21, *Renewable Energy Policy Network -Renewables 2016 Global Status Report* in *Annual Reporting on Renewables*, REN21Secretary, Editor. 2016, REN21: Paris, France. p. 272.
4. Jesson, N., *National Statistics: Solar photovoltaics deployment*, E.a.I.S. Business, Editor. 2017, gov.uk: UK.
5. Iain MacLeay, K.H., Anwar Annut *Digest of United Kingdom Energy Statistics 2015* 2015, Department of Energy and Climate Change: London. p. 1-272.
6. Bonomo, P., *Overview on international BIPV research activities*. 2016, Swiss BiPV Competence Centre: Canobbio, Switzerland. p. 1-38.
7. Menoufi, K., D. Chemisana, and J.I. Rosell, *Life Cycle Assessment of a Building Integrated Concentrated Photovoltaic scheme.* Applied Energy, 2013. **111**(0): p. 505-514.
8. Bunthof, L.A.A., et al., *Impact of shading on a flat CPV system for façade integration.* Solar Energy, 2016. **140**: p. 162-170.
9. Viswanathan, B., *Chapter 8 - Photovoltaic Systems*, in *Energy Sources*. 2017, Elsevier: Amsterdam. p. 149-160.
10. Zweibel, K., P. Hersch, and S.E.R. Institute, *Basic Photovoltaic Principles and Methods*. 1984: Van Nostrand Reinhold.
11. Wang, Z., et al., *Experimental investigation of the performance of the novel HP-BIPV/T system for use in residential buildings.* Energy and Buildings, 2016. **130**: p. 295-308.
12. Polysolar, *Guide to Building Integrated PV*, in *Polysolar Brochures & Downloads*, P. Limited, Editor. 2015, Polysolar Ltd: Cambridge, UK.
13. Ferrara, C., H.R. Wilson, and W. Sprenger, *8 - Building-integrated photovoltaics (BIPV) A2 - Pearsall, Nicola*, in *The Performance of Photovoltaic (PV) Systems*. 2017, Woodhead Publishing. p. 235-250.
14. Norton, B., et al., *Enhancing the performance of building integrated photovoltaics.* Solar Energy, 2011. **85**(8): p. 1629-1664.
15. Sarmah, N., B.S. Richards, and T.K. Mallick, *Design, development and indoor performance analysis of a low concentrating dielectric photovoltaic module.* Solar Energy, 2014. **103**(0): p. 390-401.
16. Designergy. *TCR - The innovative system for roofing with integrated photovoltaic*. 2016 [cited 2017 23 Feb 2017]; Available from: http://www.designergy.ch/index/en/triactive-core-technology/.
17. Baig, H., K.C. Heasman, and T.K. Mallick, *Non-uniform illumination in concentrating solar cells.* Renewable and Sustainable Energy Reviews, 2012. **16**(8): p. 5890-5909.
18. Luque, A., *Will we exceed 50% efficiency in photovoltaics?* Journal of Applied Physics, 2011. **110**(3): p. 031301-031301.
19. Ryu, K., et al., *Concept and design of modular Fresnel lenses for concentration solar PV system.* Solar Energy, 2006. **80**(12): p. 1580-1587.
20. Muñoz, E., et al., *CPV standardization: An overview.* Renewable and Sustainable Energy Reviews, 2010. **14**(1): p. 518-523.
21. Khamooshi, M., et al., *A Review of Solar Photovoltaic Concentrators.* International Journal of Photoenergy, 2014. **2014**: p. 17.
22. Chemisana, D., *Building Integrated Concentrating Photovoltaics: A review.* Renewable and Sustainable Energy Reviews, 2011. **15**(1): p. 603-611.

23. Shanks, K., S. Senthilarasu, and T.K. Mallick, *Optics for concentrating photovoltaics: Trends, limits and opportunities for materials and design.* Renewable and Sustainable Energy Reviews, 2016. **60**: p. 394-407.
24. Perez-Higueras, P., et al., *High Concentrator PhotoVoltaics efficiencies: Present status and forecast.* Renewable & Sustainable Energy Reviews, 2011. **15**(4): p. 1810–1815.
25. Fernández, E.F., et al., *A model based on artificial neuronal network for the prediction of the maximum power of a low concentration photovoltaic module for building integration.* Solar Energy, 2014. **100**: p. 148-158.
26. Fraas, L.M. and L.D. Partain, *Solar Cells and Their Applications*. 2nd ed. Vol. 1. 2010, Singapore: Wiley. 1-613.
27. Sala, G. and I. Antón, *Handbook of Photovoltaic Science and Engineering*, in *Handbook of Photovoltaic Science and Engineering*. 2011, John Wiley & Sons, Ltd. p. 402-451.
28. Chong, K.-K., et al., *Design and development in optics of concentrator photovoltaic system.* Renewable and Sustainable Energy Reviews, 2013. **19**(0): p. 598-612.
29. Bannerot, R.B. and J.R. Howell, *Predicted daily and yearly average radiative performance of optimal trapezoidal groove solar energy collectors.* Solar Energy, 1979. **22**(3): p. 229-234.
30. Dreger, M., et al., *Development and investigation of a CPV module with Cassegrain mirror optics.* AIP Conference Proceedings, 2014. **1616**(1): p. 177-182.
31. Miller, D.C. and S.R. Kurtz, *Durability of Fresnel lenses: A review specific to the concentrating photovoltaic application.* Solar Energy Materials and Solar Cells, 2011. **95**(8): p. 2037-2068.
32. Wang, W., et al., *Development of a Fresnel lens based high-flux solar simulator.* Solar Energy, 2017. **144**: p. 436-444.
33. Royne, A., C. Dey, and D. Mills, *Cooling of photovoltaic cells under concentrated illumination: a critical review.* Solar Energy Materials and Solar Cells, 2005. **86**(4): p. 451-483.
34. Lorenzo, E. and A. Luque, *Comparison of Fresnel lenses and parabolic mirrors as solar energy concentrators.* Applied Optics, 1982. **21**(10): p. 1851-1853.
35. Leutz, R. and A. Suzuki, *Nonimaging Fresnel Lenses: Design and Performance of Solar Concentrators*. 2012: Springer Berlin Heidelberg.
36. Weber, W.H. and J. Lambe, *Luminescent greenhouse collector for solar radiation.* Applied Optics, 1976. **15**(10): p. 2299-2300.
37. Ebrahimipour, B.A., H.R. Askari, and A.B. Ramezani, *Investigation of linear optical absorption coefficients in core-shell quantum dot (QD) luminescent solar concentrators (LSCs).* Superlattices and Microstructures, 2016. **97**: p. 495-505.
38. Gallagher, S.J., B. Norton, and P.C. Eames, *Quantum dot solar concentrators: Electrical conversion efficiencies and comparative concentrating factors of fabricated devices.* Solar Energy, 2007. **81**(6): p. 813-821.
39. Madala, S. and R.F. Boehm, *A review of nonimaging solar concentrators for stationary and passive tracking applications.* Renewable and Sustainable Energy Reviews.
40. Benítez, P. and J.C. Miñano, *Ultrahigh-numerical-aperture imaging concentrator.* Journal of the Optical Society of America A, 1997. **14**(8): p. 1988-1997.
41. Ries, H. and A. Rabl, *Edge-ray principle of nonimaging optics.* Journal of the Optical Society of America A, 1994. **11**(10): p. 2627-2632.
42. Antonini, A., et al., *Modelling of compound parabolic concentrators for photovoltaic applications.* International Journal of Optics and Applications, 2013. **3**(4): p. 40-52.
43. Sellami, N., *PhD Thesis - Design and characterisation of a novel translucent solar concentrator*, in *Institute of Mechanical, Process and Energy Engineering*. 2013, Heriot-Watt University: Edinburgh. p. 307.
44. Philipps, S.P., et al., *Current status of concentrator photovoltaic (CPV) technology*. 2016, Fraunhofer Institute for Solar Energy Systems, National Renewable Energy Laboratory p. 1-26.

45. Sellami, N. and T.K. Mallick, *Optical efficiency study of PV Crossed Compound Parabolic Concentrator.* Applied Energy, 2013. **102**(0): p. 868-876.
46. Mallick, T.K., et al., *The design and experimental characterisation of an asymmetric compound parabolic photovoltaic concentrator for building façade integration in the UK.* Solar Energy, 2004. **77**(3): p. 319-327.
47. Sellami, N. and T.K. Mallick, *Optical characterisation and optimisation of a static Window Integrated Concentrating Photovoltaic system.* Solar Energy, 2013. **91**(0): p. 273-282.
48. Baig, H., et al., *Numerical modelling and experimental validation of a low concentrating photovoltaic system.* Solar Energy Materials and Solar Cells, 2013. **113**: p. 201-219.
49. Ma, T., et al., *Using phase change materials in photovoltaic systems for thermal regulation and electrical efficiency improvement: A review and outlook.* Renewable and Sustainable Energy Reviews, 2015. **43**: p. 1273-1284.
50. Machniewicz, A., D. Knera, and D. Heim. *Effect of transition temperature on efficiency of PV/PCM panels*. in *6th International Building Physics Conference, IBPC 2015*. 2015. Elsevier Ltd.
51. Natarajan, S.K., et al., *Numerical investigations of solar cell temperature for photovoltaic concentrator system with and without passive cooling arrangements.* International Journal of Thermal Sciences, 2011. **50**(12): p. 2514-2521.
52. Solanki, C.S., *Solar Photovoltaics: Fundamentals Technologies And Applications*. 5th ed. 2009, Delhi, India: Prentice-Hall Of India Pvt. Limited.
53. Sewang, Y. and V. Garboushian. *Reduced temperature dependence of high-concentration photovoltaic solar cell open-circuit voltage (Voc) at high concentration levels*. in *Proceedings of 1994 IEEE 1st World Conference on Photovoltaic Energy Conversion - WCPEC (A Joint Conference of PVSC, PVSEC and PSEC)*. 1994.
54. Radziemska, E., *The effect of temperature on the power drop in crystalline silicon solar cells.* Renewable Energy, 2003. **28**(1): p. 1-12.
55. Chander, S., et al., *A study on photovoltaic parameters of mono-crystalline silicon solar cell with cell temperature.* Energy Reports, 2015. **1**: p. 104-109.
56. Radziemska, E., *Effect of temperature on dark current characteristics of silicon solar cells and diodes.* International Journal of Energy Research, 2006. **30**(2): p. 127-134.
57. Radziemska, E. and E. Klugmann, *Photovoltaic maximum power point varying with illumination and temperature.* Journal of Solar Energy Engineering, Transactions of the ASME, 2006. **128**(1): p. 34-39.
58. Yunaz, I.A., et al., *Effects of temperature and spectral irradiance on performance of silicon-based thin film multijunction solar cells.* Japanese Journal of Applied Physics, Part 1: Regular Papers and Short Notes and Review Papers, 2007. **46**(4 A): p. 1398-1403.
59. Singh, P., et al., *Temperature dependence of I–V characteristics and performance parameters of silicon solar cell.* Solar Energy Materials and Solar Cells, 2008. **92**(12): p. 1611-1616.
60. Mazur, A.V. and M.M. Gasik, *Thermal expansion of silicon at temperatures up to 1100°C.* Journal of Materials Processing Technology, 2009. **209**(2): p. 723-727.
61. Bharti, R., J. Kuitche, and M.G. TamizhMani. *Nominal Operating Cell Temperature (NOCT): Effects of module size, loading and solar spectrum*. in *Photovoltaic Specialists Conference (PVSC), 2009 34th IEEE*. 2009.
62. Wilson, E., *Theoretical and operational thermal performance of a 'wet' crystalline silicon PV module under Jamaican conditions.* Renewable Energy, 2009. **34**(6): p. 1655-1660.
63. Skoplaki, E. and J.A. Palyvos, *On the temperature dependence of photovoltaic module electrical performance: A review of efficiency/power correlations.* Solar Energy, 2009. **83**(5): p. 614-624.
64. Plesz, B., et al. *Thermal behaviour of thin photoactive layer crystalline solar cells*. in *Symposium on Design, Test, Integration and Packaging of MEMS/MOEMS, DTIP 2010*. 2010. Seville.

65. Aberle, A.G. and P.I. Widenborg, *Crystalline Silicon Thin-Film Solar Cells via High-Temperature and Intermediate-Temperature Approaches*, in *Handbook of Photovoltaic Science and Engineering*. 2011, John Wiley & Sons, Ltd. p. 452-486.
66. Han, X., et al., *Mechanism study of the electrical performance change of silicon concentrator solar cells immersed in de-ionized water*. Energy Conversion and Management, 2012. **53**(1): p. 1-10.
67. Hossain, M.I., A. Bousselham, and F.H. Alharbi. *Numerical analysis of the temperature effects on single junction solar cells efficiencies*. in *39th IEEE Photovoltaic Specialists Conference, PVSC 2013*. 2013. Tampa, FL: Institute of Electrical and Electronics Engineers Inc.
68. Ma, J., et al., *Approximate Single-Diode Photovoltaic Model for Efficient I-V Characteristics Estimation.* The Scientific World Journal, 2013. **2013**: p. 230471.
69. Sabry, M., *Temperature optimization of high concentrated active cooled solar cells.* NRIAG Journal of Astronomy and Geophysics, 2016. **5**(1): p. 23-29.
70. Meneses-Rodríguez, D., et al., *Photovoltaic solar cells performance at elevated temperatures.* Solar Energy, 2005. **78**(2): p. 243-250.
71. Du, D., J. Darkwa, and G. Kokogiannakis, *Thermal management systems for Photovoltaics (PV) installations: A critical review.* Solar Energy, 2013. **97**(0): p. 238-254.
72. Fernández, E.F., et al., *Analysis of the spectral variations on the performance of high concentrator photovoltaic modules operating under different real climate conditions.* Solar Energy Materials and Solar Cells, 2014. **127**: p. 179-187.
73. Villalva, M.G., J.R. Gazoli, and E.R. Filho, *Comprehensive Approach to Modeling and Simulation of Photovoltaic Arrays.* IEEE Transactions on Power Electronics, 2009. **24**(5): p. 1198-1208.
74. Sellami, N. and T.K. Mallick. *Design of nonimaging static solar concentrator for window integrated photovoltaic*. in *8TH INTERNATIONAL CONFERENCE ON CONCENTRATING PHOTOVOLTAIC SYSTEMS: CPV-8*. 2012. AIP Publishing.
75. Minoo Naebe, T.L.a.X.W.C.N.R.E.P.N., Nanofibers, Ashok Kumar (Ed.), ISBN: 978-953-7619-86-2, InTech, DOI: 10.5772/8160. Available from: http://www.intechopen.com/books/nanofibers/carbo, *Carbon Nanotubes Reinforced Electrospun Polymer Nanofibres.* Nanofibers, Ashok Kumar (Ed.), ISBN: 978-953-7619-86-2, InTech, DOI: 10.5772/8160., 2010.
76. Jelle, B.P. and C. Breivik, *State-of-the-art Building Integrated Photovoltaics.* Energy Procedia, 2012. **20**: p. 68-77.
77. Tabakovic, M., et al., *Status and Outlook for Building Integrated Photovoltaics (BIPV) in Relation to Educational needs in the BIPV Sector.* Energy Procedia, 2017. **111**: p. 993-999.
78. Toomer, G.J., *DIOCLES, On Burning Mirrors*. 1 ed, ed. G.J. Toomer. 1976, Berlin Springer-Verlag Berlin Heidelberg.
79. D. M. Powell, M.T.W., H. J. Choi, C. B. Simmons, D. Berney Needleman and T. Buonassisi, *Crystalline silicon photovoltaics: a cost analysis framework for determining technology pathways to reach baseload electricity costs.* Energy & Environmental Science, 2012. **5**(5874): p. 9.
80. Green, M.A., et al., *Solar cell efficiency tables (version 42).* Progress in Photovoltaics: Research and Applications, 2013. **21**(5): p. 827-837.
81. Branker, K., M.J.M. Pathak, and J.M. Pearce, *A review of solar photovoltaic levelized cost of electricity.* Renewable and Sustainable Energy Reviews, 2011. **15**(9): p. 4470-4482.
82. Kalogirou, S.A., *Chapter 9 - Photovoltaic Systems*, in *Solar Energy Engineering (Second Edition)*. 2014, Academic Press: Boston. p. 481-540.
83. Tan, F.L. and C.P. Tso, *Cooling of mobile electronic devices using phase change materials.* Applied Thermal Engineering, 2004. **24**(2–3): p. 159-169.

84. Teo, H.G., P.S. Lee, and M.N.A. Hawlader, *An active cooling system for photovoltaic modules.* Applied Energy, 2012. **90**(1): p. 309-315.
85. Micheli, L., et al., *Opportunities and challenges in micro- and nano-technologies for concentrating photovoltaic cooling: A review.* Renewable and Sustainable Energy Reviews, 2013. **20**: p. 595-610.
86. Krauter, S., *Increased electrical yield via water flow over the front of photovoltaic panels.* Solar Energy Materials and Solar Cells, 2004. **82**(1–2): p. 131-137.
87. Abdolzadeh, M. and M. Ameri, *Improving the effectiveness of a photovoltaic water pumping system by spraying water over the front of photovoltaic cells.* Renewable Energy, 2009. **34**(1): p. 91-96.
88. Irwan, Y.M., et al., *Indoor Test Performance of PV Panel through Water Cooling Method.* Energy Procedia, 2015. **79**: p. 604-611.
89. Turnpenny, J.R., D.W. Etheridge, and D.A. Reay, *Novel ventilation cooling system for reducing air conditioning in buildings. Part I: Testing and theoretical modelling.* Applied Thermal Engineering, 2000. **20**(11): p. 1019-1037.
90. Zhangbo, Y., et al., *The cooling technology of solar cells under concentrated system.* 2009 IEEE 6th International Power Electronics and Motion Control Conference, 2009. **3**: p. 2193-2197.
91. Belhardj, S., et al., *Using microchannels to cool microprocessors: a transmission-line-matrix study.* Microelectronics Journal, 2003. **34**(4): p. 247-253.
92. Micheli, L., K.S. Reddy, and T.K. Mallick, *Plate Micro-fins in Natural Convection: An Opportunity for Passive Concentrating Photovoltaic Cooling.* Energy Procedia, 2015. **82**: p. 301-308.
93. Clarksean, R. and Y. Chen. *Use of phase change materials for electronic cooling applications: Thermal design issues and example*. in *InterPACK '99: Pacific RIM/ASME International Intersociety Electronics Photonic Packaging Conference 'Advances in Electronic Packaging 1999'*. 1999. United States, Maui, HI, USA: ASME.
94. Krishnan, S. and S.V. Garimella, *Thermal management of transient power spikes in electronics - Phase change energy storage or copper heat sinks?* Journal of Electronic Packaging, Transactions of the ASME, 2004. **126**(3): p. 308-316.
95. Bar-cohen, A. and P. Wang, *Nano-Bio- Electronic, Photonic and MEMS Packaging*. 2010, Boston, MA: Springer US.
96. Baby, R. and C. Balaji, *Experimental investigations on phase change material based finned heat sinks for electronic equipment cooling.* International Journal of Heat and Mass Transfer, 2012. **55**(5-6): p. 1642-1649.
97. Arshad, A., et al., *Thermal performance of phase change material (PCM) based pin-finned heat sinks for electronics devices: Effect of pin thickness and PCM volume fraction.* Applied Thermal Engineering, 2017. **112**: p. 143-155.
98. Alshaer, W.G., et al., *Thermal management of electronic devices using carbon foam and PCM/nano-composite.* International Journal of Thermal Sciences, 2015. **89**: p. 79-86.
99. Alawadhi, E.M. and C.H. Amon, *PCM thermal control unit for portable electronic devices: Experimental and numerical studies.* IEEE Transactions on Components and Packaging Technologies, 2003. **26**(1): p. 116-125.
100. Yeom, J., et al., *3.16 Micro-Coolers.* 2008.
101. Sabbah, R., et al., *Active (air-cooled) vs. passive (phase change material) thermal management of high power lithium-ion packs: Limitation of temperature rise and uniformity of temperature distribution.* Journal of Power Sources, 2008. **182**(2): p. 630-638.
102. Abrahamyan, Y.A., et al., *The efficiency of solar cells immersed in liquid dielectrics.* Solar Energy Materials and Solar Cells, 2002. **73**(4): p. 367-375.
103. Kane, A., V. Verma, and B. Singh, *Optimization of thermoelectric cooling technology for an active cooling of photovoltaic panel.* Renewable and Sustainable Energy Reviews.

104. Nkwetta, D.N. and F. Haghighat, *Thermal energy storage with phase change material—A state-of-the art review.* Sustainable Cities and Society, 2014. **10**(0): p. 87-100.
105. Al-Kayiem, H.H. and S.C. Lin, *Performance evaluation of a solar water heater integrated with a PCM nanocomposite TES at various inclinations.* Solar Energy, 2014. **109**(0): p. 82-92.
106. M., D., *FEI Quanta FEG User Operation Manual*. 2013, FEI Ltd.: Oregon, USA. p. 1-238.
107. Sharma, A., et al., *Review on thermal energy storage with phase change materials and applications.* Renewable and Sustainable Energy Reviews, 2009. **13**(2): p. 318-345.
108. Xu, J., R.Z. Wang, and Y. Li, *A review of available technologies for seasonal thermal energy storage.* Solar Energy, 2014. **103**(0): p. 610-638.
109. Basecq, V., et al., *Short-term storage systems of thermal energy for buildings: a review.* Advances in Building Energy Research, 2013. **7**(1): p. 66-119.
110. Rempel, A.R. and A.W. Rempel, *Rocks, clays, water, and salts: Highly durable, infinitely rechargeable, eminently controllable thermal batteries for buildings.* Geosciences (Switzerland), 2013. **3**(1): p. 63-101.
111. Pinel, P., et al., *A review of available methods for seasonal storage of solar thermal energy in residential applications.* Renewable and Sustainable Energy Reviews, 2011. **15**(7): p. 3341-3359.
112. Pintaldi, S., et al., *Energetic evaluation of thermal energy storage options for high efficiency solar cooling systems.* Applied Energy, 2017. **188**: p. 160-177.
113. Bjurström, H. and B. Carlsson, *An exergy analysis of sensible and latent heat storage.* Journal of Heat Recovery Systems, 1985. **5**(3): p. 233-250.
114. S.A.Vijay Padmaraju, M.V., N.Nallusamy, *Comparitive study of sensible and latent heat storage systems integrated with solar water heating unit* Renewable Energy & Power Quality Journal, 2008. **1**(6): p. 55-60.
115. Kreutz, E.W., et al., *Simulation of micro-channel heat sinks for optoelectronic microsystems.* Microelectronics Journal, 2000. **31**(9–10): p. 787-790.
116. Sahoo, S.K., P. Rath, and M.K. Das, *Numerical study of phase change material based orthotropic heat sink for thermal management of electronics components.* International Journal of Heat and Mass Transfer, 2016. **103**: p. 855-867.
117. Copetti, J.B., et al., *Experiments with micro-fin tube in single phase.* International Journal of Refrigeration, 2004. **27**: p. 876–883.
118. F.Zoggia, S.F., C.Perfetti, G.Lozza, *Environmental friendly heat exchangers* in *7th IIR Gustav Lorenzen Conference on natural Working Fluids, Trondheim, Norway* 2006: Norway
119. Kim, J.S., B.K. Park, and J.S. Lee, *Natural convection heat transfer around microfin arrays.* Experimental Heat Transfer, 2008. **21**(1): p. 55-72.
120. Micheli, L., K.S. Reddy, and T.K. Mallick, *Thermal effectiveness and mass usage of horizontal micro-fins under natural convection.* Applied Thermal Engineering, 2016. **97**: p. 39-47.
121. Shokouhmand, H. and A. Ahmadpour, *Heat Transfer from a Micro Fin Array Heat Sink by Natural Convection and Radiation under Slip Flow Regime.* 2010. **II**.
122. Micheli, L., K.S. Reddy, and T.K. Mallick, *Experimental comparison of micro-scaled plate-fins and pin-fins under natural convection.* International Communications in Heat and Mass Transfer, 2016. **75**: p. 59-66.
123. Micheli, L., K.S. Reddy, and T.K. Mallick, *General correlations among geometry, orientation and thermal performance of natural convective micro-finned heat sinks.* International Journal of Heat and Mass Transfer, 2015. **91**: p. 711-724.
124. Mahmoud, S., et al., *Effect of micro fin geometry on natural convection heat transfer of horizontal microstructures.* Applied Thermal Engineering, 2011. **31**(5): p. 627-633.

125. Kulkarni, D.P. and D.K. Das, *Analytical and numerical studies on microscale heat sinks for electronic applications.* Applied Thermal Engineering, 2005. **25**(14–15): p. 2432-2449.
126. Ventola, L., et al., *Heat Transfer Enhancement by Finned Heat Sinks with Micro-structured Roughness.* Journal of Physics: Conference Series, 2014. **494**(1): p. 012009.
127. Kordás, K., et al., *Chip cooling with integrated carbon nanotube microfin architectures.* Applied Physics Letters, 2007. **90**(12): p. 123105-123105.
128. Mäklin, J., et al., *Solder transfer of carbon nanotube microfin coolers to ceramic chips.* Applied Thermal Engineering, 2014. **65**(1–2): p. 539-543.
129. Yin, S., K.J. Tseng, and J. Zhao, *Design of AlN-based micro-channel heat sink in direct bond copper for power electronics packaging.* Applied Thermal Engineering, 2013. **52**(1): p. 120-129.
130. Gong, L., J. Zhao, and S. Huang, *Numerical study on layout of micro-channel heat sink for thermal management of electronic devices.* Applied Thermal Engineering, 2015. **88**: p. 480-490.
131. Sakanova, A., et al., *Optimization and comparison of double-layer and double-side micro-channel heat sinks with nanofluid for power electronics cooling.* Applied Thermal Engineering, 2014. **65**(1–2): p. 124-134.
132. Do, K.H., et al., *General correlation of a natural convective heat sink with plate-fins for high concentrating photovoltaic module cooling.* Solar Energy, 2012. **86**(9): p. 2725-2734.
133. Micheli, L., et al., *Applicability of silicon micro-finned heat sinks for 500× concentrating photovoltaics systems.* Journal of Materials Science, 2015. **50**(16): p. 5378-5388.
134. Sargunanathan, S., A. Elango, and S.T. Mohideen, *Performance enhancement of solar photovoltaic cells using effective cooling methods: A review.* Renewable and Sustainable Energy Reviews, 2016. **64**: p. 382-393.
135. Rabienataj Darzi, A.A., M. Jourabian, and M. Farhadi, *Melting and solidification of PCM enhanced by radial conductive fins and nanoparticles in cylindrical annulus.* Energy Conversion and Management, 2016. **118**: p. 253-263.
136. Huang, M.J., P.C. Eames, and B. Norton, *Thermal regulation of building-integrated photovoltaics using phase change materials.* International Journal of Heat and Mass Transfer, 2004. **47**(12-13): p. 2715-2733.
137. Huang, M.J., P.C. Eames, and B. Norton, *Phase change materials for limiting temperature rise in building integrated photovoltaics.* Solar Energy, 2006. **80**(9): p. 1121-1130.
138. Wang, P., et al., *Numerical investigation of PCM melting process in sleeve tube with internal fins.* Energy Conversion and Management, 2016. **110**: p. 428-435.
139. Radwan, A., M. Ahmed, and S. Ookawara, *Performance enhancement of concentrated photovoltaic systems using a microchannel heat sink with nanofluids.* Energy Conversion and Management, 2016. **119**: p. 289-303.
140. Yuksel, N., A. Avci, and M. Kilic, *A model for latent heat energy storage systems.* International Journal of Energy Research, 2006. **30**(14): p. 1146-1157.
141. Zalba, B., et al., *Review on thermal energy storage with phase change: materials, heat transfer analysis and applications.* Applied Thermal Engineering, 2003. **23**(3): p. 251-283.
142. Chandel, S.S. and T. Agarwal, *Review of current state of research on energy storage, toxicity, health hazards and commercialization of phase changing materials.* Renewable and Sustainable Energy Reviews, 2017. **67**: p. 581-596.
143. Alva, G., et al., *Thermal energy storage materials and systems for solar energy applications.* Renewable and Sustainable Energy Reviews, 2017. **68, Part 1**: p. 693-706.
144. Veerakumar, C. and A. Sreekumar, *Phase change material based cold thermal energy storage: Materials, techniques and applications - A review.* International Journal of Refrigeration, 2016. **67**: p. 271-289.

145. Kylili, A. and P.A. Fokaides, *Life Cycle Assessment (LCA) of Phase Change Materials (PCMs) for building applications: A review.* Journal of Building Engineering, 2016. **6**: p. 133-143.
146. Khadiran, T., et al., *Advanced energy storage materials for building applications and their thermal performance characterization: A review.* Renewable and Sustainable Energy Reviews, 2016. **57**: p. 916-928.
147. Khan, Z., Z. Khan, and A. Ghafoor, *A review of performance enhancement of PCM based latent heat storage system within the context of materials, thermal stability and compatibility.* Energy Conversion and Management, 2016. **115**: p. 132-158.
148. Zhang, H., et al., *Thermal energy storage: Recent developments and practical aspects.* Progress in Energy and Combustion Science, 2016. **53**: p. 1-40.
149. Hasnain, S.M., *Review on sustainable thermal energy storage technologies, Part I: heat storage materials and techniques.* Energy Conversion and Management, 1998. **39**(11): p. 1127-1138.
150. Voller, V.R., *Fast implicit finite-difference method for the analysis of phase change problems.* Numerical Heat Transfer, Part B: Fundamentals, 1990. **17**(2): p. 155-169.
151. Patankar, S.V., *Numerical heat transfer and fluid flow. Von S. V. Patankar. Hemisphere Publishing Corporation, Washington – New York – London. McGraw Hill Book Company, New York 1980. 1. Aufl., 197 S., 76 Abb., geb., DM 71,90.* Chemie Ingenieur Technik, 1981. **53**(3): p. 225-225.
152. Farid, M.M. and R.M. Husian, *An electrical storage heater using the phase-change method of heat storage.* Energy Conversion and Management, 1990. **30**(3): p. 219-230.
153. Farid, M.M., et al., *A review on phase change energy storage: materials and applications.* Energy Conversion and Management, 2004. **45**(9–10): p. 1597-1615.
154. Kalaiselvam, S., R. Parameshwaran, and S. Harikrishnan, *Analytical and experimental investigations of nanoparticles embedded phase change materials for cooling application in modern buildings.* Renewable Energy, 2012. **39**(1): p. 375-387.
155. Mehling, H., *Heat and cold storage with PCM*. Heat and Mass Transfer, ed. D. Mewes, Mayinger, F. 2008, Germany: Springer Berlin Heidelberg.
156. Iten, M. and S. Liu, *A work procedure of utilising PCMs as thermal storage systems based on air-TES systems.* Energy Conversion and Management, 2014. **77**: p. 608-627.
157. Bruno, F., et al., *Using solid-liquid phase change materials (PCMs) in thermal energy storage systems*, in *Advances in Thermal Energy Storage Systems: Methods and Applications*. 2014, Elsevier Inc. p. 201-246.
158. Cabeza, L.F., *3.07 - Thermal Energy Storage*, in *Comprehensive Renewable Energy*, A. Sayigh, Editor. 2012, Elsevier: Oxford. p. 211-253.
159. Cabeza, L.F., et al., *Materials used as PCM in thermal energy storage in buildings: A review*. Renewable and Sustainable Energy Reviews, 2011. **15**(3): p. 1675-1695.
160. Sharma, S., et al., *Enhancing the performance of BICPV systems using phase change materials.* AIP Conference Proceedings, 2015. **1679**: p. 110003.
161. Su, W., J. Darkwa, and G. Kokogiannakis, *Review of solid–liquid phase change materials and their encapsulation technologies.* Renewable and Sustainable Energy Reviews, 2015. **48**: p. 373-391.
162. Sari, A. and K. Kaygusuz, *Thermal performance of a eutectic mixture of lauric and stearic acids as PCM encapsulated in the annulus of two concentric pipes.* Solar Energy, 2002. **72**(6): p. 493-504.
163. Pasupathy, A., R. Velraj, and R.V. Seeniraj, *Phase change material-based building architecture for thermal management in residential and commercial establishments.* Renewable and Sustainable Energy Reviews, 2008. **12**(1): p. 39-64.
164. Sari, H. and A. Sari, *Thermal and chemical investigation of some fatty acids subjected to accelerated thermal cycle.* Asian Journal of Chemistry, 2006. **18**(2): p. 923-930.

165. Sari, A. and K. Kaygusuz, *Poly(vinyl alcohol)/fatty acid blends for thermal energy storage.* Energy Sources, Part A: Recovery, Utilization and Environmental Effects, 2007. **29**(10): p. 873-883.
166. Sari, A. and K. Kaygusuz, *Studies on poly(vinyl chloride)/fatty acid blends as shape-stabilized phase change material for latent heat thermal energy storage.* Indian Journal of Engineering and Materials Sciences, 2006. **13**(3): p. 253-258.
167. Akgün, M., O. Aydin, and K. Kaygusuz, *Experimental study on melting/solidification characteristics of a paraffin as PCM.* Energy Conversion and Management, 2007. **48**(2): p. 669-678.
168. Zhou, X., J. Mao, and Z. Qiao, *Electroless plating of copper layer on surfaces of urea-formaldehyde microcapsule particles containing paraffin for low infrared emissivity.* Particuology, 2016. **24**: p. 159-163.
169. Zhao, X., P. Liu, and L. Ye, *Synthesis, structure and phase transition property of acrylic acid grafted paraffin.* Journal of Molecular Structure, 2014. **1064**(1): p. 37-43.
170. Zhao, L., et al., *Preparation and properties of paraffin/activated carbon composites as phase change materials for thermal energy storage*, in *2nd International Conference on Energy, Environment and Sustainable Development, EESD 2012*. 2013: Jilin. p. 1049-1053.
171. Zhang, Q. and J. Feng, *Difunctional olefin block copolymer/paraffin form-stable phase change materials with simultaneous shape memory property.* Solar Energy Materials and Solar Cells, 2013. **117**: p. 259-266.
172. Sri Rahayu, A.U., et al., *The effectiveness of organic PCM based on lauric acid from coconut oil and inorganic PCM based on salt hydrate CaCl 2 .6H 2 o as latent heat energy storage system in Indonesia.* Journal of Physics: Conference Series, 2016. **739**(1): p. 012119.
173. Muthuvel, S., et al., *Passive cooling by phase change material usage in construction.* Building Services Engineering Research and Technology, 2015. **36**(4): p. 411-421.
174. Kenisarin, M. and K. Mahkamov, *Passive thermal control in residential buildings using phase change materials.* Renewable and Sustainable Energy Reviews, 2016. **55**: p. 371-398.
175. Farnam, Y., et al., *Evaluating the use of phase change materials in concrete pavement to melt ice and snow.* Journal of Materials in Civil Engineering, 2016. **28**(4).
176. Alizadeh, M. and S.M. Sadrameli, *Development of free cooling based ventilation technology for buildings: Thermal energy storage (TES) unit, performance enhancement techniques and design considerations - A review.* Renewable and Sustainable Energy Reviews, 2016. **58**: p. 619-645.
177. Pintaldi, S., et al., *A review of thermal energy storage technologies and control approaches for solar cooling.* Renewable and Sustainable Energy Reviews, 2015. **41**(0): p. 975-995.
178. Arjun, D. and J. Hayavadana, *Thermal energy storage materials (PCMs) for textile applications.* Journal of Textile and Apparel, Technology and Management, 2014. **8**(4).
179. Sarier, N. and E. Onder, *Organic phase change materials and their textile applications: An overview.* Thermochimica Acta, 2012. **540**: p. 7-60.
180. Sweidan, A., N. Ghaddar, and K. Ghali, *Optimized design and operation of heat-pipe photovoltaic thermal system with phase change material for thermal storage.* Journal of Renewable and Sustainable Energy, 2016. **8**(2).
181. Agrawal, A. and R.M. Sarviya, *A review of research and development work on solar dryers with heat storage.* International Journal of Sustainable Energy, 2016. **35**(6): p. 583-605.
182. Bal, L.M., et al., *Review of solar dryers with latent heat storage systems for agricultural products.* Renewable and Sustainable Energy Reviews, 2011. **15**(1): p. 876-880.
183. Li, Y. and S. Liu, *Experimental study on thermal performance of a solar chimney combined with PCM.* Applied Energy, 2014. **114**(0): p. 172-178.

184. Li, Y. and S. Liu, *Numerical study on thermal behaviors of a solar chimney incorporated with PCM.* Energy and Buildings, 2014. **80**: p. 406-414.
185. Ge, H. and J. Li, *Keeping smartphones cool with gallium phase change material*. Journal of Heat Transfer, 2013. **135**(5).
186. Ling, Z., et al., *Review on thermal management systems using phase change materials for electronic components, Li-ion batteries and photovoltaic modules.* Renewable and Sustainable Energy Reviews, 2014. **31**(0): p. 427-438.
187. Lohse, E. and G. Schmitz, *Performance assessment of regularly structured Composite Latent Heat Storages for temporary cooling of electronic components.* International Journal of Refrigeration, 2012. **35**(4): p. 1145-1155.
188. Gumus, M., *Reducing cold-start emission from internal combustion engines by means of thermal energy storage system.* Applied Thermal Engineering, 2009. **29**(4): p. 652-660.
189. Malik, M., I. Dincer, and M.A. Rosen, *Review on use of phase change materials in battery thermal management for electric and hybrid electric vehicles.* International Journal of Energy Research, 2016. **40**(8): p. 1011-1031.
190. Jankowski, N.R. and F.P. McCluskey, *A review of phase change materials for vehicle component thermal buffering.* Applied Energy, 2014. **113**: p. 1525-1561.
191. Gassenfeit, B. and D. Brüggemann, *Monolithic Masonry with PCM for Thermal Management.* Energy Procedia, 2014. **48**(0): p. 1355-1364.
192. Kalnæs, S.E. and B.P. Jelle, *Phase change materials and products for building applications: A state-of-the-art review and future research opportunities.* Energy and Buildings, 2015. **94**(0): p. 150-176.
193. Fokaides, P.A., A. Kylili, and S.A. Kalogirou, *Phase change materials (PCMs) integrated into transparent building elements: A review.* Materials for Renewable and Sustainable Energy, 2015. **4**(2).
194. de Gracia, A., et al., *Thermal analysis of a ventilated facade with PCM for cooling applications.* Energy and Buildings, 2013. **65**(0): p. 508-515.
195. Kamali, S., *Review of free cooling system using phase change material for building.* Energy and Buildings, 2014. **80**: p. 131-136.
196. Koschenz, M. and B. Lehmann, *Development of a thermally activated ceiling panel with PCM for application in lightweight and retrofitted buildings.* Energy and Buildings, 2004. **36**(6): p. 567-578.
197. Ismail, K.A.R. and J.R. Henríquez, *Thermally effective windows with moving phase change material curtains.* Applied Thermal Engineering, 2001. **21**(18): p. 1909-1923.
198. Mehling, H., et al., *PCM-module to improve hot water heat stores with stratification.* Renewable Energy, 2003. **28**(5): p. 699-711.
199. Cerón, I., J. Neila, and M. Khayet, *Experimental tile with phase change materials (PCM) for building use.* Energy and Buildings, 2011. **43**(8): p. 1869-1874.
200. Nagano, K., et al., *Study of a floor supply air conditioning system using granular phase change material to augment building mass thermal storage—Heat response in small scale experiments.* Energy and Buildings, 2006. **38**(5): p. 436-446.
201. Wang, F., et al., *The novel use of phase change materials in refrigeration plant. Part 1: Experimental investigation.* Applied Thermal Engineering, 2007. **27**(17–18): p. 2893-2901.
202. Mahfuz, M.H., et al., *Performance investigation of thermal energy storage system with Phase Change Material (PCM) for solar water heating application.* International Communications in Heat and Mass Transfer, 2014. **57**(0): p. 132-139.
203. Islam, M.M., et al., *Recent progresses and achievements in photovoltaic-phase change material technology: A review with special treatment on photovoltaic thermal-phase change material systems.* Energy Conversion and Management, 2016. **126**: p. 177-204.
204. Stropnik, R. and U. Stritih, *Increasing the efficiency of PV panel with the use of PCM.* Renewable Energy, 2016. **97**: p. 671-679.

205. Aelenei, L., et al., *Thermal Performance of a Hybrid BIPV-PCM: Modeling, Design and Experimental Investigation.* Energy Procedia, 2014. **48**: p. 474-483.
206. Browne, M.C., B. Norton, and S.J. McCormack, *Phase change materials for photovoltaic thermal management.* Renewable and Sustainable Energy Reviews, 2015. **47**(0): p. 762-782.
207. Hasan, A., et al., *Evaluation of phase change materials for thermal regulation enhancement of building integrated photovoltaics.* Solar Energy, 2010. **84**(9): p. 1601-1612.
208. Hendricks, J.H.C. and W.G.J.H.M. Van Sark, *Annual performance enhancement of building integrated photovoltaic modules by applying phase change materials.* Progress in Photovoltaics: Research and Applications, 2013. **21**(4): p. 620-630.
209. Rosenthal, A.H., et al. *Phase-change material to thermally regulate photovoltaic panels to improve solar to electric efficiency*. in *ASME 2015 International Mechanical Engineering Congress and Exposition, IMECE 2015*. 2015. American Society of Mechanical Engineers (ASME).
210. Enibe, S.O., *Performance of a natural circulation solar air heating system with phase change material energy storage.* Renewable Energy, 2002. **27**(1): p. 69-86.
211. Sweet, T.K.N., et al., *Scalable solar thermoelectrics and photovoltaics (SUNTRAP).* AIP Conference Proceedings, 2016. **1766**(1): p. 080007.
212. Hasan, A., et al., *Energy and Cost Saving of a Photovoltaic-Phase Change Materials (PV-PCM) System through Temperature Regulation and Performance Enhancement of Photovoltaics.* Energies, 2014. **7**(3): p. 1318-1331.
213. GmbH, R.T., *Technical Data sheet RT50*, http://www.rubitherm.eu/media/products/datasheets/Techdata_-RT50_EN.PDF, Editor. 2013: Rubitherm Technologies GmbH - Sperenberger Str.5a - 12277 Berlin. p. 1.
214. Hasan, A. and A.A. Sayigh, *Some fatty acids as phase-change thermal energy storage materials.* Renewable Energy, 1994. **4**(1): p. 69-76.
215. Vanderbilt, D., *Phase segregation and work-function variations on metal surfaces: spontaneous formation of periodic domain structures.* Surface Science, 1992. **268**(1-3): p. L300-L304.
216. Farrell, A.J., B. Norton, and D.M. Kennedy, *Corrosive effects of salt hydrate phase change materials used with aluminium and copper.* Journal of Materials Processing Technology, 2006. **175**(1–3): p. 198-205.
217. García-Romero, A., et al., *Corrosion behaviour of several aluminium alloys in contact with a thermal storage phase change material based on Glauber's salt.* Corrosion Science, 2009. **51**(6): p. 1263-1272.
218. Kaygusuz, K., *The viability of Thermal Energy Storage.* Energy Sources, 1999. **21**(8): p. 745-755.
219. Nayak, K.C., et al., *A numerical model for heat sinks with phase change materials and thermal conductivity enhancers.* International Journal of Heat and Mass Transfer, 2006. **49**(11-12): p. 1833-1844.
220. Sahoo, S.K., M.K. Das, and P. Rath, *Application of TCE-PCM based heat sinks for cooling of electronic components: A review.* Renewable and Sustainable Energy Reviews, 2016. **59**: p. 550-582.
221. Kumar, A. and S.K. Saha, *Energy and exergy analyses of medium temperature latent heat thermal storage with high porosity metal matrix.* Applied Thermal Engineering, 2016.
222. Ling, Z., et al., *Review on thermal management systems using phase change materials for electronic components, Li-ion batteries and photovoltaic modules.* Renewable and Sustainable Energy Reviews, 2014. **31**: p. 427-438.
223. Fan, L. and J.M. Khodadadi, *Thermal conductivity enhancement of phase change materials for thermal energy storage: A review.* Renewable and Sustainable Energy Reviews, 2011. **15**(1): p. 24-46.

224. Baby, R. and C. Balaji, *Thermal management of electronics using phase change material based pin fin heat sinks.* 6th European Thermal Sciences Conference, Eurotherm 2012, 2012. **395**(1).
225. Atkin, P. and M.M. Farid, *Improving the efficiency of photovoltaic cells using PCM infused graphite and aluminium fins.* Solar Energy, 2015. **114**(0): p. 217-228.
226. Kim, K.T., et al., *Graphene coated with alumina and its utilization as a thermal conductivity enhancer for alumina sphere/thermoplastic polyurethane composite.* Materials Chemistry and Physics, 2015. **153**: p. 291-300.
227. Zhou, M., et al., *Heat transport enhancement of thermal energy storage material using graphene/ceramic composites.* Carbon, 2014. **75**: p. 314-321.
228. Liang, W., et al., *Graphene-nickel/n-carboxylic acids composites as form-stable phase change materials for thermal energy storage.* Solar Energy Materials and Solar Cells, 2014. **132**: p. 425-430.
229. Zhong, Y., et al., *Effect of graphene aerogel on thermal behavior of phase change materials for thermal management.* Solar Energy Materials and Solar Cells, 2013. **113**: p. 195-200.
230. Yavari, F., et al., *Enhanced thermal conductivity in a nanostructured phase change composite due to low concentration graphene additives.* Journal of Physical Chemistry C, 2011. **115**(17): p. 8753-8758.
231. Liu, X., J. Tie, and S. Tie, *Energy storage properties of mans nitro phase transition materials of multi-walled carbon nano-tubes of greenhouse.* Nongye Gongcheng Xuebao/Transactions of the Chinese Society of Agricultural Engineering, 2016. **32**(6): p. 226-231.
232. Tebaldi, M.L., R.M. Belardi, and S.R. Montoro, *Polymers with Nano-Encapsulated Functional Polymers: Encapsulated Phase Change Materials. Encapsulated Phase Change Materials*, in *Design and Applications of Nanostructured Polymer Blends and Nanocomposite Systems*. 2015, Elsevier Inc. p. 155-169.
233. Ye, F., et al., *Multi-walled carbon nanotubes added to Na2CO3/MgO composites for thermal energy storage.* Particuology, 2014. **15**(0): p. 56-60.
234. Liu, M., M.C. Lin, and C. Wang, *Enhancements of thermal conductivities with Cu, CuO, and carbon nanotube nanofluids and application of MWNT/water nanofluid on a water chiller system.* Nanoscale Res Lett, 2011. **6**(1): p. 297.
235. Venkata Sastry, N.N., et al., *Predicting the effective thermal conductivity of carbon nanotube based nanofluids.* Nanotechnology, 2008. **19**(5): p. 055704-055704.
236. Karkri, M., et al., *Improvement of thermal conductivity of paraffin by adding expanded graphite.* Journal of Composite Materials, 2016. **50**(19): p. 2589-2601.
237. Shin, H.K., K.Y. Rhee, and S.J. Park, *Effects of exfoliated graphite on the thermal properties of erythritol-based composites used as phase-change materials.* Composites Part B: Engineering, 2016. **96**: p. 350-353.
238. Raza, G., Y. Shi, and Y. Deng. *Expanded graphite as thermal conductivity enhancer for paraffin wax being used in thermal energy storage systems*. in *13th International Bhurban Conference on Applied Sciences and Technology, IBCAST 2016*. 2016. Institute of Electrical and Electronics Engineers Inc.
239. Khodadadi, J.M., L. Fan, and H. Babaei, *Thermal conductivity enhancement of nanostructure-based colloidal suspensions utilized as phase change materials for thermal energy storage: A review.* Renewable and Sustainable Energy Reviews, 2013. **24**: p. 418-444.
240. Sarı, A., *Form-stable paraffin/high density polyethylene composites as solid–liquid phase change material for thermal energy storage: preparation and thermal properties.* Energy Conversion and Management, 2004. **45**(13–14): p. 2033-2042.
241. Sari, A. and A. Karaipekli, *Thermal conductivity and latent heat thermal energy storage characteristics of paraffin/expanded graphite composite as phase change material.* Applied Thermal Engineering, 2007. **27**(8-9): p. 1271-1277.

242. Tian, H.Q., et al., *Preparation and properties of high thermal conductivity Mg/CaCl2 materials for heat storage and transfer*. Kung Cheng Je Wu Li Hsueh Pao/Journal of Engineering Thermophysics, 2016. **37**(8): p. 1728-1731.
243. Swaminathan Gopalan, K. and V. Eswaran, *Numerical investigation of thermal performance of PCM based heat sink using structured porous media as thermal conductivity enhancers.* International Journal of Thermal Sciences, 2016. **104**: p. 266-280.
244. Alshaer, W.G., et al., *An experimental investigation of using carbon foam–PCM–MWCNTs composite materials for thermal management of electronic devices under pulsed power modes.* Heat and Mass Transfer/Waerme- und Stoffuebertragung, 2016: p. 1-11.
245. Li, Y., S. Liu, and A. Shukla, *Experimental analysis on use of thermal conductivity enhancers (TCEs) for solar chimney applications with energy storage layer*. Energy and Buildings, 2016. **116**: p. 35-44.
246. Zamengo, M., et al., *Thermal conductivity measurements of expanded graphite-magnesium hydroxide composites for packed bed reactors of chemical heat storage/pump systems.* Journal of Chemical Engineering of Japan, 2016. **49**(3): p. 261-267.
247. Bose, P. and V.A. Amirtham, *A review on thermal conductivity enhancement of paraffinwax as latent heat energy storage material.* Renewable and Sustainable Energy Reviews, 2016. **65**: p. 81-100.
248. Zhang, G., *Nanowire Applications : Thermoelectric Cooling and Energy Harvesting.* 2008.
249. Zeng, J.-L., et al., *Effects of copper nanowires on the properties of an organic phase change material.* Solar Energy Materials and Solar Cells, 2012. **105**(0): p. 174-178.
250. Zeng, J.L., et al., *Study of a PCM based energy storage system containing Ag nanoparticles.* Journal of Thermal Analysis and Calorimetry, 2007. **87**(2): p. 371-375.
251. Zabalegui, A., D. Lokapur, and H. Lee, *Nanofluid PCMs for thermal energy storage: Latent heat reduction mechanisms and a numerical study of effective thermal storage performance*. International Journal of Heat and Mass Transfer, 2014. **78**(0): p. 1145-1154.
252. Yuan, L., et al., *Ethylene ¯ame synthesis of well-aligned multi-walled carbon nanotubes.* 2001. **346**(September): p. 23-28.
253. Yuan, H., H. Bai, and Y. Wang. *Preparation and characterization of stearic acid/SiO2 nano-encapsulated phase change materials via sol-gel method*. in *Energy Technology 2016: Carbon Dioxide Management and Other Technologies - TMS 2016: 145th Annual Meeting and Exhibition*. 2016. Minerals, Metals and Materials Society.
254. Yu, W. and H. Xie, *A Review on Nanofluids: Preparation, Stability Mechanisms, and Applications.* Journal of Nanomaterials, 2012. **2012**: p. 1-17.
255. Yu, S., et al., *Bio-based PCM/carbon nanomaterials composites with enhanced thermal conductivity.* Solar Energy Materials and Solar Cells, 2014. **120**: p. 549-554.
256. Yang, X.F., Z.-H. Liu, and J. Zhao, *Heat transfer performance of a horizontal micro-grooved heat pipe using CuO nanofluid*. Journal of Micromechanics and Microengineering, 2008. **18**(3): p. 035038-035038.
257. Li, H., et al., *Development of thermal energy storage composites and prevention of PCM leakage.* Applied Energy, 2014. **135**(0): p. 225-233.
258. Ramakrishnan, S., et al., *A novel paraffin/expanded perlite composite phase change material for prevention of PCM leakage in cementitious composites.* Applied Energy, 2015. **157**: p. 85-94.
259. Fang, G., F. Tang, and L. Cao, *Preparation, thermal properties and applications of shape-stabilized thermal energy storage materials.* Renewable and Sustainable Energy Reviews, 2014. **40**: p. 237-259.

260. Zhang, Y.Z.W.L.R.Y.Y.Z.a.Q., *Preparation and Thermal Property of Phase Change Material Microcapsules by Phase Separation.* Materials Science Forum, 2007. **561-565**(2007): p. 2293-2296.
261. Salunkhe, P.B. and P.S. Shembekar, *A review on effect of phase change material encapsulation on the thermal performance of a system.* Renewable and Sustainable Energy Reviews, 2012. **16**(8): p. 5603-5616.
262. McCann, J.T., M. Marquez, and Y. Xia, *Melt Coaxial Electrospinning: A Versatile Method for the Encapsulation of Solid Materials and Fabrication of Phase Change Nanofibers.* Nano Letters, 2006. **6**(12): p. 2868-2872.
263. Inaba, H., *New challenge in advanced thermal energy transportation using functionally thermal fluids.* International Journal of Thermal Sciences, 2000. **39**(9): p. 991-1003.
264. Ho, C.J., A.O. Tanuwijava, and C.-M. Lai, *Thermal and electrical performance of a BIPV integrated with a microencapsulated phase change material layer.* Energy and Buildings, 2012. **50**(0): p. 331-338.
265. Porisini, F.C., *Salt hydrates used for latent heat storage: Corrosion of metals and reliability of thermal performance.* Solar Energy, 1988. **41**(2): p. 193-197.
266. Mehling, H. and L.F. Cabeza, *Phase change materials and their basic properties*, in *Thermal Energy Storage for Sustainable Energy Consumption: Fundamentals, Case Studies and Design*, H.Ö. Paksoy, Editor. 2007, Springer Netherlands: Dordrecht. p. 257-277.
267. Rashidi, L. and K. Khosravi-Darani, *The applications of nanotechnology in food industry.* Crit Rev Food Sci Nutr, 2011. **51**(8): p. 723-30.
268. Weiss, J., P. Takhistov, and D.J. McClements, *Functional Materials in Food Nanotechnology.* Journal of Food Science, 2006. **71**(9): p. R107-R116.
269. FAO/WHO, *FAO/WHO Expert meeting on the application of nanotechnologies in the food and agriculture sectors: potential food safety implications.* Agriculture and Consumer Protection, 2010.
270. Cushen, M., et al., *Nanotechnologies in the food industry – Recent developments, risks and regulation.* Trends in Food Science & Technology, 2012. **24**(1): p. 30-46.
271. Khodadadi, J.M. and S.F. Hosseinizadeh, *Nanoparticle-enhanced phase change materials (NEPCM) with great potential for improved thermal energy storage.* International Communications in Heat and Mass Transfer, 2007. **34**(5): p. 534-543.
272. Hussain H. Al-Kayiem, S.C.L.a.A.L., *Review on Nanomaterials for Thermal Energy Storage Technologies.* Nanoscience & Nanotechnology Asia, 2013. **3**(1): p. 60 - 71.
273. Jeong, S.G., et al., *Improvement of the thermal properties of Bio-based PCM using exfoliated graphite nanoplatelets.* Solar Energy Materials and Solar Cells, 2013. **117**(0): p. 87-92.
274. Colla, L., et al., *Nano-PCMs for enhanced energy storage and passive cooling applications.* Applied Thermal Engineering, 2017. **110**: p. 584-589.
275. Devi, A.B., et al., *Novel synthesis and characterization of CuO nanomaterials: Biological applications.* Chinese Chemical Letters, 2014. **25**(12): p. 1615-1619.
276. Eckert, E.R.G., et al., *Heat transfer-a review of 1983 literature.* International Journal of Heat and Mass Transfer, 1984. **27**(12): p. 2179-2214.
277. Yousef, A., et al., *Inactivation of pathogenic Klebsiella pneumoniae by CuO/TiO2 nanofibers: A multifunctional nanomaterial via one-step electrospinning.* Ceramics International, 2012. **38**(6): p. 4525-4532.
278. Tran, T.H. and V.T. Nguyen, *Copper Oxide Nanomaterials Prepared by Solution Methods, Some Properties, and Potential Applications: A Brief Review.* International Scholarly Research Notices, 2014. **2014**: p. 14.
279. Phiwdang, K., et al., *Synthesis of CuO Nanoparticles by Precipitation Method Using Different Precursors.* Energy Procedia, 2013. **34**: p. 740-745.
280. Ren, G., et al., *Characterisation of copper oxide nanoparticles for antimicrobial applications.* International Journal of Antimicrobial Agents, 2009. **33**(6): p. 587-590.

281. Liu, X., et al., *Morphology- and facet-controlled synthesis of CuO micro/nanomaterials and analysis of their lithium ion storage properties.* Journal of Power Sources, 2016. **312**: p. 199-206.
282. Liu, Y., et al., *Facile fabrication of CuO nanosheets on Cu substrate as anode materials for electrochemical energy storage.* Journal of Alloys and Compounds, 2014. **586**: p. 208-215.
283. Zhang, Q., et al., *CuO nanostructures: Synthesis, characterization, growth mechanisms, fundamental properties, and applications.* Progress in Materials Science, 2014. **60**: p. 208-337.
284. Dhaidan, N.S., et al., *Experimental and numerical study of constrained melting of n-octadecane with CuO nanoparticle dispersions in a horizontal cylindrical capsule subjected to a constant heat flux.* International Journal of Heat and Mass Transfer, 2013. **67**: p. 523-534.
285. Li, Y. and S. Liu, *Effects of different thermal conductivity enhancers on the thermal performance of two organic phase-change materials: Paraffinwax RT42 and RT25.* Journal of Enhanced Heat Transfer, 2013. **20**(6): p. 463-473.
286. AlMaadeed, M.A., et al., *Effect of expanded graphite on the phase change materials of high density polyethylene/wax blends.* Thermochimica Acta, 2015. **600**: p. 35-44.
287. Moghadassi, A.R., S.M. Hosseini, and D.E. Henneke, *Effect of CuO Nanoparticles in Enhancing the Thermal Conductivities of Monoethylene Glycol and Paraffin Fluids.* Industrial & Engineering Chemistry Research, 2010. **49**(4): p. 1900-1904.
288. Putra, N., E. Prawiro, and M. Amin, *Thermal properties of beeswax/CuO nano phase-change material used for thermal energy storage.* International Journal of Technology, 2016. **7**(2): p. 244-253.
289. Arasu, A., A. Sasmito, and A. Mujumdar, *Thermal performance enhancement of paraffin wax with Al2O3 and CuO nanoparticles–a numerical study.* Frontiers in Heat and Mass Transfer (FHMT), 2012. **2**(4).
290. Purohit, R., et al., *Carbon Nanotubes and Their Growth Methods.* Procedia Materials Science, 2014. **6**(0): p. 716-728.
291. De Volder, M.F.L., et al., *Carbon Nanotubes: Present and Future Commercial Applications.* Science, 2013. **339**(6119): p. 535-539.
292. Harris, P.J. and P.J.F. Harris, *Carbon nanotube science: synthesis, properties and applications*. 2009: Cambridge University Press.
293. Dürkop, T., et al., *Extraordinary Mobility in Semiconducting Carbon Nanotubes.* Nano Letters, 2003. **4**(1): p. 35-39.
294. Ebbesen, T.W., et al., *Electrical conductivity of individual carbon nanotubes.* Nature, 1996. **382**(6586): p. 54-56.
295. Pop, E., et al., *Thermal Conductance of an Individual Single-Wall Carbon Nanotube above Room Temperature.* Nano Letters, 2005. **6**(1): p. 96-100.
296. Han, Z. and A. Fina, *Thermal conductivity of carbon nanotubes and their polymer nanocomposites: A review.* Progress in Polymer Science, 2011. **36**(7): p. 914-944.
297. Berber, S., Y. Kwon, and D. Tomanek, *Unusually high thermal conductivity of carbon nanotubes.* Physical review letters, 2000. **84**(20): p. 4613-6.
298. Carrara, S., *Nano-Bio-Technology and Sensing Chips: New Systems for Detection in Personalized Therapies and Cell Biology.* Sensors, 2010. **10**(1): p. 526.
299. Sun, B., *Deformation, Vibration, Buckling of Continuum Nanotorus.* Journal of Nanomaterials, 2010. **2010**: p. 6.
300. Pachfule, P., et al., *Fabrication of carbon nanorods and graphene nanoribbons from a metal–organic framework.* Nat Chem, 2016. **8**(7): p. 718-724.
301. Assael, M.J., et al., *Thermal Conductivity of Suspensions of Carbon Nanotubes in Water.* International Journal of Thermophysics, 2004. **25**(4): p. 971-985.

302. Mallick, T.K., P.C. Eames, and B. Norton, *Using air flow to alleviate temperature elevation in solar cells within asymmetric compound parabolic concentrators.* Solar Energy, 2007. **81**(2): p. 173-184.
303. Badiee, A., I.A. Ashcroft, and R.D. Wildman, *The thermo-mechanical degradation of ethylene vinyl acetate used as a solar panel adhesive and encapsulant.* International Journal of Adhesion and Adhesives, 2016. **68**: p. 212-218.
304. Burger, D.R. and E.F. Cuddihy, *Vacuum Lamination of Photovoltaic Modules*, in *Polymers in Solar Energy Utilization*. 1983, American Chemical Society. p. 407-419.
305. Czanderna, A.W. and F.J. Pern, *Encapsulation of PV modules using ethylene vinyl acetate copolymer as a pottant: A critical review.* Solar Energy Materials and Solar Cells, 1996. **43**(2): p. 101-181.
306. Carroll, W.F. and P. Schissel, *Polymers in Solar Energy: Applications and Opportunities*, in *Polymers in Solar Energy Utilization*. 1983, American Chemical Society. p. 3-18.
307. Kempe, M. *Overview of scientific issues involved in selection of polymers for PV applications*. in *Photovoltaic Specialists Conference (PVSC), 2011 37th IEEE*. 2011.
308. Kempe, M.D. *Accelerated UV test methods and selection criteria for encapsulants of photovoltaic modules*. in *Photovoltaic Specialists Conference, 2008. PVSC '08. 33rd IEEE*. 2008.
309. Corporation, D.C. *Product Information Sylgard® 184 Silicone Elastomer*. [Product Information] 2014 2014, April 2 [cited 2016 30 Oct 2016]; Available from: http://www.dowcorning.com/DataFiles/090276fe80190b08.pdf.
310. Corporation, D.C. *Product safety data sheet Dow Corning® 92-023 Primer*. Products : Product Finder 2016 [cited 2016 12 Mar 2016]; Available from: http://www.dowcorning.com/applications/search/default.aspx?R=141EN.
311. Sharma, S., et al., *Performance enhancement of a Building-Integrated Concentrating Photovoltaic system using phase change material.* Solar Energy Materials and Solar Cells, 2016. **149**: p. 29-39.
312. Shuja, S.Z., B.S. Yilbas, and M.M. Shaukat, *Melting enhancement of a phase change material with presence of a metallic mesh.* Applied Thermal Engineering, 2015. **79**(Supplement C): p. 163-173.
313. Mustaffar, A., A. Harvey, and D. Reay, *Melting of phase change material assisted by expanded metal mesh.* Applied Thermal Engineering, 2015. **90**(Supplement C): p. 1052-1060.
314. Zain-ul-abdein, M., et al., *Numerical investigation of the effect of interfacial thermal resistance upon the thermal conductivity of copper/diamond composites.* Materials & Design, 2015. **86**: p. 248-258.
315. Stratasys. *uPrint SE Plus Bigger and bolder*. uPrint SE Plus 2017 [cited 2017 12 Feb 2017]; Available from: http://www.stratasys.com/3d-printers/idea-series/uprint-se-plus.
316. Schaufler, M., *Super solar simulator specification*, W.E.c. Ltd, Editor. 2013, Voss electronic, GmbH: Germany.
317. Voss electronic, G. *HelioCon product specification*. 2017 [cited 2017 25 Jan 2017]; Available from: http://www.vosselectronic.de/62-heliocon/114-heliocon.
318. NETZSCH-GerätebauGmbH, *DSC 214 Polyma:The System Solution for Efficient Characterization of Polymers*, N.-G. GmbH, Editor., NETZSCH-Gerätebau GmbH: Germany.
319. GmbH, N.-G. *Differential Scanning Calorimetry DSC 214 Polyma-Method, Technique, Applications*. 2015 [cited 2016 27 Nov 2016]; Available from: https://www.netzsch-thermal-analysis.com/en/products-solutions/differential-scanning-calorimetry/dsc-214-polyma/.
320. Microscopy Core Facility, U.S.U. *FEI Quanta FEG 650 Manual*. FEI Quanta FEG 650 Manual 2014 [cited 2016 20 Feb 2016]; Available from: http://rgs.usu.edu/microscopy/wp-content/uploads/sites/28/2015/08/SEM_user_manual.pdf.

321. Company, F. *Quanta 650 datasheet*. Quanta 650 datasheet 2015 [cited 2016 20 Oct 2016]; Available from: https://www.fei.com/documents/quanta-650-datasheet/.
322. Incorporation, K.i., *Electrical Characterization of Photovoltaic Materials and Solar Cells with the Model 4200-SCS Semiconductor Characterization System*. 2010, Keithley instruments, inc.: Cleveland, Ohio,USA. p. 16.
323. Blood, P. and J.W. Orton, *The electrical characterisation of semiconductors.* Reports on Progress in Physics, 1978. **41**(2): p. 157.
324. Parthasarathy, S., et al., *Investigations on the Outdoor Performance Characteristics of Multicrystalline Silicon Solar Cell and Module.* Conference Papers in Energy, 2013. **2013**: p. 4.
325. Standards, V. *Solar reference cells product specifications*. 2008 [cited 2016 09 Nov 2016]; Available from: http://www.vlsistandards.com/products/solar/SRC.asp?SID=108.
326. Barreneche, C., et al., *Study on differential scanning calorimetry analysis with two operation modes and organic and inorganic phase change material (PCM).* Thermochimica Acta, 2013. **553**(0): p. 23-26.
327. J. Schawe, R.R., J. Widmann, M. Schubnell, U. Jörimann, *Interpreting DSC curves Part 1: Dynamic measurements*, in *UserCom 1/2000*, 1/2000, Editor. 2000, Mettler Toledo GmbH, Analytical: Schweiz.
328. Moukhina, E., *Enthalpy calibration for wide DSC peaks.* Thermochimica Acta, 2011. **522**(1–2): p. 96-99.
329. Price, D.M., *Temperature calibration of differential scanning calorimeters.* Journal of thermal analysis, 1995. **45**(6): p. 1285-1296.
330. Nassu, R.T. and L.A. Guaraldo Gonçalves, *Determination of melting point of vegetable oils and fats by differential scanning calorimetry (DSC) technique.* 1999, 1999. **50**(1): p. 6.
331. Jayalakshmi, V., et al., *Characterisation of paraffin waxes by dsc and high temperature gc.* Petroleum Science and Technology, 1999. **17**(7-8): p. 843-856.
332. Kim, K.H., et al., *Charging Effects on SEM/SIM Contrast of Metal/Insulator System in Various Metallic Coating Conditions.* MATERIALS TRANSACTIONS, 2010. **51**(6): p. 1080-1083.
333. Goldstein, J.I., et al., *The SEM and Its Modes of Operation*, in *Scanning Electron Microscopy and X-ray Microanalysis: Third Edition*. 2003, Springer US: Boston, MA. p. 21-60.
334. Inc., H.M.A.S., *Semi-Quantitative Analysis by XRD*, in *Semi-Quantitative Analysis Application Note*. 2002, H & M Analytical Services, Inc.: NJ, USA.
335. Mattei, M., et al., *Calculation of the polycrystalline PV module temperature using a simple method of energy balance.* Renewable Energy, 2006. **31**(4): p. 553-567.
336. Karunamurthy, K., K. Murugumohankumar, and S. Suresh, *Use of CuO nano-material for the improvement of thermal conductivity and performance of low temperature energy storage system of solar pond.* Digest Journal of Nanomaterials and Biostructures, 2012. **7**(4): p. 1833-1841.
337. Etefagh, R., E. Azhir, and N. Shahtahmasebi, *Synthesis of CuO nanoparticles and fabrication of nanostructural layer biosensors for detecting Aspergillus niger fungi.* Scientia Iranica, 2013. **20**(3): p. 1055-1058.
338. Reddy, T.A., *Applied Data Analysis and Modeling for Energy Engineers and Scientists*. 1 ed. Vol. 1. 2011: Springer US. XXI, 430.
339. Corcione, M., *Heat transfer correlations for free convection from upward-facing horizontal rectangular surfaces* WSEAS Trans. Heat Mass Transf, 2007. **2**(3): p. 48-60.
340. Sarmah, N., *Design and Performance Evaluation of a Low Concentrating Line-axis Dielectric Photovoltaic System*, in *Institute of Mechanical, Process and Energy Engineering*. 2012, Heriot-Watt University: Edinburgh, United Kingdom. p. 248.

341. Agency, I.E., *Snapshot of Global Photovoltaic Markets 2017*, in *International Energy Agency Photovoltaic Power System Programme (IEA PVPS)* G. Masson, Editor. 2017, International Energy Agency Switzerland.